UNIVERSITY OF CALIFORNIA
RIVERSIDE

Secondary Organic Aerosol Formation from Gasoline Direct Injection Vehicles: The Impact of Exhaust After-Treatment and Fuel Composition

A Dissertation submitted in partial satisfaction
of the requirements for the degree of

Doctor of Philosophy

in

Chemical & Environmental Engineering

by

Patrick Richard Roth

December 2018

Dissertation Committee:
Dr. Akua Asa-Awuku, Chairperson
Dr. Georgios Karavalakis
Dr. David R. Cocker III
Dr. Kelley Barsanti

The Dissertation of Patrick Richard Roth is approved:

_____

_____

_____

_____

Committee Chairperson

University of California, Riverside

Acknowledgements:

I would first like to thank and recognize my advisor, Dr. Akua Asa-Awuku for her endless support and guidance throughout my Ph.D. program. You were always available to help with revisions for writing and presentations, and also helping me decipher my data. Additionally, you have an innate ability to break down complex concepts and present them in a simple and understandable manner. These skills have been instilled in me throughout my graduate studies and has been invaluable in helping me improve both my presentation and writing styles.

I would also like to thank Dr. Georgios Karavalakis as another vital contributor to my success. You have been a great inspiration and have provided me with many tools that helped me through my graduate studies and will continue to help me throughout my career. You always made sure to push me to accomplish more, and to produce the highest quality work possible. You were instrumental in involving me in presentations early in my studies, which ultimately allowed me to grow as a presenter and a person.

I would also like to thank Dr. David Cocker for teaching me so much about the field of atmospheric chemistry. You have really pushed me as a student, from taking your classes to getting help from you in regards to my research. You have been a great resource to my success and I am grateful for your generosity with your time. In addition, I would also like to thank my final committee member Dr. Kelley Barsanti. Similar to David, you were always willing to help me with any questions I had which helped increase my understanding of the field.

I would also like to extend a thank you to particular CE-CERT faculty such as Kurt Bumiller, Mark Villela, and Daniel Gomez in addition to my numerous colleagues throughout my graduate school years; including Paul, Mary, Diep, Xinze, Derek, Weihan, Christos, Tyler, and Ayla. I would also like to acknowledge the MBBA for helping me ride the proverbial graduate school wave and not allowing my problems to go overhead.

I would like to recognize the funding sources throughout the various projects conducted that are detailed in this dissertation. First I would like to acknowledge my personal funding which came from the NCST Graduate Fellowship, NSF Atmospheric Chemistry (1151893), and the Esther F. Hays Graduate Fellowship. Next I would like to acknowledge Southern California Air Quality Management District (chapters 2, 3, and 5), Manufacturers of Emission Controls Association (chapter 2, and 5), ICM Inc (chapters 3, and 5), and Growth Energy (chapters 4, and 5).

Chapter 2, part or in full, is a reprint of the material as it appears in the Environmental Science & Technology, Patrick Roth, Jiacheng Yang, David Cocker, Thomas Durbin, Rasto Brezny Michael Geller, Akua Asa-Awuku, Georgios Karavalakis. "Catalyzed Gasoline Particulate Filters Reduce Secondary Organic Aerosol Production from Gasoline Direct Injection Vehicles". Environmental Science & Technology (under review).

Chapters 3, 4, and 5 will also be part or in full, submitted into academic journals upon completion.

Dedicated to:

My Parents & Sister

ABSTRACT OF THE DISSERTATION

Secondary Organic Aerosol Formation from Gasoline Direct Injection Vehicles: The Impacts of Exhaust After-Treatment and Fuel Content

by

Patrick Richard Roth

Doctor of Philosophy, Graduate Program in Chemical & Environmental Engineering
University of California, Riverside, December 2018
Dr. Akua Asa-Awuku, Chairperson

A majority of atmospheric aerosol in urban areas is attributed to transportation emissions, and particularly, gasoline vehicle emissions. The particulate matter (PM) emitted directly from the tailpipe consists of primary organic aerosol (POA) and black carbon. In addition to the particulate emissions, common gaseous pollutants include, nitrogen oxides (NOx), and non-methane organic gases (NMOG), which can photochemically react in the atmosphere to produce secondary organic aerosol (SOA).

SOA formation from gasoline vehicles has received considerable attention in recent years, with the majority of studies focusing on older technology port-fuel injection (PFI) engines. There is limited information on the SOA formation from current technology gasoline direct injection (GDI) engines, despite the abundance of information on the primary emissions from these engines. GDI technology is considered a major pathway to reduce greenhouse gas emissions. However, GDI engines have been measured to emit increased PM mass when compared to similar PFI engines. To counteract the increased

PM emissions, manufacturers and regulators may need to utilize various emission control strategies. The goal of this work was to investigate the effects of select emission control strategies on the secondary aerosol potential of newer technology GDI vehicles.

First, the effects of a catalyzed gasoline particulate filter (GPF) were explored. The addition of a GPF has shown drastic reduction in tailpipe PM mass for GDI vehicles, however its effect on secondary emissions were unknown. This study aided to understand if a catalyzed GPF is effective in the removal of secondary aerosol precursors, thus increasing the significance of the after-treatment technology. Next, the impacts of high ethanol fuel blends, and varying driving conditions on secondary aerosol were assessed. This study analyzed the variations in composition and morphology of the emissions from vehicles operated on 10% to 78% ethanol fuels (% volume). In addition to the effects of vehicle exhaust from high ethanol fuel blends, this study investigated how a controlled surrogate environment can affects the reaction potential of vehicle exhaust. The effects of aromatic and ethanol content were further explored with lower ethanol blends (0%-20% by volume). These fuels were more similar to current commercial fuel blends and focused on the effects of smaller variations in ethanol and aromatic content on the physicochemical properties of the secondary aerosol. Finally, connections between the different vehicle certification standards, fuels, driving cycles, and reaction conditions were explored to form relationships between measured tailpipe emission concentrations and the resulting SOA formation potential from vehicles.

Table of Contents:

List of Figures:

List of Tables:

Chapter 1: Introduction & Motivation

1.1. Motivation:

Clean air is fundamental for overall human and environmental health. Since the industrial era, in the late 18th century, technological advancement has relied on the burning of various fuel sources to meet the power demands for new manufacturing processes (fossil fuel, coal, wood, etc.). Burning these fuels increases atmospheric pollution and contributed to the illness and the death of people during significant pollution episodes; Donora, USA in 1948 (20 deaths) (Hamill, 2008), London, England in 1952 (4,000-12,000 deaths estimated) (Davis, 2002), and as recently as 2013 in Northeastern China. These events were attributed to anthropogenic emissions (human-made) paired with meteorological events, leading agencies like the Environmental Protection Agency (EPA) and the United Nations (UN), to regulate acceptable, ambient levels of pollutants.

Even with regulations in place, in 2005 the World Health Organization (WHO) attributed seven million premature deaths each year to air pollution (World Health Organization, 2007). Particulate matter (PM), in particular, is a key pollutant that has been found to cause a variety of cardiovascular and pulmonary diseases (Pope, Dockery, 2006). PM is classified in three criterions; PM_{10} (aerodynamic diameter <10 μm), and $PM_{2.5}$ (<2.5 μm), and ultrafine particles (<1.0 μm) (World Health Organization, 2007).

Gasoline powered motor vehicles have been identified as the dominant PM contributor (ultrafine, secondary aerosol) surrounding heavily urbanized areas (Bahreini, et al, 2012). Future scenarios indicate that the largest impact on premature mortality in

California will be attributed to transportation emissions, particularly vehicular exhaust (Lelieveld, et al, 2015). The PM that is emitted from gasoline vehicles is a complex mixture of black carbon (BC), and organic aerosol (POA) which varies with engine technology, age, and fuel used.

In addition to PM, gasoline vehicles emit a variety of volatile organic compounds (VOCs), NOx, CO, and CO_2. The VOC species that leave the tailpipe undergo an immense number of complex chemical reactions with a variety of atmospheric oxidants (Stephens, et al, 1969). Oxidation reactions of VOCs results in the addition of functional groups (alcohols, carbonyls, aldehydes) resulting in lower volatility gas phase products, and alternatively, increased volatilities via segmentation (Kroll, Seinfeld, 2008). If a gas phase organic compound continues to accept additional functional groups, the compound will eventually partition to the particle phase either through condensation on existing aerosols, or nucleation (Seinfeld, Pandis, 2007). Particles formed through oxidation are regarded as secondary organic aerosols or SOA.

SOA formation through oxidation reactions requires NO and NO_2 (NOx), to regenerate oxidant for continual reactions. NOx is primarily emitted from mobile sources due to its high temperature of formation (~1600 °C), and is typically formed in lean (25-45% excess air) fuel-to-air combustion (Beychok, et al, 1973). NOx also has a direct role in the formation of ozone (Ryerson, et al, 2003) which is known to be a respiratory irritant.

1.1.1 Chamber's Role in Aerosol Studies:

The overall impact of ultrafine PM on direct and indirect radiative climate forcing is currently unresolved. Atmospheric studies utilizing mass spectrometry concluded that 20% to 90% of ultrafine mass consists of OA (Jimenez, et al, 2009). The highly variable compositions are directly related to the concentration and source of biogenic and anthropogenic pollutants. Furthermore, the contribution of POA and SOA in the overall OA budget, is not fully understood (Robinson, et al, 2007). Current models cannot account for, let alone predict, the bulk of SOA measured in the atmosphere (De Gouw et al., 2005). Models rely on robust, atmospherically relevant experiments, and resulting gaseous and particle phase data to accurately predict SOA formation. Dynamic mixing effects make classification and isolation of chemical processes in the atmosphere impossible, however, researchers are able utilize atmospheric chambers to mimic these processes (Cocker, et al, 2001).

Complex and state-of-the-art chamber systems provide a controlled and comprehensive method to test and observe atmospheric reactions. Indoor environmental chambers allow researchers the ability to regulate light intensity, temperature, and humidity; all of which are variables that directly affect atmospheric reactions (Cocker, et al, 2001).

Modelers attempting to predict the formation of secondary organic aerosol from specific emissions rely on experimental data from environmental chambers. Typically, experiments simulate a wide range of reactant concentrations, and experimental conditions

for the single precursor to allow a range of yields for SOA formation. Works investigating these yields typically focus on single precursor reactions due to the complexity of the photochemistry. Yield (Y) is defined as the mass of the organic aerosol formed (M_o) divided by the amount of hydrocarbon consumed (ΔTHC) (Odum, et al, 1997). The equation for yield is shown below.

$$Y = \frac{\Delta M_o}{\Delta THC}$$

1.1.2 Aged Vehicle Studies:

Conventional environmental chambers are limited to adjacent combustion sources, or simple precursor experiments. A chamber system with the ability to change location provides opportunities to maintain the unique capabilities of static chambers, while accessing more realistic-complex combustion sources. A mobile chamber is especially useful when evaluating aged vehicle emissions over realistic driving conditions utilizing a chassis dynamometer. Previous research suggests that organic aerosol in highly urban areas are dominated by anthropogenic SOA (Zhang, et al, 2011) and as stated earlier, gasoline vehicles are considered to be major contributors of SOA in densely populated areas (Bahreini, et al, 2012). These findings demonstrate the importance of investigating SOA forming potential from gasoline vehicles with controlled atmospheric chambers.

Gasoline vehicles utilize one of two engines; port fuel injection (PFI) and gasoline direct injection (GDI) engines. The relatively new direct injection technology has experienced a remarkably speedy adoption after its initial introduction to the American

market. Currently, GDI engines account for approximately 45%, and 60% of the North American and European market respectively (Whitaker, et al, 2015). PFI vehicles have significant advantages (low PM), but are expected to struggle meeting future legislation and fuel economy regulations (Stone, et al, 1999).

GDI engines, on the other hand, have improved fuel economy through an increased compression ratio and better air/fuel ratio accuracy (Celik, et al, 2010). In GDI engines, liquid fuel is sprayed directly into the combustion chamber leading to increased cooling as the fuel volatilizes, allowing for a higher compression ratio and greater efficiency. Imperfect mixing due to incomplete fuel evaporation, however, results in increased soot emission for GDI engines when compared to traditional port fuel injection (PFI) engines (Karavalakis, et al, 2015; Chen, et al, 2017). Poor mixing creates pockets with high temperatures, but insufficient oxygen, leading to pyrolysis reactions and soot formation. Additionally, as the fuel comes directly into contact with the cold cylinder walls and piston, a small amount of fuel may impinge on the piston, which may lead to diffusion combustion and tailpipe PM formation (Stevens, et al, 2001; Karlsson, et al, 2001; Piock, et al, 2011).

Previous studies have concluded that approximately 31% of gasoline related VOC's in Riverside can be attributed to fuel vapor emissions (Gentner, et al, 2009). One of the earliest chamber studies examining evaporated fuel, determined the SOA produced could explained solely by the aromatic content of the fuel (Odum, et al, 1997). However, atmospheric chemists are now realizing that the SOA mass that would form due to the oxidation reaction of aromatic compounds doesn't fully explain masses formed in laboratory experiments (Zhao, et al, 2016). The unexplained mass in evaporative emissions

is predicted to come from various IVOCs which fall into an unresolved complex mixture which cannot be separated with traditional GC/MS (Zhao, et al, 2016). Because of this, more detailed gaseous analysis is needed to try to tighten the predicted and observed SOA formation mass.

1.1.3 Potential Emission Controls:

One strategy to reduce PM emissions from GDI vehicles is through the use of a gasoline particulate filter (GPF) (Yang, et al, 2018; Mamakos, et al, 2013). The use of GPFs in GDI vehicles have been shown to dramatically reduce PM mass, black carbon, and particle number (PN) emissions, as well as toxic pollutants such as polycyclic aromatic hydrocarbons (PAHs) and nitrated PAHs (Yang, et al, 2018; Chan, et al, 2014). Previous studies have displayed PM removal efficiencies from 10%-91% (Chan, et al, 2014; Xia, et al, 2017). Currently, there is no previous work on how a catalyzed GPF (in place of stock TWC) will affect SOA formation.

Altering fuel composition has also been shown to effectively reduce particulate emissions. Fuel composition has remained relatively consistent (average toluene to benzene ratios: 1.5 in 2013 vs 1.2-1.4 in mid-90's) since the initial evaporative fuel chamber tests. One major difference is the transition from methyl tert-butyl ether (MTBE) to ethanol as an oxygenate; due to ground water contamination associated with MTBE (Getner, et al, 2013). Ethanol at increased levels has been shown to improve vehicle emission by lowering carbon emissions, and sulfur content, while also acting as a clean octane replacement (Karavalakis, et al, 2012). Currently conventional gasoline has 10%

ethanol content but it has been found that higher ethanol blends could possibly lead to greater fuel efficiencies and lower greenhouse gas emissions. As a result of the increase in ethanol content, the amount of aromatics in the fuel would decrease, which could directly decrease the overall SOA potential from these vehicles (EESI, 2015).

1.2. Outline of Dissertation:

This thesis seeks to quantify and characterize the secondary potential from stock GDI vehicles representative of the current fleet. Furthermore, the focus is explore how emission control strategies will affect the secondary aerosol formation potential from new technology GDI vehicles, and attempt to quantify the effect of the controls. First, in chapter 2, the effect of a catalyzed GPF are tested. To the best of our knowledge, only Pieber et al (2018) evaluated the SOA production from GDI vehicles equipped with prototype GPFs using a batch and flow reactor. The authors found no difference in SOA formation with the non-catalyzed and catalytically coated GPFs, they suggested that future work with catalyzed GPFs installed in the position of the underfloor TWC is necessary. Here, for the first time, we report results on SOA formation with catalyzed GPFs or 4-way catalysts when exercising the GDI vehicles over a cold-start LA92 test cycle.

Chapter 3 focuses on the evaluation of high ethanol fuel blends on the secondary aerosol potential from FFV-GDI vehicles. The vehicles were tested on four fuels varying from 10% to 78% ethanol content by volume, and contributes to the growing body of literature examining the use of ethanol fuel s in current GDI technology. In addition the effects of the driving conditions, and the SOA formation potential of vehicular exhaust to

different oxidation environments are investigated. To the best of our knowledge, no researchers have studied the reactivity of vehicle exhaust with the addition of a surrogate mixture and NOx with the intent of creating consistency between tests.

Chapter 4 is also focused on the secondary aerosol effects from varying fuel content, however focuses on lower ethanol fuels (0% to 20% ethanol by volume). The fuel parameters studied as part of this program included ethanol, aromatics, vapor pressure, T50, and T90 as well as interactions between these parameters that were thought to be important in understanding the impacts of widespread blending of ethanol. The attempt of the study was to relate the SOA formation measured in chamber studies, along with a complex analysis of the gas phase compounds.

Chapter 5 includes an aggregation of all data collected from the vehicles tested thus far utilizing UCR's Mobile Atmospheric Chamber (MACh), and attempt to relate to previously peer reviewed works, and find trends in the SOA formation potential (including all vehicles in this dissertation, and four additional vehicles). This chapter will focus on SOA formation and only touch on the inorganic secondary aerosol. Specifically, the trends in the SOA formation potential for gasoline vehicle exhaust which may ultimately allow modelers to more accurately predict atmospheric SOA concentrations from anthropogenic vehicular exhaust will be explored.

1.3. References:

1) Hamill, Sean D.; A Pennsylvania Town Remembers the Smog That Killed 20, New York Times **2008**

2) Davis, D.; A Look Back at the London Smog of 1952 and Half Century Since, Environmental Health Perspectives, 110, A734-A735, **2002**

3) World Health Organization, 2007. WHO Air quality guidelines for particulate matter, ozone, nitrogen dioxide and sulfur dioxide. WHO

4) Pope, C, Dockery, D.W., 2006. Health Effects of Fine Particulate Air Pollution: Lines that Connect, J. Air & Waste Manage. Assoc, 56, 709-742

5) Bahreini, R.; Middlebrook, A. M.; de Gouw, J. A.; Warneke, C.; Trainer, M.; Brock, C. A.; Stark, H.; Brown, S. S.; Dube, W. P.; Gilman, J. B.; Hall, K.; Holloway, J. S.; Kuster, W. C.; Perring, A. E.; Prevot, A. S. H.; Schwarz, J. P.; Spackman, J. R.; Szidat, S.; Wagner, N. L.; Weber, R. J.; Zotter, P.; Parrish, D. D. Gasoline emissions dominate over diesel in formation of secondary organic aerosol mass. *Geophys. Res. Lett*. **2012**, *39*, L06805, doi: 10.1029/2011GL050718.

6) Lelieveld, J.; Evans, J. S.; Fnais, M.; Giannadaki, D.; Pozzer, A. The contribution of outdoor air pollution sources to premature mortality on a global scale. *Nature* **2015**, *525*, 367-371.

7) Stephens, Edgar R, **1969**. The formation, reactions, and properties of peroxyacyl nitrates (PANs) in photochemical air pollution. Wiley

8) Kroll, J.H.; Seinfeld, J.H. Chemistry of secondary organic aerosol: Formation and evolution of low-volatility organics in the atmosphere. *Atmospheric Environment* **2008**, *42*, 3593-3624.

9) Seinfeld, J.H.; Pandis, S.N.; Atmospheric Chemistry and Physics, From Air Pollution to Climate Change, Wiley-Interscience Publications **2007**.

10) Beychok, M.R..; NOx emission from fuel combustion controlled. The Oil and Gas Journal: 53–56. **1973**

11) Ryerson, T. B., M. Trainer, W. M. Angevine, C. A. Brock, R. W. Dissly, F. C. Fehsenfeld, G. J. Frost, et al. **2003**. “Effect of Petrochemical Industrial Emissions

of Reactive Alkenes and NOx on Tropospheric Ozone Formation in Houston, Texas." *Journal of Geophysical Research, D: Atmospheres* 108 (D8). https://onlinelibrary.wiley.com/doi/abs/10.1029/2002JD003070.

12) Jimenez, J. L., M. R. Canagaratna, N. M. Donahue, A. S. H. Prevot, Q. Zhang, J. H. Kroll, P. F. DeCarlo, et al. **2009**. "Evolution of Organic Aerosols in the Atmosphere." *Science* 326 (5959): 1525–29.

13) Robinson A, N.M. Donahue, M.K. Shrivastava, et al, **2007**. Rethinking OA: SV Emissions and Photochemical Aging. AAAS, 315, 1259-1262

14) De Gouw, J. A., A. M. Middlebrook, C. Warneke, P. D. Goldan, W. C. Kuster, J. M. Roberts, F. C. Fehsenfeld, et al. **2005**. "Budget of Organic Carbon in a Polluted Atmosphere: Results from the New England Air Quality Study in 2002." *Journal of Geophysical Research, D: Atmospheres* 110 (D16).

15) Cocker, D. R., 3rd, R. C. Flagan, and J. H. Seinfeld. **2001**. "State-of-the-Art Chamber Facility for Studying Atmospheric Aerosol Chemistry." *Environmental Science & Technology* 35 (12): 2594–2601.

16) Zhang, Yongxin, Shan Sun, Seth C. Olsen, Manvendra K. Dubey, and Jinhai He. **2011**. "CCSM3 Simulated Regional Effects of Anthropogenic Aerosols for Two Contrasting Scenarios: Rising Asian Emissions and Global Reduction of Aerosols." *International Journal of Climatology* 31 (1): 95–114.

17) Whitaker, P.; **2015**. Powertrain Strategies for the 21st Century. AVL Powertrain Eng. Inc.

18) Stone, R.; **1999**. Introduction to Internal Combustion Engines. Springer, 131-164

19) Celik, M.B., Ozdalyan, B.; **2010**. Gasoline Direct Injection. InTech, 116, 9

20) Karavalakis, G.; Short, D.; Vu, D.; Russell, R.; Hajbabaei, M.; Asa-Awuku, A.; Durbin, T.D. Evaluating the effects of aromatics content in gasoline on gaseous and particulate matter emissions from SI-PFI and SI-DI vehicles. *Environ. Sci. Technol.* **2015**, *49*, 7021-7031.

21) Chen, L.; Liang, Z.; Zhang, X.; Shuai, S. Characterizing particulate matter emissions from GDI and PFI vehicles under transient and cold start conditions. *Fuel* **2017**, 189, 131-140.

22) Stevens, E.; Steeper, R. Piston wetting in an optical DISI engine: Fuel films, pool fires, and soot generation. SAE Technical Paper **2001**, 2001-01-1203.

23) Karlsson, R.B.; Heywood, J.B. Piston fuel film observations in an optical access GDI engine. SAE Technical Paper **2001**, 2001-01-2022.

24) Piock, W.; Hoffmann, G.; Berndorfer, A.; Salemi, P.; Fusshoeller, B. Strategies towards meeting future particulate matter emission requirements in homogeneous gasoline direct injection engines. *SAE Int. J. Engines* **2011**, *4*, 1455-1468.

25) Gentner, Drew R., Robert A. Harley, Angela M. Miller, and Allen H. Goldstein. **2009**. "Diurnal and Seasonal Variability of Gasoline-Related Volatile Organic Compound Emissions in Riverside, California." *Environmental Science & Technology* 43 (12): 4247–52.

26) Odum, J. R., T. P. Jungkamp, R. J. Griffin, R. C. Flagan, and J. H. Seinfeld. **1997**. "The Atmospheric Aerosol-Forming Potential of Whole Gasoline Vapor." *Science* 276 (5309): 96–99.

27) Zhao, Yunliang, Ngoc T. Nguyen, Albert A. Presto, Christopher J. Hennigan, Andrew A. May, and Allen L. Robinson. **2016**. "Intermediate Volatility Organic Compound Emissions from On-Road Gasoline Vehicles and Small Off-Road Gasoline Engines." *Environmental Science & Technology* 50 (8): 4554–63.

28) Yang, J.; Roth, P.; Durbin, T. D.; Johnson, K. C.; Cocker III, D. R.; Asa-Awuku, A.; Brezny, R.; Geller, M.; Karavalakis, G. Gasoline particulate filters as an effective tool to reduce particulate and PAH emissions from GDI vehicles: A case study with two GDI vehicles. *Environ. Sci. Technol.* **2018**, *52*, 3275-3284.

29) Mamakos, A.; Martini, G.; Marotta, A.; Manfredi, U. Assessment of different technical options in reducing particle emissions from gasoline direct injection vehicles. *Journal of Aerosol Science* **2013**, 63, 115-125.

30) Chan, T. W.; Meloche, E.; Kubsh, J.; Brezny, R. Black carbon emissions in gasoline exhaust and a reduction alternative with a gasoline particulate filter. *Environ. Sci. Technol.* **2014**, *48*, 6027-6034.

31) Xia, Wenzheng, Yi Zheng, Xiaokun He, Dongxia Yang, Huifang Shao, Joesph Remias, Joseph Roos, and Yinhui Wang. **2017**. "Catalyzed Gasoline Particulate Filter (GPF) Performance: Effect of Driving Cycle, Fuel, Catalyst Coating." SAE Technical Paper. http://papers.sae.org/2017-01-2366/.

32) Karavalakis, Georgios, Thomas D. Durbin, Manish Shrivastava, Zhongqing Zheng, Mark Villela, and Heejung Jung. **2012**. "Impacts of Ethanol Fuel Level on Emissions of Regulated and Unregulated Pollutants from a Fleet of Gasoline Light-Duty Vehicles." *Fuel* 93 (March): 549–58.

33) EESI; **2015**. 18th Annual Congressional Renewable Energy and Energy Efficiency EXPO. EESI

34) Pieber, S. M.; Kumar, N. K.; Klein, F.; Comte, P.; Bhattu, D.; Dommen, J.; Bruns, E. A.; Kilic, D.; El Haddad, I.; Keller, A.; Czerwinski, J.; Heeb, N.; Baltensperger, U.; Slowik, J. G.; Prévôt, A. S. H. Gas phase composition and secondary organic aerosol formation from gasoline direct injection vehicles investigated in batch and flow reactors: effects of prototype gasoline particle filters. *Atmos. Chem. Phys.* **2018**, *18*, 9929-9954.

Chapter 2: Catalyzed Gasoline Particulate Filters Reduce Secondary Organic Aerosol Production from Gasoline Direct Injection Vehicles

Patrick Roth [1,2], Jiacheng Yang [1,2], Tyler Berte [1,2], David R. Cocker III [1,2], Thomas D. Durban [1,2], Rasto Brezny [3], Michael Geller [3], Georgios Karavalakis [1,2], Akua Asa-Awuku [1,2,4]

1. Bourns College of Engineering, Center for Environmental Research and Technology (CE-CERT), University of California, 1084 Columbia Avenue, Riverside, California 92507, United States
2. Department of Chemical and Environmental Engineering, Bourns College of Engineering, University of California, Riverside, California 92521, United States
3. Manufacturers of Emission Controls Association, 2200 Wilson Boulevard, Suite 310, Arlington, Virginia 22201, United States
4. Department of Chemical and Bimolecular Engineering, A. James Clark School of Engineering, University of Maryland, College Park, 4418 Stadium Dr., College Park, MD, 20702

2.1. Abstract:

This study investigated the aged gaseous, and particulate emissions from two low mileage gasoline direct injection (GDI) vehicles tested in the stock configuration on E10 California gasoline. A catalyzed gasoline particulate filter (GPF) was installed in place of the original three-way catalyst (TWC) and the aged emissions were compared to the stock configuration. Primary emissions were collected into a 30 m^3 Mobile Atmospheric Chamber (MACh) and were subsequently aged for 7-10 hours. The potential secondary aerosol mass and composition were measured and the stock and GPF configurations were compared.

The use of a catalyzed GPF drastically reduced the tailpipe mass and particle number and considerably changed the average aerosol chemical composition of primary and secondary pollutants. The addition of the GPF reduced the total carbonaceous aerosol (black carbon, primary organic aerosol, and secondary organic aerosol) by 73% and 59% for GDI_1 and GDI_2, respectively. The total secondary aerosol mass formed was vehicle dependent; the secondary inorganic ammonium nitrate formed varied with vehicle NOx reduction technology. The GPF was the most efficient in the removal of aerosol with electrical mobility diameters >200nm, (99.0% ± 0.9% average removal for both vehicles). The GPF was least efficient (88.7% ± 1.8%) in the 18 -30 nm range.

The catalyzed GPF efficiently removed reactive gaseous pollutants, specifically NMHCs and NOx. This reduction in reactive gases was found to drive the differences in the potential secondary aerosol (SA) formed with the GPF and without the catalyzed GPF in stock configuration. A 41% and 65% reduction in NMHCs, for GDI_1 and GDI_2

reduced SOA formation by 39% and a 35%, respectively. Specifically, reducing PAH emissions with the catalyzed GPF may also reduce SOA formation from GDI vehicle technology. Ultimately, our findings indicate that SOA production from GDI vehicles with be significantly reduced with the application of catalyzed GPFs through the mitigation of reactive hydrocarbon precursors.

2.2. Introduction:

Mobile sources are major contributors of emissions, especially in urban areas (Heal, et al 2012). On-road vehicles equipped with internal combustion engines are known to emit nitrogen oxides (NOx), carbon monoxide (CO), particulate matter (PM), and volatile organic compounds (VOCs) (Dallmann, et al 2014). While vehicular NOx, CO, and VOC emissions have been reduced considerably over the past years as a result of the imposed environmental regulations (McDonald, et al, 2012 & 2013), some urban regions still struggle to meet atmospheric regulatory standards (CARB). PM directly emitted from the vehicle's exhaust is comprised of a complex mixture of constituents, including black carbon, sulfate, metals, and organic materials referred to as primary organic aerosol (POA) (May, et al, 2013). Studies have shown that PM emissions can be deposited deep into the lungs, inducing oxidative stress and respiratory diseases (Samet, et al, 2000; Lelieveld, et al, 2015). Other studies have shown that PM emissions influence the cardiovascular system (Pope, et al 2002).

Furthermore, after emission, NOx, and VOCs can undergo atmospheric photo-oxidation, resulting in the formation of secondary lower volatility organic gases. As the gases continue to react, the volatility of the gases decrease until ultimately condensing onto existing particles, thus increasing the atmospheric organic aerosol mass. The formation of organic mass as a result of VOC oxidation is classified as secondary organic aerosol or SOA (Odum, et al, 1997; Gentner, et al, 2017)

Studies have reported that SOA accounts for the largest fraction of atmospheric organic aerosol (OA), accounting for approximately 30-90% of total OA in megacities

(Jimenez, et al, 2009; Zhang, et al, 2007; Hu, et al, 2016). The contribution of SOA from anthropogenic and biogenic sources is not entirely clear as it involves complex processes, with the number of organic compounds participating in SOA formation being unknown (Hallquist, et al, 2009; Jimenez, et al 2009). Recent studies have shown that United States (US) gasoline vehicles are a major source of VOC emissions (compared to the diesel vehicle fleet) and dominate the production of SOA in US urban areas (Bahreini, et al, 2012). This phenomenon is amplified by the domination in market share of gasoline vehicles in the US compared to the European Union, and also by the fact that gasoline engines typically emit higher concentrations of VOCs (McDonald, et al, 2015).

The significant contribution of gasoline vehicles to the SOA budget has been shown in several studies (Saliba, et al, 2017; Ma, et al, 2018; Zhao, et al, 2017). Gordon et al. (2014) tested pre-LEV and newer gasoline vehicles and they concluded that SOA formation exceeds primary PM emissions. They also found lower SOA production from the newer vehicles compare to the pre-LEV gasoline vehicles and less SOA production during the hot-start testing compared to cold-start cycles. In another study, when a gasoline vehicle was tested over the New European Driving Cycle (NEDC), the authors confirmed the production of 15 times higher SOA production compared to POA (Platt, et al, 2013). Nordin et al. (2013) showed that C_6-C_9 light aromatic hydrocarbons contributed up to 60% of the formed SOA when they tested Euro 1 and Euro 4 compliant passenger cars under idling conditions. Liu et al. (2015) tested Euro 1 and Euro 4 gasoline vehicles under idling conditions and found that single-ring aromatics and naphthalene were responsible for 51-90% of the formed SOA.

Driven by stringent legislative measures on vehicle fuel efficiency and greenhouse gas emissions, the transportation sector has changed significantly in the past decade with the introduction of gasoline direct injection (GDI) engines. In GDI engines, liquid fuel is sprayed directly into the combustion chamber leading to increased cooling as the fuel volatilizes, allowing for a higher compression ratio and greater efficiency. Imperfect mixing due to incomplete fuel evaporation, however, results in increased soot emission for GDI engines when compared to traditional port fuel injection (PFI) engines (Karavalakis, et al, 2015; Chen, et al, 2017). Poor mixing creates pockets with high temperatures, but insufficient oxygen, leading to pyrolysis reactions and soot formation. Additionally, as the fuel comes directly into contact with the cold cylinder walls and piston, a small amount of fuel may impinge on the piston, which may lead to diffusion combustion and tailpipe PM formation (Stevens, et al, 2001; Karlsson, et al, 2001; Piock, et al, 2011).

One strategy to reduce PM emissions from GDI vehicles is through the use of a gasoline particulate filter (GPF) (Yang, et al, 2018; Mamakos, et al, 2013). The use of GPFs in GDI vehicles have been shown to dramatically reduce PM mass, black carbon, and particle number (PN) emissions, as well as toxic pollutants such as polycyclic aromatic hydrocarbons (PAHs) and nitrated PAHs (Yang, et al, 2018; Chan, et al, 2014). Previous studies have displayed PM removal efficiencies from 10%-91% (Chan, et al, 2014; Xia, et al, 2017), however, the GPFs used in these studies were not catalyzed with the intent to replace the stock TWC.

Despite the increased popularity of GDI engines in the light-duty vehicle sector across the US and Europe, there is limited information on the SOA production from current

technology GDI vehicles (Vu, et al; Saliba, et al, 2017; Pieber, et al, 2018) and no information on how a catalyzed GPF (in place of stock TWC) will affect SOA formation. In a recent study, Du et al (2018) tested both a PFI and GDI vehicle over the NEDC and reported much higher SOA production for the GDI vehicle compared to the PFI vehicle. In a different study, on the other hand, Zhao et al (2018) showed no differences in SOA production between PFI and GDI vehicles. Finally, Karjalainen et al (2016) tested a GDI vehicle over the NEDC and showed reduced SOA formation when the engine was warm and higher SOA formation during the cold-start phase when the three-was catalyst (TWC) was below its light-off temperature.

In this study, we investigate the SOA production from two low mileage GDI vehicles with and without a catalyzed GPF. To the best of our knowledge, only Pieber et al (2018) evaluated SOA production from GDI vehicles equipped with prototype GPFs using a batch and a flow reactor. While the authors did not find differences in SOA formation with the tested non-catalyzed and catalytically coated GPFs, they suggested that future work with catalyzed GPFs installed in the position of the underfloor TWC is necessary. Here, for the first time, we report results on SOA formation with catalyzed GPFs or 4-way catalysts when exercising the GDI vehicles over a cold-start LA92 test cycle. This work is also a companion study to Yang et al (2018), in which detailed tailpipe (primary) toxic pollutants, and criteria gaseous, and particulate emissions are reported.

2.3. Experimental:

2.3.1 Facilities:

All testing was conducted at the Center for Environmental Research and Technology (CE-CERT) in Riverside, CA. Emissions testing was conducted at the Ford Motor Vehicle Emissions Research Laboratory (VERL). Vehicles were operated on a 48" Burke E. Porter single roller chassis dynamometer. Exhaust was directed into a Pierburg positive displacement pump-constant volume sampler (PDP-CVS) where standard bag measurements for total hydrocarbon (THC), carbon monoxide (CO), nitrogen oxides (NOx), non-methane hydrocarbons (NMHC), and carbon dioxide (CO_2) were analyzed with a Pierburg AMA-400 bench. More details for the measurement methods and analysis of the tailpipe emissions can be found elsewhere (Yang, et al, 2018).

The photochemical portion of the experimental procedure utilized the Atmospheric Processes Laboratory (APL). All photochemical experiments were conducted in University of California Riverside's 30 m^3 Mobile Atmospheric Chamber (MACh) (2 mil fluorinated ethylene propylene Teflon film reactor). The reactor is enclosed in a segmented, lightweight aluminum frame fitted with wheels and a static resistant/UV blackout tarp to aid in the movement between labs. In APL, the chamber is surrounded by 600 15 W, 18", T8 black light fluorescent bulbs to act as the controlled UV source. Extended details on the construction and characterization of MACh can be found in Vu, et al, 2018.

2.3.2 Test Vehicles & Drive Cycle:

The experiments included two 2016 GDI vehicles which will be referred to as GDI_1 and GDI_2 for the duration of the chapter. GDI_1 was equipped with a 2.0 liter (L), wall guided DI SI Atkinson cycle engine and was certified to meet the LEV III SULEV30 (PZEV) standard. GDI_2 was LEV II certified and equipped with a 1.5 L downsized turbocharged centrally mounted direct injection engine. Both vehicles were equipped with three way catalysts (TWC) and were operated stoichiometrically. The vehicles had 14,780 and 24,600 miles at the start of testing respectively.

The vehicles were tested in duplicate over a cold-start LA92 with commercial California E10 fuel. The LA92 test cycle (Unified Cycle) was developed for light-duty vehicles by California Air Resources Board (CARB) to represent the more aggressive driving style observed in California. The cycle has higher speeds, higher accelerations, fewer stops per mile, and less idle time than the traditional FTP cycle. The LA92 cycle has three phases (i.e., cold-start, urban, and hot-start phase) with a similar three-bag structure to the FTP cycle (Figure 2-12).

GDI_1 and GDI_2 were tested on the same E10 California commercial fuel in the stock configuration to obtain baseline measurements. The primary emissions were analyzed to certification standards (Yang, et al, 2018).

After completing the baseline testing, both vehicles were retrofitted with a catalyzed GPF on the underfloor of the vehicle, replacing the stock TWC. The catalyzed GPFs were provided by the Manufacturers of Emissions Controls Association (MECA).

The GPFs were sized and fitted in relation to the engine displacement (4.66" diameter, 4.5" length, 8 mm wall thickness, 300 cpsi), and the precious metal loadings were matched to the certification levels of the two vehicles. The GPFs were covered with a wash coat with approximately 1.0 g/L loading of palladium (Pd) and rhodium (Rh) (4:1 ratio) to act as a in place of the TWC.

2.3.3 Irradiation Experiments:

Prior to each chamber experiment, MACh was cleaned by injecting O_3, H_2O_2, and purified air (AADCO 737 air purifier) and was irradiated with UV light. The AADCO air consists of no detectable reactive compounds (H_2O, NOx, CO, O_3, Hydrocarbons) to minimize background reactions in experiments. The chamber was then subsequently emptied and filled repeatedly until all gases and particles were measured to be below detection limit (H_20 < -50°C dew point, {NOx, CO, HC, O_3}~0 ppb, PM=0 µg m^{-3}) then flushed with purified air overnight. Prior to the injection of vehicle exhaust, the chamber was half-filled with the AADCO air, and transported to VERL.

The dilute exhaust was injected from the PDP-CVS into MACh during the LA92 test cycle (excluding the hot soak). The exhaust was injected with two Ejector Dilutors (Air-Vac TD11OH) in parallel, connected to a house built clean air system with filters and desiccants to remove the PM (HEPA Filters), water (silica gel columns), NOx (Purafil), CO (Carulite canister), and hydrocarbons (activated charcoal) from the house compressed air. The injection lines consisted of 8.5 m of ½" stainless steel tubing. The dilution setup was designed to allow a variation of dilution from 50:1 up to 200:1 by varying the dilution

air and CVS flow. A detailed schematic of the UC, Riverside APL and VERL facilities that were utilized can be found in Figure 2-1.

MACh utilized gravitational forces to ensure a positive pressure inside the reactor, such that potential holes in the Teflon surface of the chamber will force air to flow out of the reactor. This minimized the contamination and dilution of the exhaust throughout the experiment (average measured dilution of 1.3% ± 1.2% throughout 7 hour experiments (Equation 2-2) which is within the measurement error of the instrument).

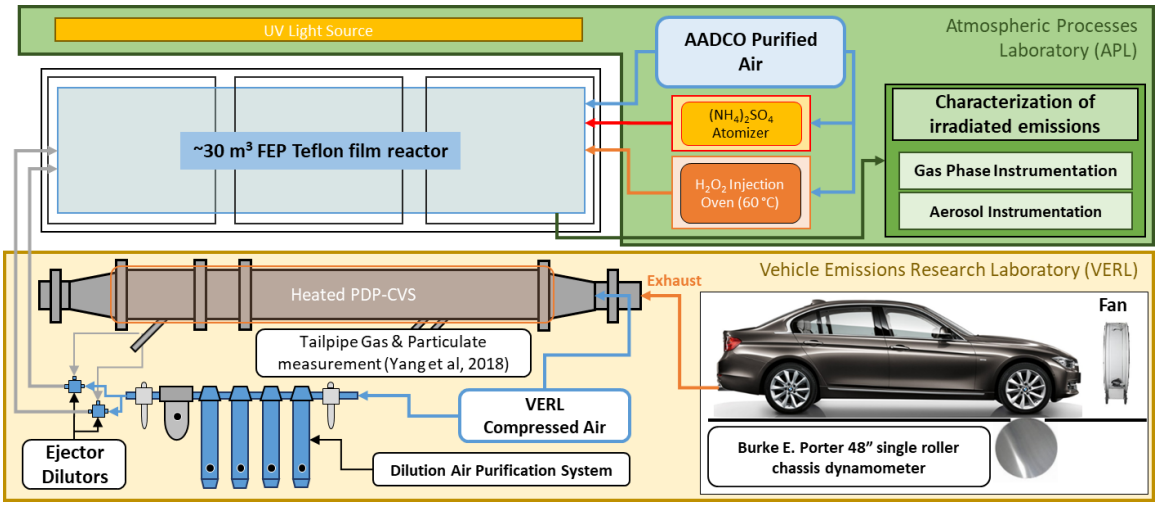

Figure 2-1: Experimental setup (not to scale) for testing. Vehicle was operated in VERL, where the criteria pollutants were measured, and MACh was injected with vehicle emissions. Irradiation testing of the exhaust was then conducted in APL.

2.3.4 Stock Experiments:

After the exhaust was collected, the chamber was filled to maximum volume with purified air. 1.0 ppm of H_2O_2 was also injected utilizing an oven (60° C) to act as an initial

hydroxyl radical source. Prior to irradiation, the diluted primary exhaust was evaluated for about 30 min to characterize initial tailpipe composition. The emissions were then photo-oxidized continuously for 7-10 hours. The exhaust was carefully monitored during photo-oxidation, utilizing a host of gaseous and particulate instruments allowing for real time evaluation of the aging exhaust (See Section 2.3.6. Instrumentation). All chamber experiments were concluded when the wall-loss corrected aerosol mass formation, and the ozone concentration plateaued.

2.3.5 GPF Experiments:

In stock configuration experiments, the black carbon tailpipe particles could act as a seed for the condensation of low volatility gases. However, it was anticipated that the initial tailpipe PM in the GPF experiments would be significantly lower (e.g., Yang, et al, 2018) and inert seeds would be necessary to mimic a similar condensable particulate surface area for low volatility gases to partition as they age. After the dilute exhaust was characterized, ammonium sulfate was added to GPF experiments to ensure a similar seed particle number and surface area when compared to stock experiments. The ammonium sulfate seed was injected into the chamber utilizing an atomizer with a 2.40 M, aqueous ammonium sulfate solution (Acros, 99.5 % in Millipore © DI water (18mΩ, <100 ppb)), and subsequently heated and dried via silica gel. The dried seed was then passed through a ^{210}Po neutralizer to minimize charged particles. Experiments were seeded for ~24.2 min. The aerosol was again classified to obtain a ratio of seed to tailpipe aerosol such that the total contribution of seed mass could be determined and ultimately subtracted from final secondary mass calculations. Finally, then the remaining volume of the chamber was filled

with AADCO purified air, and the remaining procedure was identical to stock configuration experiments. Ultimately, the condensable surface areas of the particles were brought to within an average of 15% for GDI_1 and 5% for GDI_2.

No propene or HONO was added to experimentally alter the VOC:NOx ratio; this decision was designed to reduce the added variables to the experiments and allow us to observe the secondary aerosol formation from the raw exhaust. The initial conditions for all experimental configurations are displayed in Table 2-1.

Table 2-1: Initial conditions for stock configuration and GPF configuration experiments for GDI_1 and GDI_2

Vehicle	Dilution Ratio	Initial NOx (ppb)	VOC:NOx	CO (ppm)
GDI_1	105 ± 7	26.4 ± 1.1	7.1 ± 0.1	2.12 ± 0.34
GDI_2	91 ± 5	174.3 ± 6.6	2.7 ± 0.1	4.93 ± 0.28
GDI_1 GPF	60 ± 1	50.4 ± 2.8	5.2 ± 0.1	2.54 ± 0.82
GDI_2 GPF	62 ± 1	64.2 ± 3.6	6.3 ± 0.2	2.63 ± 0.12

2.3.6 Instrumentation

Gas phase instrumentation included a Thermo Environmental Instruments Inc. (MA) Model 42 chemiluminescent NOx analyzer (NO, NO_2, NOx). A Dasibi Environmental (CA) nondispersive ultraviolet ozone analyzer will monitor the chamber ozone concentration. A Dasibi Model 48C was used to measure CO concentrations with IR analysis. A LI-COR ® LI-840A CO_2/H_2O analyzer was used to monitor the CO_2 and relative humidity during the irradiation experiments. VOC concentrations were measured

with the Pierburg AMA-400 bench. Dilution ratios were calculated by monitoring the CO_2 concentrations of the exhaust, dilution air, and initial experimental concentration (Equation 2-3).

The physical and chemical properties of the aerosol were measured throughout the experiment. Particle phase instrumentation included a commercial scanning mobility particle sizer (SMPS) consisting of a TSI 3080 electrostatic classifier, TSI 3081 long column differential mobility analyzer (DMA) column and a TSI ultrafine condensation particle counter (CPC) 3776. The 3776 CPC was operated in 'low flow mode', with a sample flow of 0.3 LPM and the sheath flow for the classifier was set to 3.0 LPM. The SMPS measured electrical mobility diameters from 14.6 nm to 661.2 nm. The mass of black carbon was measured using an AVL micro soot sensor (MSS) with a high power laser diode operating at 802 nm with a photoacoustic sensor (Petzold., Niessner, 1996).

For chemical composition, the non-refractory aerosol chemical composition data was measured with an Aerodyne high-resolution, time-of-flight, aerosol mass spectrometer (HR-ToF-AMS) (Aiken, et al, 2008). HR-ToF-AMS was operated in both V and W mode, and the data processing was completed using the ToF-AMS Analysis Toolkit 1.57 and ToF-AMS HR analysis 1.16. The Unit Mass Resolution (UMR) and HR Frag table for CO_2 were altered from the assumed concentration of 370 ppm to the measured CO_2 concentration using a LI-COR ® LI-840A CO_2/H_2O analyzer. The organic, ammonium, nitrate, and sulfate ratios were calculated and applied to the remaining mass calculated by the SMPS and APM (after subtracting out the black carbon contribution). Wall loss

corrected black carbon mass was assumed to be constant throughout irradiation experiment.

A house built, tandem differential mobility analyzer (TDMA) consisting of two TSI 3081 DMAs and a TSI Model 3760A CPC provided volatility measurements (Villani, et al, 2008). The first column selects a particle electrical mobility diameter, typically at the peak mode. The size selected particles then travel through a heated column (100°C) with a residence time of ~17 sec. The heated aerosol is then classified by scanning mode via second DMA column such that a new size distribution of the aerosol is measured. The initial diameter is then compared to the final diameter to obtain the volume fraction remaining (VFR) of the particles (i.e, $VFR = \frac{Volume_{final}}{Volume_{initial}}$, assuming a spherical aerosol).

A Kanomax aerosol particle mass analyzer system (APM) measured particle effective density. The APM is paired with a house built SMPS. Particles are initially selected by mass and later pass through a scanning DMA column where an effective density based on the electrical mobility diameter is calculated. The APM has the ability to select aerosol with a mass from 0.30 to 50.0 fg which is equivalent to a particle of unit density with a diameter of 50 to 400 nm. A more detailed summary of the APM-SMPS system is described in Malloy, et al (2009).

A DMT Inc. single growth column CCN Counter (CCNC) measured CCN activity and a Hygroscopic Tandem Differential Mobility Analyzer (HTDMA) measured super-saturated and sub-saturated hygroscopicity respectively during the irradiation experiments. The results and analysis of the hygroscopicity and cloud droplet formation will be

published in a separate manuscript. Here, the discussion on aerosol physical properties (size, number, mass, effective density and volatility) is limited to the properties that advance our understanding of the characteristics of the secondary particulate mass formation and composition.

SMPS data was used for the calculation of the volume of aerosol throughout the irradiation experiment. All SMPS data was corrected for particle wall losses, using first order wall loss kinetics (Equation 2-1), described in detail by Cocker et al (2001). Vapor wall losses from vehicle exhaust have been assumed and measured to be insignificant in past chamber experiments (Vu, et al, 2018). From the volume, mass was calculated by using effective density measurements. Final mass calculations were determined from the effective density and volume calculated at the end of the irradiation experiments.

2.4. Results and Discussion:

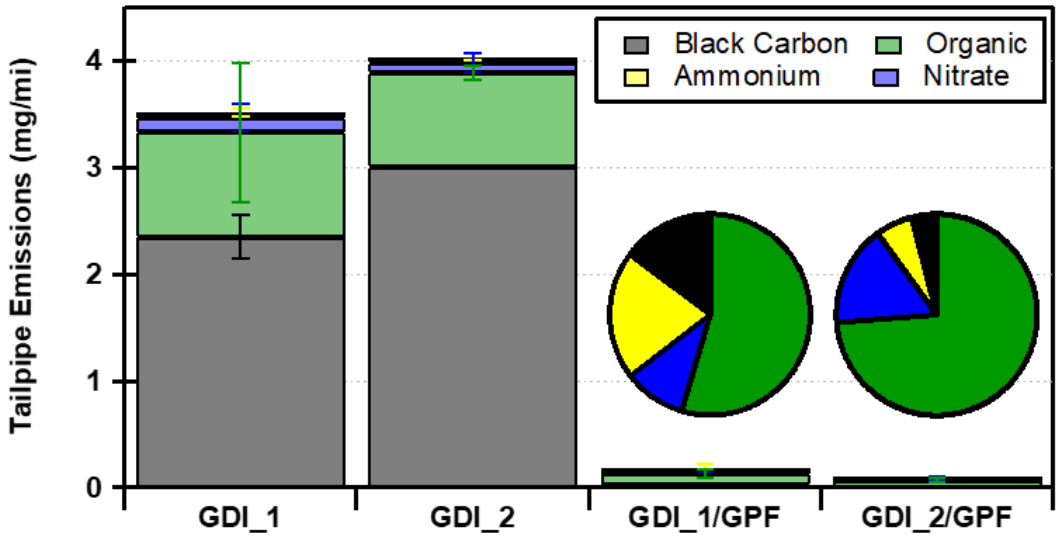

Figure 2-2: Composition of tailpipe PM for GDI_1 and GDI_2. Pie charts display composition for GPF configurations. Organic material was considered POA.

Figure 2-2 shows the PM mass and composition emitted directly from the tailpipe. In the stock configuration, GDI_1 emitted an average of 3.53 mg/mi of PM over the three LA-92 driving cycles. GDI_2 emitted a similar, but slightly larger tailpipe concentration at 4.05 mg/mi of PM. Vehicle emissions from the more aggressive LA-92 driving cycle may struggle to achieve the current FTP (Federal Test Procedure Cycle) standard of 3.0 mg/mi, and would not meet California's future LEV III standard of 1.0 mg/mi. The two vehicles emitted a similar composition of tailpipe PM, with 66.7 % and 74.3 % of the tailpipe PM being black carbon, 27.9% and 21.8% POA, and the remaining ~5% ammonium and nitrate for GDI_1 and GDI_2 respectively. Tailpipe composition primarily

composed of black carbon is consistent with other works (Maricq, et al, 2012, Yang et al, 2019).

The catalyzed GPF accounted for a 95% and a 98% reduction in total tailpipe PM mass for GDI_1 and GDI_2 (Figure 2-2) (Yang, et al, 2018). The emitted mass from GDI_1/GPF and GDI_2/GPF were 0.18 mg/mi and 0.09 mg/mi respectively. Both were well below any proposed future regulation limit. The GPF was most efficient in removing black carbon (over 99.8% removal for both vehicles), considerably altering the average fraction composition of the aerosol emitted from the tailpipe. Only 15% and 4% of the tailpipe mass was black carbon for GDI_1/GPF and GDI_2/GPF respectively. The GPF also removed a considerable amount of POA mass, however was less efficient when compared to black carbon (90%, 92% POA removal respectively). This phenomenon is likely due to varying volatilities of the VOCs emitted (Pieber, et al, 2017). The hot, lower volatility gases, remain in the gas phase through the catalyzed GPF, but as the emissions dilute and cool, the lower volatility organic compounds condense onto existing particles. This organic material, although emitted as a gas, condensed without any reaction and is therefore measured as POA. The GPF decreased POA mass but increased the average percentage contribution to the total PM (55% and 74%, GDI_1/GPF and GDI_2/GPF, respectively). The remaining 20-30% of the primary aerosol was composed of ammonium and nitrate (Figure 2-2).

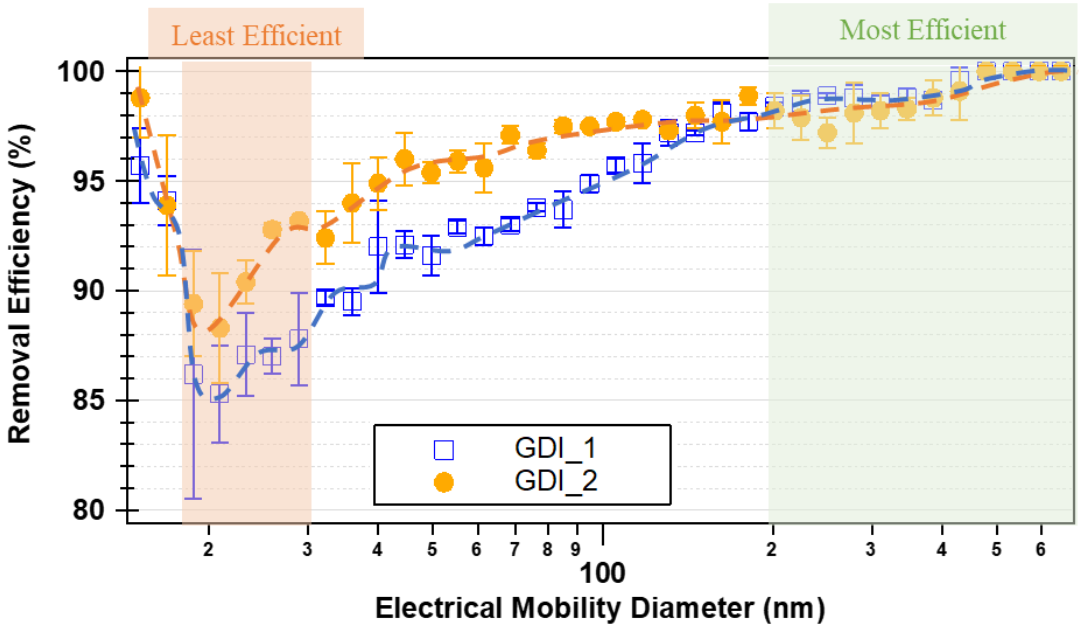

Figure 2-3: Removal efficiencies of tailpipe particles measured by electrical mobility diameter for GDI_1 and GDI_2 after dilution

The effect of the GPF on particle number (PN) was not consistent across measured particle diameters. Yang, et al (2018) observed that the total PN emissions decreased by an average of 95% for GDI_1 and 97% for GDI_2 when fitted with the catalyzed GPF. Here, we show that the GPF exhibited varying efficiencies across a range of ultrafine particle diameters (Figure 2-3). The removal efficiencies shown in Figure 2-3 were measured by the SMPS in MACh after a dilution of ~60:1 for the GPF configurations, and ~95:1 for the stock configurations, and were corrected with the measured dilution ratios to more accurately calculate removal efficiencies. The catalyzed GPF was most effective in the removal of particles > 200nm (99.2% ± 0.7% and 98.8% ± 1.2% in PN removal for GDI_1 and GDI_2 respectively (Figure 2-3)). In comparison, the catalyzed GPF was least

efficient in the removal of particles in the 18nm-30nm range, however, still removed 86.2% ± 2.8% for GDI_1 and 91.1% ± 2.3% for GDI_2.

The variation in efficiency can be explained by the two mechanisms of interception for the tailpipe PM. For the smaller particles (<30nm), Brownian diffusivity dominates the capture of particles, however decreases in efficiency as particle sizes increase. For the particles emitted between 30-100 nm, a mix of Brownian diffusivity and inertial capture are utilized for the particle removal. In regards to the larger diameter particles (>100nm), inertial capture is the dominant mechanism of particle removal. Similar results have been reported when investigating the effectiveness of diesel particulate filters (DPFs) (Tandon, et al, 2010).

Due to the varying removal efficiency of the catalyzed GPF, the size distribution of the tailpipe aerosol after dilution also changed. Initial size distribution can be observed by analyzing the cross-sections of Figure 2-4 at time, t =0 (for GPF experiments, distribution at t=0 is that of the seed). Size distribution comparisons of the exhaust and seed for the GPF experiments can also be found in the supplemental section (Figure 2-11). For GDI_1, stock configuration, the exhaust peak mode was a broad unimodal peak at approximately 95 nm (Figure 2-4a). With the addition of the catalyzed GPF, the exhaust peak shifted to 50 nm (Figure 2-11). A similar peak shift occurred for GDI_2, where the stock configuration had a broad unimodal peak at ~75 nm (Figure 2-4c), while the GPF emissions peak was at ~45 nm (Figure 2-11).

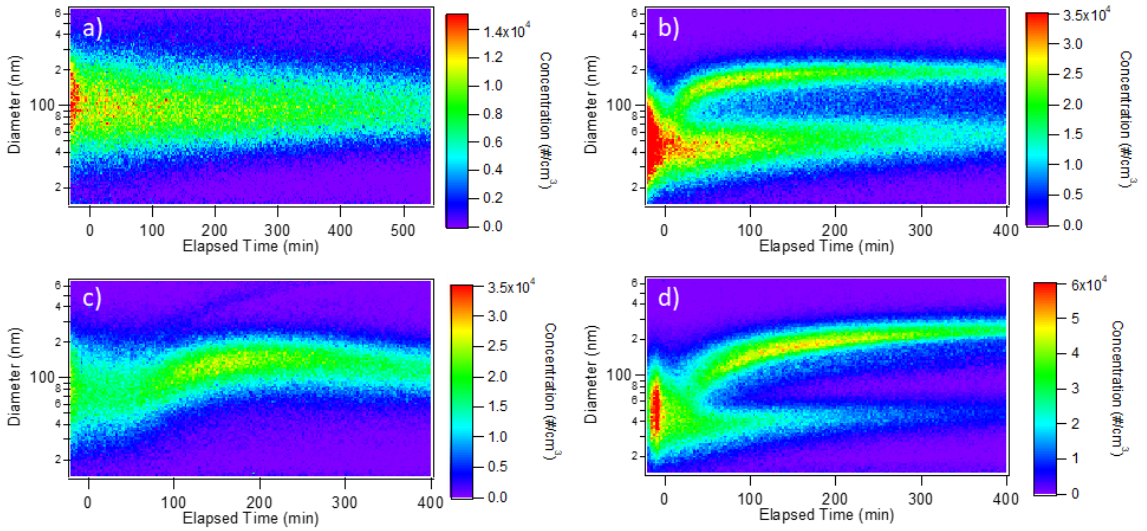

Figure 2-4: Electrical mobility size distribution image plot for GDI_1 (a), GDI_1/GPF (b), GDI_2 (c), and GDI_2/GPF (d) measured with the SMPS. t=0 corresponds to illumination of UV lights.

Figure 2-4a-d shows the electrical mobility size distribution and evolution of the aerosol during the irradiation experiments. UV lights were turned on at $t = 0$. The tailpipe emissions from GDI_1 in the stock configuration (Figure 2-4a), was initially a broad unimodal distribution peaked at ~95 nm with an effective density of approximately 0.58 g cm^{-3} (Figure 2-5a). The effective density is consistent with fractal black carbon particles (Nakao, et al, 2011). As the emissions aged, no notable shift in electrical mobility diameter was observed, however the effective density of the ~100 nm particles increased to 1.43 g cm^{-3} (Figure 2-5a), thus increasing aerosol mass by ~2.5 times. Particle number concentrations in the stock configuration above 200 nm are small and therefore effective density measurements were not available in this range.

GDI_2 stock configuration (Figure 2-4c) irradiation experiment did yield a shift in the particle electrical mobility diameter of the main distribution as the emissions aged. Similar to GDI_1, the tailpipe aerosol consisted of a broad, unimodal peak centering at ~75nm with a density of 0.67 g cm^{-3}, consistent with fractal black carbon. As gases condensed throughout the irradiation experiment, the broad peak sharpened and shifted to ~ 120nm. The density of the aerosol quickly increased to ~1.70 g cm^{-3} (t=75min). This change in density is indicative of ammonium nitrate condensation (1.72 g cm^{-3}) onto the black carbon backbone; after ~ 100 min, the contribution of less dense SOA to total aerosol mass increased, thus decreasing the effective density to 1.53 g cm^{-3} (t=200min). (Figure 2-5c).

A small number of particles grew outside of the main distribution at t~75 min, and eventually grew out of the detection limit of the SMPS at t~250 min. Because of this, the volumes calculated from the SMPS data for GDI_2 experiments were corrected from ~250 min and onwards, by calculating the contribution of each mode to total volume. This ratio was then applied through the duration of the experiment which likely resulted in a slight underproduction in the total mass formed. The underestimation is expected to be minimal as the particle mass formation of the smaller peak plateaued at 280 min, indicating aerosol mass formation had completed.

Figure 2-4 b and d display the results for GDI_1/GPF and GDI_2/GPF respectively. The initial effective density of the tailpipe emissions for both vehicles was ~0.96 g cm^{-3}, indicating the aerosol still contained a fractal black carbon backbone, however the increased POA contribution observed in Figure 2-2, resulted in a more spherical tailpipe

aerosol. The initial distribution in the irradiation experiment consists of the ammonium sulfate seed with a peak at approximately 50 nm for both (the densities are consistent with ammonium sulfate at ~1.78 g cm^{-3}, (Figure 2-4 b, d, and Figure 2-5 b, d). The seed/primary aerosol ratio (volume) was 24.6 and 11.4 for GDI_1 and the GDI_2 respectively. As the gases aged, the final distribution was bimodal with peak modes at ~230 nm and 50 nm for both vehicles. The aerosol density for both vehicles ended ~1.49 g cm^{-3} consistent with the composition of the ammonium sulfate seed (1.77 g cm^{-3}), ammonium nitrate (1.72 g cm^{-3}), and SOA (~1.40 g cm^{-3}). The distinguishing criteria between the experiments of the two GPF equipped vehicles was the number of particles in the larger diameter peak, which drastically changed the total mass calculated when compared the emissions from both vehicles.

Figure 2-5 shows the volume fraction remaining (VFR) for the aerosol throughout the irradiation experiment. In all four experimental conditions, the initial VFR was equal to 1.0. This value was consistent with non-volatile black carbon (stock configuration experiments) and ammonium sulfate seed (GPF configuration experiments).

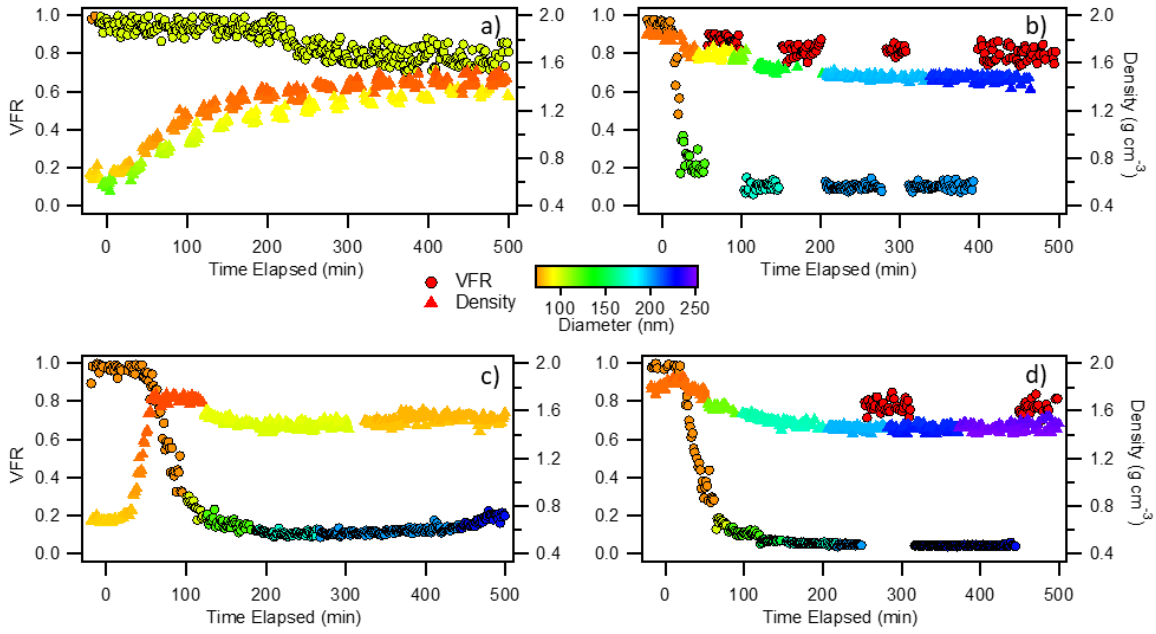

Figure 2-5: Volume fraction remaining (left y-axis) and the effective density (right y-axis) for GDI_1 (a), GDI_1/GPF (b), GDI_2 (c), and GDI_2/GPF (d). Color scale relates to electrical mobility diameter selected.

The VFR for GDI_1 (Figure 2-5a) was unique when compared to GDI_2 with and without GPF measurements due to the high VFR throughout the experiment. This phenomenon can be explained by the nature of the fractal black carbon seed particle and the relatively small amount of secondary aerosol formed. When the gas-to-particle phase partitioning occurred, the void space of the fractal black carbon backbone filled, which increased the mass of the aerosol, but had no effect on the electrical mobility diameter. Therefore, even if the additional aerosol mass formed was volatile when heated, the fractal black carbon backbone remained resulting in a VFR value of around 1.0. Once the density reached ~1.40 g cm-3, the VFR dropped from 1.0 to ~0.8. This indicated the particle's

morphology was more sphere-like, and the additional condensation of SOA resulted in a decreasing VFR, which was also confirmed with the HR-ToF-AMS results (Figure 2-6). Similar findings have been reported by Nakao, et al 2011, when they investigated the aging of diesel exhaust. For GDI_2, the aerosol mass condensed onto the initial black carbon was found to be completely volatile at 100 °C, resulting in a VFR of ~0.10. The initial aerosol that condensed was predominantly inorganic ammonium nitrate, but also comprised of SOA (Figure 2-6). As the organic gases continued to age and condense, the contribution of SOA to the total mass in the experiment increased, ultimately increasing the VFR to ~0.25.

GDI_1/GPF and GDI_2/GPF (Figure 2-5 b, d) followed similar trends to GDI_2 (c). The low diameter mode maintained similar properties to the ammonium sulfate seed with a high VFR. There was evidence of condensation of gases onto the smaller mode of particles as the VFR fell to around 0.8; indicative of condensation of ammonium nitrate and SOA mass. The large diameter mode displayed properties indicative to an ammonium nitrate and SOA dominated aerosol (VFR~0.10). The larger mode for both GPF configured vehicles related most similarly to Figure 2-5c (GDI_2) aerosol and was found to have similar composition distribution as well (Figure 2-6).

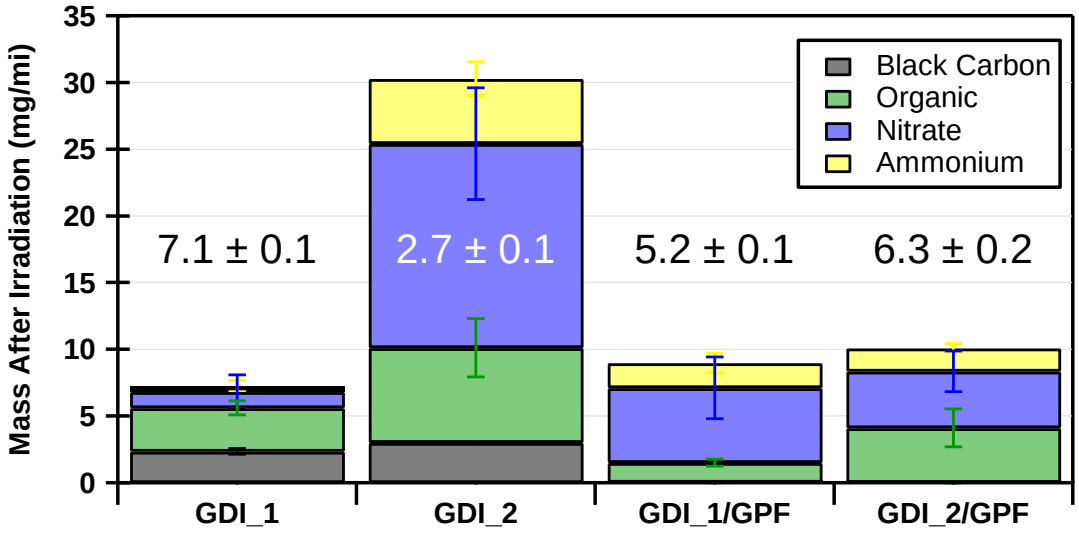

Figure 2-6: Measured mass and composition of PM at the conclusion of the irradiation experiment. Values across graph are the average VOC:NOx (ppm_v:ppm_v) ratios

Figure 2-6 shows the estimated aerosol mass composition after 400 minutes of irradiation in the atmospheric chamber (primary and secondary aerosol combined). The values shown on the graph indicate the VOC:NOx ratio (Table 2-1) in the experiments. The stock GDI_1 experiments formed the least amount of secondary aerosol. Approximately 45% of the total 7.24 mg/mi of aerosol composition after irradiation was comprised of organics. This compared to the stock configuration of GDI_2, where only 24% of the total aerosol after irradiation was organic, and the majority of the aerosol that formed was inorganic ammonium nitrate. Ammonium nitrate is formed when nitric acid (formed through the oxidation of NOx) reacts with gaseous NH_3 (Squizzato, et al, 2013). The total formation of salt will depend on the concentration of NOx, and NH_3 (not

measured for these experiments) emitted from the tailpipe. GDI_2 had the lowest VOC to NOx ratio. The low ratio was due to the high NOx emissions from the vehicle (Yang, et al, 2018). A VOC to NOx ratio of 2.7 is relatively low and considered to be in a VOC limited regime for secondary chemistry in relation to ozone production (Kroll, Seinfeld, 2008).

The total aerosol formed with and without the GPF after irradiation showed different trends for the two vehicles. GDI_1/GPF showed an increased mass of ammonium nitrate formation which was attributed to a higher NOx concentration in the GPF experiments (50.4 ppb vs 26.4 ppb NOx). The GPF reduced tailpipe PM by 16.6% (Yang, et al, 2018), however due to difference in dilution ratios between the two sets of experiments (60 vs 105), resulted in the formation of more ammonium nitrate in the chamber for the GPF tests. It was theorized that if the dilution ratio was constant between experimental conditions, the ammonium nitrate formation would have followed similar patterns with tailpipe NOx emissions.

The opposite was true for the secondary aerosol for GDI_2/GPF experiments. Once again, the most notable difference between the two irradiation experiments was the mass of ammonium nitrate that formed. In the stock configuration experiments, the NOx emissions were considerably higher from the tailpipe and in the mobile chamber (174.3 ppb vs 64.2 ppb for the stock, and GPF configuration respectively), despite the difference in dilutions (Table 2-1). The total reduction of tailpipe NOx for GDI_2 with the addition of the catalyzed GPF was 87.6% (Yang, et al, 2018).

Overall, the role of NH_3 should be further investigated in GDI vehicles with and without GPFs, as it may significantly contribute to the production of secondary inorganic aerosols mainly in the form of ammonium nitrate. Ammonia could be produced from the front TWC brick using H_2 generated from the engine (Huai, et al, 2003, Heeb, et al, 2006). The NH_3 from the front TWC will either pass through the underfloor TWC/GPF system or be oxidized to N_2O, NOx or N_2. While NH_3 emissions measurements were not made possible for this study, it is reasonable to assume that the differences in the oxygen storage component (OSC) materials levels of the GPF versus the TWC was the most likely cause of the difference in the amount of NH_3 at the tailpipe.

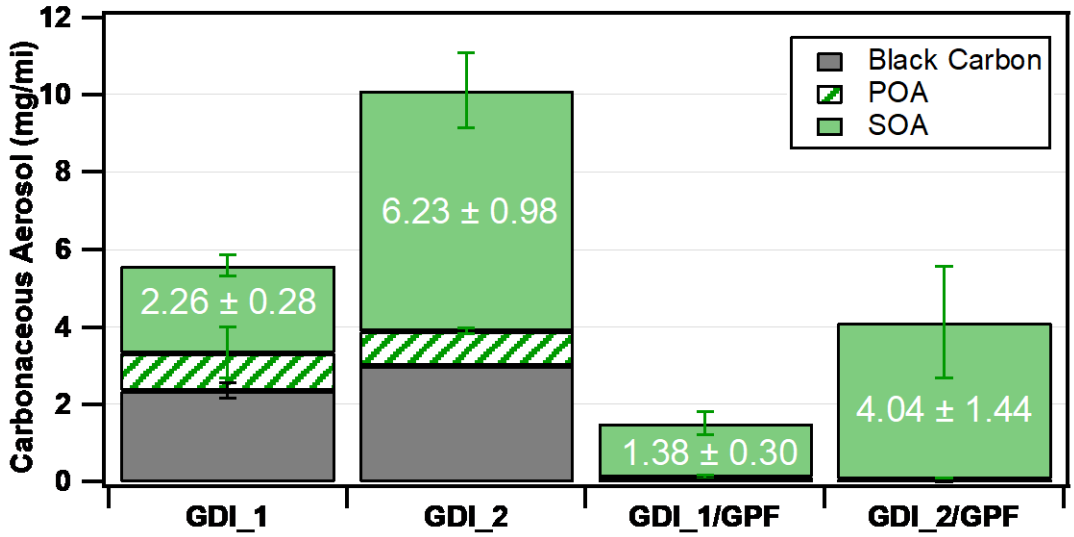

Figure 2-7: Total carbonaceous aerosol composition (black carbon, primary organic aerosol (POA), and secondary organic aerosol (SOA)) at the conclusion of the irradiation experiments, values indicate SOA formed (mg/mi)

Figure 2-7 shows the contribution of black carbon, POA and SOA to the total carbonaceous aerosol at the end of the irradiation experiments. The addition of a GPF resulted in 73% and 59% lower total carbonaceous aerosol (black carbon, POA, and SOA) for GDI_1 and GDI_2, respectively. For all experiments, there was a larger estimated mass of SOA formed compared to the POA mass, ranged from 2.3 to 60 times (Figure 2-7). Both vehicles without the catalyzed GPF produced more SOA than with the GPF configuration, with GDI_2 showing significantly higher SOA production than GDI_1. The reductions in SOA formed with the addition of a GPF were 39% and 35%, respectively, for GDI_1/GPF and GDI_2/GPF. In a previous study by Pieber et al (2017) it was reported that the use of GPF did not result in reductions in the gas phase pollutants responsible for SOA formation.

It should be noted, however, that in that study the GPF was not designed to replace the original TWC. The results reported here showed that a catalyzed GPF can be more efficient in the removal of gas phase pollutants and tailpipe PM, which are contributing factors to SOA production.

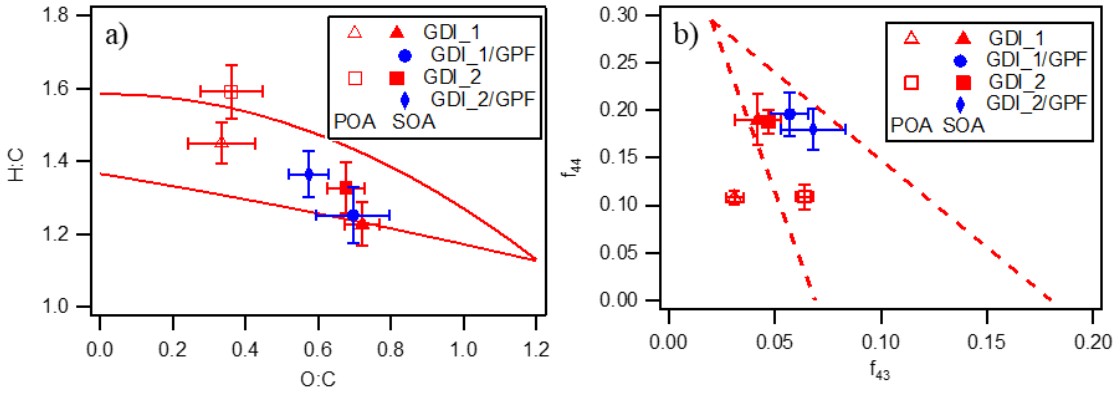

Figure 2-8: High resolution AMS results for; a)H:C, O:C ratios for POA (only stock configurations) and SOA (all configurations), b) f44 and f43 relationships for the POA (only stock configurations) and SOA (all configurations)

Another distinction between the properties of the POA and SOA is the oxygen content in the organic aerosol, which can be derived from the high resolution data of the AMS. Two important measures of this are fraction of the mass to charge ratio, total normalized ion fragments of *m/z* 44 (CO_2^+) versus *m/z* 43 ($C_2H_3O^+$), and the molar oxygen to carbon ratio (molar), as shown in Figure 2-8 (a-b) (Aiken, et al, 2008). Although the GPF vehicles did not emit sufficient amount of tailpipe aerosol to quantify the POA properties, the SOA values are still shown in Figure 2-8 (a-b). Average oxygenated organic aerosol (OOA) typically has an O:C ratio of 0.5 to 0.9; with semi-volatile OOA (SV-OOA)

classified with an O:C of 0.4 to 0.6, and low-volatility OOA (LV-OOA) from 0.7 to 1.0 (Jimenez et al, 2009). Figure 2-8a shows the POA for GDI_1 and GDI_2 with an average O:C ratio of ~0.35. As the aerosol ages and the organic aerosol fraction increases, the O:C ratio increases to an average of 0.67, indicating the final organics were more oxidized than the tailpipe OA.

Our results compare well to previous studies conducted on gasoline vehicles and reported O:C ratios from 0.3 to 0.7 (Presto, et al 2014, Liu, et al 2015, Nordin, et al 2013). The slopes from the POA to the SOA were found to be -0.58 and -0.83 for GDI_1 and GDI_2, respectively. A slope of -1.0 designates the addition of an alcohol or peroxide, and a slope of -0.5 and 0 indicate the addition of a carboxylic acid with and without fragmentation, respectively (Ng, et al 2011). The slopes in this study are comparable to those found in other studies for gasoline vehicle exhaust (Liu, et al, 2015; Presto et al 2014) and showed that SOA production could be explained by a combination of the addition of both alcohol/peroxide and carboxylic acid (with and without C-C bond cleavage) (Heald et al., 2010; Ng et al., 2011).

Another method used to measure the amount of oxidation in the aerosol is the f_{44} (ratio of *m/z* 44 to total signal in the component mass spectrum) and f_{43} (defined similarly to f_{44}). SV-OOA typically has an f_{44} from 0.03 to 0.12, while the LV-OOA is typically in the 0.13-0.21 range (Liu, et al, 2015). It has also been found that the majority of the atmospheric aerosols fall within the triangle developed by Ng et al (2010) depicted in Figure 2-8b. For both vehicles without the GPF, POA started with an f_{44} of ~0.11 and increased to an average of 0.19, suggesting the SOA formed was highly oxidized and likely

to contain polyacidic or acid-derived moieties (Figure 2-8b). For the GPF vehicles, SOA had similar compositional fraction of f_{44} and f_{43} compared to the original configurations. The fraction of total organic signal found in this work fell in the LV-OOA region (upper portion of the tringle shown in Figure 2-8b) and exceeded other f_{44} found in previous studies conducting experiments with gasoline vehicles, which varied from 0.10 (Nordin et al, 2013, Presto, et al, 2014) up to 0.15 (Liu, et al, 2015), indicating the aerosol formed was highly oxidized.

The difference in SOA production between the test vehicles, reveals that the engine design played some role in both the primary and secondary emissions formation. In addition to primary PM mass emissions (Yang, et al, 2018), GDI_2 also produced more SOA compared to GDI_1. GDI_1 was characterized by a relatively high compression ratio (14.0:1) relative to GDI_2 (10.0:1) that is typically higher than those found in commercially available passenger car GDI engines. The higher compression ratio for GDI_1 led to a homogeneous mixture for fuel with air due to more time for perfect mixture preparation, as well as to higher in-cylinder temperatures, hence higher flame temperatures during combustion to suppress PM and assist to a more complete oxidation of particles, particularly the volatile organic fraction. Additionally, the close contact between fuel and oxygen and the increasing wall temperatures due to increasing combustion temperatures will likely increase the heat flux and hence will result in less unburned hydrocarbons, which are all precursors for SOA production.

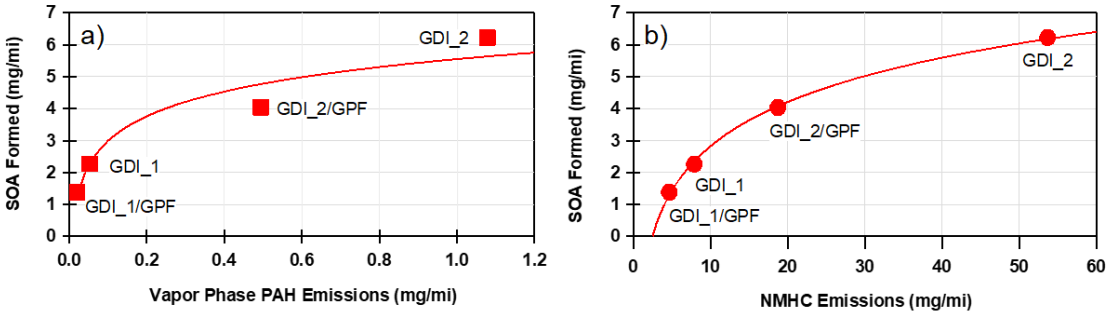

Figure 2-9: Measured SOA mass relationships to a) Vapor phase PAH emissions, and b) NMHC emissions for GDI_1 and GDI_2 stock and GPF configured irradiation experiments with a log normal fit trend-line.

The vapor phase PAH emissions and the total NMHC emissions (Figure 2-9 a, b) were directly correlated to the experimental SOA formation. The catalyzed GPF reduced the NMHC emissions for GDI_1 by 41% and 65% for GDI_2. GDI_2 emitted a higher concentration of NMHC in both configurations at 53.7 mg/mi and 18.7 mg/mi for the GDI_2 and GDI_2/GPF configurations respectively. GDI_1 exhibited much lower NMHC emissions at 9.7 mg/mi and 6.2 mg/mi for GDI_1 and GDI_1/GPF configurations respectively. The substantial difference in volatile organic gas emissions drives the variability in SOA formation between the two vehicles. The order of magnitude difference in NMHC emissions are easily explained by the differences in certification standards (GDI_1: LEVII SULEV30, GDI_2: LEV II). As shown in Yang et al. (2018), vapor-phase PAH emissions were dominated by two-ring and three-ring aromatic species, mainly naphthalenes and methyl/ethyl-naphthalenes, and phenanthrene. These low molecular

weight PAH compounds are known for their crucial role for the production of SOA (Chan, et al, 2009; Peng, et al, 2017).

The stock configuration of GDI_2 emitted the largest concentration of NMHC, however produced a smaller SOA yield when compared to the other experiments. This phenomena is the opposite of what is expected, where more VOC's typically result in an equal or larger SOA yield relative to reactive gas concentrations. The best explanation for this disparity, may be a consequence of multiple variables. First, due to particles growing out of range, the total aerosol calculated may be an underestimation of actual SOA formed in the experiment. Secondly, and most likely, GDI_2 experiments had an average VOC:NOx ratio of 2.7 which is more than two times less than other vehicle configuration experiments. Due to the large initial NOx concentration, a suppression of organic reactions may have occurred. In future experiments, it may be valuable to control the concentration of NOx injected (rather than attempting to add additional VOCs) into the chamber from the emissions, so NOx concentrations do not exceed typical urban concentrations (10-50 ppb).

2.5. Implications:

The addition of the catalyzed GPF to current GDI configurations will significantly reduce the tailpipe PM mass and drastically modify the tailpipe PM composition, and size distribution. For both GDI_1 and GDI_2, the tailpipe mass was reduced by 94.8% and a 97.8% respectively (Yang, et al, 2018). The GPF was most efficient in the removal of the accumulation mode particles and black carbon aerosol. The GPF was quite efficient in the removal of POA as well, however, due to volatility effects with the cooling of the exhaust, a greater POA fraction was observed relative to the stock configuration. GPF reduction in the tailpipe particle number, size, and black carbon composition will reduce the primary emissions of light-duty GDI vehicles and reduce the near-road traffic pollutant impact of the growing GDI vehicle market.

Changes in effective density and chemical composition data from the HR-ToF-AMS, were used to measure the formation of secondary material. If primary particles were black carbon (fractal), condensation of low volatility gasses did not change the secondary aerosol particle mobility diameter until the aerosol was more spherical (density ~1.4 g cm^{-3}). This work showed that the measurement of the effective density is vital for the accurate prediction of secondary aerosol mass due to variations throughout single experiments and across different experimental configurations. Single experiments can contain multiple particle modes of different compositions, leading to varying characteristics.

In all irradiation experiments, considerable secondary aerosol formed, and (excluding stock GDI_1) the size distribution of the particles emitted changed substantially. In the stock configuration experiments, total mass increased after photo-

oxidation by 2.1 and 7.5 times compared to the tailpipe mass for GDI_1 and GDI_2 respectively. This large difference was due to the large variation in emitted tailpipe gases and was most likely as a result of the different certification standards of the two vehicles (GDI_1: LEVII SULEV30, GDI_2: LEV II).

Furthermore, the catalyzed GPF reduced many of the gas phase pollutants known to react and form secondary aerosol. With the reduction of unburnt and partially oxidized fuel (NMHC), the SOA formation potential of the vehicles also decreased. The GPF was also effective in the removal of NOx which should in turn decrease the total ammonium nitrate formation potential (seen for GDI_2 but not GDI_1 most likely due to dilution effects and starting chamber experimental conditions). Overall, the catalyzed GPF was able to reduce the total carbonaceous aerosol potential from the vehicle exhaust (black carbon, POA, and SOA) by 73% and 59%. However, the data obtained across multiple aerosol instruments was consistent and indicated that vehicle stock and GPF configuration emissions have the potential to form additional mass downwind of the tailpipe source.

When comparing the stock LEV II vehicle (GDI_2) to the LEV III vehicle (GDI_1), there was a 13% reduction in tailpipe mass. However, due to the considerable decrease in reactive gas emissions, the estimated total secondary aerosol formation showed a 76% reduction. The reduction in SOA may be amplified by the difference in lower dilution of laboratory work compared to actual dilution of the atmosphere. Nevertheless, regional pollutants impacted by increased GDI use may still influence the total secondary aerosol that can form in high density urban areas. If regulators focus more on gas phase reduction, the results from this work indicates the potential of a more influential reduction in sub-

micron, atmospheric aerosol mass. Similarly, with the addition of the catalyzed GPF, there was a 10.8% reduction between the LEV II and LEVIII certified vehicles (70% and 67% reduction when compared to the LEVII, stock GDI_2) suggesting the catalyzed GPF has the ability to decrease the discrepancy in secondary mass formation between different certification standard vehicles, which can retroactively improve emissions from vehicles without relying on the consumer to purchase a new, lower emitting vehicle.

This work can confidently conclude that the addition of a catalyzed GPF will aid manufacturers of GDI vehicles meet the future stringent regulations aimed to reduce the tailpipe PM from GDI vehicles. Additionally, a catalyzed GPF can reduce the gas phase pollutants, which directly decreases the SOA formation potential of the vehicles. These results suggest that more work must be completed to explore the secondary nature of PM formation from mobile sources. Even with the exceptional improvements in technology and emission reduction after-treatment technologies, a considerable amount of mass per mileage of PM can form downwind from the original exhaust emission source.

The secondary chamber scenarios here only consider one driving cycle. Future studies should look into the effects of different driving cycles, and driving conditions (hot-start vs cold-start) on the emissions and the secondary potential of the exhaust. Also, fuel composition may change the relationship observed with NMHC emissions and SOA formation if the compound composition of the NMHC in the emissions changes drastically. The reactivity of the experiments in this work are dependent on the compounds emitted from the tailpipe, and all other reactive compounds were removed. In an atmospheric environment, the exhaust will react as a result the atmosphere, not dictate the overall

reactions. It may be worthwhile to look into controlling the reactivity of the experiments with the addition of surrogate similar to the atmosphere to see if there is a considerable effect on the secondary aerosol formation from mobile sources.

Supporting Information:

Further details on the experimental procedures and protocols, emissions methods analyses, and emissions results are provided. This material is available free of charge via the Internet at http://pubs.acs.org.

Funding Sources:

We acknowledge funding from the South Coast Air Quality Management District (SCAQMD) under contract 15625 and the Manufacturers of Emission Controls Association (MECA) under contract 15040420. We would also like to acknowledge the funding from NCST Graduate Fellowship

Notes:

The authors declare no competing financial interest.

Acknowledgements:

The authors thank Mr. Mark Villela and Mr. Daniel Gomez of the University of California, Riverside for their contribution in contacting this research program. We also thank MECA for providing the catalyzed GPF for this program and also for their technical support and guidance.

2.6. References:

1) Heal, M. R.; Kumar, P.; Harrison, R. M. Particles, air quality, policy and health. *Chem. Soc. Rev.* **2012**, *41*, 6606-6630.
2) Dallmann, T.R.; Onasch, T.B.; Kirchstetter, T.W.; Worton, D.R.; Fortner, E.C.; Herndon, S.C.; Wood, E.C.; Franklin, J.P.; Worsnop, D.R.; Goldstein, A.H.; Harley, R.A. Characterization of particulate matter emissions from on-road gasoline and diesel vehicles using a soot particle aerosol mass spectrometer. *Atmos. Chem. Phys.* **2014**, *14*, 7585-7599.
3) McDonald, B. C.; Dallmann, T. R.; Martin, E. W.; Harley, R. A. Long-term trends in nitrogen oxide emissions from motor vehicles at national, state, and air basin scales. *J. Geophys Res-Atmos* **2012,** *117*, D00V18.
4) McDonald, B. C.; Gentner, D. R.; Goldstein, A. H.; Harley, R. A. Long-term trends in motor vehicle emissions in U.S. urban areas. *Environ. Sci. Technol.* **2013**, *47*, 10022-31.
5) California Air Resources Board, https://www.arb.ca.gov/desig/adm/adm.htm
6) May, A.A.; Presto, A.A.; Hennigan, C.J.; Nguyen, N.T.; Gordon, T.D.; Robinson, A.L. Gas-particle partitioning of primary organic aerosol emissions: (1) Gasoline vehicle exhaust. *Atmospheric Environment **2013**, 77*, 128-139.
7) Samet, J. M.; Dominici, F.; Curriero, F. C.; Coursac, I.; Zeger, S. L. Fine particulate air pollution and mortality in 20 US cities, 1987 −1994. *N. Engl. J. Med.* **2000**, *343*, 1742-1749.
8) Lelieveld, J.; Evans, J. S.; Fnais, M.; Giannadaki, D.; Pozzer, A. The contribution of outdoor air pollution sources to premature mortality on a global scale. *Nature* **2015**, *525*, 367-371.
9) Pope, C. A.; Burnett, R. T.; Thun, M. J.; Calle, E. E.; Krewski, D.; Ito, K.; Thurston, G. D. Lung cancer, cardiopulmonary mortality, and long-term exposure to fine particulate air pollution. *JAMA* **2002**, *287*, 1132-1141.

10) Odum, J.R.; Junkkamp, T.P.; Griffin,, W.R.; Forstner, H.J.L.; Flagan, R.C.; Seinfeld, J.H. Aromatics, reformulated gasoline, and atmospheric organic aerosol formation. *Environ. Sci. Technol.* **1997**, *31*, 1890-1897.

11) Gentner, D.R.; Jathar, S.H.; Gordon, T.D.; Bahreini, R.; Day, D.A.; Haddad, I.E.; Haynes, P.L.; Pieber, S.M.; Platt, S.M.; De Gouw, J.; Goldstein, A.H.; Harley, R.A.; Jimenez, J.L.; Prevot, A.S.H.; Robinson A.L. Review of urban secondary organic aerosol formation from gasoline and diesel motor vehicle emissions. *Environ. Sci. Technol.* **2017**, *51*, 1074-1093.

12) Jimenez, J. L.; Canagaratna, M. R.; Donahue, N. M.; Prevôt, A. S. H.; Zhang, Q.; Kroll, J. H.; Decarlo, P. F.; Allan, J. D.; Coe, H.; Ng, N. L.; Aiken, A. C.; Ulbrich, I. M.; Grieshop, A. P.; Duplissy, J.; Wilson, K. R.; Lanz, V. A.; Hueglin, C.; Sun, Y. L.; Tian, J.; Laaksonen, A.; Raatikainen, T.; Rautiainen, J.; Vaattovaara, P.; Ehn, M.; Kulmala, M.; Tomlinson, J. M.; Cubison, M. J.; Dunlea, E. J.; Alfarra, M. R.; Williams, P. I.; Bower, K.; Kondo, Y.; Schneider, J.; Drewnick, F.; Borrmann, S.; Weimer, S.; Demerjian, K.; Salcedo, D.; Cottrell, L.; Takami, A.; Miyoshi, T.; Shimono, A.; Sun, J. Y.; Zhang, Y. M.; Dzepina, K.; Sueper, D.; Jayne, J. T.; Herndon, S. C.; Williams, L. R.; Wood, E. C.; Middlebrook, A. M.; Kolb, C. E.; Baltensperger, U.; Worsnop, D. R. Evolution of organic aerosols in the atmosphere. *Science* **2009**, *326*, 1525–1529.

13) Hallquist, M.; Wenger, J. C.; Baltensperger, U.; Rudich, Y.; Simpson, D.; Claeys, M.; Dommen, J.; Donahue, N. M.; George, C.; Goldstein, A. H.; Hamilton, J. F.; Herrmann, H.; Hoffmann, T.; Iinuma, Y.; Jang, M.; Jenkin, M. E.; Jimenez, J. L.; Kiendler-Scharr, A.; Maenhaut, W.; McFiggans, G.; Mentel, Th. F.; Monod, A.; Prévôt, A. S. H.; Seinfeld, J. H.; Surratt, J. D.; Szmigielski, R.; Wildt, J. The formation, properties and impact of secondary organic aerosol: current and emerging issues. *Atmos. Chem. Phys.* **2009**, *9*, 5155-5236.

14) Hu, W.; Hu, M.; Hu, W.; Jimenez, J. L.; Yuan, B.; Chen, W.; Wang, M.; Wu, Y.; Chen, C.; Wang, Z.; Peng, J.; Zeng, L.; Shao, M. Chemical composition, sources, and

aging process of submicron aerosols in Beijing: Contrast between summer and winter. *J. Geophys. Res.-Atmos.*, **2016**, *121*, 1955-1977.

15) Zhang, Q.; Jimenez, J. L.; Canagaratna, M. R.; Allan, J. D.; Coe, H.; Ulbrich, I.; Alfarra, M. R.; Takami, A.; Middlebrook, A. M.; Sun, Y. L.; Dzepina, K.; Dunlea, E.; Docherty, K.; DeCarlo, P. F.; Salcedo, D.; Onasch, T.; Jayne, J. T.; Miyoshi, T.; Shimono, A.; Hatakeyama, S.; Takegawa, N.; Kondo, Y.; Schneider, J.; Drewnick, F.; Borrmann, S.; Weimer, S.; Demerjian, K.; Williams, P.; Bower, K.; Bahreini, R.; Cottrell, L.; Griffin, R. J.; Rautiainen, J.; Sun, J. Y.; Zhang, Y. M.; Worsnop, D. R. Ubiquity and dominance of oxygenated species in organic aerosols in anthropogenically-influenced Northern Hemisphere mid latitudes. *Geophys. Res. Lett.*, **2007**, *34*, L13801, https://doi.org/10.1029/2007gl029979.

16) Bahreini, R.; Middlebrook, A. M.; de Gouw, J. A.; Warneke, C.; Trainer, M.; Brock, C. A.; Stark, H.; Brown, S. S.; Dube, W. P.; Gilman, J. B.; Hall, K.; Holloway, J. S.; Kuster, W. C.; Perring, A. E.; Prevot, A. S. H.; Schwarz, J. P.; Spackman, J. R.; Szidat, S.; Wagner, N. L.; Weber, R. J.; Zotter, P.; Parrish, D. D. Gasoline emissions dominate over diesel in formation of secondary organic aerosol mass. *Geophys. Res. Lett*. **2012**, *39*, L06805, doi: 10.1029/2011GL050718.

17) McDonald, B.C.; Goldstein, A.H.; Harley, R.A. Long-term trends in California mobile source emissions and ambient concentrations of black carbon and organic aerosol. *Environ. Sci. Technol.* **2015**, *49*, 5178-5188.

18) Saliba, G.; Saleh, R.; Zhao, Y.; Presto, A.A.; Lamber, A.T.; Frodin, B.; Sardar, S.; Maldonado, H.; Maddox, C.; May, A.A.; Drozd, G.T.; Goldstein, A.H.; Russell, L.M.; Hagen,, F.; Robinson, A.L. Comparison of gasoline direct-injection (GDI) and port fuel injection (PFI) vehicle emissions: Emission Certification standards, cold-start, secondary organic aerosol formation potential, and potential climate impacts. *Environ. Sci. Technol.* **2017**, *51*, 6542-6552.

19) Ma, P.; Zhang, P.; Shu, J.; Yang, B.; Zhang, H. Characterization of secondary organic aerosol from photo-oxidation of gasoline exhaust and specific sources of major components. *Environmental Pollution* **2018**, *232*, 65-72.

20) Zhao, Y.; Saleh, R.; Saliba, G.; Presto, A.A.; Gordon, T.D.; Drozd, G.T.; Goldstein, A.H.; Donahue, N.M.; Robinson, A.L. Reducing secondary aerosol formation from gasoline vehicle exhaust. *Proc Natl Acad Sci USA* **2017**, *114*, 6984-6989.

21) Gordon, T. D.; Presto, A. A.; May, A. A.; Nguyen, N. T.; Lipsky, E. M.; Donahue, N. M.; Gutierrez, A.; Zhang, M.; Maddox, C.; Rieger, P.; Chattopadhyay, S.; Maldonado, H.; Maricq, M. M.; Robinson, A. L. Secondary organic aerosol formation exceeds primary particulate matter emissions for light-duty gasoline vehicles. *Atmos. Chem. Phys.* **2014**, *14*, 4661–4678.

22) Platt, S. M.; El Haddad, I.; Zardini, A. A.; Clairotte, M.; Astorga, C.; Wolf, R.; Slowik, J. G.; Temime-Roussel, B.; Marchand, N.; Ježek, I.; Drinovec, L.; Močnik, G.; Möhler, O.; Richter, R.; Barmet, P.; Bianchi, F.; Baltensperger, U.; Prévôt, A. S. H.: Secondary organic aerosol formation from gasoline vehicle emissions in a new mobile environmental reaction chamber. *Atmos. Chem. Phys.* **2013**, *13*, 9141-9158.

23) Nordin, E. Z.; Eriksson, A. C.; Roldin, P.; Nilsson, P. T.; Carlsson, J. E.; Kajos, M. K.; Hellén, H.; Wittbom, C.; Rissler, J.; Löndahl, J.; Swietlicki, E.; Svenningsson, B.; Bohgard, M.; Kulmala, M.; Hallquist, M.; Pagels, J. H. Secondary organic aerosol formation from idling gasoline passenger vehicle emissions investigated in a smog chamber. *Atmos. Chem. Phys.* **2013**, *13*, 6101-6116.

24) Liu, T.; Wang, X.; Deng, W.; Hu, Q.; Ding, X.; Zhang, Y.; He, Q.; Zhang, Z.; Lu, S.; Bi, X.; Chan, J.; Yu, J. Secondary organic aerosol formation from photochemical aging of light-duty gasoline vehicle exhausts in a smog chamber. *Atmos. Chem. Phys.* ***2015***, *15*, 9049-9062.

25) Karavalakis, G.; Short, D.; Vu, D.; Russell, R.; Hajbabaei, M.; Asa-Awuku, A.; Durbin, T.D. Evaluating the effects of aromatics content in gasoline on gaseous and particulate matter emissions from SI-PFI and SI-DI vehicles. *Environ. Sci. Technol.* **2015**, *49*, 7021-7031.

26) Chen, L.; Liang, Z.; Zhang, X.; Shuai, S. Characterizing particulate matter emissions from GDI and PFI vehicles under transient and cold start conditions. *Fuel* **2017**, 189, 131-140.

27) Stevens, E.; Steeper, R. Piston wetting in an optical DISI engine: Fuel films, pool fires, and soot generation. SAE Technical Paper **2001**, 2001-01-1203.

28) Karlsson, R.B.; Heywood, J.B. Piston fuel film observations in an optical access GDI engine. SAE Technical Paper **2001**, 2001-01-2022.

29) Piock, W.; Hoffmann, G.; Berndorfer, A.; Salemi, P.; Fusshoeller, B. Strategies towards meeting future particulate matter emission requirements in homogeneous gasoline direct injection engines. *SAE Int. J. Engines* **2011**, *4*, 1455-1468.

30) Yang, J.; Roth, P.; Durbin, T. D.; Johnson, K. C.; Cocker III, D. R.; Asa-Awuku, A.; Brezny, R.; Geller, M.; Karavalakis, G. Gasoline particulate filters as an effective tool to reduce particulate and PAH emissions from GDI vehicles: A case study with two GDI vehicles. *Environ. Sci. Technol.* **2018**, *52*, 3275-3284.

31) Mamakos, A.; Martini, G.; Marotta, A.; Manfredi, U. Assessment of different technical options in reducing particle emissions from gasoline direct injection vehicles. *Journal of Aerosol Science* **2013**, 63, 115-125.

32) Chan, T. W.; Meloche, E.; Kubsh, J.; Brezny, R. Black carbon emissions in gasoline exhaust and a reduction alternative with a gasoline particulate filter. *Environ. Sci. Technol.* **2014**, *48*, 6027-6034.

33) Xia, Wenzheng, Yi Zheng, Xiaokun He, Dongxia Yang, Huifang Shao, Joesph Remias, Joseph Roos, and Yinhui Wang. 2017. “Catalyzed Gasoline Particulate Filter (GPF) Performance: Effect of Driving Cycle, Fuel, Catalyst Coating.” SAE Technical Paper. http://papers.sae.org/2017-01-2366/.

34) Du, Z.; Hu, M.; Peng, J.; Zhang, W.; Zheng, J.; Gu, F.; Qin, Y.; Yang, Y.; Li, M.; Wu, Y.; Shao, M.; Shuai, S. Comparison of primary aerosol emission and secondary aerosol formation from gasoline direct injection and port fuel injection vehicles. *Atmos. Chem. Phys.* **2018**, *18*, 9011-9023.

35) Zhao, Y.; Lamber, A.T.; Saleh, R.; Saliba, G.; Robinson, A.L. Secondary organic aerosol production from gasoline vehicle exhaust: Effects of engine technology, cold start, and emission certification standard. *Environ. Sci. Technol.* **2018**, *52*, 1253-1261.

36) Karjalainen, P.; Timonen, H.; Saukko, E.; Kuuluvainen, H.; Saarikoski, S.; Aakko-Saksa, P.; Murtonen, T.; Dal Maso, M.; Ahlberg, E.; Svenningsson, B.; Brune, W. H.; Hillamo, R.; Keskinen, J.; Rönkkö, T. Time-resolved characterization of primary and secondary particle emissions of a modern gasoline passenger car. *Atmos. Chem. Phys.* **2016**, *16*, 8559–8470.

37) Pieber, S. M.; Kumar, N. K.; Klein, F.; Comte, P.; Bhattu, D.; Dommen, J.; Bruns, E. A.; Kilic, D.; El Haddad, I.; Keller, A.; Czerwinski, J.; Heeb, N.; Baltensperger, U.; Slowik, J. G.; Prévôt, A. S. H. Gas phase composition and secondary organic aerosol formation from gasoline direct injection vehicles investigated in batch and flow reactors: effects of prototype gasoline particle filters. *Atmos. Chem. Phys.* **2018**, *18*, 9929-9954.

38) Vu, D.; Roth, P.; Berte, T.; Yang, J.; Cocker D.; Durbin T.; Karavalakis, G.; Asa-Awuku, A. Using a new Mobile Atmospheric Chamber (MACh) to investigate the formation of secondary aerosols from mobile sources: The case of gasoline direct injection vehicles. Journal of Aerosol Science, Manuscript Under Review.

39) Petzold, A., and R. Niessner. 1996. "Photoacoustic Soot Sensor for in-Situ Black Carbon Monitoring." *Applied Physics. B, Lasers and Optics* 63 (2): 191–97.

40) Aiken, A. C.; DeCarlo, P. F.; Kroll, J. H.; Worsnop, D. R.; Huffman, J. A.; Docherty, K. S.; Ulbrich, I. M.; Mohr, C.; Kimmel, J. R.; Sueper, D.; Sun, Y.; Zhang, Q.; Trimborn, A.; Northway, M.; Ziemann, P. J.;, Canagaratna, M. R.; Onasch, T. B.; Alfarra, M. R.; Prevot, A. S. H.,; Dommen, J.,; Duplissy, J.; Metzger, A.; Baltensperger, U.; Jimenez, J. L. O/C and OM/OC ratios of primary, secondary, and ambient organic aerosols with high-resolution time-of-flight aerosol mass spectrometry. *Environ. Sci. Technol.* **2008**, *42*, 4478-4485.

41) Villani, P.; Picard, D.; Michaud, V.; Laj, P.; Wiedensohler, A. Design and validation of a Volatility Hygroscopic Tandem Differential Mobility Analyzer (VH_TDMA) to characterize the relationships between the thermal and hygroscopic properties of atmospheric aerosol particles. *Aerosol Sci. Technol.* **2008**, *42*, 729-741.

42) Malloy, Q.; Nakao, S.; Qi, L.; Austin, R. L.; Stothers, C.; Hagino, H.; Cocker, D. R. Real-Time Aerosol Density Determination Utilizing a Modified Scanning Mobility Particle Sizer-Aerosol Particle Mass Analyzer system. *Aerosol Sci. Technol.* **2009**, *43*, 673–678.

43) Cocker, D. R.; Flagan, R. C.; Seinfeld, J. H. State-of-the-art chamber facility for studying atmospheric aerosol chemistry. *Environ. Sci. Technol.* **2001**, *35*, 2594-2601.

44) Maricq, M.M.; Szente, J.J.; Jahr, K. The impact of ethanol fuel blends on PM emissions from a light-duty GDI vehicle. *Aerosol Sci. Technol.* **2012**, *46*, 576-583.

45) Yang, J.; Roth, P.; Ruehl, C.R.; Shafer, M.M.; Antkiewicz, D.S.; Durbin, T.D.; Cocker D.; Asa-Awuku, A.; Karavalakis, G. Physical, chemical, and toxicological characteristics of particulate emission from current technology gasoline direct injection vehicles. *Science of the Total Environment* **2019**, *650*, 1182-1194.

46) Tandon, P.; Heibel, A; Whitmore, J; Kekre, N.; Chithapragada, K. Measurement and prediction of filtration efficiency evolution of soot loaded diesel particulate filters. *Chemical Engineering Science* **2010**, *65*, 4751-4760.

47) Nakao, S.; Shrivastava, M.; Nguyen, A.; Cocker III, D. Interpretation of secondary organic aerosol formation from diesel exhaust photooxidation in an environmental chamber. *Aerosol Sci. Technol.* **2011**, *45*, 964-972.

48) Squizzato, S.; Masiol, M.; Brunelli, A.; Pistollato, S.; Tarabotti, E.; Rampazzo, G.; Pavoni, B. Factors determining the formation of secondary inorganic aerosol: a case study in the Po Valley (Italy). *Atmos. Chem. Phys.* **2013**, *13*, 1927-1939.

49) Kroll, J.H.; Seinfeld, J.H. Chemistry of secondary organic aerosol: Formation and evolution of low-volatility organics in the atmosphere. *Atmospheric Environment* **2008**, *42*, 3593-3624.

50) Huai, T.; Durbin, T.D.; Miller, W.J.; Pisano, J.T.; Sauer, C.G.; Rhee, S.H.; Norbeck J.M. Investigation of NH_3 emissions from new technology vehicles as a function of vehicle operating conditions. *Environ. Sci. Technol.* **2003**, *37*, 4841-4847.

51) Heeb, N.V.; Forss, A.M.; Bruhl,ann, S.; Luscher, R.; Saxer, C.J.; Hug, P. Three-way catalyst-induced formation of ammonia-velocity and acceleration-dependent emission factors. *Atmospheric Environment* **2006**, *40*, 5986-5997.

52) Presto, A. A.; Gordon, T. D.; and Robinson, A. L. Primary to secondary organic aerosol: evolution of organic emissions from mobile combustion sources. *Atmos. Chem. Phys.* **2014**, *14*, 5015-5036.

53) Ng, N. L.; Canagaratna, M. R.,; Zhang, Q.; Jimenez, J. L.; Tian, J.,; Ulbrich, I. M.; Kroll, J. H.; Docherty, K. S.; Chhabra, P. S.; Bahreini, R.;, Murphy, S. M.; Seinfeld, J. H.; Hildebrandt, L.; Donahue, N. M.; DeCarlo, P. F.; Lanz, V. A.; Prévôt, A. S. H.; Dinar, E.; Rudich, Y.; Worsnop, D. R. Organic aerosol components observed in Northern Hemispheric datasets from Aerosol Mass Spectrometry. *Atmos. Chem. Phys.* **2010**, *10*, 4625- 4641.

54) Heald, C.L.; Kroll J.H.; Jimenez, J.L.; Cocherty K.S.; DeCarlo, P.F.; Aiken, A.C.; Chen, Q.; Martin, S.T.; Farmer, D.K.; Artaxo, P. A simplified description of the evolution of organic aerosol composition in the atmosphere. *Geophysical Research Letters* **2010**, *37*, L08803.

55) Chan, A.W.H.; Kautzman, K.E.; Chhabra, P.S.; Surratt, J.D.; Chan, M.N.; Crounse, J.D.; Kurten, A.; Wennberg, P.O.; Flagan, R.C.; Seinfeld, J.H. Secondary organic aerosol formation from photooxidation of naphthalene and alkylnaphthalenes: implications for oxidation of intermediate volatility organic compounds (IVOCs). *Atmos. Chem. Phys.* **2009**, *9*, 3049-3060.

56) Peng, J.; Hu, M.; Du, Z.; Wang, Y.; Zheng, J.; Zhang, W.; Yang, Y.; Qin, Y.; Zheng, R.; Xiao, Y.; Wu, Y.; Lu, S.; Wu, Z.; Guo, S.; Mao, H.; Shuai, S. Gasoline aromatics: a critical determinant of urban secondary organic aerosol formation. *Atmos. Chem. Phys.* **2017**, *17*, 10743-10752.

2.7. Supplemental Information:

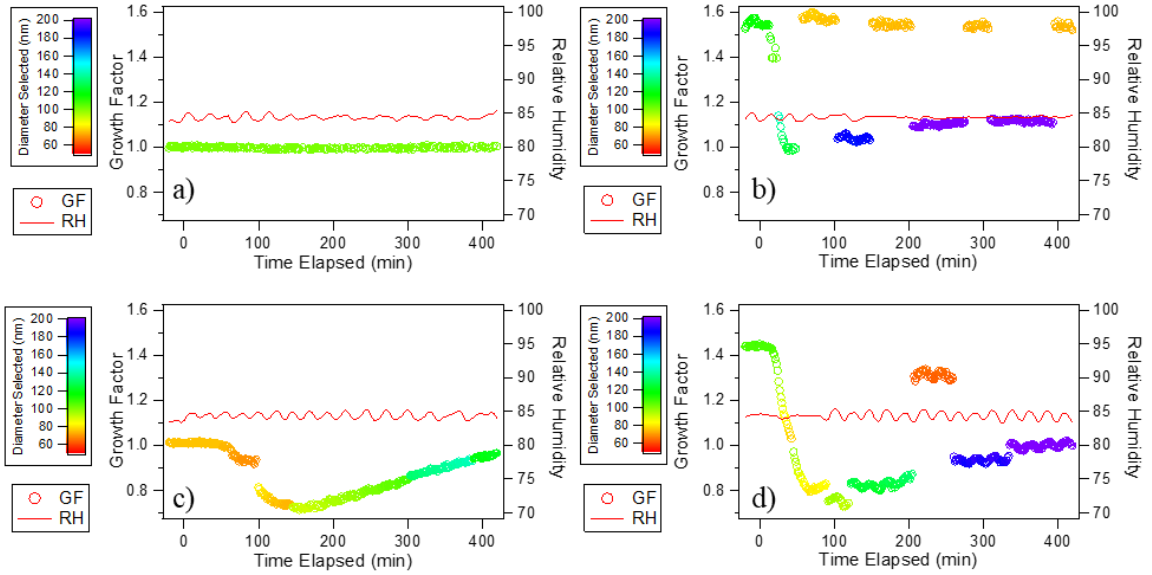

Figure 2-10: Growth factor for GDI_1 (a), GDI_1/GPF (b), GDI_2 (c), and GDI_2/GPF (d). Red line is the relative humidity in the instrument, and the color scale relates to the particle mode measured.

Figure 2-10 shows the growth factor for the aerosol throughout the irradiation experiment. This is measured using the hygroscopicity tandem differential mobility analyzer (HTDMA). The first DMA column is set to a specific voltage, to select particles with a specific aerodynamic diameter. After the selection, all of the particles of the specific aerodynamic diameter goes through a column set to a specific relative humidity (~88%). After passing through the humid column, the particles then pass through the second DMA column which scans through a range of aerodynamic diameter to see how the size of the aerosol changed. The selected diameter is then compared to the final diameter (volume

final divided by volume initial) to get the growth factor of the aerosol. This method is important to see the particles' affinity to taking up water in the sub saturated regime.

In Figure 2-10 a, the growth factor initially starts at 1.0, consistent to previous values observed from black carbon. As the aerosol ages, and organics condense, the growth factor remains consistent at 1.0 throughout the experiment. Figure 2-10 b (GDI_1/GPF) starts with a growth factor around 1.55 which is consistent with the ammonium sulfate seed. There are two main modes seen for the growth factor, red which is the smaller diameter peak, and the blue and purple which is the peak were the majority of the secondary aerosol mass is present. The smaller peak maintains a similar growth factor to the ammonium sulfate seed. The larger diameter peak however dips close to 1.0 and levels off around a growth factor of 1.1. This is consistent with a mix of ammonium nitrate and SOA.

In Figure 2-10 (c, d), the growth factors of the aerosol dip below 1.0 for a period of time in the middle of the experiments, and then level off above 1.0 at the end of irradiation. This would be consistent with a re-organization of the aerosol from a more fractal particle to a more spherical particle in the presence of water.

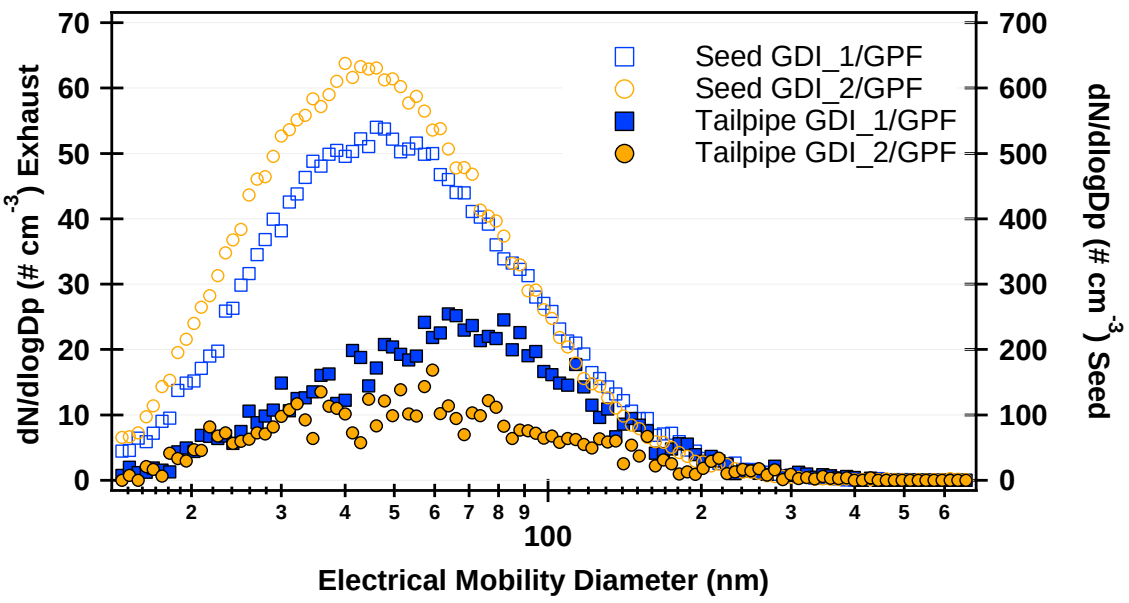

Figure 2-11: Initial size distribution of diluted GPF exhaust (closed) and seed (open) for GDI_1/GPF (orange) and GDI_2/GPF (blue). Exhaust values correspond to the left axis and were measured before seed was added (right axis).

Figure 2-11 shows the differences in initial diluted distribution for the tailpipe emissions (left axis) and the seed (right axis). Note the difference in amplitude for the two scales. The tailpipe aerosol emitted for both GDI_1/GPF and GDI_2/GPF were broad and unimodal. With the injection of the seed, the concentration of the aerosol went up a full order of magnitude and the peak shifted from ~60 nm to ~40 nm for both vehicles. The seed was injected to ensure a large enough surface area available to avoid any nucleation events as the gases aged and started condensing.

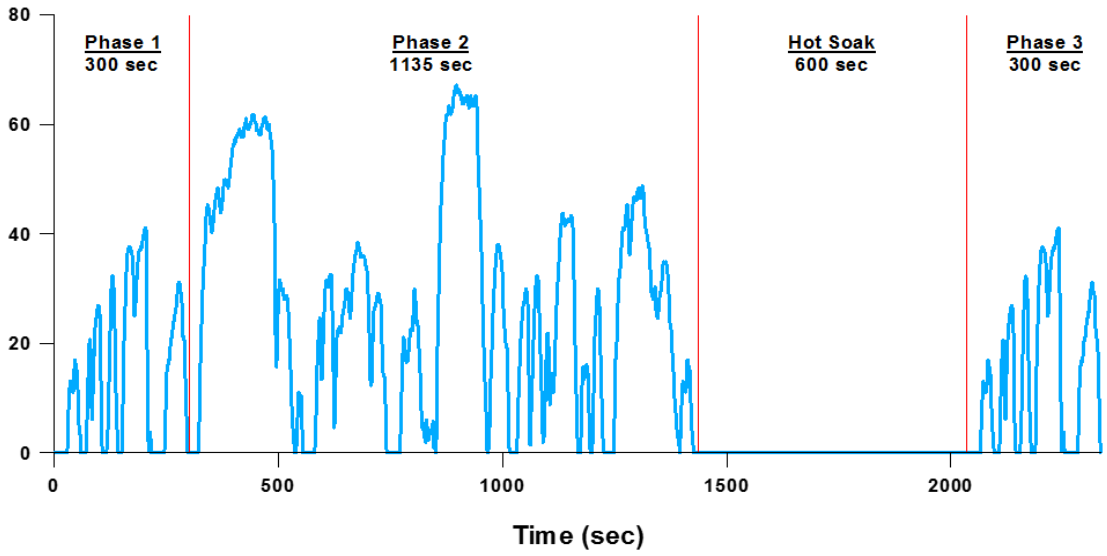

Figure 2-12: LA92 or Unified Driving Cycle (UC) comprised of three phases; Cold-start, Urban, and Hot-start phases. The vehicle's engine is turned off for the duration of the hot soak.

Figure 2-12 shows the LA92 driving cycle. The two vehicles were not operated for at least 16 hours before the test to ensure that the engine and catalyst were at room temperature at light off (ie cold-start). MACh was connected to the CVS and began injecting exhaust at the ignition event and continued to collect the exhaust at a consistent rate throughout the duration of the driving cycle. The chamber was then disconnected during the hot soak and reconnected for phase three. Dilutions of the experiments were altered by changing the CVS flow, and the flow of the injection lines into the chamber.

2.8. Equations:

$$\frac{dN(D_p,t)}{dt} = -\beta(D_p)N(D_p,t)$$

Equation 2-1: First order wall loss equation (Cocker, et al, 2001)

Equation 2-1 was used in all of the calculations utilizing the SMPS. This is the equation for the wall loss correction throughout the irradiation experiments. Once the particle number has stabilized, there will be a consistent decrease (slope) of particle number. This slope is then used to correct the number so it is a flat line at the time of plateau. This correction can then be applied to the volume allowing for a wall loss corrected mass.

$$C_i V_1 + C_a V_2 = C_f V_{MACh} \qquad \text{(a)}$$

$$V_1 + V_2 = V_{MACh} \qquad \text{(b)}$$

$$Dil_{\%} = \frac{V_2}{V_{MACh}} = \frac{(C_f - C_i)}{(C_a - C_i)} \qquad \text{(c)}$$

Equation 2-2: Equations for bag dilution % calculations, a) Concentration mass balance equation used b) Volume relationships, c) Calculation for dilution % with substituted variables. (subscripts; a=ambient, i=initial, f=final)

Equation 2-2 show the equations used to calculate the bag dilution throughout the experiment. The main method of calculation is looking at the concentration of carbon dioxide throughout the irradiation experiments. The carbon dioxide concentration is quite high due to the exhaust of the vehicle, thus if the outside air leaks into the chamber, there is a noticeable decrease in the carbon dioxide concentrations. In these experiments the subscript *a* relates to ambient, *i* relates to initial, and *f* relates to final concentration. The volume *1* is the amount of air initially in the chamber, and volume *2* is the amount of ambient air that goes into the chamber. The final dilution can be calculated when the amount of air that goes into the chamber is divided by the total volume of air in MACh.

$$C_e V_e + C_v V_v + C_a V_a = C_i V_{MACh} \quad \text{(a)}$$

$$V_e + V_v + V_a = V_{MACh} \quad \text{(b)}$$

$$DR = \frac{V_a + V_v}{V_e} = \frac{V_{MACh} - V_e}{V_e} \quad \text{(c)}$$

$$V_v = F_{psi} t_{cycle} \quad \text{(d)}$$

$$DR = \frac{\frac{V_{MACh}(C_i - C_a) - F_{psi} t_{cycle}(C_v - C_a)}{(C_e - C_a)}}{V_{MACh} - \frac{V_{MACh}(C_i - C_a) - F_{psi} t_{cycle}(C_v - C_a)}{(C_e - C_a)}} \quad \text{(e)}$$

Equation 2-3: Equations to calculate dilution ratio of exhaust, a) Concentration mass balance b)Volume relationships c)Dilution ratio (DR) equation d)Volume of air from VERL, e) Final DR calculation with substituted variables. (subscripts e=exhaust, v=VERL clean air, a=APL clean air, i=Initial CO_2 in chamber before lights on, F_{psi}=Flow of VERL at given pressure, t_{cycle}=time of injection in cycle)

Equation 2-3 are used to calculate the total dilution ratios of the vehicle exhaust from the tailpipe to the irradiation experiment. The subscripts *e* relates to exhaust, *v* relates to VERL clean air, *a* relates to APL clean air, *i* relates to initial CO_2 in chamber before lights on, F_{psi} is the flow of VERL at given pressure, and t_{cycle} is the time of injection in cycle. With all of the known concentrations of carbon dioxide of the different modes of dilution, and the measured concentration of the exhaust, the final dilution can be calculated by relating the volume of dilution air to the volume of the exhaust injected into the chamber.

Chapter 3: Investigating the Effect of Varying Ethanol Content and Driving Conditions on FFV-GDI Vehicle Emissions with the Addition of an Anthropogenic Surrogate

Patrick Roth [1,2], Jiacheng Yang [1,2], Ayla Moretti [1,2], David R. Cocker III [1,2], Thomas D. Durban [1,2], Georgios Karavalakis [1,2], Akua Asa-Awuku [1,2,3]

1. Bourns College of Engineering, Center for Environmental Research and Technology (CE-CERT), University of California, 1084 Columbia Avenue, Riverside, California 92507, United States
2. Department of Chemical and Environmental Engineering, Bourns College of Engineering, University of California, Riverside, California 92521, United States
3. Department of Chemical and Bimolecular Engineering, A. James Clark School of Engineering, University of Maryland, College Park, 4418 Stadium Dr., College Park, MD, 20702

3.1. Abstract:

This focus of this study was to investigate the effect of fuel properties on the secondary aerosol formation potential from two new technology flexible fuel, gasoline direct injection (FFV-GDI) vehicles. The two vehicles were tested on four test fuels; a baseline E10 fuel (28.1% aromatic by volume), a high aromatic (HA) E10 fuel (36.7% aromatic by volume), an intermediate E30 fuel, and a high ethanol E78 fuel blend. Another focus of this project was to observe the effects of driving conditions on the tailpipe and secondary emissions from the two FFV-GDI vehicles, by testing over cold-start and hot-start LA92 driving cycles.

Primary emissions were collected into UCR's 30m^3 MACh and were subsequently aged for 7-10 hours. The tailpipe emissions were diluted and classified to certification standards. Increasing the tailpipe PM from E10 to E78, the PM emissions were effectively reduced by 64% and 94% for FFV-1 and FFV-2 respectively. The HA E10 fuel increased the tailpipe emissions by 2.9 and 1.4 times for FFV-1 and FFV-2 respectively. Driving conditions also played a large role in the PM emissions from the tailpipe, as the hot-start tests emitted an average of 53% less tailpipe mass compared to the cold-start tests. In addition to the reduction of tailpipe PM, fuel composition and driving cycle affected the composition of the emitted tailpipe PM drastically.

The secondary aerosol formation trends in relation to the secondary aerosol formation were similar to the trend observed for tailpipe emissions for the two vehicles. As the ethanol content increased, the secondary aerosol formation potential decreased. The reductions in secondary aerosol mass from E78 were 34% and 78% compared to the

baseline E10 fuel for FFV-1 and FFV-2. These results were similar to the results observed by Timonen et al 2017 reporting limited secondary aerosol formation for E85 and E100 fuels utilizing a PAM chamber. Driving cycle had variable results in regards to secondary aerosol formation, where FFV-1 formed increased aerosol in the hot-start, while FFV-2 formed reduced secondary aerosol in the hot-start tests.

When focusing on the SOA formation in the irradiation tests, the observed trends were once again consistent with what was observed for the tailpipe emissions. The increase in ethanol content from E10 to E78 resulted in a 50% reduction in the NMHC emissions leading to an average of a 47% reduction in the SOA formation from the aged exhaust. In total, the SOA formed (15-60 mg/kg-fuel) was comparable to past studies (Gordon et al 2014, Liu et al 2015, Nordin et al 2013). With the VOC's measured in this work, we were able to account for 40% of the total SOA formation, indicating more work must be done to understand the lower volatile gases that complete the SOA closure.

The results displayed in this work indicate that high ethanol content is not only extremely effective in the reduction of tailpipe PM, however has the potential to greatly decrease the secondary aerosol formation potential of the emitted exhaust. This work also determined that the driving conditions can have variable effects on the secondary aerosol formation potential of the exhaust, where variable results were observed.

3.2. Introduction:

Transportation emissions are a dominant source of urban air pollution and significantly influence climate change and human health (Pachauri, et al, 2014; Han, et al, 2006). Particulate matter (PM) directly emitted from the tailpipe are dominated by primary organic aerosol (POA) and black carbon. Common primary gaseous pollutants include, nitrogen oxides (NOx), and non-methane organic gases (NMOG), which photochemically react in the atmosphere to produce secondary organic aerosol (SOA) (Robinson, et al, 2007). Several investigations have shown that SOA concentrations exceed POA levels (e.g, but not limited to, Karjalainen, (2015); Vu (2018), previous chapter, etc). Studies have also shown that gasoline vehicles can dominate the urban organic aerosol (Bahreini, et al, 2012). Gasoline fuel contains hundreds of light hydrocarbon species (less than C10) that are known SOA precursors with varying vapor pressures (Gentner, et al, 2017). Unburnt and partially combusted gasoline results in the emission of volatile organic compounds (VOCs) and intermediate VOCs (IVOCs) which account for the majority of urban SOA (Gentner, et al, 2012). In particular, light aromatic species with one benzene ring and with one or more alkyl groups have been recognized as major contributors to SOA (Odum, et al, 1997). However, recent research indicates that more complex IVOCs may play a key role in SOA formation from vehicle exhaust (Robinson et al 2007).

SOA formation from gasoline vehicles has received considerable attention in recent years, with the majority of studies focusing on older technology port-fuel injection (PFI) engines (Gentner, et al, 2017; Platt, et al, 2013; Zhao, et al, 2018; Liu, et al, 2015). There is limited information on the SOA formation from current technology gasoline direct

injection (GDI) engines, despite the abundancy of information on the primary emissions from these engines (e.g., but not limited to; Karavalakis, et al, 2014; Catapano, et al, 2016; Jin, et al, 2017). Vehicles equipped with GDI engines have increased their market share in both the US and Europe. GDI technology is considered one of the pathways to reduce greenhouse gas emissions and fuel consumption. However, in GDI engines the fuel is injected directly into the combustion chamber, which may lead to excessive fuel wetting in the cylinder and piston surfaces. This liquid fuel spray can result in pool fires that are sources of PM and unburned hydrocarbons (Piock, et al, 2011). A recent study by Zhao et al (2018) did not show significant differences in SOA production when they tested 16 vehicles including both GDI and PFI vehicles certified to the same standard over the LA92 cycle. The authors also suggested that a dramatic shift from PFI to GDI vehicle market is unlikely to alter the SOA production. In contrast, Du et al (2018) reported significant higher SOA formation from GDI vehicles compared to PFI vehicles. Vu et al (2018), tested 4 GDI vehicles and found the SOA forming potential to be vehicle and not engine technology specific.

Vehicle exhaust is also influenced by engine fuels. Specifically, ethanol fuel is blended into gasoline to meet current U.S renewable fuel standard (RFS) mandates and has also been aggressively promoted by the Energy Independence and Security Act (EISA 2007). While most gasoline in the US contains 10% by volume of ethanol, ethanol can be also blended in higher concentrations (up to 85%) for use in flexible fuel vehicles (FFVs). Several previous studies have shown that with increasing ethanol content, reductions in the primary emissions of total hydrocarbons (THC), non-methane hydrocarbons (NMHC), and

carbon monoxide (CO) were observed (Karavalakis, et al, 2014b; Dardiotis, et al, 2015; Hubbard, et al, 2014). Studies have also reported increases in toxic emissions of formaldehyde and acetaldehyde with higher ethanol blends (Karavalakis, et al, 2014b; Chen, et al, 2007; Suarez-Bertoa, et al, 2015). Ethanol has also the potential of suppressing soot formation, with a number of studies showing lower particulate emissions with ethanol blending (Karavalakis, et al, 2014a; Maricq, et al, 2012; Khosousi, et al, 2015). Gramsch et al (2018) tested one GDI-FFV and one PFI-FFV with different ethanol blends and pure ethanol and found reduced secondary particle formation in the chamber with increased ethanol fraction in the fuel. They also showed increased time period required for secondary PM production with higher ethanol blends. Timonen et al (2017) also found lower SOA production with higher ethanol blending when they tested a GDI FFV over the NEDC using a potential aerosol mass (PAM) reactor. They also reported that the cold-start phase of the cycle dominated the SOA production. Suarez-Bertoa et al (2015) investigated the SOA formation from a Euro 5a GDI FFV over the New European Driving Cycle (NEDC) when fueled with E75 and E85 blends. They showed that secondary aerosol was highly oxidized and suggested that SOA can result from the oxidation of short-chain VOCs, such as acetaldehyde and ethanol.

The SOA formation potential from vehicle exhaust is complex, and can be affected by a host of different conditions. Previous works have altered the concentration of VOC's and NOx have been altered by adding compounds such as propene and HONO (Gordon, et al, 2014) in an attempt to create similar reaction conditions test to test. One method utilized by few researchers looking at the incremental reactivity of single compound and simple

compound mixtures includes the use of a specialized surrogate with NOx (Kacarab, 2016). The goal of a surrogate is to simulate a consistent reactivity (ie radical concentration) between tests, so the emission of interest is reacting as a result of the environment instead of setting the reactivity of the experiment. To the best of our knowledge, no researchers have studied the reactivity of vehicle exhaust with the addition of a surrogate mixture and NOx with the intent of creating consistency between tests.

This study evaluates the primary and secondary aerosol production from two current technology FFVs equipped with GDI engines when operated over the cold-start and hot-start LA92 cycles. Both vehicles are tested over four fuels with fuel varying from 10%-78% ethanol by volume and contributes to the growing body of literature that examines the use of ethanol fuels in current GDI technology. In addition to the fuel and driving condition effects, we explore the SOA forming potential of vehicle exhaust exposed to different oxidation environments. We employ a surrogate-mixture to gain better control of the gas-phase chemical environment within the chamber system, enabling one to explore SOA formation from the mixture.

The exhaust emissions from each vehicle/fuel/cycle combination were introduced into a mobile atmospheric chamber and the physicochemical properties of secondary aerosol were monitored. The influence of low, mid-, and high ethanol fueling on SOA production, were investigated and discussed. In addition, the impacts of fuel composition and the increase of gasoline aromatic hydrocarbon content on SOA formation are discussed.

3.3. Experimental:

3.3.1 Experimental Fuels:

Four fuels were used in this study with the intention of observing the effects of a wide range of ethanol blends and comparing them to a commercially available ethanol fuel (E10). Thus the baseline fuel was an E10 blend with a measured aromatic content of 28.1% by volume, which represents the US EPA Tier 3 fuel. The second fuel was an E10 fuel with 36.7% by volume of aromatics (HA E10) to observe the effects of aromatic content on the emissions. An intermediate ethanol blend was used, which was a splash blended E30 fuel (using the Tier 3 E10 fuel with an additional 20% ethanol). A high ethanol blend (E78) was also used that was blended following the US EPA Tier 3 and California Air Resources Board (CARB) certification requirements for E85 fuels. The lower ethanol content was selected in order to meet the Reid vapor pressure (RVP) requirements of fuels. A detailed table of the fuel analysis can be found in the supplemental material.

3.3.2 Test Vehicles & Driving Cycles:

This study utilized two flexible fuel gasoline direct injection vehicles (FFV-GDI) which will be referred to as FFV-1 and FFV-2 throughout this manuscript. FFV-1 was a 2016 model year passenger vehicle with a 2.0L 4-cylinder spark ignition wall guided, direct injection engine. The engine was rated for a 12.0:1 compression ratio, at 160 hp at 6500 rom with a torque of 198 Nm at 4450 rpm. The vehicle was certified under the Federal Tier 2 Bin 5 standards. FFV-2 was equipped with a 2.4L 4-cylinder spark ignition wall guided, direct injection engine. FFV-2 was rated with a compression ratio of 11.2:1 and a

horsepower of 182 hp at 6700 rpm with a torque of 172 ft-lbs at 4900 rpm. The vehicle was certified to the Federal Tier 2 standards. Both test vehicles were equipped with three-way catalysts (TWCs).

Both vehicles were tested over cold-start and hot-start LA92 test cycles in triplicate. The LA92 or Unified Cycle (UC) is a driving schedule designed by the California Air Resources Board (CARB) with the aim to mimic the more aggressive driving observed on California roadways. Similar to the typical Federal Test Procedure (FTP) cycle, the LA92 consists of three phases, and a similar three-bag structure. The defining differences of the LA92 compared to the FTP cycle, is the higher speeds, faster accelerations, fewer stops per mile, and less idle time.

The six tests on a particular fuel were conducted sequentially, and only changed once all testing on a given fuel was completed. The vehicles were prepared according to the preconditioning procedure similar to that specified in the Code of Federal Regulations (40 CFR 86.132-00). For each fuel change there were multiple drain and fills and 2 LA-4s along with idle periods between the testing on each fuel to condition the vehicle and minimize any potential carryover effects. The order of fuels tested for both vehicles were randomized.

3.3.3 Emissions Testing

All vehicle tests were conducted in CE-CERT's Vehicle Emissions Research Laboratory (VERL), on a Burke E. Porter 48-inch single-roll electric dynamometer. The exhaust was collected into a Pierburg Positive Displacement Pump-Constant Volume

Sampling (PDP-CVS) where gas phase bag measurements were analyzed with a Pierburg AMA-4000 bench. PM mass, volatile and solid particle number, particle size distributions, and black carbon emissions were also measured via the CVS. For selected gas phase speciation, a 2,4-dinitrophenylhydrazine (DNPH) coated silica cartridge (Waters Corp., Milford, MA), and a specially-prepared 6.0 L SUMMA passivated canister, were connected to the CVS system. A more detailed analysis of the primary measurements can be found in Yang et al 2018.

In line with the primary emissions measurements, diluted exhaust from the CVS was introduced to UCR's Mobile Atmospheric Chamber (MACh) over the duration of the driving cycles (excluding the hot soak). The exhaust was injected into the chamber utilizing two ejector dilutors (Air-Vac TD11OH) in parallel, connected to a home built clean air system with filters and desiccants to remove the PM, water, NOx, CO, and hydrocarbons from the dilution air. More detail on the injection setup can be found in Roth et al (2018).

3.3.4 Irradiation Experiments

Prior to each chamber experiment, MACh was cleaned and prepared for testing. More information on the preparation of the chamber, and the injection of the exhaust can be found in Roth et al (2018). After the exhaust was injected into the chamber, the remaining volume of the chamber was filled with AADCO purified air, and the primary exhaust was analyzed for at least 30 min so the tailpipe exhaust could be characterized. During this time, 1.0 ppm of H_2O_2 was injected which acted as the initial hydroxyl radical source. The 600

15 W, 18", T8 black light fluorescent bulbs were then turned on, and the exhaust was allowed to react for at least 400 min, or until the particle formation, or ozone formation subsided.

Particle and gas-phase concentrations (O_3, NOx, NH_3) were measured as with previous MACh experiments (Roth et al 2018). The total aerosol volume was monitored throughout the chamber experiment utilizing a scanning mobility particle sizer (SMPS) consisting of a TSI 3080 electrostatic classifier, TSI 3081 long column differential mobility analyzer (DMA) column and a TSI ultrafine condensation particle counter (CPC) 3776. The change in effective density throughout the chamber experiments were monitored with a Kanomax aerosol particle mass analyzer system (APM), which when coupled with the volume found with the SMPS, resulted in a calculated mass.

The mass of black carbon was measured using an AVL micro soot sensor (MSS) with a high power laser diode operating at 802 nm with a photoacoustic sensor (Petzold, A., Niessner, R, 1996). All remaining non-refractory aerosol chemical composition data was measured with an Aerodyne high-resolution, time-of-flight, aerosol mass spectrometer (HR-ToF-AMS) (Aiken, et al, 2008).

3.3.5 Surrogate Experiments

In addition to one exhaust only experiment, an anthropogenic surrogate was injected into the chamber for the final two tests of FFV-2 on each fuel and driving cycle configuration. The surrogate was developed to simulate the reactivity of a primarily anthropogenic region with the ability to consistently inject into chamber experiments. The

surrogate was developed utilizing VOC concentrations measured by Hoyle et al (2011) and lumped into categories based on reactivity (SAPRAC model). After the VOCs were weighted by reactivity and abundance in the atmosphere, one to two representative compounds were chosen to constitute the bulk percentage of that category. Light hydrocarbons were chosen for the surrogate mixture to minimize secondary organic aerosol formation (<1 μg m^{-3}). Classification experiments were conducted with only the surrogate to measure a baseline for particle and ozone formation. A more detailed description of the surrogate mixture can be found in the dissertation of Kacarab (2016).

With the added surrogate, the incremental aerosol formation from the vehicle exhaust could be observed and compared between fuels. The goal of the surrogate mixture was to control the gas-phase chemical environment within the chamber system, enabling the exploration of SOA formation from the mixture. More details of the composition of the anthropogenic surrogate can be found in the supplemental section.

In the surrogate experiments, a total of 1.0 ppmC of the anthropogenic surrogate was injected into the chamber along with an additional ~45 ppb NOx after the vehicle exhaust had been injected. The goal of the NOx addition was to increase the concentration to similar VOC:NOx ratios to the FFV-1 experiments. The mixture of the vehicle exhaust, and the anthropogenic surrogate was irradiated and characterized with the same procedure as the exhaust only experiments. The final SOA formation measured in the chamber experiments was corrected utilizing the average SOA mass formation in surrogate only experiments. All reported data utilizing the anthropogenic surrogate displays the additional secondary aerosol only.

3.4. Results & Discussion:

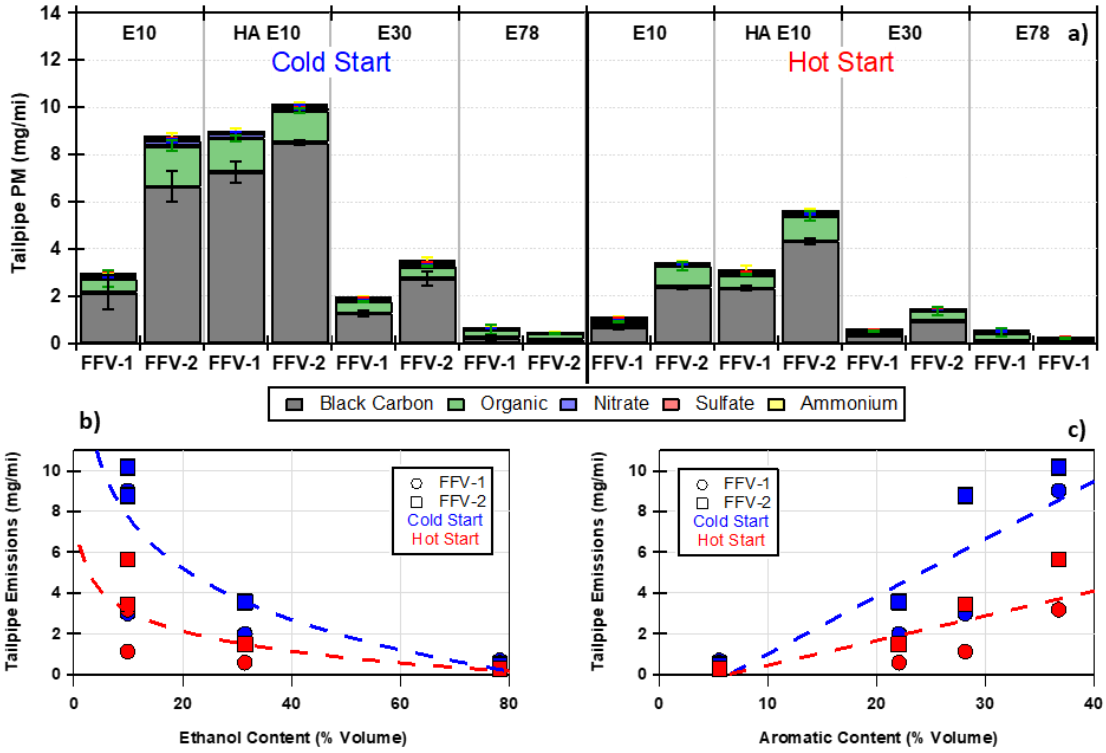

Figure 3-1: a) Composition and mass of the tailpipe PM for FFV-1 and FFV-2, over cold-start (left) and hot-start (right) LA92 cycles for the four fuels (E10, HA E10, E30, and E78), and the b) Ethanol content (% volume) and c) Aromatic content (% volume), vs the total tailpipe emissions for FFV-1 and FFV-2 over the hot-start and cold-start LA92 driving cycles

Figure 3-1 a shows the mass and composition of the tailpipe PM emitted for FFV-1 and FFV-2 over the cold-start and hot-start LA92 cycles on the four different test fuels. Tailpipe mass was inversely related to ethanol and aromatic content and had a similar trend for both vehicles. As the ethanol content in the fuel increased there was a substantial decrease in the mass of aerosol emitted (Figure 3-1 b,c). When compared to the E10 fuel,

the E78 fuel displayed an average reduction of 64% and 94% in tailpipe PM mass for FFV-1 and FFV-2, respectively. This result is consistent with previous work who observed tailpipe PM was reduced with increased ethanol fuel blends (Price, et al, 2007). Inversely, when comparing the E10 to the high aromatic E10 fuel, there was a 2.9 and 1.4 times more tailpipe PM mass for FFV-1 and FFV-2, respectively, consistent to past fuel studies (Karavalakis, et al, 2015a).

Tailpipe aerosol was also significantly influenced by the driving conditions. Hot-start LA92 experiments produced on average 53% less tailpipe PM mass than cold-start LA92 experiments for both vehicles. The fuel effect trends on tailpipe mass emitted remained consistent and the reduction due to driving conditions were similar for each fuel (Figure 3-1 b,c). The largest reduction in particle composition was black carbon. Black carbon concentrations decreased by 60% from cold-start to hot-start LA92 tests (average reduction of 43% of POA), resulting in a difference in fractional composition for the two driving conditions. On average, the hot-start LA92 tests had 7% less black carbon in the total PM composition; confirming that the cold-start is a key contributor to the total black carbon mass emitted (Figure 3-2). Cold-starts favor the formation of PM and black carbon emissions because the engine is cold and the combustion temperature and pressure are lower than those with a warmed up engine. This will result in less fuel vaporization and less time for fuel to mix with air, leading to fuel wetting in the cold cylinder surfaces and localized fuel-rich regions (Piock, et al, 2011; Stevens, et al, 2001).

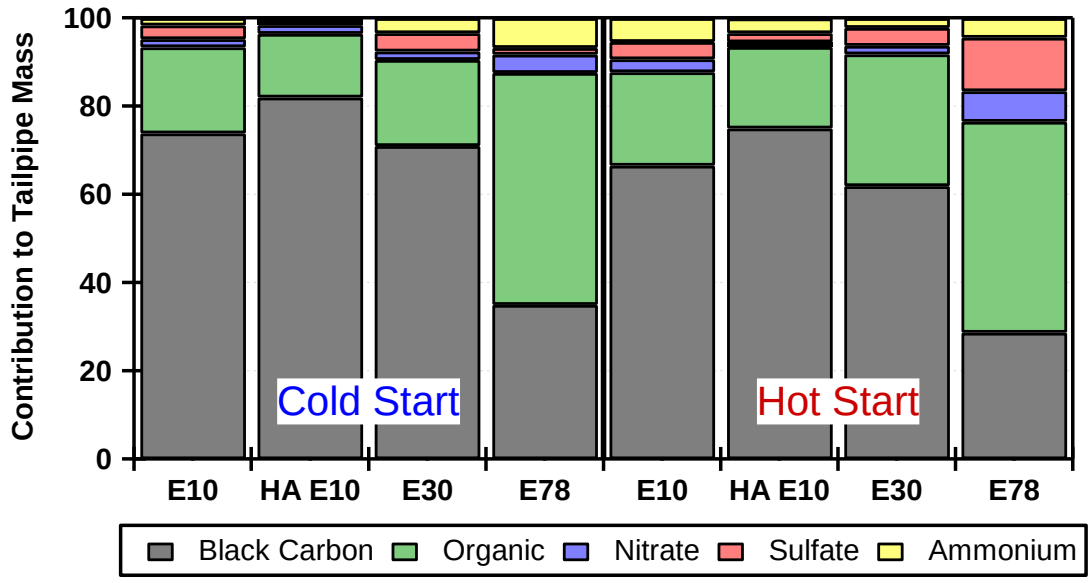

Figure 3-2: Average fractional composition (for both FFV-1 and FFV-2) for the four fuels over hot-start and cold-start LA92 driving cycles

Another common trend between the two vehicles was the variation of fractional composition of the tailpipe aerosol in regards to fuel composition. Figure 3-2 shows the fractional composition of the tailpipe aerosol for the cold-start and hot-start LA92 cycles averaged for both FFV-1 and FFV-2. The fractional contribution of black carbon to the total emitted mass was reliant once again on the ethanol content of the fuels. The high aromatic E10 fuel emitted 78% black carbon when compared to E78, where only 32% of the tailpipe PM was composed of black carbon. There was also an increase in the total fractional composition of black carbon during the cold-start LA92 compared to the hot-start LA92 between fuels (average of 7.4% increase cold vs hot). The trend in respect to fuel composition and black carbon content remained constant in both driving conditions. The majority of the remainder of the tailpipe aerosol was POA. It is therefore reasonable

to state that higher ethanol blends not only will greatly reduce tailpipe PM from GDI vehicles, but will also decrease the contribution of black carbon to total aerosol. This increase in POA/BC ratio in the tailpipe aerosol as the ethanol content increased, was also observed in Timonen et al 2017.

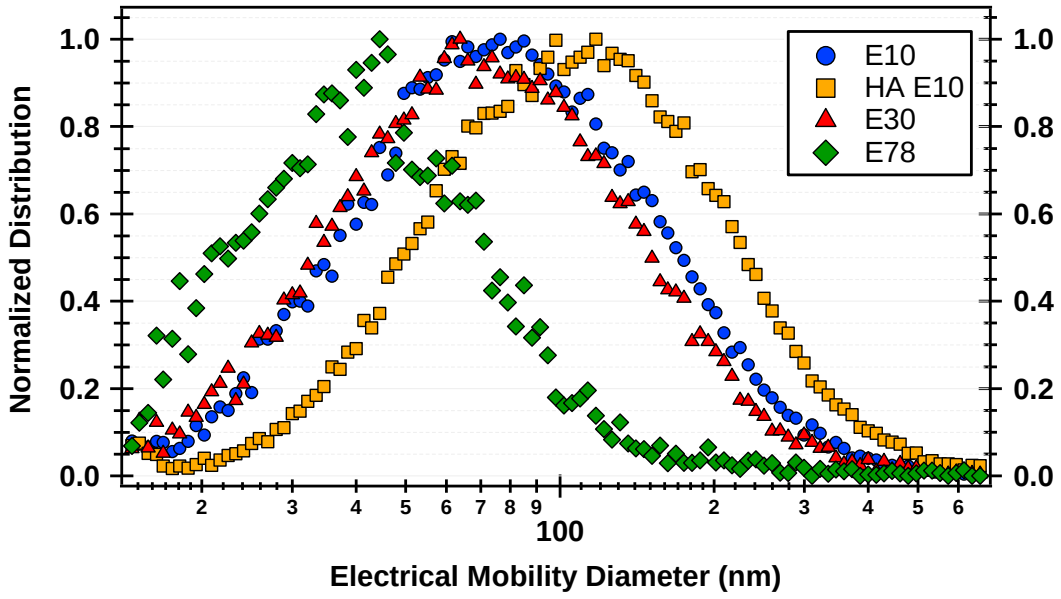

Figure 3-3: Initial size distribution for FFV-1 cold-start tests after dilution

As a result of the altered composition of the aerosol, the initial diluted size distributions also varied due to the ethanol/aromatic content of the fuels and the driving conditions. As shown in Figure 3-3, it was found that as the ethanol content of the fuel was increased, the average peak diameter of the diluted exhaust decreased. This result was consistent across all similar vehicle and driving cycle configurations (Figure 3-18). Similarly, when the cold-start tests were compared to the hot-start tests, there was a shift

of the aerosol to a smaller diameter size by on average of 15 nm for both vehicles and all fuels (Figure 3-19).

In addition, the average initial density was also dependent on the ethanol content of the fuel. On average, the initial densities were 0.487 g cm^{-3}, 0.516 g cm^{-3} and 0.552 g cm^{-3} for the E10, E30, and E78 respectively (for both FFV-1 and FFV-2). There was no statistical difference in density however between driving conditions. The change in density is most likely due to the differences in the composition of the tailpipe aerosol (Roth et al 2019). The fuels which contain the high black carbon content (two E10 fuels) have a more fractal thus less dense morphology. Contrarily, the higher ethanol fuel blends contain a larger fraction of POA which increases the density of the diluted aerosol.

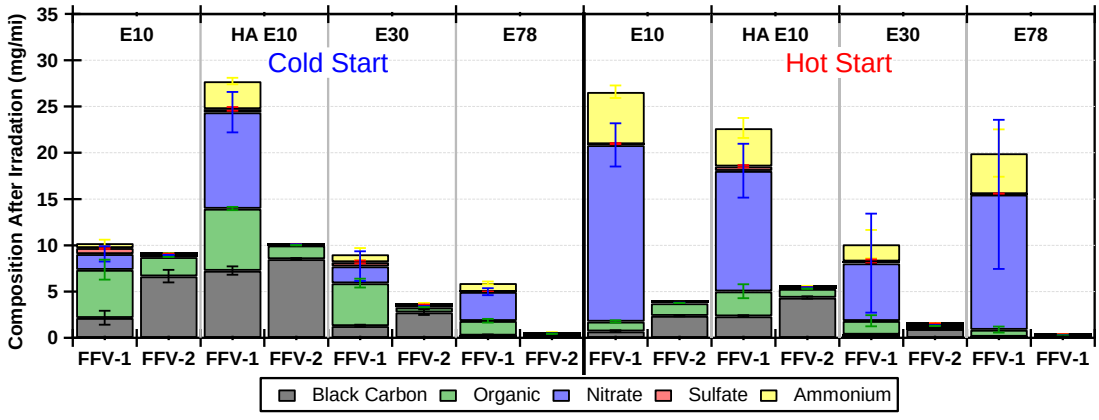

Figure 3-4: Aerosol composition after irradiation of exhaust only experiments (for both FFV-1 and FFV-2) over the cold-start and hot-start LA92 driving cycles

As shown in Figure 3-4, FFV-1 exhibited a dramatic increase in the total aerosol. For these experiments, only the vehicle exhaust was introduced to the chamber. For FFV-2, there was no appreciable secondary aerosol formation when only the exhaust was

introduced to the chamber. During the cold-start LA92 for FFV-1, the HA E10 fuel formed the largest secondary aerosol mass, which primarily consisted of ammonium nitrate. For both E10 fuels and the E30, the organic aerosol mass was very similar, whereas E78 showed the lowest formation of organic aerosol. During the hot-start LA92, all fuels produced higher mass of secondary aerosol compared to the cold-start LA92, with the exception of HA E10. The main contributor to secondary aerosol for the hot-start LA92 was the excess formation of ammonium nitrate. It should be noted that organic aerosol mass for the hot-start LA92 was considerably lower for all test fuels compared to the cold-start LA92.

The results reported here suggest that during warmed up engine operation with a fully operated TWC, more nitrogenous species are emitted or formed inside the catalyst system. It was theorized that more ammonia (NH_3) emissions were formed during hot-start driving conditions and when the TWC light-off temperature was reached. Ammonia is a secondary pollutant of the TWC rather than combustion product and is generated from NO and H_2 during the water gas shift reaction of CO (Suarez-Bertoa, et al, 2014). Ammonia formation in the TWC is enhanced at rich conditions where more CO can produce more H_2 (Calirotte, et al, 2013). During the hot-start LA92, more CO emissions were seen than the cold-start LA92. Our results showed that ammonia as a reactive nitrogen compound can be protonated in the presence of acids (ie nitric acid) inside the chamber forming ammonium nitrate.

As discussed earlier, there was no appreciable aerosol formation for FFV-2 despite the fact that both vehicles had comparable tailpipe PM emissions (1.3 times more PM for

FFV-2 compared to FFV-1). On average, FFV-1 emitted 2.5 times higher total hydrocarbon (THC) and about 12 times higher NOx emissions relative to FFV-2. Although both vehicles were certified under the same emissions standards, FFV-1 produced higher gaseous emissions than FFV-2 and thus higher secondary aerosol. For all the chamber experiments conducted with the FFV-2 exhaust emissions, there was ozone formation in the chamber indicative of photochemistry. However, the gases did not reach a low enough volatility to condense and form secondary aerosol. Additionally, the lower NOx emissions from FFV-2 resulted in no secondary inorganic aerosol formation (i.e., ammonium nitrate) despite the presence of gaseous ammonia in the chamber experiments.

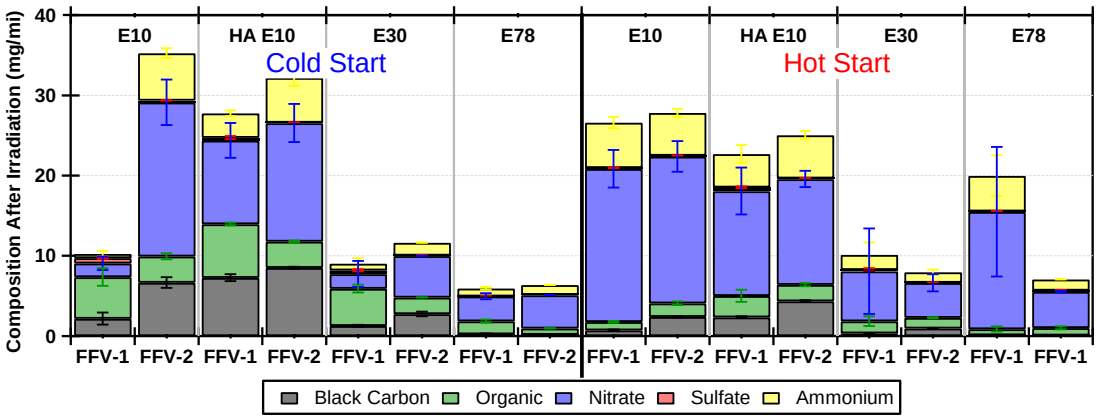

Figure 3-5: Aerosol composition after irradiation of exhaust experiments (FFV-1) and the surrogate with exhaust experiments (FFV-2) over the cold-start and hot-start LA92 driving cycles

Figure 3-5 shows the composition of the secondary aerosol for both vehicles, however, for FFV-2 irradiation experiments, the surrogate and NOx mixture were added to the vehicle exhaust. The addition of the surrogate and NOx mixture resulted in

significant increases of secondary aerosol mass production for FFV-2, which were similar to FFV-1 over the hot-start LA92 but higher over the cold-start LA92. In contrast to the results obtained for FFV-1, FFV-2 showed reduced secondary aerosol mass formation during the hot-start LA92 when compared to the cold–start LA92. This result indicates a reduction in the total nitrogenous species emitted from this vehicle when the engine was warm.

For the FFV-2 experiments with the surrogate mixture, there was also an increase in the organic aerosol formation indicating an increased reactivity in the experiments with the surrogate. This was likely due to two main reasons; first, the injected hydrocarbons in the surrogate mixture maintained an increased radical concentration throughout the duration of the irradiation experiments, and secondly the increased NOx facilitated more photochemical reactions. With the introduction of the NOx and surrogate mixture, there was enough NOx present in the chamber for the oxidation of the VOCs, as well as excess NOx available to form inorganic salts (i.e., ammonium nitrate). For both experimental conditions for FFV-2 (without and with the surrogate mixture), there was a similar amount of emitted ammonia at the tailpipe, however, the excess NOx was the primary pathway for the production of ammonium nitrate in the chamber. Our results for this particular vehicle showed that NOx was the limiting reagent in the inorganic salt formation.

The fuel effects were particularly noticeable in the formation of total secondary aerosol mass from both GDI vehicles. An increase in ethanol content in gasoline resulted in reductions of the total aerosol mass, with E78 showing the lowest total aerosol mass formation. There were considerable reductions in secondary aerosol mass for the E30

(49%, and 70%) and the E78 (34% and 78%), compared to E10 for FFV-1 and FFV-2 respectively (average of both hot-start and cold-start LA92 cycles). Our results displaying reduced formation of total secondary aerosol with higher ethanol blends are in line with previous studies reporting limited formation of secondary aerosol for E85 and E100 fuels using a PAM chamber (Timonen et al 2017).

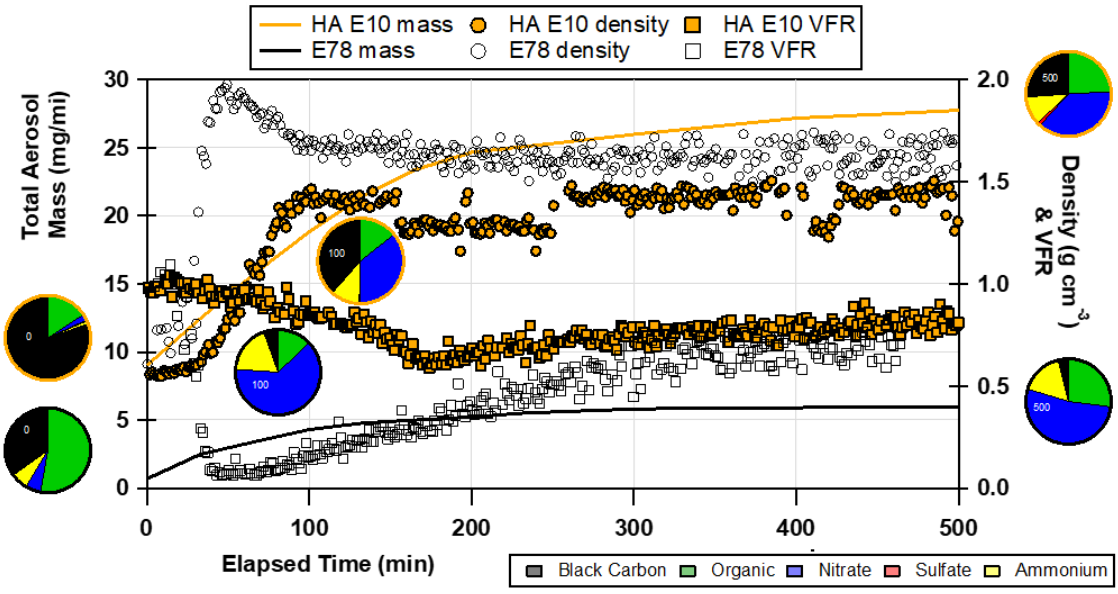

Figure 3-6: Mass evolution (left axis) for FFV-1 operated on the high aromatic E10 (orange) and the E78 (black) fuels. Pie charts signify the composition of the aerosol at the given time. Density (circles) and volume fraction remaining (squares) are represented for both testing configurations on the right axis.

The high aromatic E10 fuel did not show consistent trends in total aerosol formation when compared to E10. For FFV-1 there was a 1.8 times increase in total aerosol formation when compared to the E10 fuel, versus a 9% reduction for FFV-2.

Figure 3-6 shows the evolution of the aerosol for the high aromatic E10 (orange) and the E78 (black) fuels for FFV-1. Also included in Figure 3-6 is the evolution of the density (circles), and also the evolution of the volume fraction remaining (squares) of the aerosol when exposed to a heated column (100 °C) for the two fuels.

In addition to the large difference in the total mass that formed, Figure 3-6 also displays variation in the properties of the aerosol between the two experimental conditions and throughout the irradiation experiments. The tailpipe aerosol for both fuels were fractal with a density of ~0.5 g cm^{-3} and had a VFR of 1.0 which are properties of fractal, non-volatile black carbon particles.

After 100 min of irradiation, the two fuels not only varied in the mass, but also the chemical makeup of the aerosol. The E78 fuel initially forms a majority of its mass in the form of ammonium nitrate while the E10 formed a more even mix of organic, ammonium nitrate, and black carbon. These differences were noted in the density (1.5 g cm^{-3} for HA E10 and 1.8 g cm^{-3} for the E78) and the VFR (0.9 for HA E10 and 0.1 for E78). The increased density and the decreased VFR confirm for the E78 the composition data from the AMS (ammonium nitrate has a density 1.77 g cm^{-3} and is completely volatile at 100 °C). For the HA E10 experiments, the density and VFR are indicative of a mix of black carbon, SOA (1.4 g cm^{-3}) and ammonium nitrate (1.77 g cm^{-3}) which can once again be confirmed by the measurements from the AMS.

As the aerosol continued to age, the density decreased for both (1.48 and 1.55 g cm^{-3} for the HA E10 and the E78 respectively) indicating the organic fraction was increasing.

The VFR also increased for both (0.75, and 0.68 for the HA E10 and the E78 respectively) indicating the gases condensing near the end of the experiment were lower volatility organic gases.

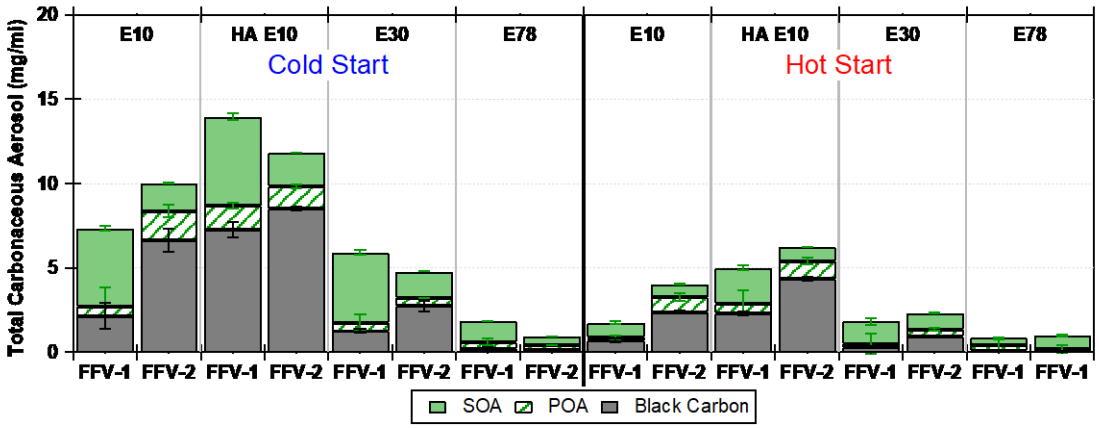

Figure 3-7: Composition of the carbonaceous mass after the exhaust only irradiation experiments (FFV-1) and the surrogate and exhaust experiments (FFV-2) for the cold-start and hot-start LA92 driving cycles on the four fuels.

Figure 3-7 shows the total carbonaceous aerosol for both vehicles and all fuels over the LA92 cycles. Overall, hot-start operation led to lower formation rates of total carbonaceous aerosol and SOA. This was due to the lower formation of VOC precursors and NMHC emissions during warmed up operation, as these compounds were more efficiently oxidized in the TWC (Yao, et al, 2017). It is expected that GDI combustion during cold-start conditions will generate larger quantities of unburned hydrocarbon species because of fuel films formation on the piston crown and cylinder walls. In fact, both vehicles showed reduced NMHC emissions by 48% over the hot-start LA92 relative to the cold-start LA92, resulting in about 43% reduction in SOA formation. For the cold-

start LA92, FFV-1 formed higher mass of total carbonaceous aerosol and more SOA production compared to FFV-2. For the hot-start LA92, total carbonaceous aerosol was higher with FFV-2 compared to FFV-1, but SOA production was still higher for FFV-1. The only exception during the hot-start LA92 was seen for E78, where more SOA mass was produced for FFV-2. The reduced formation of SOA with FFV-2 was due to the decreased tailpipe NMHC emissions for this vehicle, with FFV-1 emitting more than 2.0 times higher NMHC emissions than FFV-2.

Production of SOA mass from both vehicles, expressed in mg/kg-fuel, ranged from 5 mg/kg-fuel to 55 mg/kg-fuel. Our results are comparable to previous studies evaluating SOA production from gasoline vehicles over different driving cycles, where measured SOA ranged from 15 mg/kg-fuel to 60 mg/kg-fuel (Gordon et al 2014, Liu et al 2015, and Nordin et al 2013). Different investigations with gasoline vehicles, however, have found about an order of magnitude higher SOA production than the values reported in this work (Du et al 2017, Platt et al 2013, and Tkacik et al 2014).

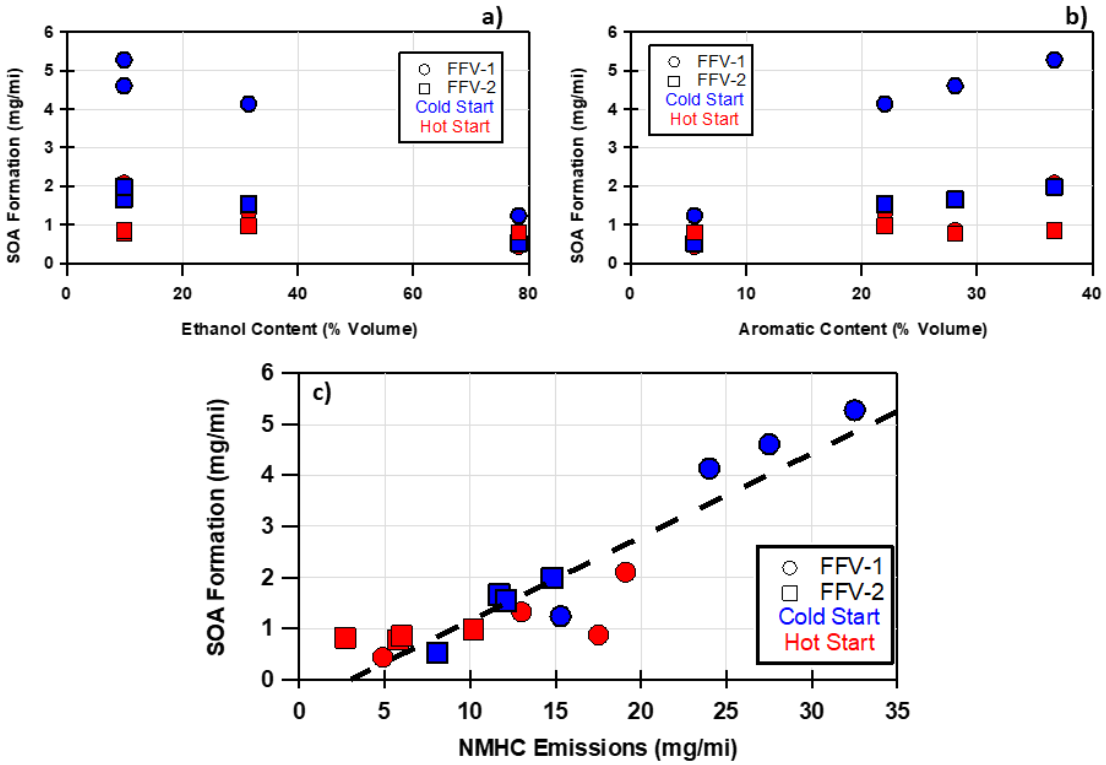

Figure 3-8: SOA formation vs a) Ethanol content (% volume) b) Aromatic content (% volume), c) NMHC emissions for both FFV-1 (exhaust only), FFV-2 (surrogate and exhaust) on the four fuels

Formation of SOA showed inverse relationships with ethanol and aromatic contents in gasoline, as shown in Figure 3-8. The SOA formation decreased as the ethanol content increased, primarily due the reductions of SOA precursors with higher ethanol fueling such as NMHC and VOC emissions. These reductions were likely a result of the higher oxygen content in the fuel, which increased the local oxygen content in the fuel rich regions leading to more complete combustion (Liu, et al, 2011; Catapano, et al, 2014). The results reported here showed a strong correlation between SOA formation and NMHC emissions. These

trends are in agreement with a recent study conducted by the same group of authors (Roth, et al, 2019). The trend related to NMHC emissions and SOA formation was not influenced by the driving conditions (cold-start versus hot-start LA92s) or fuel composition, but rather on the mass of gases emitted at the tailpipe. The reduction in the NMHC emissions along with the subsequent reduction in the secondary aerosol with increasing ethanol content was also measured by Gramsch et al (2018) when they tested GDI FFVs.

The lower SOA for the higher ethanol blends, with the high aromatic HA E10 fuel showing the higher SOA formation, was also a consequence of the lower aromatic content in these fuels. Aromatic hydrocarbons are precursors for SOA production (Odum, et al, 1997). Previous studies have shown that higher aromatic content gasoline fuels produce more tailpipe NMHC and aromatic VOCs emissions (Karavalakis, et al., 2015b). Other studies have shown that higher aromatic levels increase SOA production (Odum, et al, 1997). Under the present test conditions, the dilution of aromatics in the E30 and E78 fuel streams effectively lowered the formation rates of soot and VOC precursors and subsequently SOA production.

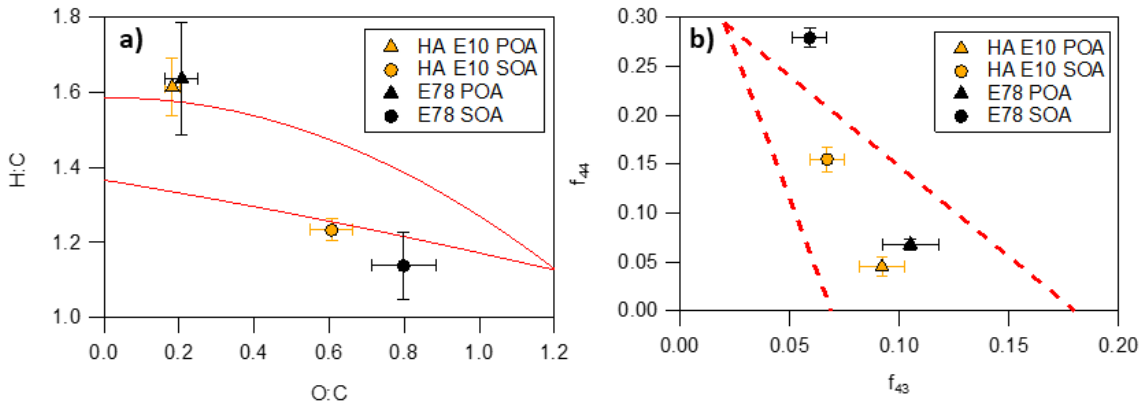

Figure 3-9: High resolution AMS results for; a) H:C & O:C ratios and b) f_{44} and f_{43} relationships for the POA (triangles) and SOA (circles) for FFV-1 operated on the high aromatic E10 (orange) and E78 (black) fuels

Another distinction in the organic mass that formed was the differences in the oxidation state of the organic aerosol. Two important measures of this are fraction of the mass to charge ratio, total normalized ion fragments of *m/z* 44 (CO_2^+) versus *m/z* 43 ($C_2H_3O^+$), and the molar oxygen to carbon ratio (molar), as shown in Figure 3-9 (a-b) (Aiken, et al, 2008). Average oxygenated organic aerosol (OOA) typically has an O:C ratio of 0.5 to 0.9; with semi-volatile OOA (SV-OOA) classified with an O:C of 0.4 to 0.6, and low-volatility OOA (LV-OOA) from 0.7 to 1.0 (Jimenez et al, 2009). Shown in Figure 3-9 are only the HA E10 fuel and the E78 fuel for FFV-1 to explore the differences between the most different fuels. The POA emitted from both testing configurations were very similarly with an O:C of ~0.13. As the emissions aged, it was found that the SOA formed in the E78 experiment were more oxygenated with an O:C of 0.80 placing the aerosol in

the LV-OOA region. The HA E10 on the other hand formed SOA with an average O:C ratio of ~0.61 which is placed at the higher end of the SV-OOA region.

Another method used to measure the amount of oxidation in the aerosol is the f_{44} (ratio of *m/z* 44 to total signal in the component mass spectrum) and f_{43} (defined similarly to f_{44}). SV-OOA typically has an f_{44} from 0.03 to 0.12, while the LV-OOA is typically in the 0.13-0.21 range (Liu, et al, 2015). It has also been found that the majority of the atmospheric aerosols fall within the triangle developed by Ng et al (2010) depicted in Figure 3-9b. Once again the POA for both testing configurations were similar, with an f_{44} of 0.05 however, once again it was observed that the E78 produced SOA with a higher oxidation state at 0.28 compared to the 0.15 formed in the HA E10 experiments. In both experiments, the SOA that formed was highly oxidized, however in the E78 experiments, this f_{44} fraction was much higher. The difference in the SOA mass and composition indicate that the fuel composition plays a major role in the oxidation state of the organic aerosol that forms.

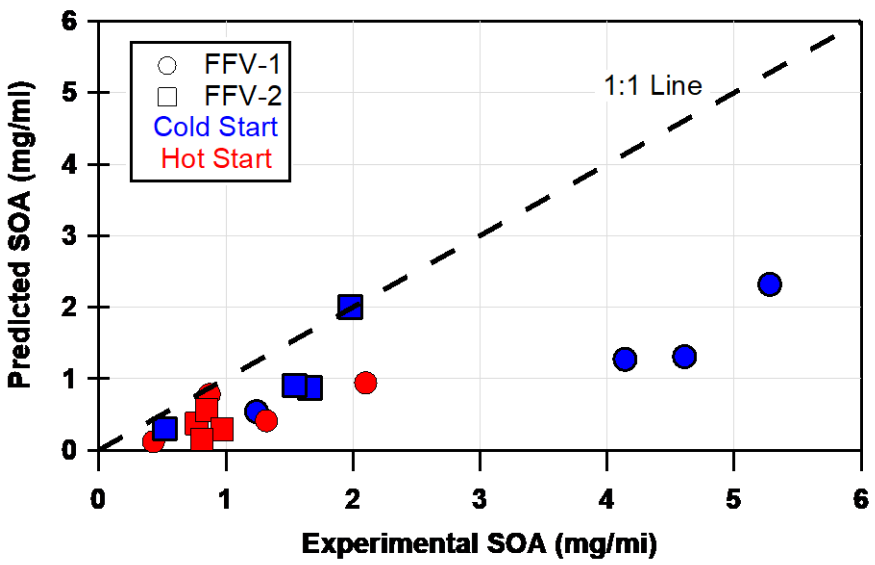

Figure 3-10: Predicted SOA from the speciated gas emissions utilizing yield percentages reported by Derwent et al (2010). Black line represents the 1:1 line.

$$\Delta SOA_{pred} = \sum_{i} (\Delta HC_i * Y_i)$$

Equation 3-1: Equation for predicted yield of SOA from the measured VOCs

Figure 3-10 shows the predicted SOA formation versus the measured SOA formation during the chamber experiments (black line is a 1:1 trend). The SOA values listed for FFV-1 are exhaust only experiments, while the FFV-2 values are for the exhaust and surrogate mixture experiments. The calculation for the predicted SOA values is shown in Equation 3-1. The emission factor of the speciated gases (ΔHC_i) multiplied by the measured yield (Y_i) of the various gas phase compounds in a low NOx regime (Derwent, et al, 2010). The values calculated for each species was then summed resulting in a predicted change in SOA mass throughout the irradiation experiment. The gases were

assumed to react completely over the 8 hour irradiation experiments and low NOx values were used to estimate a maximum yield from the exhaust of the given gases emitted.

The cold-start, HA E10 fuel for FFV-2, appeared to be an outlier where the predicted organic aerosol formation accounted for 100% of the SOA production. With the measurements collected in this work, 43%, and 54% of the formed SOA was predicted for FFV-1 and FFV-2 respectively. For both vehicles, the predicted SOA formation was dominated by aromatic hydrocarbons contribution (>97%), with the BTEX (benzene, toluene, ethylbenzene, and xylenes) compounds contributing the majority of the formation. As a result of this contribution, the highest closure accomplished was for the HA E10 (average of 64% of organic aerosol accounted for) and the least for the higher ethanol fuel blends (E30 and E78 emissions accounted for 37% of organic aerosol). The predicted contribution to the measured SOA mass found in this work was larger than the values found in previous gasoline vehicle aging studies conducted by Platt et al. (2013) and Gordon et al. (2014) who suggested about 20% and 25% of organic aerosol, respectively, may be explained by aromatic oxidation. It should be noted that both of these studies only accounted for SOA formation the aromatic compounds of toluene, benzene, xylenes and naphthalene. Our results more closely agree with the predicted SOA values reported by Nordin et al (2013) and Du et al (2015), who showed around 60% and 43%, respectively, of SOA from aromatic emissions. Overall, predicted SOA formation from the tailpipe VOCs from both vehicles showed an average of 17% reduction when ethanol increased from 10% to 30%. Predicted SOA formation was also 66% lower for E78 compared to E10.

3.5. Conclusion:

The experiments done in this work explored how high ethanol fuel blends could affect the particle and gaseous emissions of two flexible fuel gasoline direct injection vehicles. Similarly, the effect of the driving cycle, and preconditioning of the vehicle was also explored. The tailpipe exhaust was tested to certification standards, while also being collected into an atmospheric chamber for secondary aerosol testing.

The largest tailpipe aerosol mass measured for both vehicles was the high aromatic E10 fuel in the cold-start tests. As the ethanol content was increased, it was found that there was an average reduction of 64% and 94% for FFV-1 and FFV-2 respectively. Inversely, when the HA E10 was compared to the commercial E10 fuel, there was a 2.9 and 1.4 times increase in the tailpipe aerosol for FFV-1 and FFV-2 respectively. In addition to the tailpipe mass, the composition of the aerosol also varied greatly, which in turn affected both the size distribution and the morphology of the aerosol as well. On average, the E78 was only composed of 32% black carbon compared to the 78% black carbon of the HA E10 (averaged for both vehicles). With this reduction in black carbon there was a decrease in the peak diameter as the fuels ethanol content increased.

In addition to the fuel effects, there were obvious differences related to the different driving conditions. The hot-start tests emitted on average 53% less aerosol mass with the largest reduction measured being black carbon, with an average reduction of 60%. Similar to the fuel effects, the reduction in black carbon coincided with a decrease in the peak diameter by an average of 15 nm for all testing configurations.

When comparing the aged emissions, there were variable results. FFV-1 displayed a 3-35 times increase of secondary aerosol to the tailpipe aerosol. This large increase was vastly different from the FFV-2 experiments where no detectable secondary aerosol formed in the exhaust only experiments. The large difference was most likely due to the large discrepancy in hydrocarbon emissions (2.5 times higher in FFV-1), and the NOx emissions (11.7 times higher in FFV-1). Even though the particulate emissions of the vehicles were very similar, the large variations in the gaseous emissions resulted in drastic differences in the secondary aerosol formation.

When the exhaust only experiments were then compared to the exhaust and surrogate experiments for FFV-2, there were very similar results between the two in terms of fuel effects. As the ethanol content increased, the secondary aerosol concentration consistently decreased (with the exception of FFV-1 E78 hot-start experiments). Less drastic than the tailpipe exhaust there was a decrease in the secondary aerosol formation in the higher ethanol fuel blends compared to the lower ethanol fuel blends.

The differences in secondary aerosol formation in the hot-start vs cold-starts varied between vehicles. FFV-1 formed more aerosol in the hot-start tests compared to the cold-start tests for all fuels excluding the HA E10, with the majority of the aerosol being inorganic ammonium nitrate. From this and the measured concentration of both NOx and ammonia it can be concluded that when the engine is hot, the vehicle is producing more nitrogenous species resulting in larger inorganic aerosol formation. Inversely, for FFV-2, the hot-start tests formed less secondary aerosol. As a result of the reduction in aerosol

formation it can be concluded that warm engine and catalyst were actually more effective in the removal of the nitrogenous species.

When focusing on the organic aerosol formation in the chamber experiments, it was found that the organic aerosol formation most closely correlated to the NMHC emissions measured from the tailpipe. In regards to the fuel composition of the experiments, as the ethanol content of the fuel increased, there was a drastic decrease in the NMHC emitted, which resulted in a smaller SOA formation potential from the vehicle exhaust. This was a trend that was consistent between the two vehicles.

The concentrations of specific VOCs were also measured utilizing a summa canister utilizing a GC-FID for detection where a more accurate picture of the VOC composition could be assessed. Also, with this information, a predicted SOA mass was calculated utilizing the low NOx yield values provided by Derwent et al (2010). In this work the predicted aerosol was measured to 43% and 54% of the experimental SOA formed for FFV-1 (exhaust only) and FFV-2 (exhaust and surrogate) which was similar to the measured amount by Nordin et al (2013) and Du et al (2017), however was almost double the closure compared to Platt et al 2013, and Gordon et al 2014. In this work, we were able to more accurately speciate a larger number of gases which may have led to the closer prediction. Even with the increased closure, a majority of the SOA was still unaccounted for so more work will be needed in the future to fully speciate some of the less volatile IVOCs, and SVOCs to more accurately predict SOA potential of vehicle exhaust.

Ultimately, the trends in in this work utilizing an atmospheric chamber were consistent with Timonen et al (2017), where with the increasing ethanol content, there was decreasing secondary aerosol formation. From this work we are able to conclude that the increase in the ethanol content of fuel is effective in the reduction of both tailpipe and secondary aerosol. Alternatively, this work was not able to distinguish whether the decreased in the secondary aerosol, or more specifically SOA was due to the increasing ethanol or decreasing aromatic content, so more work will be needed in the future with more similar fuels to see whether ethanol or aromatic content are most influential in affecting the secondary aerosol potential of vehicle exhaust.

Funding Sources:

We acknowledge funding from the South Coast Air Quality Management District (SCAQMD) under contract 15625 and the ICM Inc. We would also like to acknowledge the funding from NCST Graduate Fellowship

Notes:

The authors declare no competing financial interest.

Acknowledgements:

The authors thank Mr. Mark Villela and Mr. Daniel Gomez of the University of California, Riverside for their contribution in contacting this research program. We also thank MECA for providing the catalyzed GPF for this program and also for their technical support and guidance.

3.6. References:

1) Timonen, Hilkka, Panu Karjalainen, Erkka Saukko, Sanna Saarikoski, Päivi Aakko-Saksa, Pauli Simonen, Timo Murtonen, et al. **2017**. "Influence of Fuel Ethanol Content on Primary Emissions and Secondary Aerosol Formation Potential for a Modern Flex-Fuel Gasoline Vehicle." *Atmospheric Chemistry and Physics* 17 (8): 5311–29.
2) Gordon, T. D., A. A. Presto, A. A. May, N. T. Nguyen, E. M. Lipsky, N. M. Donahue, A. Gutierrez, et al. **2014**. "Secondary Organic Aerosol Formation Exceeds Primary Particulate Matter Emissions for Light-Duty Gasoline Vehicles." *Atmospheric Chemistry and Physics* 14 (9): 4661–78.
3) Nordin, E. Z.; Eriksson, A. C.; Roldin, P.; Nilsson, P. T.; Carlsson, J. E.; Kajos, M. K.; Hellén, H.; Wittbom, C.; Rissler, J.; Löndahl, J.; Swietlicki, E.; Svenningsson, B.; Bohgard, M.; Kulmala, M.; Hallquist, M.; Pagels, J. H. Secondary organic aerosol formation from idling gasoline passenger vehicle emissions investigated in a smog chamber. *Atmos. Chem. Phys.* **2013**, *13*, 6101-6116.
4) Liu, T.; Wang, X.; Deng, W.; Hu, Q.; Ding, X.; Zhang, Y.; He, Q.; Zhang, Z.; Lu, S.; Bi, X.; Chan, J.; Yu, J. Secondary organic aerosol formation from photochemical aging of light-duty gasoline vehicle exhausts in a smog chamber. *Atmos. Chem. Phys.* **2015**, *15*, 9049-9062.
5) Pachauri, R. K., Allen, M. R., Barros, V. R., Broome, J., Cramer, W., Christ, R., Church, J. A., Clarke, L., Dahe, Q., Dasgupta, P., Dubash, N. K., Edenhofer, O., Elgizouli, I., Field, C. B., Forster, P., Friedlingstein, P., Fuglestvedt, J., Gomez-Echeverri, L., Hallegatte, S., Hegerl, G., Howden, M., Jiang, K., Jimenez Cisneroz, B., Kattsov, V., Lee, H., Mach, K. J., Marotzke, J., Mastrandrea, M. D., Meyer, L., Minx, J., Mulugetta, Y., O'Brien, K., Oppenheimer, M., Pereira, J. J., Pichs-Madruga, R., Plattner, G. K., Pörtner, H.-O., Power, S. B., Preston, B., Ravindranath, N. H., Reisinger, A., Riahi, K., Rusticucci, M., Scholes, R., Seyboth, K., Sokona, Y., Stavins, R., Stocker, T. F., Tschakert, P., van Vuuren, D., and van Ypserle, J. P.: Climate Change **2014**: Synthesis Report, in: Contribution of

Working Groups I, II and III to the Fifth Assessment Report of the Intergovernmental Panel on Climate Change, edited by: Pachauri, R. K. and Meyer, L., IPCC, Geneva, Switzerland, 151 pp., 2014.

6) Han, Xianglu, and Luke P. Naeher. **2006**. "A Review of Traffic-Related Air Pollution Exposure Assessment Studies in the Developing World." *Environment International* 32 (1): 106–20.

7) Robinson, Allen L., Neil M. Donahue, Manish K. Shrivastava, Emily A. Weitkamp, Amy M. Sage, Andrew P. Grieshop, Timothy E. Lane, Jeffrey R. Pierce, and Spyros N. Pandis. **2007**. "Rethinking Organic Aerosols: Semivolatile Emissions and Photochemical Aging." *Science* 315 (5816): 1259–62.

8) Karjalainen, P., H. Timonen, E. Saukko, H. Kuuluvainen, S. Saarikoski, P. Aakko-Saksa, T. Murtonen, et al. **2015**. "Time-Resolved Characterization of Primary and Secondary Particle Emissions of a Modern Gasoline Passenger Car." *Atmospheric Chemistry & Physics Discussions* 15 (22).

9) Vu, D.; Roth, P.; Berte, T.; Yang, J.; Cocker D.; Durbin T.; Karavalakis, G.; Asa-Awuku, A. Using a new Mobile Atmospheric Chamber (MACh) to investigate the formation of secondary aerosols from mobile sources: The case of gasoline direct injection vehicles. Journal of Aerosol Science, Manuscript Under Review.

10) Bahreini, R.; Middlebrook, A. M.; de Gouw, J. A.; Warneke, C.; Trainer, M.; Brock, C. A.; Stark, H.; Brown, S. S.; Dube, W. P.; Gilman, J. B.; Hall, K.; Holloway, J. S.; Kuster, W. C.; Perring, A. E.; Prevot, A. S. H.; Schwarz, J. P.; Spackman, J. R.; Szidat, S.; Wagner, N. L.; Weber, R. J.; Zotter, P.; Parrish, D. D. Gasoline emissions dominate over diesel in formation of secondary organic aerosol mass. *Geophys. Res. Lett*. **2012**, *39*, L06805, doi: 10.1029/2011GL050718.

11) Gentner, D.R.; Jathar, S.H.; Gordon, T.D.; Bahreini, R.; Day, D.A.; Haddad, I.E.; Haynes, P.L.; Pieber, S.M.; Platt, S.M.; De Gouw, J.; Goldstein, A.H.; Harley, R.A.; Jimenez, J.L.; Prevot, A.S.H.; Robinson A.L. Review of urban secondary organic aerosol formation from gasoline and diesel motor vehicle emissions. *Environ. Sci. Technol.* **2017**, *51*, 1074-1093.

12) Gentner, Drew R., Gabriel Isaacman, David R. Worton, Arthur W. H. Chan, Timothy R. Dallmann, Laura Davis, Shang Liu, et al. **2012**. "Elucidating Secondary Organic Aerosol from Diesel and Gasoline Vehicles through Detailed Characterization of Organic Carbon Emissions." *Proceedings of the National Academy of Sciences of the United States of America* 109 (45): 18318–23.

13) Odum, J.R.; Junkkamp, T.P.; Griffin,, W.R.; Forstner, H.J.L.; Flagan, R.C.; Seinfeld, J.H. Aromatics, reformulated gasoline, and atmospheric organic aerosol formation. *Environ. Sci. Technol.* **1997**, *31*, 1890-1897.

14) Platt, S. M.; El Haddad, I.; Zardini, A. A.; Clairotte, M.; Astorga, C.; Wolf, R.; Slowik, J. G.; Temime-Roussel, B.; Marchand, N.; Ježek, I.; Drinovec, L.; Močnik, G.; Möhler, O.; Richter, R.; Barmet, P.; Bianchi, F.; Baltensperger, U.; Prévôt, A. S. H.: Secondary organic aerosol formation from gasoline vehicle emissions in a new mobile environmental reaction chamber. *Atmos. Chem. Phys.* **2013**, *13*, 9141-9158.

15) Zhao, Y.; Lamber, A.T.; Saleh, R.; Saliba, G.; Robinson, A.L. Secondary organic aerosol production from gasoline vehicle exhaust: Effects of engine technology, cold start, and emission certification standard. *Environ. Sci. Technol.* **2018**, *52*, 1253-1261.

16) Karavalakis G, Short D, Vu D, Villela M, Asa-Awuku A, Durbin TD. Evaluating the regulated emissions, air toxics, ultrafine particles, and black carbon from SI-PFI and SI-DI vehicles operating on different ethanol and iso-butanol blends. Fuel **2014a**;128:410-421.

17) Catapano, F.; Sementa, P.; Vaglieco, B.M. Air-fuel mixing and combustion behavior of gasoline-ethanol blends in a GDI wall-guided turbocharged multi-cylinder optical engine. *Renewable Energy* **2016**, *96*, 319-332.

18) Jin, D.; Choi, K.; Myun, C.L.; Lim, Y., Lee, J.; Park, S. The impact of various ethanol-gasoline blends on particulates and unregulated gaseous emissions characteristics from a spark ignition direct injection (SIDI) passenger vehicle. *Fuel* **2017**, *209*, 702-712.

19) Piock, W.; Hoffmann, G.; Berndorfer, A.; Salemi, P.; Fusshoeller, B. Strategies towards meeting future particulate matter emission requirements in homogeneous gasoline direct injection engines. *SAE Int. J. Engines* **2011**, *4*, 1455-1468.

20) Du, Z.; Hu, M.; Peng, J.; Zhang, W.; Zheng, J.; Gu, F.; Qin, Y.; Yang, Y.; Li, M.; Wu, Y.; Shao, M.; Shuai, S. Comparison of primary aerosol emission and secondary aerosol formation from gasoline direct injection and port fuel injection vehicles. *Atmos. Chem. Phys.* **2018**, *18*, 9011-9023.

21) Hubbard, C.P.; Anderson, J.E.; Wallington, T.J. Ethanol and air quality: Influence of fuel ethanol content on emissions and fuel economy of flexible fuel vehicles. *Environ. Sci. Technol.* **2014**, *48*, 861-867.

22) Dardiotis, C.; Fontaras, G.; Marotta, A.; Martini, G.; Manfredi, U. Emissions of modern light duty ethanol flex-fuel vehicles over different operating and environmental conditions. *Fuel* **2015**, *140*, 531-540.

23) Karavalakis, G.; Short, D.; Russell, R.L.; Jung, H.; Johnson, K.C.; Asa-Awuku, A.; Durbin, T.D. Assessing the Impacts of Ethanol and Iso-butanol on Gaseous and Particulate Emissions from Flexible Fuel Vehicles. *Environ. Sci. Technol.* **2014b**, *48*, 14016-14024.

24) Chen, Hu, Shuai Shi-Jin, and Wang Jian-Xin. **2007**. "Study on Combustion Characteristics and PM Emission of Diesel Engines Using Ester–ethanol–diesel Blended Fuels." *Proceedings of the Combustion Institute* 31 (2): 2981–89.

25) Suarez-Bertoa, R.; Zardini, A.A.; Keuken, H.; Astorga, C. Impact of ethanol containing gasoline blends on emissions from a flex-fuel vehicle tested over the Worldwide Harmonized Light duty Test Cycle (WLTC). *Fuel* **2015**, *143*, 173-182.

26) Khosousi, A.; Liu, F.; Dworkin, S.B.; Eaves, N.A.; Thomson, M.J.; He, X., Dai, Y.; Gao, Y.; Liu, F.; Shuai, S.; Wang, J. Experimental and numerical study of soot formation in laminar coflow diffusion flames off gasoline/ethanol blends. *Combustion and Flame* **2015**, *162*, 3925-3933.

27) Maricq, M.M.; Szente, J.J.; Jahr, K. The impact of ethanol fuel blends on PM emissions from a light-duty GDI vehicle. *Aerosol Science and Technology* **2012**, *46*, 576-583.

28) Gramsch, E., V. Papapostolou, F. Reyes, Y. Vásquez, M. Castillo, P. Oyola, G. López, et al. **2018**. "Variability in the Primary Emissions and Secondary Gas and Particle Formation from Vehicles Using Bioethanol Mixtures." *Journal of the Air & Waste Management Association* 68 (4): 329–46.

29) Kacarab, Mary, "Impacts of Controlling Reactivity and Temperature on Advanced Study of Secondary Organic Aerosol Formation" Ph.D. Diss, University of Califonria, Riverside, 2016, scholarship.org/uc/item/4sq547tq

30) Roth, P., Yang, J., Cocker, D.R., Durbin, T., Brezney, R., Geller, M., Asa-Awuku, A., Karavalakis, G.; "Catalyzed Gasoline Particulate Filters Reduce Secondary Organic Aerosol Production from Gasoline Direct Injection Vehicles." Journal of Energy & Fuels, Under Review

31) Petzold, A., and R. Niessner. 1996. "Photoacoustic Soot Sensor for in-Situ Black Carbon Monitoring." *Applied Physics. B, Lasers and Optics* 63 (2): 191–97.

32) Aiken, A. C.; DeCarlo, P. F.; Kroll, J. H.; Worsnop, D. R.; Huffman, J. A.; Docherty, K. S.; Ulbrich, I. M.; Mohr, C.; Kimmel, J. R.; Sueper, D.; Sun, Y.; Zhang, Q.; Trimborn, A.; Northway, M.; Ziemann, P. J.;, Canagaratna, M. R.; Onasch, T. B.; Alfarra, M. R.; Prevot, A. S. H.,; Dommen, J.,; Duplissy, J.; Metzger, A.; Baltensperger, U.; Jimenez, J. L. O/C and OM/OC ratios of primary, secondary, and ambient organic aerosols with high-resolution time-of-flight aerosol mass spectrometry. *Environ. Sci. Technol.* **2008**, *42*, 4478-4485.

33) Hoyle, C. R., M. Boy, N. M. Donahue, J. L. Fry, Marianne Glasius, A. Guenther, A. G. Hallar, et al. **2011**. "A Review of the Anthropogenic Influence on Biogenic Secondary Organic Aerosol." *Atmospheric Chemistry and Physics* 11 (1): 321–43.

34) Price, Philip, Ben Twiney, Richard Stone, Kenneth Kar, and Harold Walmsley. **2007**. "Particulate and Hydrocarbon Emissions from a Spray Guided Direct Injection Spark Ignition Engine with Oxygenate Fuel Blends." SAE Technical Paper. http://papers.sae.org/2007-01-0472/.

35) Karavalakis, Georgios, Daniel Short, Diep Vu, Robert Russell, Maryam Hajbabaei, Akua Asa-Awuku, and Thomas D. Durbin. **2015a**. "Evaluating the Effects of

Aromatics Content in Gasoline on Gaseous and Particulate Matter Emissions from SI-PFI and SIDI Vehicles." *Environmental Science & Technology* 49 (11): 7021–31.

36) Stevens, E.; Steeper, R. Piston wetting in an optical DISI engine: Fuel films, pool fires, and soot generation. SAE Technical Paper **2001**, 2001-01-1203.

37) Suarez-Bertoa, R., A. A. Zardini, and C. Astorga. **2014**. "Ammonia Exhaust Emissions from Spark Ignition Vehicles over the New European Driving Cycle." *Atmospheric Environment* 97 (November): 43–53.

38) Clairotte, M., T. W. Adam, A. A. Zardini, U. Manfredi, G. Martini, A. Krasenbrink, A. Vicet, E. Tournié, and C. Astorga. **2013**. "Effects of Low Temperature on the Cold Start Gaseous Emissions from Light Duty Vehicles Fuelled by Ethanol-Blended Gasoline." *Applied Energy* 102 (February): 44–54.

39) Tkacik, Daniel S., Andrew T. Lambe, Shantanu Jathar, Xiang Li, Albert A. Presto, Yunliang Zhao, Donald Blake, et al. **2014**. "Secondary Organic Aerosol Formation from in-Use Motor Vehicle Emissions Using a Potential Aerosol Mass Reactor." *Environmental Science & Technology* 48 (19): 11235–42.

40) Liu, F.-J.; Liu, P.; Wei, Y.-J.; Liu, S.-H. Regulated and unregulated emissions from a spark-ignition engine fuelled with low-blend ethanol-gasoline mixtures. *Proceedings of the Institution of Mechanical Engineers, Part D: Journal of Automobile Engineering* **2011**, *226*, 517-528.

41) Catapano, F.; Di Iorio, S.; Sementa, P.; Vaglieco, B.M. Characterization of ethanol-gasoline blends combustion processes and particle emissions in a GDI/PFI small engine. SAE Technical Paper **2014**, 2014-01-1382.

42) Yao, C.; Dou, Z.; Wang, B.; Liu, M.; Lu, H.; Feng, J.; Feng, L. Experimental study of the effect of heavy aromatics on the characteristics of combustion and ultrafine particle in DISI engine. *Fuel* **2017**, *203*, 290-297.

43) Karavalakis, Georgios, Daniel Short, Diep Vu, Robert L. Russell, Akua Asa-Awuku, Heejung Jung, Kent C. Johnson, and Thomas D. Durbin. **2015b**. "The Impact of Ethanol and Iso-Butanol Blends on Gaseous and Particulate Emissions from Two

Passenger Cars Equipped with Spray-Guided and Wall-Guided Direct Injection SI (spark Ignition) Engines." *Energy* 82 (March): 168–79.

44) Jimenez, J. L., M. R. Canagaratna, N. M. Donahue, A. S. H. Prevot, Q. Zhang, J. H. Kroll, P. F. DeCarlo, et al. **2009**. "Evolution of Organic Aerosols in the Atmosphere." *Science* 326 (5959): 1525–29.

45) Ng, N. L.; Canagaratna, M. R.,; Zhang, Q.; Jimenez, J. L.; Tian, J.,; Ulbrich, I. M.; Kroll, J. H.; Docherty, K. S.; Chhabra, P. S.; Bahreini, R.;, Murphy, S. M.; Seinfeld, J. H.; Hildebrandt, L.; Donahue, N. M.; DeCarlo, P. F.; Lanz, V. A.; Prévôt, A. S. H.; Dinar, E.; Rudich, Y.; Worsnop, D. R. Organic aerosol components observed in Northern Hemispheric datasets from Aerosol Mass Spectrometry. *Atmos. Chem. Phys.* **2010**, *10*, 4625- 4641.

46) Derwent, Richard G., Michael E. Jenkin, Steven R. Utembe, Dudley E. Shallcross, Tim P. Murrells, and Neil R. Passant. **2010**. "Secondary Organic Aerosol Formation from a Large Number of Reactive Man-Made Organic Compounds." *The Science of the Total Environment* 408 (16): 3374–81.

3.7. Supplemental Data:

Table 3-1: Main physiochemical properties of the four test fuels

Property	Test Method	E10	HAE10	E30	E78
Research Octane Number	ASTM D2699	92.1	93.5	100.5	
Motor Octane Number	ASTM D2700	84	83.9	87.5	
Octane Rating		88.1	88.7	94	
Sulfur Content (wt. %)	ASTM D5453	8	7.2	6	3
Total Aromatics (vol %)	ASTM D5769	28.1	36.7	22	5.57
C6 Aromatics (vol %)	ASTM D5769	0.60	0.57	0.46	0.17
C7 Aromatics (vol %)	ASTM D5769	7.58	9.14	5.90	1.41
C8 Aromatics (vol %)	ASTM D5769	6.55	7.27	5.11	1.16
C9 Aromatics (vol %)	ASTM D5769	6.12	10.23	4.81	1.79
C10+ Aromatics (vol %)	ASTM D5769	5.56	7.02	4.40	0.83
Olefins Content	ASTM D6550	8.50	10.63	6.45	1.37
Hydrogen Content (wt. %)	ASTM D5291	13.59	13.21	13.33	13.07
Carbon Content (wt. %)	ASTM D5291	82.77	83.19	75.28	59.41
Oxygen Content (wt. %)	ASTM D4815	3.63	3.59	11.39	27.52
C/H Ratio		6.09	6.297	5.647	4.545
Heat of Comb. (MJ/Kg)	ASTM D240	41.94	41.65	38.17	30.30
Density at 15.56 °C (g/cc)	ASTM D4052	0.749	0.754	0.760	0.783
RVP at 100 F (psi)	ASTM D5191	8.89	9.39	8.20	5.05
Distillation (°C)	ASTM D86				
IBP		35	34.5	36.5	49.9
10%		51.7	53.5	57	71.1
50%		94	96.3	74.5	77.4
70%		129.1	130	78.8	77.9
90%		163.5	165.9	158.1	78.6
95%		179.1	181.8	175.7	79.4
FBP		203.5	209.1	198.8	168.2
Ethanol Content (vol%)	ASTM D4815	9.86	9.85	31.44	78.27

Table 3-2: Initial NOx and NH_3 concentrations (ppb) in the chamber before the irradiation experiment for FFV-1. Ozone concentrations (ppb) were recorded at the time of plateau at the end of the irradiation experiments

FFV-1	Fuel	NOx (ppb)	NH_3 (ppb)	O_3 (ppb)
Cold-Start	E10	105	130	204
	HA E10	158	227	231
	E30	101	132	252
	E78	59	137	248
Hot-Start	E10	119	145	141
	HA E10	111	190.	216
	E30	106	175	138
	E78	68	157	186

Table 3-3: Initial NOx and NH_3 concentrations (ppb) in the chamber before the irradiation experiment for FFV-2. Ozone concentrations (ppb) were recorded at the time of plateau at the end of the irradiation experiments

FFV-2	Fuel	NOx (ppb)	NH3 (ppb)	O_3 (ppb)
Cold-Start	E10	78	63	214
	HA E10	56	76	220
	E30	47	63	217
	E78	46	81	193
Hot-Start	E10	72	51	200.
	HA E10	85	72	161
	E30	48	105	217
	E78	54	91	190.

Table 3-4: Compounds in the anthropogenic surrogate mixture

ppb/ppmC	Compound
46	Acetaldehyde
17	Methyl Ethyl Ketone
5	*m*-Xylene
5	1,2,4-Trimethylbenzene
14	Toluene
90	n-Butane
22	2-Methylbutane
13	Methylcyclopentane
14	trans-2-Butene
16	Ethylene
14	Propylene
3	1-Pentene
2	Isoprene

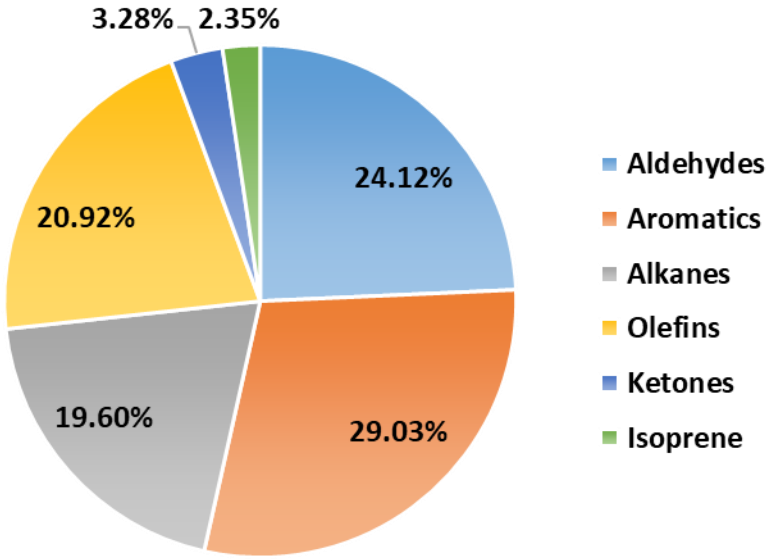

Figure 3-11: Fractional composition of the compound classes making up the anthropogenic surrogate

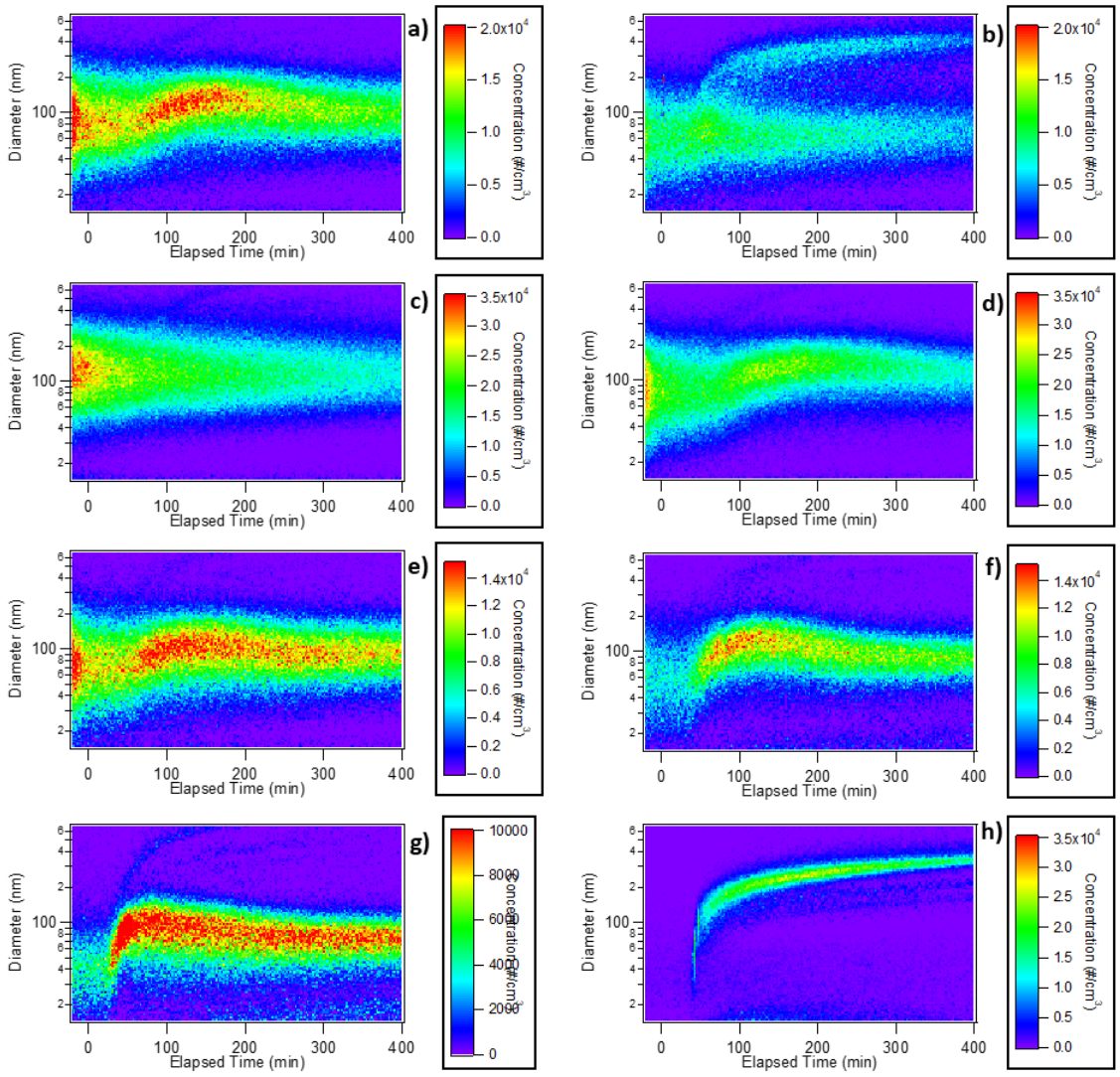

Figure 3-12: Evolution of aerosol distribution for FFV-1 exhaust only experiments operated on the four fuels, E10 (a,b), HA E10 (c,d), E30 (e,f), E78 (g,h), for the cold-start (a,c,e,g) and hot-start (b,d,f,h) LA92 driving cycles

Figure 3-12 shows the image plots for the FFV-1 experiments. The aerosol emitted in the cold-start experiments evolved similarly, with the distinguishing difference being the initial particles emitted. The HA E10 CS experiment (Figure 3-12 c) formed the largest

mass of SOA, however the peak does not appear to shift much. This is due to the large number of particles and the filling in of the particles. Also there was a small subset of particles that grew away from the initial peak which contained a large portion of the mass formed in the irradiation experiments. Similar to the HA E10, the traditional E10 and E30 had a similar evolution of aerosol (Figure 3-12 a, e). The initial, broad, unimodal peak shifted slightly to a larger size, and there was once again a small subset of aerosol particles that grew away from the initial distribution. Once again, one large difference between the two was the difference in initial particle number. Finally, the most unique of the cold-start experiments was the E78 fuel. In the case of this fuel, the initial broad peak sharpened quickly as the gases condensed. That peak grew slightly and the final peak was observed around 100nm. Once again a small group of particles grew from the initial peak.

The hot-start experiments for FFV-1 were quite similar to the cold-start, however in the case of the E10, E30 and the E78, more aerosol mass formed in the hot-start experiments. This additional mass can be observed in the E10, where the subset of particles separating from the initial peak has a much higher number for the hot-start experiments (Figure 3-12 b). Similarly, the hot-start E30 experiment (Figure 3-12 f) was quite similar to the cold-start, however the initial broad peak grew to a larger final diameter which would account for the increased mass. Finally, the E78 was the most unique once again in the hot-start (Figure 3-12 h). In this experiment, there is an obvious nucleation burst of particles around 45 min into the irradiation experiment. In this burst, it appeared that all particles grew simultaneously and ended up growing to approximately 400 nm.

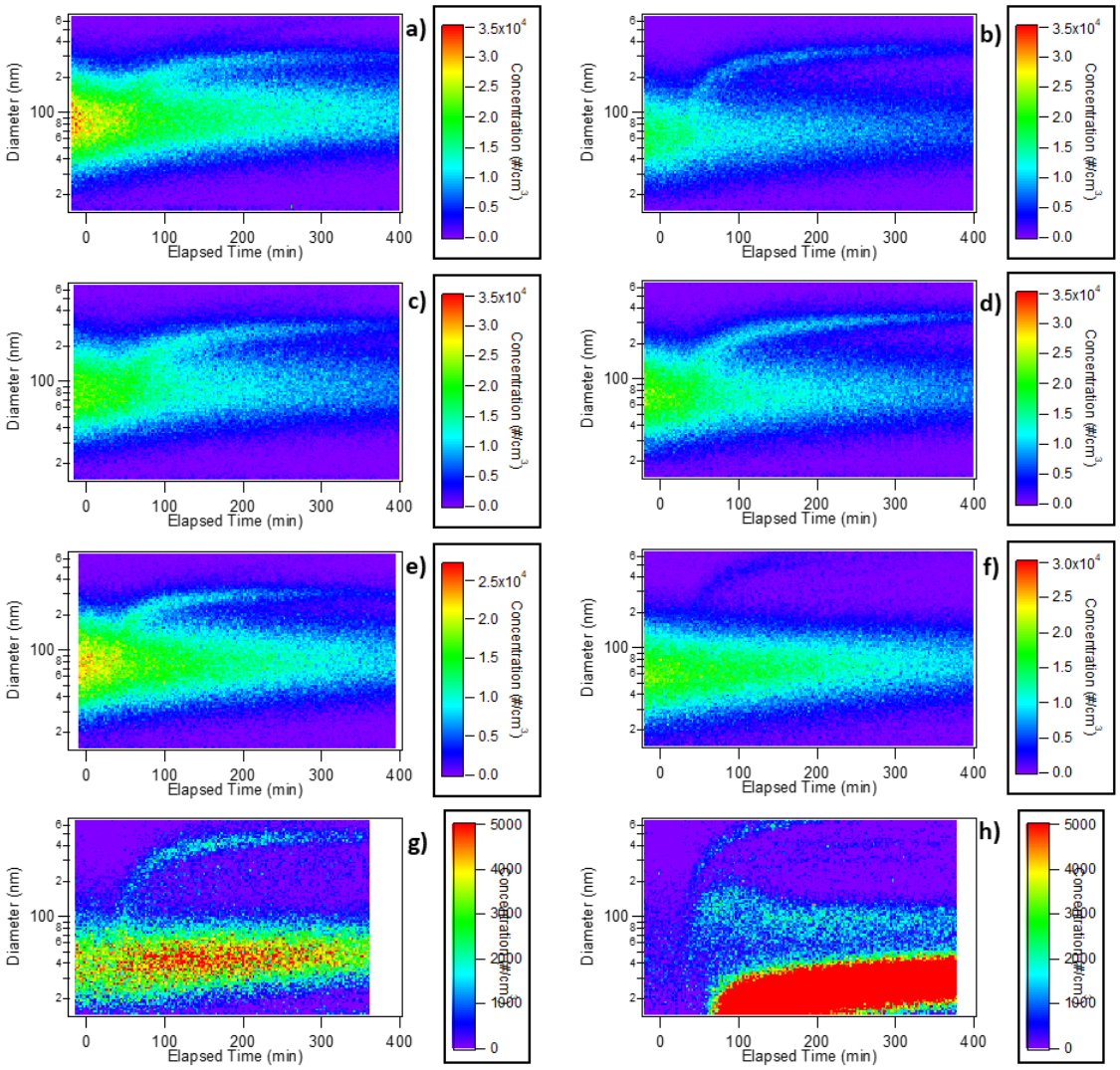

Figure 3-13: Evolution of aerosol distribution for FFV-2 surrogate and exhaust experiments operated on the four fuels, E10 (a,b), HA E10 (c,d), E30 (e,f), E78 (g,h), for the cold-start (a,c,e,g) and hot-start (b,d,f,h) LA92 driving cycles

Figure 3-13 shows the size distribution changes for the FFV-2 exhaust and surrogate experiments. For these experiments, the cold-start experiments formed more aerosol than the similar hot-start experiments for all fuels (E78 formed a similar mass of

total aerosol in both driving cycles). All cold and hot-start experiments were quite similar for the two E10 fuels and the E30 fuels, once again with the main difference being the initial number of particles in the distribution. For the E10 experiments (Figure 3-13 a, b), a subset of particles grew away from the initial distribution. E10 fuel cold-start formed the most aerosol out of all configurations for FFV-2, and was mainly due to the number of particles that grew away from the initial distribution (second small peak grew away at around 100 min and grew out of range). Similarly for all the hot-start tests (Figure 3-13 b, d, f) excluding the E78, the difference in mass was due to the number of particles which grew out of the initial peak.

Similar to the FFV-1 experiments, the E78 was the most unique fuel. In the case of FFV-2, the hot-start and cold-start experiments formed a similar mass of secondary aerosol. In the cold-start test, (Figure 3-13 g), the initial peak shifted slightly, however the majority of the mass formed was in the peak that grew to approximately 500 nm. This was similar to the hot-start configuration, however, in these experiments there was a nucleation burst. The color scale for the hot-start test (Figure 3-13 h) was kept consistent to the cold-start, so the peak that grew could be seen, however there was a large increase in the number of the smaller diameter peak. In this experiment, even though a majority of the number concentration was distributed in the lower diameter peak, the majority of the mass that formed was due to the small subset of particles which ended up growing out of the measureable range of the SMPS system.

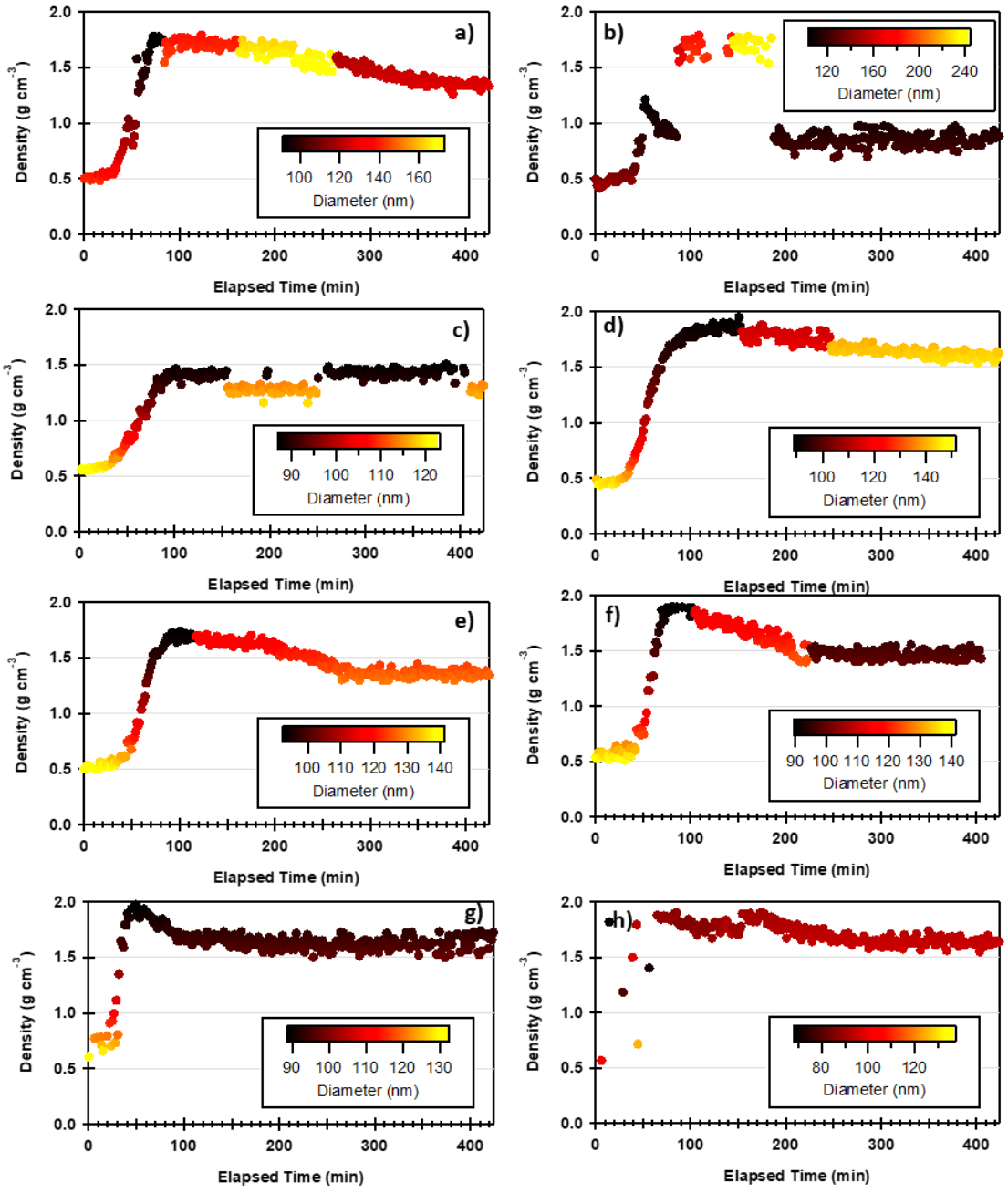

Figure 3-14: FFV-1 Density change with time for E10 (a,b), HA E10 (c,d), E30 (e,f), E78 (g,h), for the cold-start (a,c,e,g) and hot-start (b,d,f,h) LA92 driving cycles

Figure 3-14 shows the changes in density throughout the irradiation experiments for the FFV-1 experiments. The cold-start experiments were all quite similar in the

evolution of the density as the gases and aerosol aged. Initially, the aerosol all started with a fractal density ~0.5. As the gases condensed, the initial particle grew which filled in the initial fractal particle. In regards to the E10 fuel and the E30 cold-start experiments (Figure 3-14 a, e) the initial growth moved the density up to approximately 1.7 which is consistent with the addition of ammonium nitrate. Then as the aerosol continued to age, the density decreased to approximately 1.4 which is consistent with the density of SOA. This varied from the HA E10 where the density initially reached around 1.5 after the first growth, then leveled around 1.4 which is once again consistent with SOA. Finally, the E78 fuel displayed the largest density with the initial growth to 1.8 and leveled off just under 1.6. This once again indicates ammonium nitrate with a smaller fractional composition of SOA which was confirmed by the AMS measurements.

The hot-start tests were quite similar for the HA E10 and the E30 (Figure 3-14 d, f) to the cold-start comparable tests (Figure 3-14 c, e). The HA E10 (Figure 3-14 d) displayed a larger density after the initial growth indicating more ammonium nitrate fraction in the aerosol and leveled off over 1.5 indicating a mix of inorganic and organic species. The E10 (Figure 3-14 b) however was quite different from cold-start E10 (Figure 3-14 a). In the hot-start test, the peak that separated from the initial broad peak grew to a similar density, however the initial peak maintained a fractal morphology and a density below 1.0. The E78 hot-start test displayed a very low initial particle number concentration so an accurate density could not be read. However, after the nucleation burst, the density was measured to be ~1.8 indicating the growth was most likely due to the nucleation of ammonium nitrate.

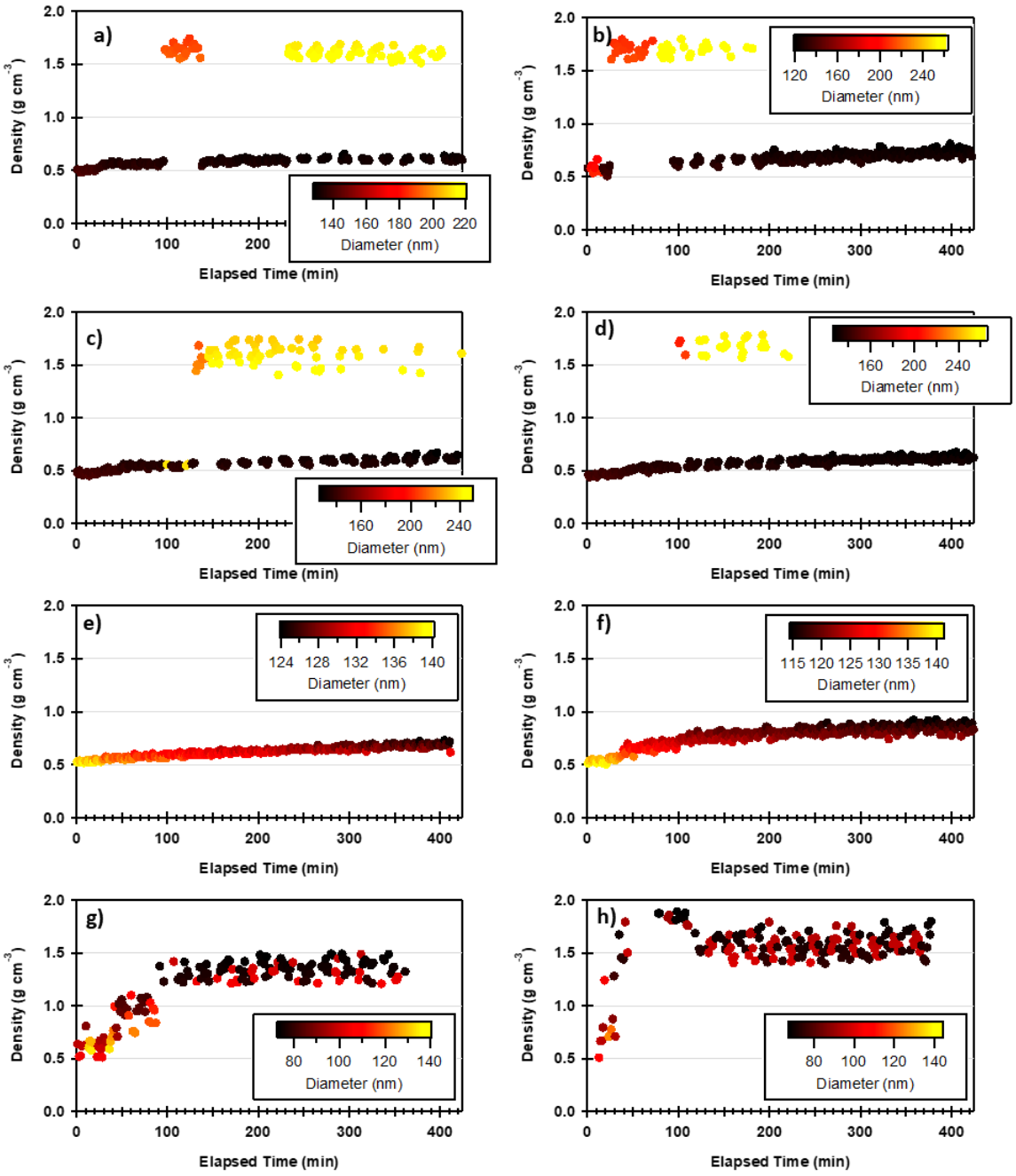

Figure 3-15: FFV-2 density change with time for E10 (a, b), HA E10 (c, d) E30 (e, f), E78 (g, h), for the cold-start (a,c,e,g) and hot-start (b,d,f,h) LA92 driving cycles

Figure 3-15 shows the density evolution throughout the irradiation experiments for FFV-2 hot-start and cold-start experiments. Similar to the FFV-1 experiments, the density of the initial tailpipe aerosol was fractal with a density of ~0.5. However, the density evolution was much different than the FFV-1 experiments. The measured density of the initial broad unimodal peak for the two E10 fuels and the E30 fuels did not change much (Figure 3-15a-f). The density increased slightly, however still remained fractal in these configurations. However, when measuring the density of the larger diameter peak for the two E10 fuels (Figure 3-15a-d), it was found that the density increased to over 1.5 indicating the addition of ammonium nitrate and SOA. This was once again consistent between the hot-start and cold-start experiments. In the E30 tests (Figure 3-15 e, f), the small peak that separated from the initial distribution was too small for measurement, however it was assumed that it had the density similar to the two E10 fuels based on the similarities measured from the AMS.

Similar to the size distribution, the E78 displayed the most differences to the other fuels in density evolution as well (Figure 3-15 g, h). The density of the cold-start test was measured to grow to approximately 1.45 indicating the fractal tailpipe particle filled in with both SOA and inorganic salt which is consistent with the measured composition from the AMS (Figure 3-15g). The hot-start E78 (Figure 3-15h) density grew to over 1.5 indicating that a majority of the aerosol was ammonium nitrate which is once again confirmed with the AMS.

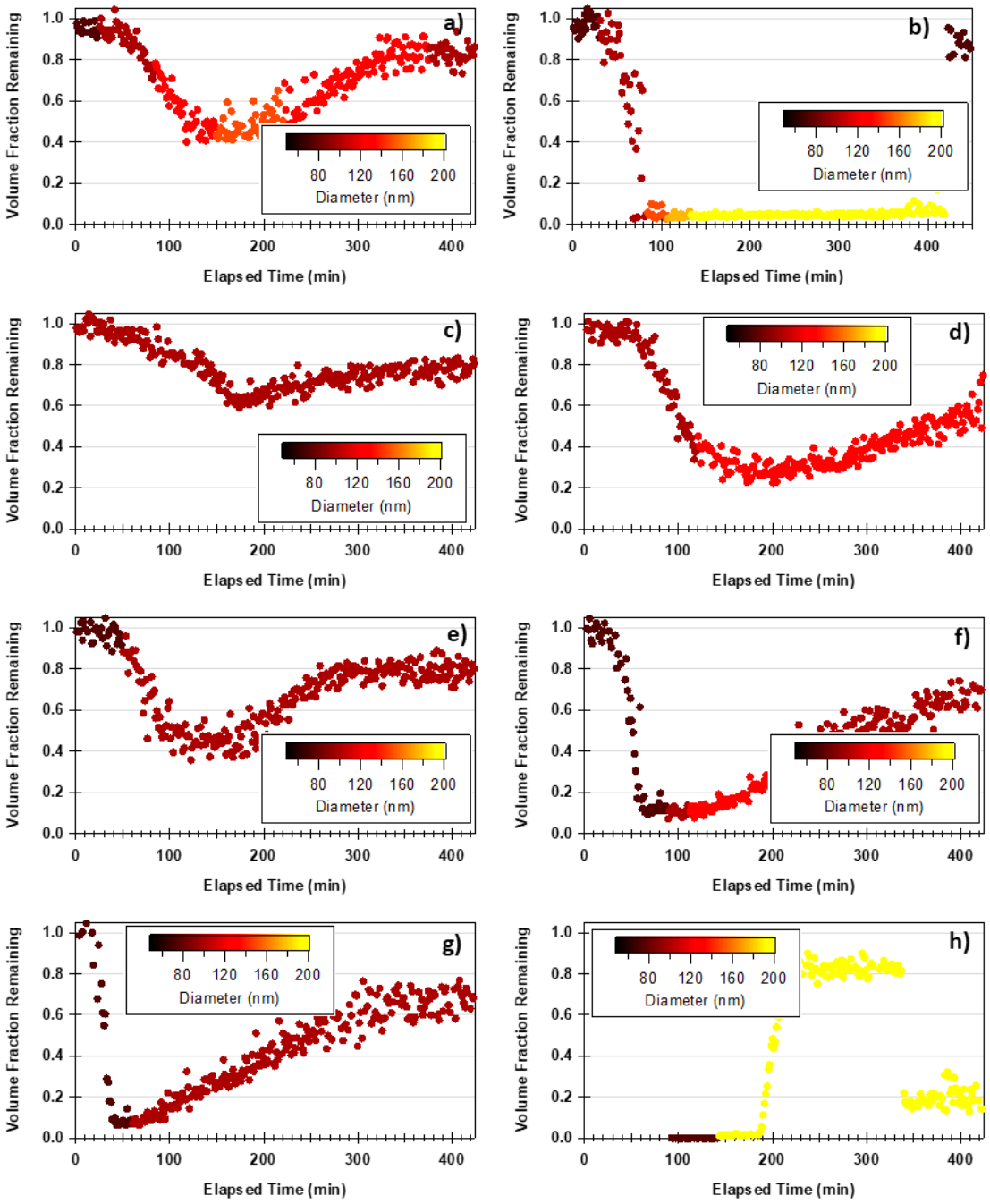

Figure 3-16: FFV-1 volatility measurements vs irradiation time for E10 (a,b), HA E10 (c,d), E30 (e,f), E78 (g,h), for the cold-start (a,c,e,g) and hot-start (b,d,f,h) LA92 driving cycles

Figure 3-16 shows the VFR data for FFV-1 which was collected using the volatility tandem differential mobility analyzer with the heated portion of the system at a temperature of 100 °C. Initially all particles start with a VFR of 1.0 which is indicative of a black carbon particle which is non-volatile (Figure 3-16 a-h). As the gases condense and the particles grow, the VFR drops drastically. The cold-start tests for the two E10 fuels and the E30 fuels display similar properties (Figure 3-16 a, c, e). In these tests, the VFR drops to approximately 0.5 however as the gases condensing continue to age, the volatility continues to decrease resulting in the VFR increasing to approximately 0.8 at the end of the experiment. The smallest differences in VFR is seen from the HA E10 (Figure 3-16 c), which is most likely due to the larger number of particles in the system.

The cold-start E78 fuel (Figure 3-16 g) shows the largest drop in VFR in relation to the other three cold-start tests where the VFR drops to under 0.1 which is indicative of a majority of the volume being ammonium nitrate which is completely volatile at 100 °C. As the SOA condenses on to the particle and the organic fraction increases, the VFR increases drastically. And as a result ends with a VFR of ~0.7.

The hot-start tests in all cases displayed much more drastic changes in the VFR (Figure 3-16 b,d,f,g). This is most likely due to the increased ammonium nitrate that formed in all experiments, and the reduced seed primary aerosol for the gases to condense onto. In regards to the E10 and the E78 (Figure 3-16 b, g), both tests a VFR of 0 is observed for the majority of the test which is indicative of a particle that is mostly ammonium nitrate. However, once again as the particles fill in with more organics, the VFR increased. The HA E10 and E30 were most similar to their cold-start counterparts (Figure 3-16 d, f).

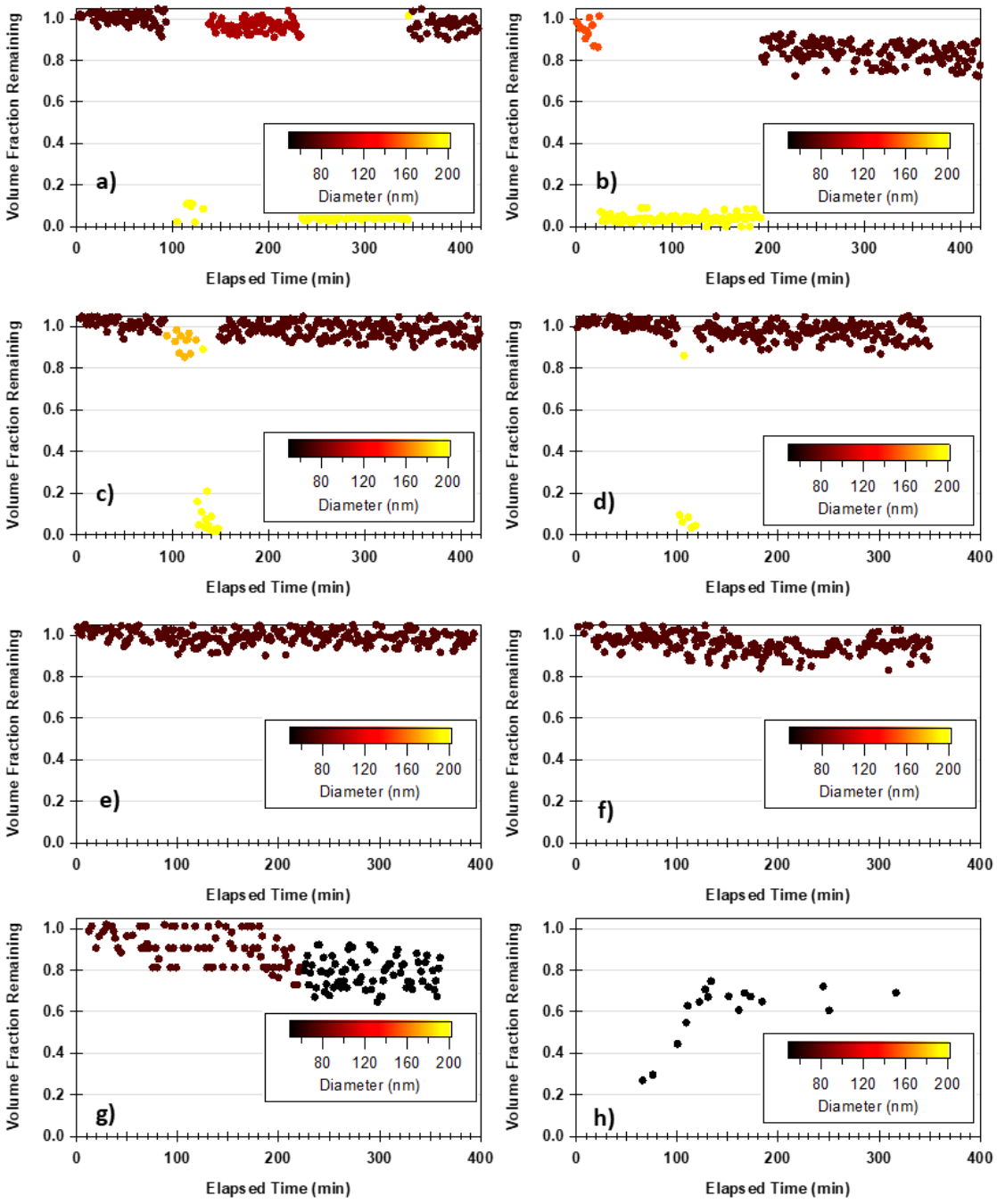

Figure 3-17: FFV-2 volatility measurements vs irradiation time for E10 (a,b), HA E10 (c,d), E30 (e,f), E78 (g,h), for the cold-start (a,ce,g) and hot-start (b,d,f,h) LA92 driving cycles

As shown in Figure 3-17, similar to FFV-1, all of the initial VFR measurements were 1.0 which once again can be attributed to black carbon particles. The VFR data for FFV-2 (Figure 3-17) confirmed what was found in the density data. In all of the tests, the smaller diameter peak maintained a similar composition and similar properties to the initial fractal black carbon particles. The two E10 fuels and the E30 fuel (Figure 3-17a, c, e) maintained a VFR of 1.0 for the whole experiment for the smaller diameter mode of particles. The larger diameter mode of particles however showed a VFR of near 0. This is indicative of the particle being composed of a majority of ammonium nitrate which is similar to what was seen by the AMS. The trends for the similar hot-start tests (Figure 3-17b, d, f) showed the same trend for the two diameter modes however the smaller diameter mode did show a larger decrease in VFR for the E10 and E30 fuel (Figure 3-17 b, f). This is most likely due to there being less particles in the hot-start tests so the condensation of the gases is more concentrated on the smaller number of particles.

The E78 fuel experiments (Figure 3-17g, h) had a much smaller number distribution of particles so it was more difficult to get a reading for the VFR. However, for the cold-start test, (Figure 3-17g) similar to the other cold-start tests, the VFR remained high throughout the irradiation experiment. In the hot-start experiment (Figure 3-17h), the particle concentration was too low to measure throughout a majority of the experiment. However, when the nucleation peak grew into range, the values for the VFR were much lower than the other experimental conditions, but increased in volatility as the aged gases continued to condense on the existing particulate.

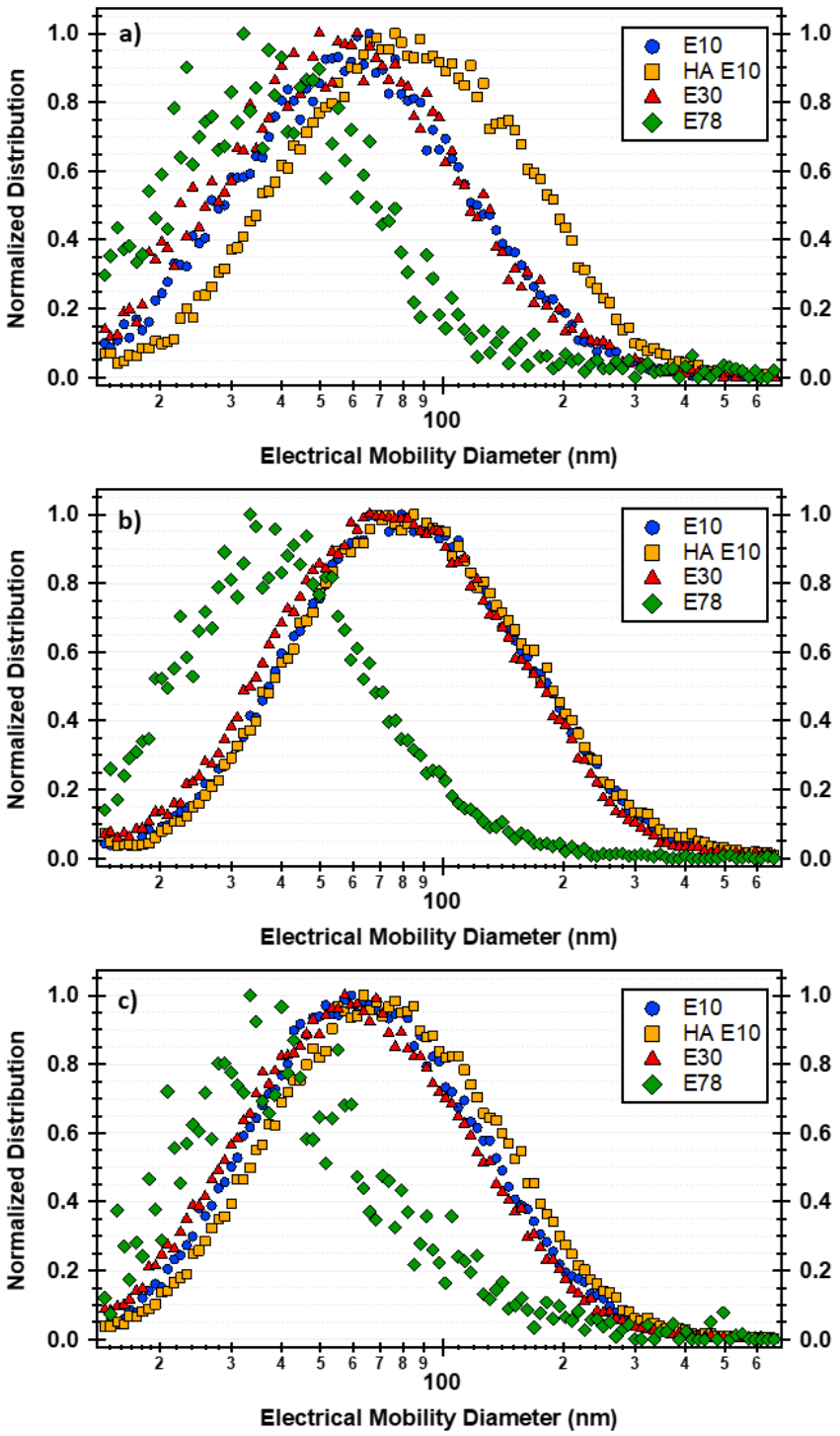

Figure 3-18: Average initial aerosol distributions after dilutions for a)FFV-1 hot-start b) FFV-2 cold-start c) FFV-2 hot-start for the E10, HA E10, E30, and E78 fuels

Figure 3-18 shows the initial, diluted, normalized size distributions for FFV-1 hot-start (Figure 3-18 a), FFV-2 cold-start (Figure 3-18 b), and FFV-2 hot-start (Figure 3-18 c), while FFV-1 cold-start is in the main text. For these values, the initial size distributions were taken from each of the three tests in each configuration, and were averaged. After averaging, the maximum number was taken and used to normalize the values.

Similar to the FFV-1 cold-start test, FFV-1 hot-start displays a similar strong trend where, as the ethanol is increased, the peak diameter decreases for all fuels. This differs compared to FFV-2 (Figure 3-18 b, c) where in both the hot-start and cold-start tests the two E10 fuels and the E30 fuel appear to be stacked on one another. The peak diameter of these still follows a similar trend to FFV-1 where the peak diameter is smaller for the E30 fuels, however the differences are much less obvious. However, in all four comparisons, the E78 fuel displayed the larges differences in the peak diameter which is most likely to do with the drastically different composition of the E78 emissions for all tests. The higher POA composition and higher density means the particles will be more spherical. The reduction of the black carbon also means that there will be a reduction in the accumulation mode particles.

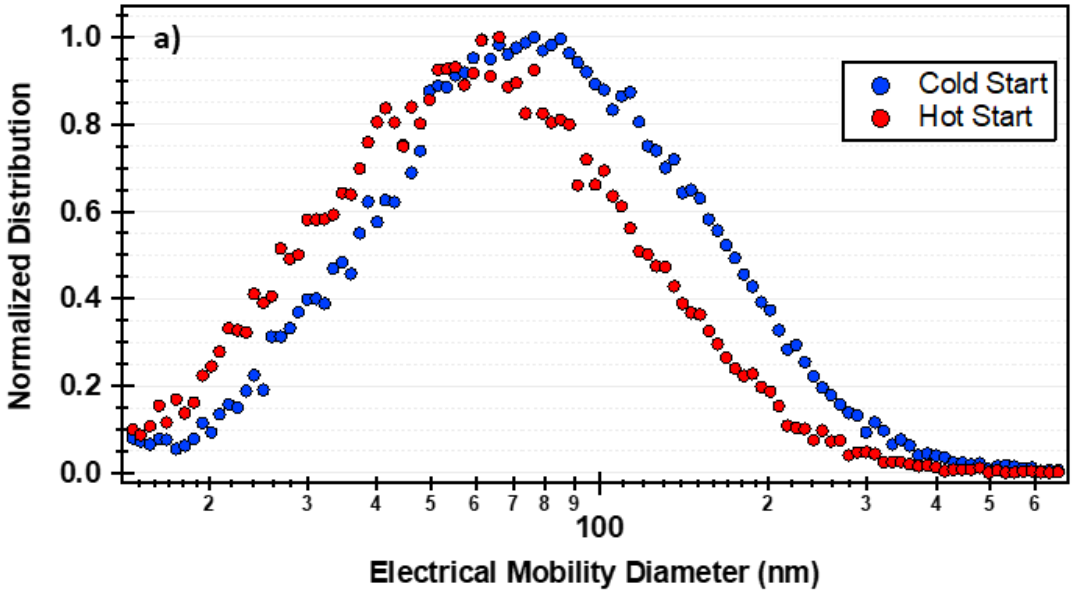
a)
Cold Start
Hot Start
Normalized Distribution
1.0
0.8
0.6
0.4
0.2
0.0
2
3
4
5
6
7
8
9
100
2
3
4
5
6
Electrical Mobility Diameter (nm)

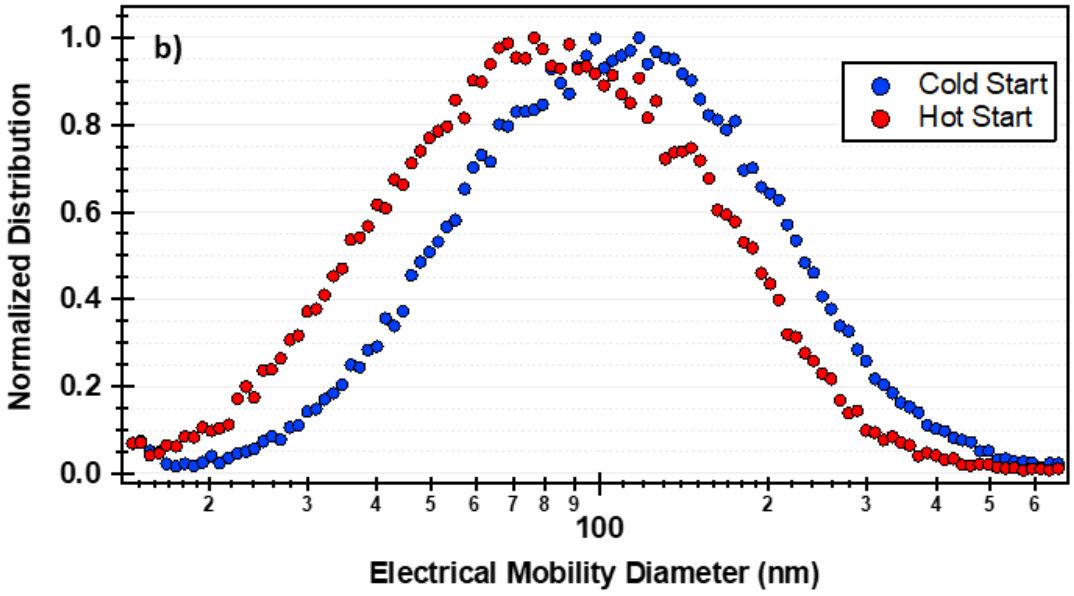
b)
Cold Start
Hot Start
Normalized Distribution
1.0
0.8
0.6
0.4
0.2
0.0
2
3
4
5
6
7
8
9
100
2
3
4
5
6
Electrical Mobility Diameter (nm)

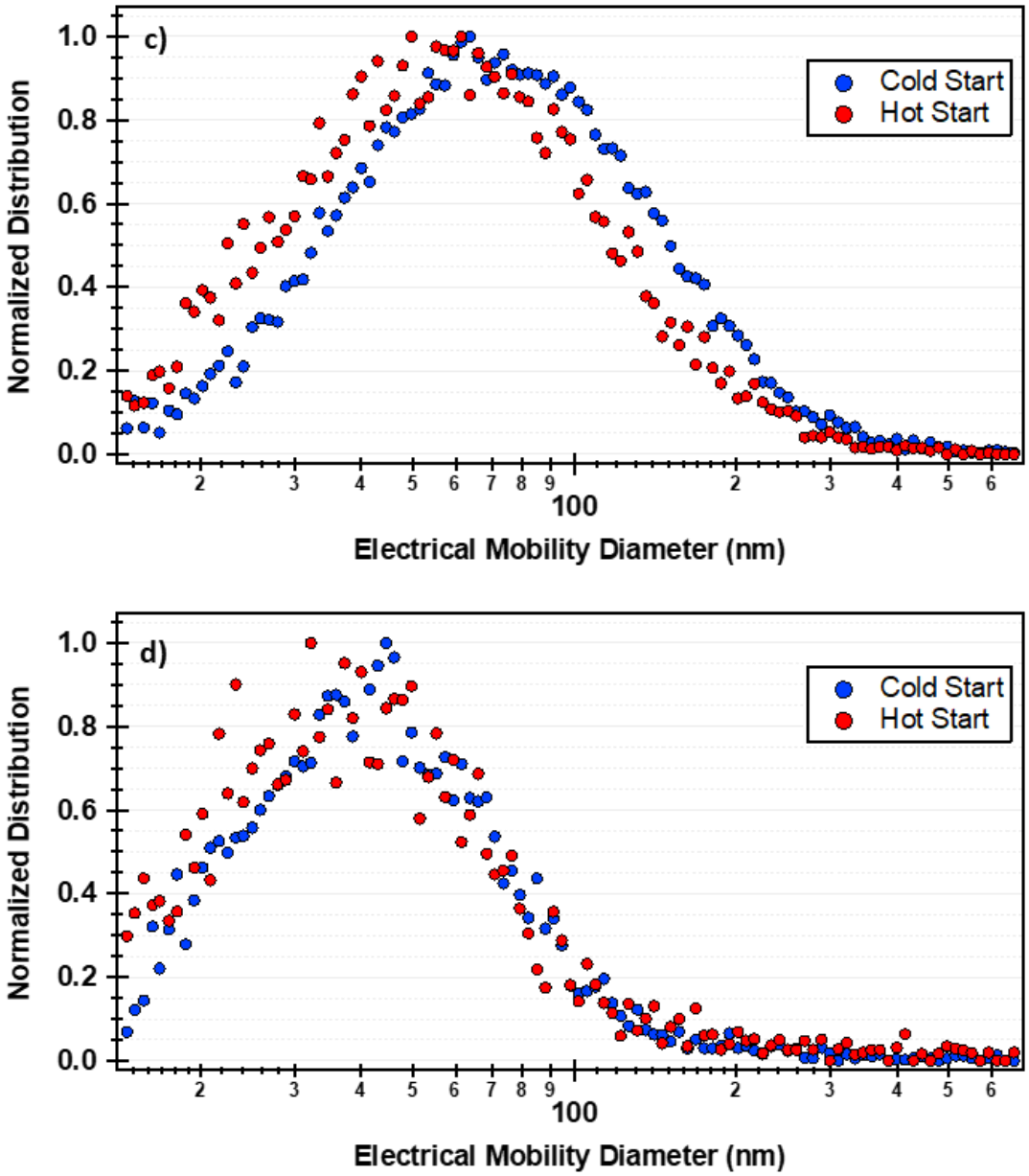

Figure 3-19: Average initial aerosol distributions after dilution for a) E10 b) HA E10 c) E30 and d) E78 fuels for FFV-1 tests comparing the hot-start and cold-start distributions

Figure 3-19 shows the comparison between the hot-start and cold-start distributions for FFV-1 only (the trends were the same for FFV-2). In all cases, the number distribution was much larger for the cold-start compared to the hot-start, and when the peaks were normalized to the largest number measured in a size bin.

For all fuels, the peak shifted towards a smaller diameter mode in the hot-start test compared to the similar cold-start test. Once again this is most likely attributable to the differences in the composition, where on average the hot-start emissions were composed of 7% less of a fractional composition. This difference is most likely what lead to the shift towards the smaller diameter particles. All trends were similar for FFV-2 as well.

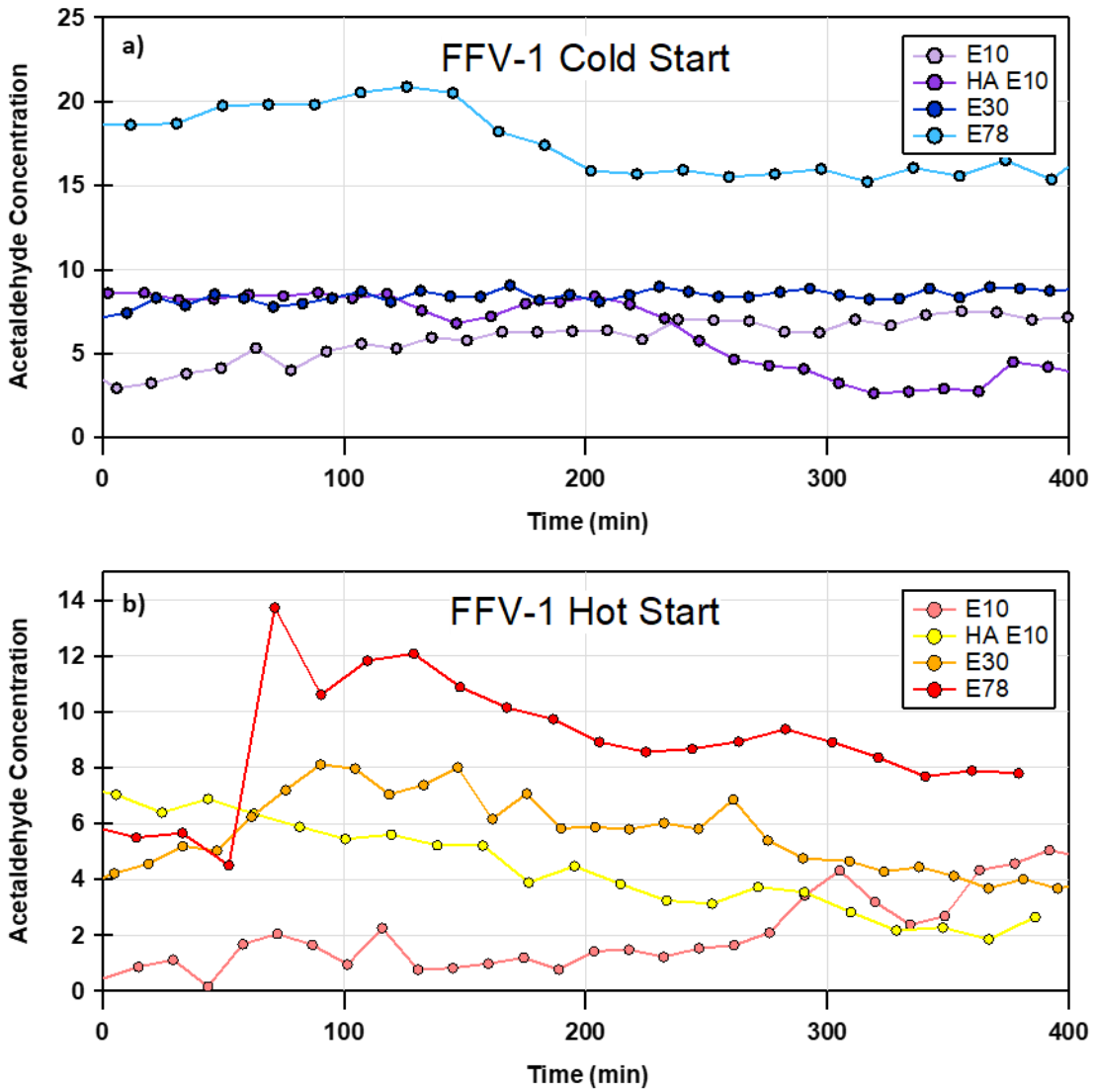

Figure 3-20: Acetaldehyde concentration vs time in the irradiation experiments for FFV-1 for the a) cold-start and b) hot-start tests

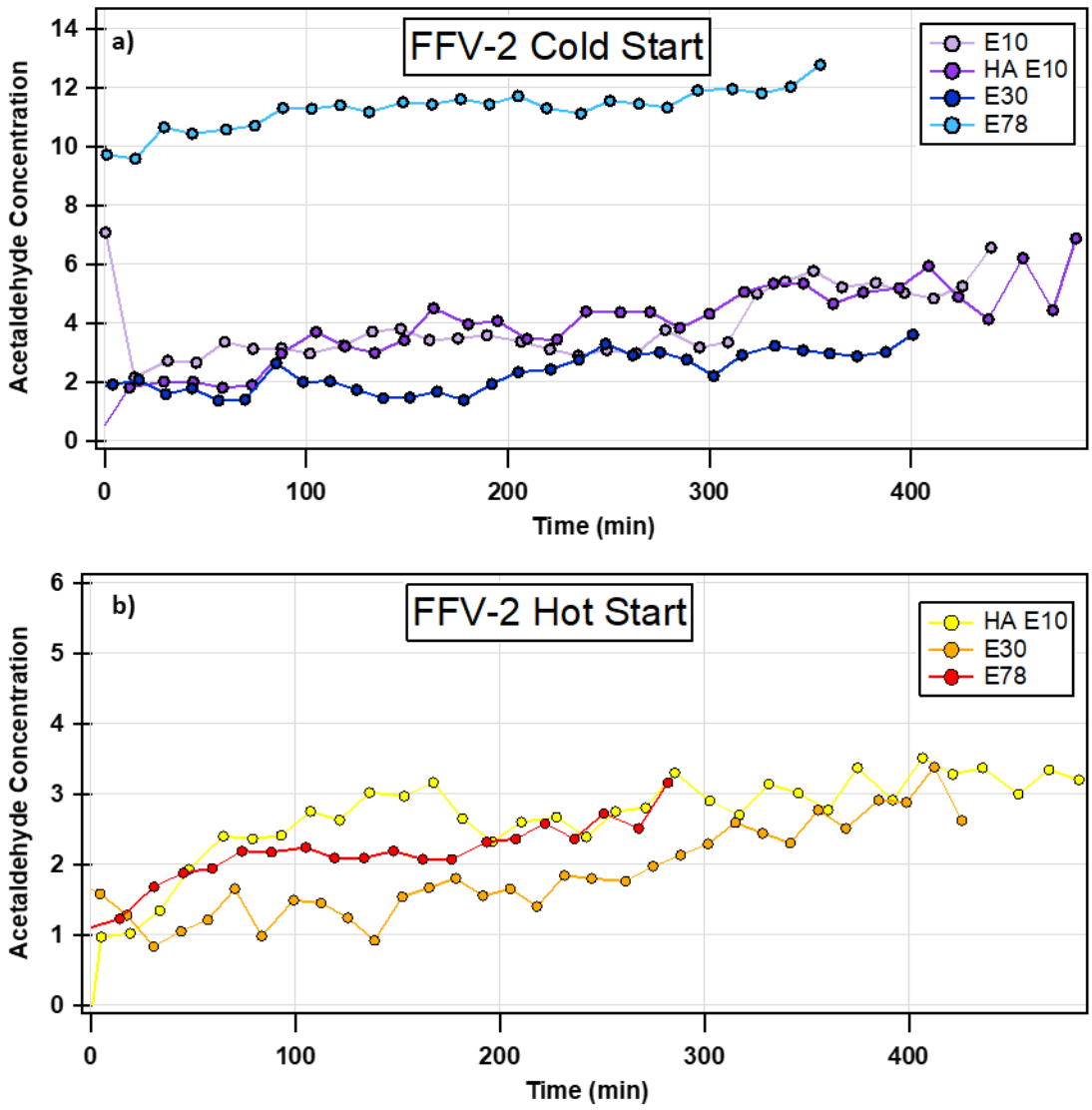

Figure 3-21: Acetaldehyde concentration vs time in the irradiation experiments for FFV-2 for the a) cold-start and b) hot-start tests (no data for the E10 hot-start test)

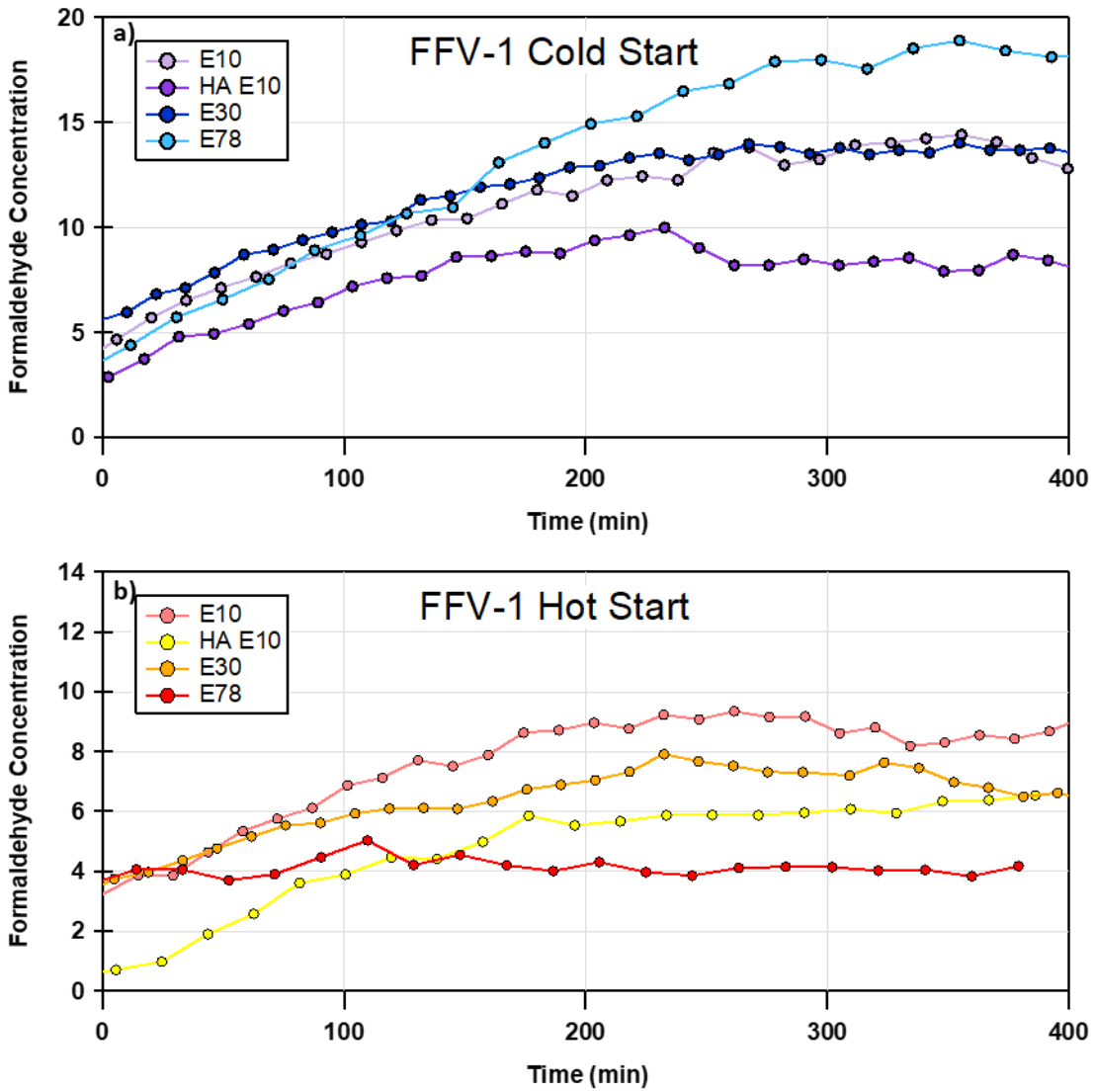

Figure 3-22: Formaldehyde concentration vs time in the irradiation experiments for FFV-1 for the a) cold-start and b) hot-start tests

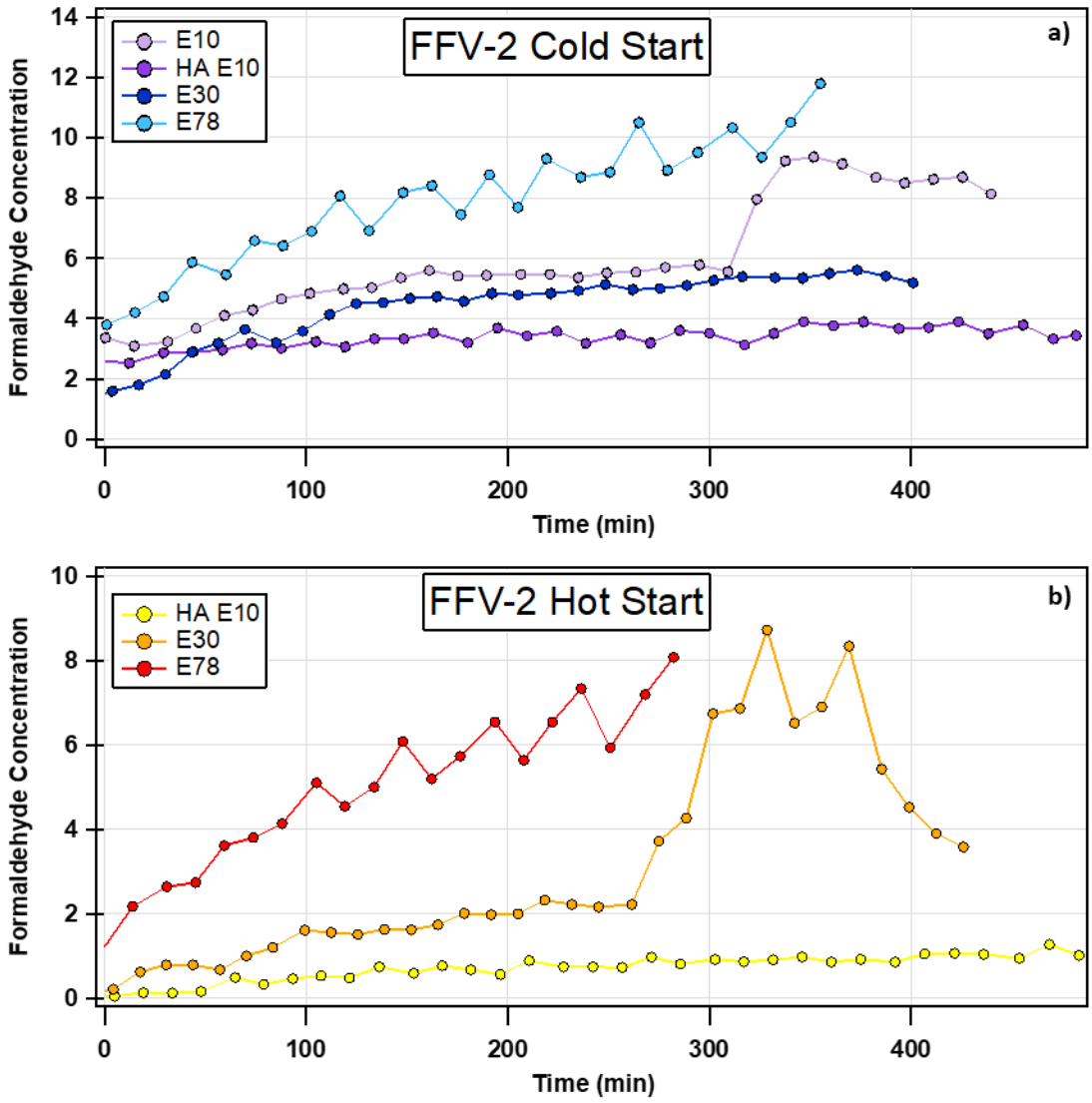

Figure 3-23: Formaldehyde concentration vs time in the irradiation experiments for FFV-2 for the a) cold-start and b) hot-start tests (no data for the E10 hot-start test)

Figure 3-20, Figure 3-21, Figure 3-22, Figure 3-23 show the evolution of different gases for the hot-start and cold-start tests for both FFV-1 (Figure 3-20, Figure 3-22.) and FFV-2 (Figure 3-21, Figure 3-23). The evolution for Acetaldehyde (Figure 3-20, Figure 3-21) and for Formaldehyde (Figure 3-22, Figure 3-23) are shown. These concentrations and trends were measured with the Syft MS and the initial concentrations were calculated using the Suma canister.

In all experiments for FFV-1 cold-start (Figure 3-20) the acetaldehyde concentrations remained relatively constant with a slight decrease for both the hot-start and cold-start experiments. The most notable outlier was for the E78 fuel in the hot-start, where there was a sharp increase at approximately 50 min into the experiment and then a steady decline. In both the hot-start and cold-start experiments, the E78 had the largest concentration of acetaldehyde. Also, it was found that in all test the cold-start tests emitted more acetaldehyde than the hot-start tests. Only the E10 fuel hot-start showed an increasing trend throughout the irradiation experiment. The decreasing trend in concentration is most likely due to the reaction of the acetaldehyde with other VOCs without a similar regeneration. In all cases the levels of acetaldehyde seem to level off at the end of the experiment meaning the gas had reached an equilibrium.

The FFV-2 tests (Figure 3-21) showed the inverse in relation to the typical trend for the acetaldehyde throughout the irradiation experiments. Once again, the E78 had the highest acetaldehyde concentration for the cold-start test however the E78 had a similar concentration to the other two measured fuels in the hot-start test (no Syft data for the E10 fuel hot-start FFV-2). The increasing trend that was observed for all experiments for FFV-

2 indicate an increased formation of acetaldehyde in relation to the photochemical reaction of the acetaldehyde. This difference from FFV-1 may be due to the addition of the surrogate which may have increased the overall radical reactivity, resulting in an overall increasing acetaldehyde concentration.

The FFV-1 formaldehyde concentrations are shown in Figure 3-22. In all tests for FFV-1 the concentration of the formaldehyde increases throughout the irradiation experiments, and ultimately levels off at the end of the experiment. In the cold-start experiment, the E78 ultimately forms the largest mass of formaldehyde, however this trend is not observed for the hot-start experiment. Similar to the acetaldehyde, the cold-start did form a larger mass of formaldehyde for all fuels when compared to the hot-start test.

Similar trends were observed with the FFV-2 tests (Figure 3-23). In both experiments, once again there was an increasing trend of the measured formaldehyde as the gases aged. The E78 once again had the highest mass of formation for the cold and hot-start tests. In the hot-start test, there was a large jump in concentration for the formaldehyde in the hot-start E30 fuel. The concentration of the formaldehyde then quickly decreased down to a similar level to before. The large jump is most likely due to a measurement issue as it does not fit the trends measured for the other tests can most likely be ignored.

The SOA formation of the vehicle exhaust was then related to the NMHC emissions from the vehicle (Figure 3-8). Similar to previous work done (Roth, et al, 2019) it was found that as the NMHC emissions increased, the SOA formation potential from the exhaust did as well. Unlike the previous comparisons to SOA formation, the trend observed when related to NMHC emissions did not seem to be reliant on the driving conditions or fuel composition, only on the mass of gases emitted. From this regulators and modelers may have the ability to predict the SOA formation potential from the vehicles in the future without running long chamber tests. However, NMHC is a broad generalization for the gases, and the composition of the NMHC could be drastically different for each fuel's emissions.

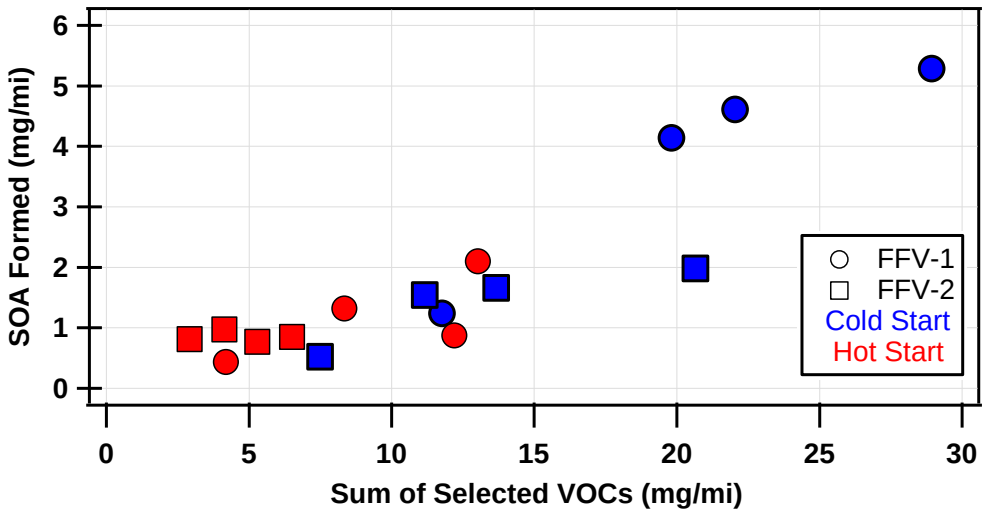

Figure 3-24: SOA formation vs the sum of selected VOCs measured by the summa canister

Figure 3-24 shows the trend when comparing the sum of selected VOCs is very similar to what was observed in the NMHC graph, with one notable outlier. The most

notable difference was the cold-start HA E10 for FFV-2, where a much higher VOC emissions level was measured in the summa canister compared to the bag readings from the bench. The most likely reason for the differences measured in the canister compared to the bag measurements can be attributed to weighting when calculating emission factors. The NMHC measured by the bag has weighting values applied to the concentrations found in the different phases of the test cycle, where the canister has one set flow rate throughout the duration of the test. Because of this, no weighting is possible, and the constant pull to the canister more similarly mimics the injection of the exhaust into the chamber.

As shown in this work, SOA formation potential of vehicles is largely determined by the total mass of NMHC species in the emissions. Ultimately, by increasing the ethanol content in the fuel from E10 to E30 there was an average of a 17% reduction in predicted SOA formation from the measured ROGs for both vehicles. That predicted SOA formation was measured to be reduced by 66% when comparing the E78 fuel emissions to the E10 fuel. The inverse was once again true when comparing the HA E10 to the E10 fuel, where the SOA potential increase on average by 1.7 times for the two vehicles. From these results it can be concluded both the tailpipe and the secondary aerosol can be greatly reduced by substituting the commercial E10 fuel with a higher ethanol fuel blend. More work will need to be completed to determine if the decrease in aerosol formation is due to the increased ethanol content or the decreased aromatic content of the fuel.

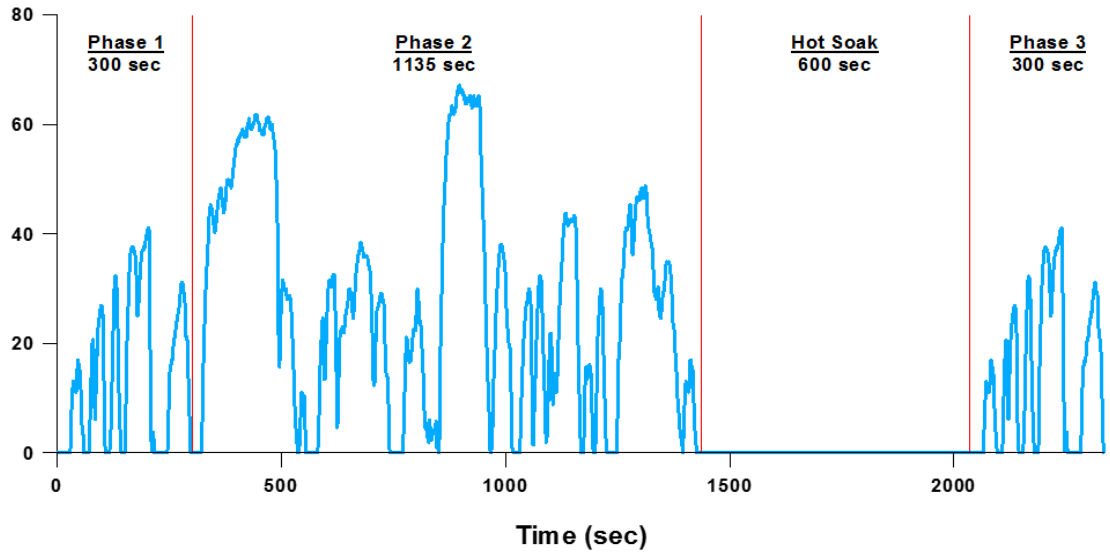

Figure 3-25: LA92 or Unified Driving Cycle (UC) comprised of three phases; cold-start, urban and hot-start phases. The vehicle's engine is turned off for the duration of the hot soak

Figure 3-25 shows the LA92 driving cycle. For the cold-start tests, the vehicle was off for at least 16 hours before the test to ensure that the engine and catalyst were at room temperature at light off. For the hot-start LA92 tests, the vehicle was prepped with phase 1 and phase 2. The vehicle then was subjected to a 10 min hot soak and restarted again at phase 1. During this second phase 1 was when the tailpipe instrumentation and the chamber were connected to the CVS for the collection of the vehicle exhaust.

Chapter 4: Gasoline Aromatic and Oxygen Content Impact on Formation of Secondary Aerosols from a GDI Vehicle

Patrick Roth [1,2], Jiacheng Yang [1,2], Ayla Moretti [1,2], Christos Stamatis [1,2], David R. Cocker III [1,2], Kelley Barsanti[1,2], Thomas D. Durban [1,2], Georgios Karavalakis [1,2], Akua Asa-Awuku [1,2,3]

1. Bourns College of Engineering, Center for Environmental Research & Technology (CE-CERT), University of California, 1084 Columbia Avenue, Riverside, California 92507, United States
2. Department of Chemical and Environmental Engineering, Bourns College of Engineering, University of California, Riverside, California 92521, United States
3. Department of Chemical and Bimolecular Engineering, A. James Clark School of Engineering, University of Maryland, College Park, 4418 Stadium Dr., College Park, MD, 20702

4.1. Abstract:

The focus of this study was to investigate the effects of fuel properties on the tailpipe gaseous and particulate emissions, and the subsequent effect on the secondary aerosol formation of one low mileage GDI vehicle. The vehicle was tested on eight fuels with ethanol contents ranging from 0% to 20% by volume and also with varying aromatic content (20%-30% by volume). The main goal was to compare the trends of the secondary formation of the exhaust of the vehicle operating on similar fuels and evaluate the impacts of changing fuel properties. The attempt of the study was to relate the SOA formation measured in the smog chamber studies to various fuel properties aid in future estimations and regulations when it comes to the emissions from gasoline exhaust.

Tailpipe PM emissions were primarily dependent on the aromatic content of the fuel tested as the higher aromatic fuels emitted 4.27 ± 0.82 mg/mi vs only 2.65 ± 0.82 mg/mi on average for the low aromatic fuels. The tailpipe PM emissions were less dependent on ethanol content, however when the fuels were separated into the different aromatic subgroupings, there was a positive correlation between PM and ethanol where a higher ethanol content resulted in a larger PM emission.

The secondary aerosol formation trends in regards to aromatic content were similar to the tailpipe PM where increased secondary aerosol formed with increasing aromatic content. A majority of the secondary aerosol that formed for all fuels tested consisted of ammonium nitrate, which was found to be dependent on the ammonia concentrations. From this it was determined that ammonia was the limiting reagent in this inorganic salt formation.

The secondary organic aerosol formation was then related to a variety of exhaust measurements and fuel properties to understand which properties drove the SOA formation potential of the exhaust. The correlation between SOA formation and the measured emissions increased with the specificity of measurement where the strongest correlation was with the aromatics measured with the GCxGC (R^2=0.83). When relating the SOA to the fuel properties, once again aromatic content dictated the SOA formation potential of the exhaust. It was because of this, the strongest correlations were found to be the lower volatility properties (i.e. T70, T90, & T100). The lower volatility compounds in the gasoline determined the SOA potential of the vehicle exhaust. If these compounds evaporated or partially combusted, they would readily oxidize and contribute additional SOA mass.

The results displayed in this work concluded that aromatic content dictates tailpipe PM, total secondary, and SOA formation potential of the exhaust. As seen in previous works, ethanol can have varying effects on the tailpipe PM emissions, and in this work it was found that with increasing ethanol, there was increasing PM. However, ethanol content does play a minor role in the overall reduction in the SOA potential of the vehicle. In the future it may be valuable to replace some of the heavier, less volatile compounds in fuel with ethanol to aid in the reduction of secondary potential from the emissions.

4.2. Introduction:

A significant fraction of the total ambient aerosol mass consists of organic aerosol that forms in the atmosphere via photo-oxidation reactions of reactive organic gases (ROGs). Organic aerosol that is formed in this manner are classified as secondary organic aerosol (SOA) (Hallquist et al., 2009). These organic gas phase compounds can come from a host of biogenic and anthropogenic emission sources, and consist of methane, other alkanes, alkenes, and aromatic hydrocarbons. ROG's or volatile organic compounds (VOCs) have varying volatilities based on the compounds' molecular weight and substituents which allows researchers to separate the gases into subcategories based the saturation concentrations of the gases. Similarly as the ROG's react in the atmosphere, their subsequent volatilities will decrease via photo-oxidation reactions.

A considerable source of VOCs emitted in urban areas, can be attributed to mobile sources operating on fossil fuel. Gasoline vehicles (in comparison with diesel vehicles) are more influential emitters of ROG gases; gasoline vehicle emissions can lead to increased SOA formation in high traffic areas. For example, Bahreini et al (2012) showed that gasoline exhaust is the main source of SOA in the Los Angeles basin. Several factors (e.g., oxidants, temperature, RH) can influence atmospheric SOA formation from tailpipe emissions yet there is poor understanding on the effects of ethanol and aromatics contents in gasoline on SOA formation from current technology GDI vehicles.

The impacts of aromatic fuels effects on emissions from port fueled injection (PFI) equipped gasoline vehicles have been the most extensively studied in the past (Hochhauser et al., 1991; Jeffrey and Elliot, 1993; McDonald et al., 1996; Wedekin et al., 1995;

Goodfellow et al., 1996; Hochhauser 2008). Several extensive early studies showed that increasing aromatics will increase the emissions of total hydrocarbons (THC) and carbon monoxide (CO) and have varying effects on nitrogen oxides (NOx) emissions. Less work exploring emissions from aromatic fuel content has been conducted on newer technology GDI vehicles.

The addition of oxygenates (i.e., ethanol) in fuel have complex impacts on particulate and gaseous emissions. It has been observed that when ethanol is added to gasoline, it can displace aromatic compounds with high sooting tendency, resulting in lower black carbon emissions (Pepiot-Desjardins et al., 2008). Maricq et al. (2012) showed small benefits in PM mass and particle number emissions as the ethanol level in gasoline increased from 0 to 20% when they tested a SI-DI turbocharged vehicle with two engine calibrations. Another study showed that ethanol exacerbates the propensity of low-volatility fuel components to form PM (Butler et al., 2015). This phenomenon was further confirmed by a follow up study from the same group of authors where they showed that the presence of ethanol was found to have a reinforcing interaction with PM index resulting in augmented PM emissions. The authors suggested that ethanol's high heat of vaporization hinders evaporation of the higher molecular weight components of the fuels (Sobotowski et al., 2015).

Storey et al. (2010) reported that NOx emissions decreased with increased ethanol concentration, while some increases were seen in THC emissions from a turbocharged DI vehicle over the Federal Test Procedure (FTP) cycle and the more aggressive US06 cycle. Storey et al. (2010) also showed reduced PM mass and particle number emissions with

ethanol blends. Jin et al (2017) tested a GDI vehicle over the FTP cycle on different ethanol blends and found large reductions in particulate emissions, but higher carbonyl emissions. They also reported reduced VOC emissions with medium and high-ethanol concentrations due to the lower proportion of aromatic components in these fuels.

The variation in gaseous emission from varying ethanol content lead to differences in the fractional chemical composition of the THC emissions which directly affects the SOA formation potential. Little work has been done to understand the effect of fuel composition on the SOA formation potential from vehicle exhaust.

Reduced nitrogen species can also be emitted and may readily react to form considerable secondary aerosol mass. Ammonia present in the atmosphere readily reacts with the atmospheric oxidant, OH radical. Additionally, ammonia is highly soluble in water and highly reactive to liquid and gaseous acids in the atmosphere, ammonia will also react with gaseous nitric acid to form an inorganic ammonium nitrate solid. In low RH conditions, nitric acid (HNO_3) forms when NO_2 reacts with a hydroxyl radical. As the ammonia and nitric acid react, it will condense onto existing particulate that is available, increasing the aerosol mass. Ammonium nitrate is extremely dependent on temperature due to its high volatility and the ammonium nitrate dissociation constant can vary over two orders of magnitude over typical atmospheric conditions.

In this study, we investigated the effects of various fuel blends on the tailpipe gaseous and particulate emissions, and the subsequent effect on the secondary aerosol formation of one low mileage GDI vehicle on eight different fuels. The fuel parameters

studied as part of this program included ethanol, aromatics, vapor pressure, T50, and T90 as well as interactions between these parameters that were thought to be important in understanding the impacts of widespread blending of ethanol. As regulations relating to the next generation of gasoline vehicles are being implemented, it is important to continue to evaluate the impacts of changing fuel properties in the context of changing vehicle technologies. The attempt of the study was to relate the SOA formation measured in the smog chamber studies to various fuel properties aid in future estimations and regulations when it comes to the emissions from gasoline exhaust.

4.3. Experimental:

4.3.1 Vehicle & Test Cycle:

The vehicle that was selected for this study was certified to meet the Federal Tier 3 exhaust emission standards (T3B30 LDV) and the LEV-III, SULEV30/PZEV exhaust emission standards. The vehicle selected was a 2017 Ford Fusion with an initial odometer reading of 24,491 miles. The vehicle is equipped with a turbocharged, spray guided gasoline direct injection engine which can reduce emissions by ~6 times when compared to similar wall-guided GDI engines (Short et al, 2017). The engine (HFMXV01.5VZ3) displacement was 1.5 L, and was equipped with a 6-speed automatic transmission.

The vehicle was tested in duplicate over a cold-start, LA92 driving cycle. The LA92 driving cycle (Figure 4-15) was developed by the California Air Resources Board (CARB). The cycle has a similar 3 bag structure to the standard FTP cycle, but is more aggressive, contains faster accelerations, higher speeds, less idle time, and fewer stops per mile. The test cycle consists of three phases, the cold-start phase, intermediate phase, and the hot-start phase. The vehicle's engine was off for 10 min between the intermediate phase and the hot-start phase. The cold-start and hot-start phase are identical in speed profile.

4.3.2 Fuels:

Eight fuels with varying oxygen and aromatic contents were used in this study. Fuel production and blending was made at Gage Product Company and all fuels were tested for fuel properties according to the ASTM D4814 standard. The properties of these fuels are

provided in Table 4-1. A more detailed fuel analysis on the fuel properties based on different hydrocarbon classes and some individual hydrocarbon species can be found in the supplemental section (Table 4-3). The fuels were blended to meet nominal total aromatics targets of 20% and 30% by volume. For the remainder of the work, the fuels that fit into the 20% volume aromatic range will be referred to as 'low aromatic', and the fuels that were blended to contain 30% aromatic content by volume will be referred to as 'high aromatic'.

Ethanol levels ranged from 0 to 20% by volume. One fuel was a Tier 3 E10 certification fuel (Fuel 3). Fuels 5 (E15) and 8 (E20) were splash blended with denudated ethanol with the Tier 3 E10 (Fuel 3). The other five fuels were matched blended to meet high and low aromatics and ethanol levels. The five match blended fuels also had uniform octane, but the splash blended fuels had higher octane than the match blends. Fuels 5 and 6 are similar in that they both have E15 and low aromatic content but differ in blending technique. As a result, the emission effects of a splash blended E15 versus match blended E15 high and low aromatics fuels can be investigated.

Table 4-1: Properties of the Fuels used in study

	Fuel 1	**Fuel 2**	**Fuel 3**	**Fuel 4**	**Fuel 5**	**Fuel 6**	**Fuel 7**	**Fuel 8**
Fuel Classification	LA E0	HA E0	LA E10	HA E10	LA E15	LA E15	HA E15	LA E20
Blending Technique	Match	Match	Cert.	Match	Splash	Match	Match	splash
Octane Rating	88.1	87.2	87.8	87.0	89.8	88.6	87.4	91.5
Total Aromatic (vol %)	21.2	29.4	21.4	29.1	20.3	21.8	29.3	19.1
Ethanol Content (vol %)	0.00	0.00	9.98	9.62	14.72	14.77	14.74	19.61

The fuel testing sequence for the vehicle was selected randomly, and the order of testing for this vehicle was, F1, F6, F3, F4, F8, F7, F2, F5.

4.3.3 Experimental Preparation:

Upon receiving the vehicle, the oil, oil filter, and lubricant oil were replaced. The vehicle was then driven for approximately 500 miles on the road (highway driving). Before each fuel test, the existing fuel was drained from the vehicle, and was flushed then filled to 40% of maximum with the testing fuel. Preconditioning included 2 LA4s, 2 vehicle coast downs, and two additional drain, and 40% fills. The vehicle was then prepped over an LA92 driving cycle, idled for 2 min, then shut off for 12-24 hours to soak before testing. Detail schematic for vehicle prep can be found in the supplemental section (Figure 4-16).

The Mobile Atmospheric Chamber (described in detail below) was cleaned prior to each experiment by injecting O_3 and H_2O_2 with purified with no detectible reactive species (AADCO 737 purifier) and subsequently irradiated with UV light. If particle formation is observed, the chamber is irradiated until formation subsides and the chamber was then emptied and filled until gases and particulate were below the detectible limit, and the chamber was flushed overnight. On the morning of the vehicle testing, the chamber was half-filled with purified air and transported.

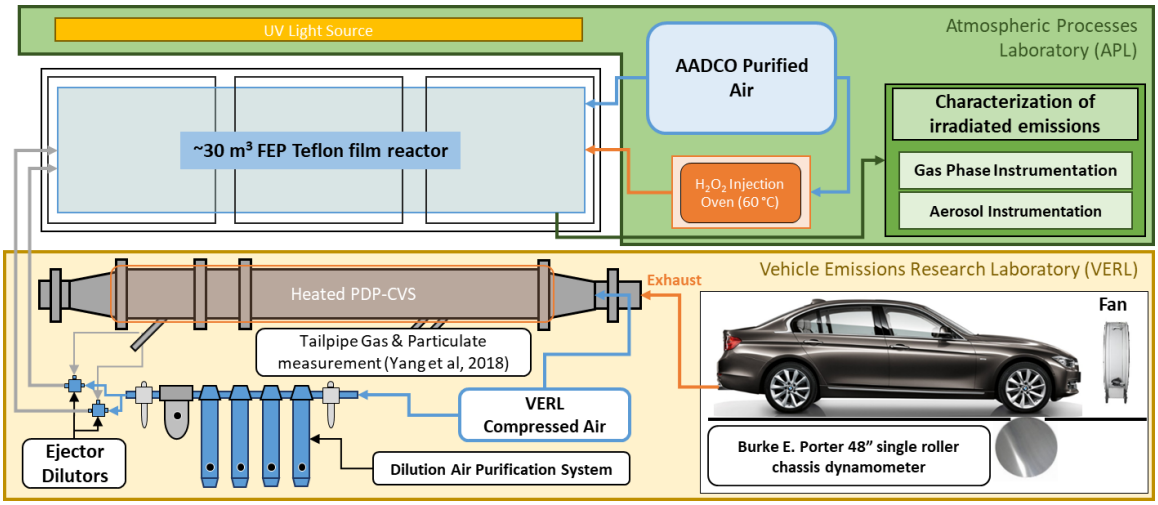

Figure 4-1: Experimental setup (not to scale) for testing. Vehicle was operated in VERL where the criteria pollutants were measured, and MACh was injected with the vehicle emissions. Irradiation testing of the exhaust was then conducted in APL.

4.3.4 Experimental Setup:

All testing was conducted at the Center for Environmental Research and Technology (CE-CERT) in Riverside, CA. The vehicle operation and test cycle were conducted in the Ford Motor Vehicle Emissions Research Laboratory (VERL) on a 48" Burke E. Porter single roller chassis dynamometer. The exhaust is directed into a heated Pierburg positive displacement pump-constant volume sampler (PDP-CVS). Standard bag measurements were analyzed with a Pierburg AMA-400 bench for total hydrocarbon (THC), carbon monoxide (CO), nitrogen oxides (NOx), non-methane hydrocarbons (NMHC), and carbon dioxide (CO_2).

The aged emissions experiments utilized UCR's 30 m^3 Mobile Atmospheric Chamber (MACh). MACh consists of a single, collapsible, 30 m^3 2 mil fluorinated

ethylene propylene Teflon film chamber suspended in a mobile lightweight aluminum frame. The mobile frame allows the chamber to be positioned next to the emissions source in VERL where the emissions were collected from the CVS throughout the LA92 driving cycle (not including hot soak). The exhaust was injected using two ejector dilutors (Air-Vac TD11OH) in series, and the injection lines consist of ~8.5 m of ½" stainless steel tubing. The dilution air used, utilizes a house built clean air system with filters and desiccants to remove the PM (HEPA Filters), water (silica gel columns), NOx (Purafil), CO (Carulite canister), and hydrocarbons (activated charcoal) to minimize background effects.

With the dilute exhaust, MACh was then transported to CE-CERT's Atmospheric Processes Laboratory (APL). The remaining volume of the chamber was then filled with the AADCO purified air and the diluted tailpipe exhaust was evaluated for at least 30 min. 1.0 ppm of H_2O_2 was injected to help initiate photochemistry. The dilute exhaust was then irradiated for 7-10 hours utilizing the 600 15 W, 18", T8 black light fluorescent bulbs which acted as the controlled UV source. Before, and throughout the irradiation experiments, the exhaust was monitored in real time with a host of aerosol and gaseous instruments.

4.3.5 Instrumentation:

Gas phase instrumentation included a Thermo Environmental Instruments Inc. (MA) Model 42 chemiluminescent NOx analyzer (NO, NO_2, NOx). A Dasibi Environmental (CA) nondispersive ultraviolet ozone analyzer will monitor the chamber ozone concentration. A Dasibi Model 48C was used to measure CO concentrations with

IR analysis. A LI-COR ® LI-840A CO_2/H_2O analyzer was used to monitor the CO_2 and relative humidity during the irradiation experiments. VOC concentrations were measured with the Pierburg AMA-400 bench. Dilution ratios were calculated by monitoring the CO_2 concentrations of the exhaust, dilution air, and initial experimental concentration.

The physical and chemical properties of the aerosol were measured throughout the experiment. Particle phase instrumentation included a commercial scanning mobility particle sizer (SMPS) consisting of a TSI 3080 electrostatic classifier, TSI 3081 long column differential mobility analyzer (DMA) column and a TSI ultrafine condensation particle counter (CPC) 3776. The 3776 CPC was operated in 'low flow mode', with a sample flow of 0.3 LPM and the sheath flow for the classifier was set to 3.0 LPM. The SMPS measured electrical mobility diameters from 14.6 nm to 661.2 nm. The mass of BC was measured using an AVL micro soot sensor (MSS) with a high power laser diode operating at 802 nm with a photoacoustic sensor (Petzold, A., Niessner, R, 1996). Non-refractory aerosol chemical composition data was measured with an Aerodyne high-resolution, time-of-flight, aerosol mass spectrometer (HR-ToF-AMS) (Aiken, et al, 2008). HR-ToF-AMS was operated in both V and W mode, and the data processing was completed using the ToF-AMS Analysis Toolkit 1.57 and ToF-AMS HR analysis 1.16. The Unit Mass Resolution (UMR) and HR Frag table for CO_2 were altered from the assumed concentration of 370 ppm to the measured CO_2 concentration using a LI-COR ® LI-840A CO_2/H_2O analyzer. The organic, ammonium, nitrate, and sulfate ratios were calculated and applied to the remaining mass calculated by the SMPS and APM (after subtracting out the

BC contribution). Wall loss corrected black carbon mass was assumed to be constant throughout irradiation experiment.

A Kanomax aerosol particle mass analyzer system (APM) measured particle effective density. The APM is paired with a house built SMPS. Particles are initially selected by mass and later pass through a scanning DMA column where an effective density based on the electrical mobility diameter is calculated. The APM has the ability to select aerosol with a mass from 0.30 to 50.0 fg which is equivalent to a particle of unit density with a diameter of 50 to 400 nm. A more detailed summary of the APM-SMPS system is described in Malloy, et al, 2009.

SMPS data was used for the calculation of the volume of aerosol throughout the irradiation experiment. All SMPS data was corrected for particle wall losses, using first order wall loss kinetics described in detail by Cocker et al. 2001. Vapor wall losses have been assumed and measured to be insignificant in past chamber experiments (Vu, et al., 2018). From the volume, mass was calculated by using effective density measurements. Final mass calculations were determined from the effective density and volume calculated at the end of the irradiation experiments.

Speciated emissions measurements were carried out for BTEX species (benzene, 1,3-butadiene, toluene, ethylbenzene, xylenes) and carbonyl compounds over the entire LA92 driving cycle. BTEX species were collected using a 6 L specially-prepared SUMMA passivated canister, which was connected to the CVS system. Analysis of the hydrocarbon species was conducted using a Gas Chromatography/Mass Spectrometry/Flame Ionization

Detector (GC/MS/FID). Samples for carbonyl analysis were collected onto 2, 4-DNPH coated silica cartridges (Waters Corp. Milford, MA). A critical flow orifice controlled the flow to 1.0 L/min through the cartridge. Analysis of DNPH cartridges for 14 C_1-C_8 carbonyl compounds was performed at the Organic Analytical Laboratory of the Desert Research Institute and is described elsewhere (Khlystov and Samburova, 2016).

For each irradiation experiment, gas samples were collected from both the CVS and MACh for GCxGC analysis. When sampling from the CVS, the apparatus was connected via a Teflon sample line (~30 cm long x 0.64 cm od) directly to the CVS. Samples were collected at 100 mL/min for the duration of each driving cycle (excluding the hot soak). Samples collecting diluted exhaust from MACh collected for 30 min at 100 mL/min prior to irradiation. For all collection, a Teflon filter was placed upstream of the sorbent tube to prevent particles from reaching the sorbent tube.

Three background samples that mimicked a driving cycle were taken from the CVS; three blank sorbent tubes were also retained. One breakthrough test was conducted per fuel to determine which compounds were incompletely trapped on a single sorbent tube. Three background samples were also collected from the mobile chamber. More information on the operating conditions of the GCxGC can be found in the supplemental section.

4.4. Results and Discussion:

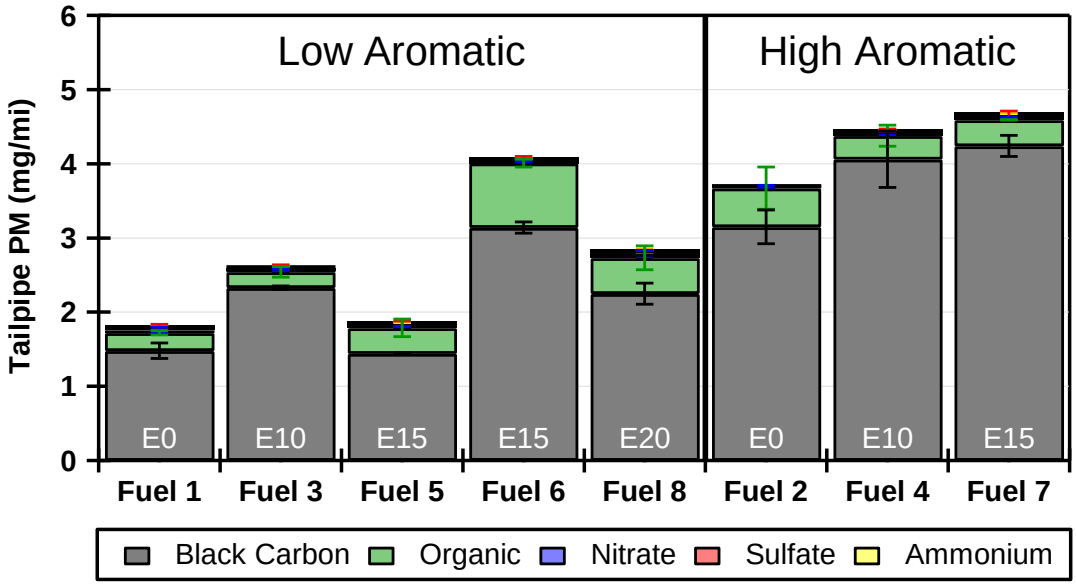

Figure 4-2: Composition of tailpipe aerosol diluted in MACh, before irradiation. Fuels grouped by low aromatic (left) and high aromatic (right) and subsequently ordered from low ethanol to high ethanol within the aromatic groupings

Figure 4-2 shows the mass and composition of the tailpipe emissions. Consistent with previous chassis dynamometer studies conducted on GDI vehicles, the initial PM emitted from the GDI vehicle was primarily composed of black carbon (from ~75% to 92%) (Karavalakis et al., 2014; Karavalakis et al., 2015a, 2015b) for all fuels. The high aromatic fuel blends consistently displayed increased tailpipe PM emissions compared to the equivalent ethanol, low aromatic fuels. On average, the high aromatic fuels emitted 4.27 ± 0.82 mg/mi vs only 2.65 ± 0.82 mg/mi on average for the low aromatic fuels. One unique fuel that deviated furthest from this trend was fuel 6, which had the highest tailpipe

emissions of all the low aromatic fuels with an average tailpipe PM emission of 4.07 mg/mi.

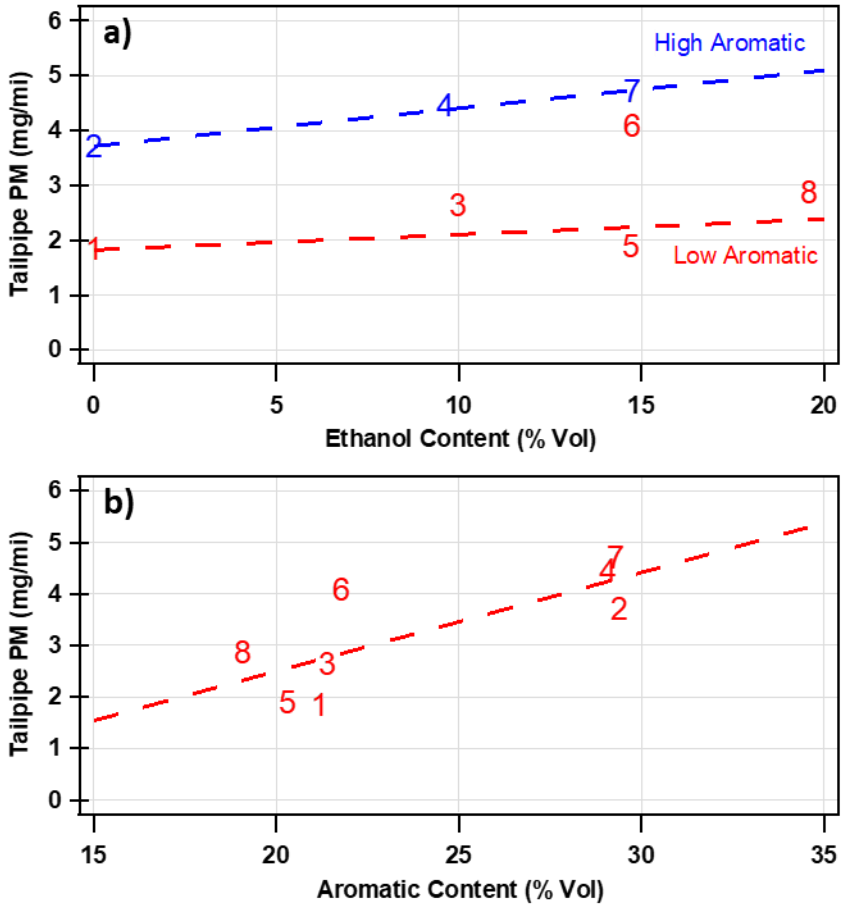

Figure 4-3: Tailpipe PM emissions vs the a) Ethanol Content (% volume) where fuels separated by high aromatic (blue) and low aromatic (red), b) Aromatic Content (% volume) of the eight fuels. Fuels are signified by number on the plot.

When comparing similar aromatic blended fuels, the tailpipe aerosol mass emissions also increased with ethanol content (i.e., F1 versus F3 and F6, F2 versus F4 and F7) (Figure 4-3). The three high aromatic fuels displayed primary masses of 3.69 mg/mi

(F2, E0 HA), 4.44 mg/mi (F4, E10 HA), and 4.69 mg/mi (F7, E15 HA) (Figure 4-2). The low aromatic fuels did not follow this trend as closely, with emitted masses of 1.84 mg/mi, 2.63 mg/mi (F1, E0 LA), 1.87 mg/mi (F3, E10 LA), 4.07 mg/mi (F5, splash blended E15 LA), and 2.85 mg/mi (F8, splash blended E20 LA) (Figure 4-2).

The fractional composition of the tailpipe aerosol also changed with fuel composition. The black carbon content of the primary PM averaged 80.4% ± 4.3% for the low aromatic fuels, and 89.2% ± 2.6% for the high aromatic fuels. There was no statistically significant trend with the ethanol content of the fuel and the fractional contribution of black carbon to the primary aerosol for this vehicle. Inversely, as aromatic content increased, the fractional composition of tailpipe PM that consisted of POA decreased (15.6% ± 4.7 % for low aromatic, and 9.6% ± 3.2 % for high aromatic fuels). The trend of POA contribution to ethanol content was once again not statistically significant.

As the ethanol content increased, the fractional contribution to tailpipe particle contribution of black carbon and POA displayed varying trends. The BC content was 82.9%, 90.0%, 81.5%, 78.9%, and POA content was 13.6%, 7.6%, 16.0%, and 16.8% for the E0, E10, E15, and E20 fuels, respectively. The highest BC contribution was emitted when the vehicle was operated on the E10 fuels for both the high and low aromatic fuel blends.

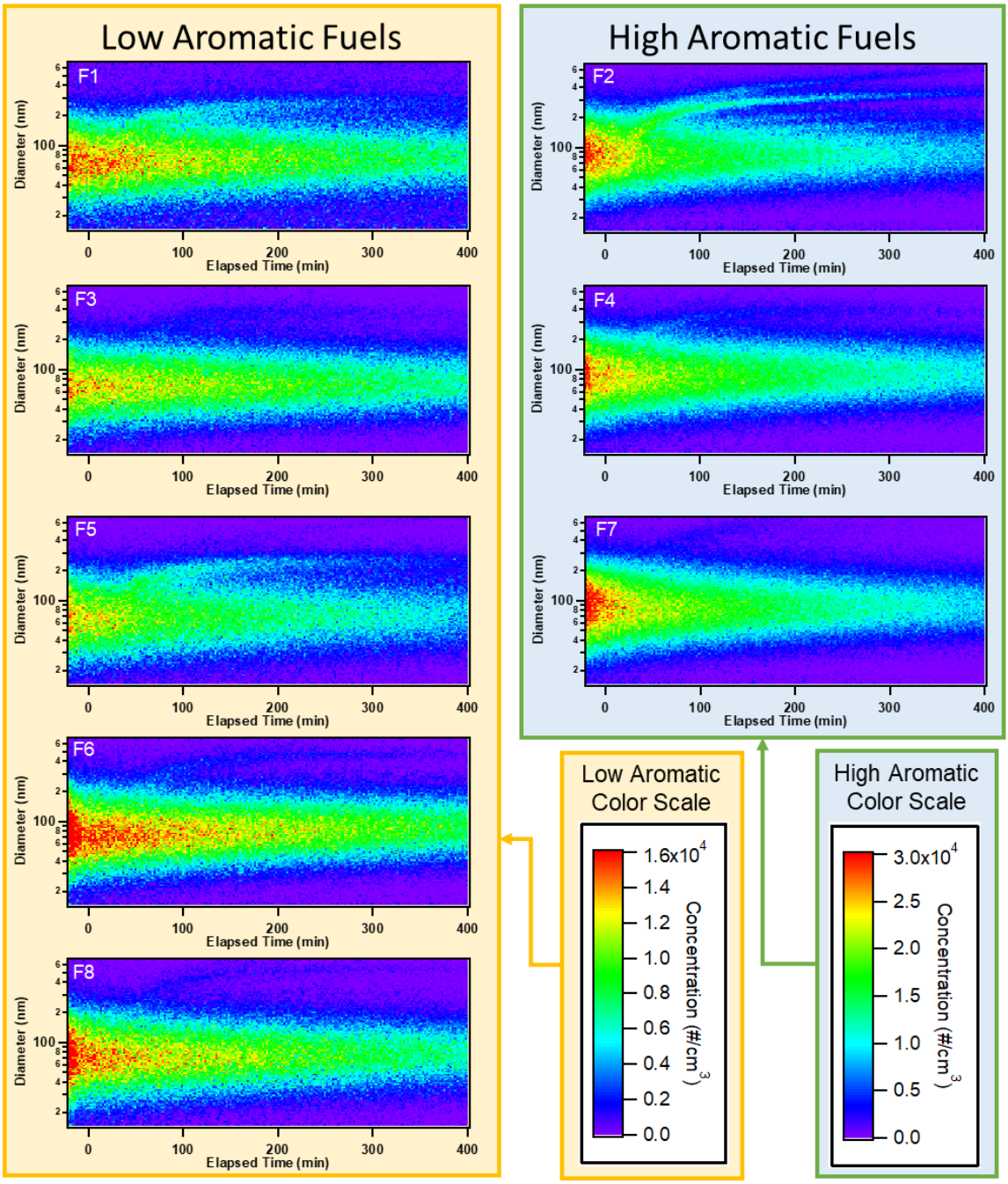

Figure 4-4: Size distribution image plot measured by the SMPS throughout the irradiation experiments. At elapsed time=0 the lights were turned on. Low aromatic fuels (left) and higher aromatic fuels (right) are on different color scales

The average density of the particles emitted were 0.548 g cm^{-3} ± 0.010 g cm^{-3} and there were no statistically significant trends in relation to aromatic or ethanol content of the fuel. The density measured was consistent with previous studies looking at GDI vehicle emissions (Roth, et al, 2018). With a density less than 1.0, the particles had properties coinciding with a fractal BC particle, which confirms the fractional composition measured from the tailpipe.

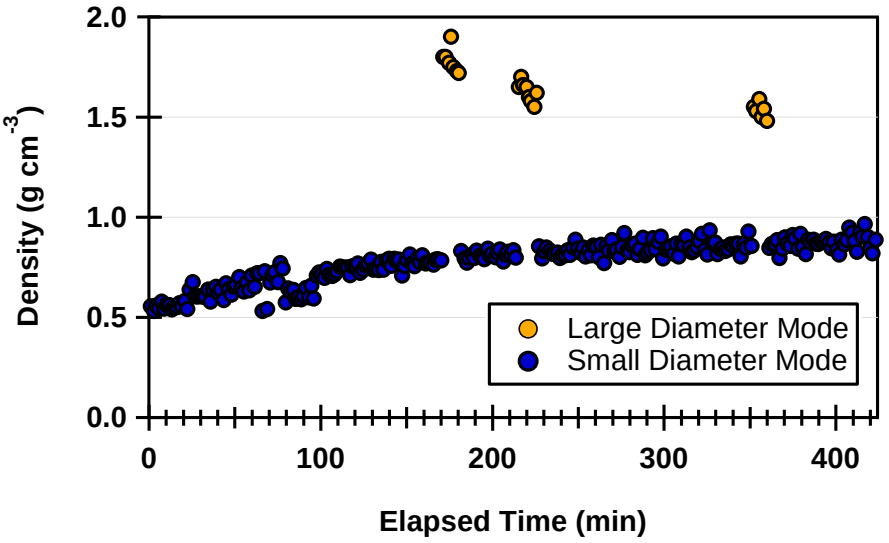

Figure 4-5: Representative example of the change of density throughout an irradiation experiment. The small diameter (blue circles, 50-100 nm), and the large diameter (orange circles, >150 nm) modes had different densities

There was also a similar evolution of the particles throughout the irradiation experiments (Figure 4-4). In all cases, the broad, unimodal peak, did not shift throughout the experiments. The majority of the mass formation that occurred, was due to a small subset of particles that grew, and separated from the initial distribution. The density of the

smaller diameter mode of particles maintained a fractal morphology, however did increase in density to an average of 0.718 g cm^{-3} ± 0.056 g cm^{-3} (Figure 4-5). The larger diameter mode particles were measured to have an average density of ~1.78 g cm^{-3} after separating from the initial peak. This density is consistent with the density of ammonium nitrate (1.77 g cm^{-3}). As the larger diameter mode particles continued to grow, the density decreased slightly down do an average of ~1.53 g cm^{-3} which is consistent with a combination of ammonium nitrate and SOA (~1.4 g cm^{-3}). An example of a representative density (F3) distribution throughout the irradiation experiment is shown in Figure 4-5.

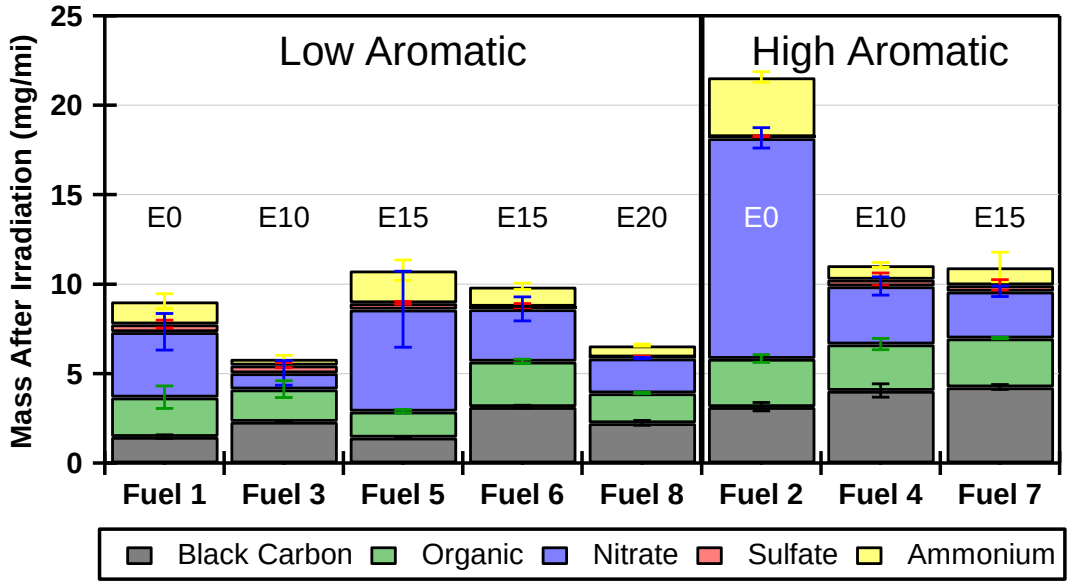

Figure 4-6: Composition of aerosol after 400-500 min of photo-oxidation. Fuels grouped by low aromatic (left) and high aromatic (right) and subsequently ordered from low ethanol to high ethanol within the aromatic groupings

Figure 4-6 shows the overall aerosol composition after 400 to 500 minutes of irradiation in the atmospheric chamber. Similar to the tailpipe emissions, the highest masses of aerosol at the end of irradiation were all attributed to the high aromatic fuels. The largest mass contribution to the total aerosol after irradiation for the majority of fuels was inorganic ammonium nitrate (F3 is the most notable exception). The secondary aerosol mass increased by 2.2 to 5.9 times when compared to the tailpipe masses. This increase is low compared to previous work done on vehicle emissions (Roth, et al 2018, Gramsch et al 2018). The largest total aerosol mass formation from the vehicle emissions was from fuel F2 (E0 with high aromatics), which formed close to two times as much

secondary aerosol compared to other fuels. There was no statistically significant trend in relationship to ethanol content and total aerosol formation.

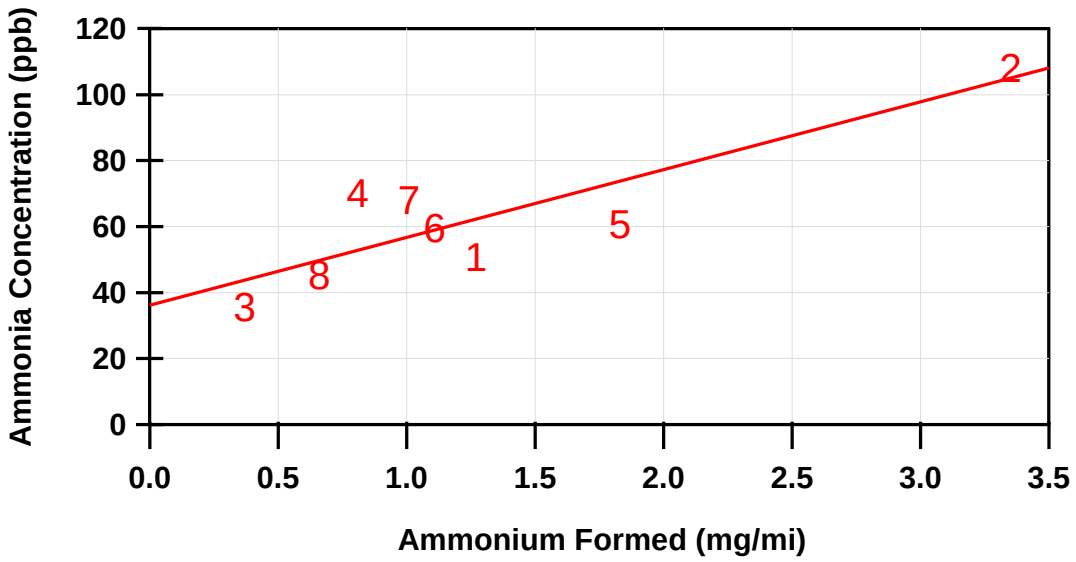

Figure 4-7: Comparison of initial ammonia concentration in the chamber experiments, to total ammonium particulate mass formed. Numbers are Fuels 1-8

When comparing the initial concentration of ammonia in the experiments to the mass of ammonium formed, there was a correlation with an R^2 value of 0.75. This is compared to the R^2 value of the initial concentration of NOx to mass of nitrate formed, which had an R^2 of < 0.01. From these relationships, it was determined that the magnitude of formation of ammonium nitrate was driven by the initial ammonia concentrations rather than the initial NOx concentrations inside the environmental chamber. From this result, it can be concluded that there was excess NOx present for these reactions, and the limiting reagent in the formation of ammonium nitrate was ammonia.

Ammonia is formed in the TWC after catalyst light-off, though a mechanism that involves NO and H_2. Molecular hydrogen is produced from water-gas shift reaction between CO and water or via stream reforming from hydrocarbons. Due to the water shift reaction, ammonia emissions typically increase with increased tailpipe CO concentrations (Suarez-Bertoa, et al, 2014). In this work, the CO concentrations increased by 26.6% (1.94 ppm vs 2.45 ppm) when comparing the low aromatic to the high aromatic, while the tailpipe ammonia increased by 35.5%. The increasing ethanol content had a weaker, inverse effect on both the CO and ammonia concentrations emitted. The CO concentrations measured were 2.95, 2.09, 1.84, and 1.45 ppm for the E0, E10 E15 and E20 fuels respectively and average NH_3 concentrations were 79.3, 52.9, 62.6, 45.2 ppb respectively.

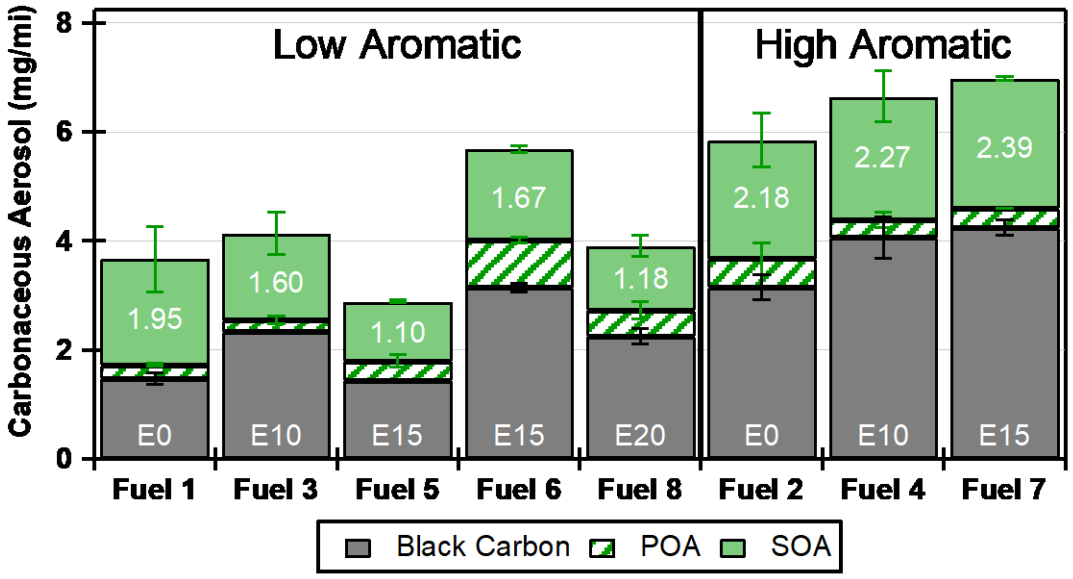

Figure 4-8: Composition of the carbonaceous aerosol after ~500 min of irradiation; Fuels grouped by low aromatic (left) and high aromatic (right) and subsequently ordered from low ethanol to high ethanol within the aromatic groupings

Figure 4-8 shows the composition of the carbonaceous aerosol at the end of the irradiation experiments. In all experiments, there was a larger mass of SOA (green) formed compared to POA (green pattern) mass (from 2.5 to 8.2 times increase) as seen in Figure 4-8. Similar to tailpipe measurements, the high aromatic fuel blends accounted for the largest total carbonaceous aerosol masses when compared to the similar low aromatic fuels.

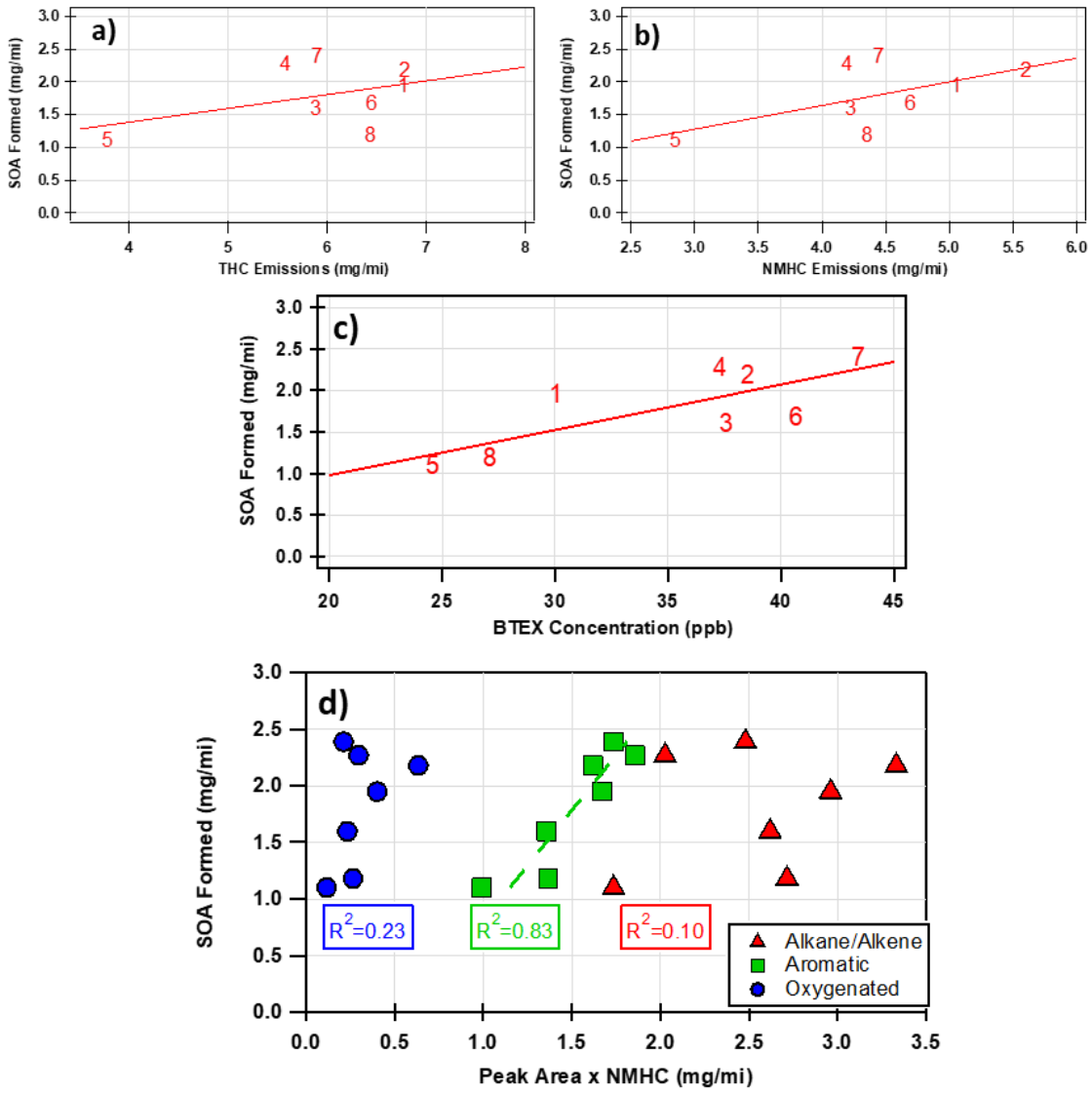

Figure 4-9: Correlation of the average gaseous emissions for the vehicle on the eight different fuels, a) THC emissions, b) NMHC emissions, c) sum of BTEX chamber concentrations measured by canister d) sum of GCxGC gaseous measurements

Comparisons of the volatile organic gaseous emissions to SOA formation displayed a positive correlation to the SOA formation (Figure 4-9 a-d) as expected. The comparisons of the emitted THC and NMHC emissions were statistically significant, however had poor

linear correlations (0.18, and 0.35) (Figure 4-9 a, b). When increased specificity of the gases, the calculated chamber concentration for the BTEX gases collected with a sumac canister and detected with GC-MS, correlated much more strongly to SOA formation (0.58). The variation that is seen in this formation is most likely due to the varying NOx concentrations in the chamber experiments due to the varying amount of NOx emitted from the vehicle on the different fuels, the additional unspeciated gaseous compounds that were emitted from the tailpipe.

To look deeper at the relationship of the SOA formation of the gases, the measurements from the GCxGC were utilized. In these experiments, on average 178 compounds were identified in each test from the vehicle emissions. This additional speciation allowed for a more comprehensive analysis of the potential aerosol forming potential from the gaseous compounds emitted from the tailpipe. For simplicity, in calculation and in the presentation of the data, the compounds were split into three main groups, oxygenated, alkanes/alkenes, and aromatic compounds. It should be noted, the values shown in Figure 4-9 display the average peak area % of the total signal, multiplied by the NMHC emissions measured on the tailpipe. With this an approximate mass can be assumed, however the response factor will not be consistent test to test, thus no quantitative concentrations can be reported.

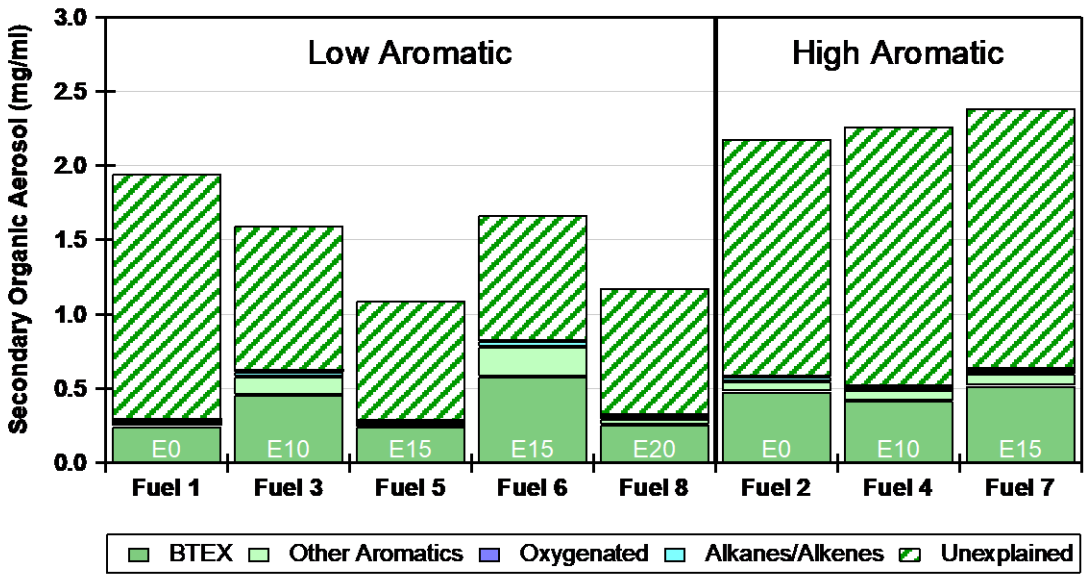

Figure 4-10: Predicted SOA formation from measured gases using maximum yields in low NOx conditions

With the speciated gas phase concentrations measured, and an assumed maximum yield in a low NOx environment as quantified by Derwent et al 2010, on average only 30% ± 10% of the aerosol could be accounted for with the two measurement techniques used for this work. From these test, the BTEX compounds (benzene, toluene, ethyl-benzene, and the xylenes) accounted for 81% ± 5% of the predicted SOA, with the total aromatic contribution consisting of 94% ± 1% of the total predicted SOA. The predicted SOA to experimental SOA ratios reported in this work are in line with Gordon et al 2014, and Platt et al 2013, however are lower than work done by Du et al 2017, Nordin et al 2013, and Roth et al 2018.

In addition to the emission relationships with SOA, the relationships between fuel composition and SOA formation were also explored. It is well established that intermediate

volatility organic compounds (IVOCs) may play a key role in SOA formation (Zhao et al., 2016). Therefore, the correlation between the distillation temperatures of T50, T70, T90, and the temperature of complete volatilization (Figure 4-11a-d) to SOA formation were investigated.

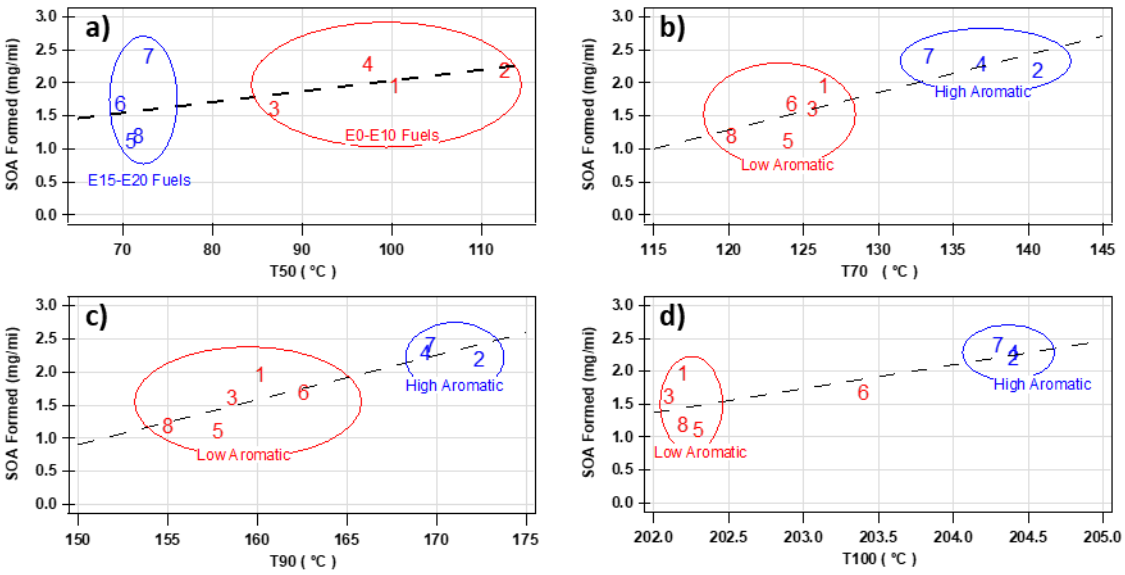

Figure 4-11: Fuel distillation comparisons to SOA formation, x-axis is the temperature (°C) necessary to distill a) 50% b) 70% c) 90% and d) 100% of the fuel

In all cases, as the distillation temperature increased, SOA formation also increased. The correlation of T50, T70, T90, and T100 (Figure 4-11 a-d) displayed R^2 values of 0.31, 0.70, 0.79, and 0.65 respectively. The boiling point for ethanol is 78.4 °C, meaning the impact of ethanol content is most apparent in the T50, where all high ethanol fuel blends are clumped on the left side of the graph and high ethanol blends on the right (Figure 4-11 a). As the distillation fraction increases (T70 and T90) the fuels begin to separate by aromatic content (Figure 4-11 b,c) and display the strongest trend to SOA formation. In

regards to the T70, there is still a distinct ethanol trend left to right in both the low and high clusters indicating ethanol still has a role in the properties at 70 % distillation indicating that both ethanol and aromatic content play a role in the concentration of the lower volatility components in fuel. The role of ethanol is near zero for the T90 and T100 distillations. In the temperature of complete volatilization (Figure 4-11 d), Fuel 6 appears to stand out as an outlier in regards to heavier less volatile compounds. This fuel neither fits with the low or high aromatic cluster in regards to the complete volatilization which may explain why F6 stood out in terms of tailpipe emissions. All compounds that are measured at these distillation temperatures would have too low of a volatility to be measured by previously mentioned gas phase instruments, and could account for the unexplained SOA mass.

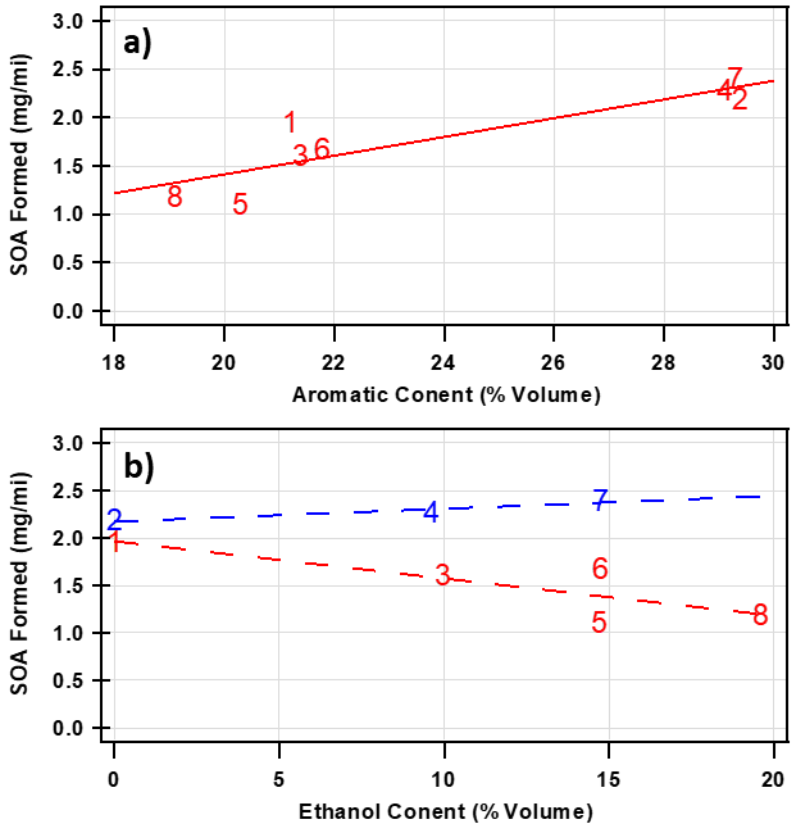

Figure 4-12: SOA formation with respect to fuel a) Aromatic content (% volume), b) Ethanol content (% volume) where fuels are separated by low aromatic (red) and high aromatic (blue). Fuels are signified by number on the plot.

The trend of SOA mass formed most closely correlates with the fuel aromatic content as shown in Figure 4-12a (R^2=0.79). The relationship between SOA formation to aromatic content in the fuel is not expected to be linear, however, the trend of Figure 4-12a clearly shows increasing SOA formation with higher aromatic content fuels. The largest deviation to this trend is due to F1 (E0 with low aromatics), the point at 1.95 mg/mile in the low aromatic cluster. There was a less statistically significant, negative correlation, between SOA formation when compared to ethanol content (R^2=0.26) when comparing all

fuels. In Figure 4-12b the ethanol content of the fuel is plotted against the SOA formation however the low aromatic (red) is separated from the high aromatic (blue). It can be seen that there is no significant trend with the high aromatic fuels, however, in the low aromatic fuels, there is a decrease in the SOA formation when the ethanol content of the fuel increases. Similar results have been observed when exploring the SOA formation from higher ethanol fuel blends (Timonen et al 2017, Roth et al, 2018). The results in Figure 4-12 display that aromatic content drives SOA formation. However, when aromatic content is constant, the addition of ethanol has the potential to decrease the SOA formation which is inverse to what was observed in the tailpipe emissions.

4.5. Implications:

Fuel composition altered the concentration and composition of both the gaseous and particulate exhaust from this current technology GDI vehicle. Aromatic content of the fuel had a positive correlation with the tailpipe aerosol emitted. The high aromatic fuels emitted an average of 4.27 ± 0.82 mg/mi vs only 2.65 ± 0.82 mg/mi for the low aromatic fuels. Similarly, within the aromatic subgroupings, it was observed that as the ethanol content increased, the tailpipe mass increased as well.

Similar to previous studies (Storey et al, 2014) it was found that the high aromatic fuels not only formed a larger mass of black carbon, but black carbon also made up a larger fractional contribution to the total mass emitted for the high aromatic fuels (80.4% ± 4.3% vs 89.2% ± 2.6%), and had the inverse effect on POA. There was no significant trend of black carbon mass emitted or fractional contribution with ethanol content of the fuels. Overall, the distribution of the tailpipe exhaust were all quite similar with slight differences in the peak diameter for the diluted emissions in relation to aromatic content as well.

When aged, there was a 2.2 to 5.9 times increase in the total aerosol mass. When compared to previous GDI experiments conducted using MACh, the increases in SOA mass was relatively small, which can be directly attributed to the low VOC emissions. The evolution of the aerosol distribution throughout the irradiation experiments were consistent, and in all experiments the final aerosol distribution was bimodal with a more dense large diameter mode of particles, and a less dense small diameter mode of particles. With the exception of Fuel 3, a large contribution of the total aerosol mass after irradiation was due to ammonium nitrate formation. The total ammonium nitrate formation strongly

correlated with tailpipe ammonia emissions and had no correlation to the NOx emissions from the vehicle, indicating ammonia was the limiting reagent in the inorganic salt formation. In the future to reduce the secondary aerosol formation potential from vehicle exhaust, it may be important to measure, and regulate the reduced nitrogen species.

The relationship of the SOA to the THC and NMHC gaseous emissions measured at the tailpipe displayed a positive correlation with the SOA formation however displayed variability. When comparing the BTEX gaseous data to the SOA formed, a more consistent trend was observed. Similarly, the GCxGC was used to more accurately speciate more gaseous compounds. The overall contribution of aromatics to the total gases emitted strongly correlated (R^2 0.83) to the SOA formation confirming aromatic emissions are vital to the SOA formation in the atmosphere. Utilizing the two gaseous classification methods, only 30% ± 10% (94% of which being aromatic) of the aerosol could be accounted for indicating more work must be done to identify the heavier IVOC, and LVOC compounds to get the SOA closure.

The carbonaceous aerosol formation, and more specifically the SOA, changes significantly by the fuel composition. In the effort to relate the SOA to various fuel properties, it was found that SOA most closely correlated with the T70 and T90 of the fuels, which most closely relate to the aromatic content of the fuels. The compounds that evaporate within this temperature range would be the least volatile compounds in the fuel. If these compounds evaporated or partially combusted, they would readily oxidize and contribute additional SOA mass. There was a poor relationship between the bulk ethanol content and SOA, however if the fuels were separated by aromatic content, an inverse trend

was present for the low aromatic subgroup As the ethanol content increased, there was a decrease in SOA formation potential (no difference in high aromatic).

From this work it can be concluded that the aromatic content of the fuel is plays the largest role in both the tailpipe emissions and the secondary aerosol potential of the fuel. As seen in previous works, ethanol can have varying effects on the tailpipe PM emissions, and in this work it was found that with increasing ethanol, there was increasing PM. However, ethanol content does play a minor role in the overall reduction in the SOA potential of the vehicle. In the future it may be valuable to replace some of the heavier, less volatile compounds in fuel with ethanol to aid in the reduction of secondary potential from the emissions.

Funding Sources:

We acknowledge funding from the Growth Energy. We would also like to acknowledge the funding from NCST Graduate Fellowship

Notes:

The authors declare no competing financial interest.

Acknowledgements:

The authors thank Mr. Mark Villela and Mr. Daniel Gomez of the University of California, Riverside for their contribution in contacting this research program. We also thank MECA for providing the catalyzed GPF for this program and also for their technical support and guidance.

4.6. References:

1) Hallquist, M.; Wenger, J. C.; Baltensperger, U.; Rudich, Y.; Simpson, D.; Claeys, M.; Dommen, J.; Donahue, N. M.; George, C.; Goldstein, A. H.; Hamilton, J. F.; Herrmann, H.; Hoffmann, T.; Iinuma, Y.; Jang, M.; Jenkin, M. E.; Jimenez, J. L.; Kiendler-Scharr, A.; Maenhaut, W.; McFiggans, G.; Mentel, Th. F.; Monod, A.; Prévôt, A. S. H.; Seinfeld, J. H.; Surratt, J. D.; Szmigielski, R.; Wildt, J. The formation, properties and impact of secondary organic aerosol: current and emerging issues. *Atmos. Chem. Phys.* **2009**, *9*, 5155-5236.
2) Bahreini, R.; Middlebrook, A. M.; de Gouw, J. A.; Warneke, C.; Trainer, M.; Brock, C. A.; Stark, H.; Brown, S. S.; Dube, W. P.; Gilman, J. B.; Hall, K.; Holloway, J. S.; Kuster, W. C.; Perring, A. E.; Prevot, A. S. H.; Schwarz, J. P.; Spackman, J. R.; Szidat, S.; Wagner, N. L.; Weber, R. J.; Zotter, P.; Parrish, D. D. Gasoline emissions dominate over diesel in formation of secondary organic aerosol mass. *Geophys. Res. Lett*. **2012**, *39*, L06805, doi: 10.1029/2011GL050718.
3) Hochhauser A.M., Koehl W.J., Painter L.J., Rippon B.H., Reuter R.M., Rutherford J.A., et al., **1991**, The Effect of Aromatics, MTBE, Olefins, and T90 on Mass Exhaust Emissions from Current and Older Vehicles. SAE Technical Paper 912322.
4) Jeffrey J.G., Elliott N.G., **1993**, Gasoline Composition Effects in a Range of European Vehicle Technologies. SAE Technical Paper 932680.
5) McDonald C.R., Morgan T. D. B., Graupner O., Wilkinson E., **1996**, The Independent Effects of Fuel Aromatic Content and Mid-Range Volatility on Tailpipe Emissions from Current Technology European Vehicle Fleets. SAE Technical Paper 962026.
6) Wedekind B., Bennett P.J., Goodfellow C.L., Jeffrey J.G., **1995**, Marchesi G.F., McDonald C.R. The independent effect of mid-range, back-end volatility and aromatics on emissions from two European gasoline engines. SAE Technical Paper 952522.

7) Goodfellow C.L., Gorese R.A., Hawkins M.J. McArragher J.S., **1996**, European Programme on Emission, Fuels and Engine Technologies – Gasoline Aromatics/E100 Study. SAE Technical Paper 961072.

8) Hochhauser, A.M., **2008**, Review of Prior Studies of Fuel Effects on Vehicle Emissions; Final Report for Coordinating Research Council Inc. (CRC) under program E-84.

9) Pepiot-Desjardins, P. Pitsch H., Malhotra R., Kirby S. R., Boehman, A. L. Structural group analysis for soot reduction tendency of oxygenated fuels. Combustion and Flame **2008**, 154, 191-205.

10) Maricq M.M., Szente J.J., Jahr K., **2012.** The impact of ethanol fuel blends on PM emissions from a light-duty GDI vehicle. Aerosol Science and Technology 46:576-583.

11) Butler A.D., Sobotowski R.A., Hoffman G.J. Influence of fuel PM index and ethanol content on particulate emissions from light-duty gasoline vehicles. SAE Technical Paper **2015**; 2015-01-1072.

12) Sobotowski RA, Butler AD, Guerra Z. A pilot study of fuel impacts on PM emissions from light-duty gasoline vehicles. SAE Technical Paper, **2015**, 2015-01-9071.

13) Storey J.M., Barone T., Norman K., Lewis S., 2010, Ethanol blend effects on direct injection spark-ignition gasoline vehicle particulate matter emissions. SAE Technical Paper **2010**; 2010-01-2129.

14) Jin D., Choi K., Myun C.L., Lim Y., et al. The impact of various ethanol-gasoline blends on particulates and unregulated gaseous emissions characteristics from a spark ignition direct injection (SIDI) passenger vehicle. Fuel **2017**, 209, 702-712.

15) Short, D., D. Vu, V. Chen, and C. Espinoza. **2017**. "Understanding Particles Emitted from Spray and Wall-Guided Gasoline Direct Injection and Flex Fuel Vehicles Operating on Ethanol and Iso-Butanol Gasoline Blends." *Aerosol Science and Technology: The Journal of the American Association for Aerosol Research*. https://www.tandfonline.com/doi/abs/10.1080/02786826.2016.1265080.

16) Aiken, A. C.; DeCarlo, P. F.; Kroll, J. H.; Worsnop, D. R.; Huffman, J. A.; Docherty, K. S.; Ulbrich, I. M.; Mohr, C.; Kimmel, J. R.; Sueper, D.; Sun, Y.; Zhang, Q.; Trimborn, A.; Northway, M.; Ziemann, P. J.;, Canagaratna, M. R.; Onasch, T. B.; Alfarra, M. R.; Prevot, A. S. H.,; Dommen, J.,; Duplissy, J.; Metzger, A.; Baltensperger, U.; Jimenez, J. L. O/C and OM/OC ratios of primary, secondary, and ambient organic aerosols with high-resolution time-of-flight aerosol mass spectrometry. *Environ. Sci. Technol.* **2008**, *42*, 4478-4485.

17) Malloy, Q.; Nakao, S.; Qi, L.; Austin, R. L.; Stothers, C.; Hagino, H.; Cocker, D. R. Real-Time Aerosol Density Determination Utilizing a Modified Scanning Mobility Particle Sizer-Aerosol Particle Mass Analyzer system. *Aerosol Sci. Technol.* **2009**, *43*, 673–678.

18) Cocker, D. R.; Flagan, R. C.; Seinfeld, J. H. State-of-the-art chamber facility for studying atmospheric aerosol chemistry. *Environ. Sci. Technol.* **2001**, *35*, 2594-2601.

19) Vu, D.; Roth, P.; Berte, T.; Yang, J.; Cocker D.; Durbin T.; Karavalakis, G.; Asa-Awuku, A. Using a new Mobile Atmospheric Chamber (MACh) to investigate the formation of secondary aerosols from mobile sources: The case of gasoline direct injection vehicles. Journal of Aerosol Science, Manuscript Under Review.

20) Karavalakis, G.; Short, D.; Russell, R.L.; Jung, H.; Johnson, K.C.; Asa-Awuku, A.; Durbin, T.D. Assessing the Impacts of Ethanol and Iso-butanol on Gaseous and Particulate Emissions from Flexible Fuel Vehicles. *Environ. Sci. Technol.* **2014**, *48*, 14016-14024.

21) Karavalakis, G.; Short, D.; Vu, D.; Russell, R.; Hajbabaei, M.; Asa-Awuku, A.; Durbin, T.D. Evaluating the effects of aromatics content in gasoline on gaseous and particulate matter emissions from SI-PFI and SI-DI vehicles. *Environ. Sci. Technol.* **2015**, *49*, 7021-7031.

22) Karavalakis, Georgios, Daniel Short, Diep Vu, Robert L. Russell, Akua Asa-Awuku, Heejung Jung, Kent C. Johnson, and Thomas D. Durbin. **2015b**. “The Impact of Ethanol and Iso-Butanol Blends on Gaseous and Particulate Emissions from Two

Passenger Cars Equipped with Spray-Guided and Wall-Guided Direct Injection SI (spark Ignition) Engines." *Energy* 82 (March): 168–79.

23) Roth, P., Yang, J., Cocker, D.R., Durbin, T., Brezney, R., Geller, M., Asa-Awuku, A., Karavalakis, G.; "Catalyzed Gasoline Particulate Filters Reduce Secondary Organic Aerosol Production from Gasoline Direct Injection Vehicles." Journal of Energy & Fuels, Under Review

24) Gramsch, E., V. Papapostolou, F. Reyes, Y. Vásquez, M. Castillo, P. Oyola, G. López, et al. **2018**. "Variability in the Primary Emissions and Secondary Gas and Particle Formation from Vehicles Using Bioethanol Mixtures." *Journal of the Air & Waste Management Association* 68 (4): 329–46.

25) Suarez-Bertoa, R., A. A. Zardini, and C. Astorga. **2014**. "Ammonia Exhaust Emissions from Spark Ignition Vehicles over the New European Driving Cycle." *Atmospheric Environment* 97 (November): 43–53.

26) Derwent, Richard G., Michael E. Jenkin, Steven R. Utembe, Dudley E. Shallcross, Tim P. Murrells, and Neil R. Passant. **2010**. "Secondary Organic Aerosol Formation from a Large Number of Reactive Man-Made Organic Compounds." *The Science of the Total Environment* 408 (16): 3374–81.

27) Gordon, T. D., A. A. Presto, A. A. May, N. T. Nguyen, E. M. Lipsky, N. M. Donahue, A. Gutierrez, et al. **2014**. "Secondary Organic Aerosol Formation Exceeds Primary Particulate Matter Emissions for Light-Duty Gasoline Vehicles." *Atmospheric Chemistry and Physics* 14 (9): 4661–78.

28) Platt, S. M.; El Haddad, I.; Zardini, A. A.; Clairotte, M.; Astorga, C.; Wolf, R.; Slowik, J. G.; Temime-Roussel, B.; Marchand, N.; Ježek, I.; Drinovec, L.; Močnik, G.; Möhler, O.; Richter, R.; Barmet, P.; Bianchi, F.; Baltensperger, U.; Prévôt, A. S. H.: Secondary organic aerosol formation from gasoline vehicle emissions in a new mobile environmental reaction chamber. *Atmos. Chem. Phys.* **2013**, *13*, 9141-9158.

29) Du, Z.; Hu, M.; Peng, J.; Zhang, W.; Zheng, J.; Gu, F.; Qin, Y.; Yang, Y.; Li, M.; Wu, Y.; Shao, M.; Shuai, S. Comparison of primary aerosol emission and secondary

aerosol formation from gasoline direct injection and port fuel injection vehicles. *Atmos. Chem. Phys.* **2018**, *18*, 9011-9023.

30) Nordin, E. Z.; Eriksson, A. C.; Roldin, P.; Nilsson, P. T.; Carlsson, J. E.; Kajos, M. K.; Hellén, H.; Wittbom, C.; Rissler, J.; Löndahl, J.; Swietlicki, E.; Svenningsson, B.; Bohgard, M.; Kulmala, M.; Hallquist, M.; Pagels, J. H. Secondary organic aerosol formation from idling gasoline passenger vehicle emissions investigated in a smog chamber. *Atmos. Chem. Phys.* **2013**, *13*, 6101-6116.

31) Zhao, Bin, Shuxiao Wang, Neil M. Donahue, Shantanu H. Jathar, Xiaofeng Huang, Wenjing Wu, Jiming Hao, and Allen L. Robinson. **2016**. "Quantifying the Effect of Organic Aerosol Aging and Intermediate-Volatility Emissions on Regional-Scale Aerosol Pollution in China." *Scientific Reports* 6 (June): 28815.

32) Timonen, Hilkka, Panu Karjalainen, Erkka Saukko, Sanna Saarikoski, Päivi Aakko-Saksa, Pauli Simonen, Timo Murtonen, et al. **2017**. "Influence of Fuel Ethanol Content on Primary Emissions and Secondary Aerosol Formation Potential for a Modern Flex-Fuel Gasoline Vehicle." *Atmospheric Chemistry and Physics* 17 (8): 5311–29.

33) Storey, John M., Sam Lewis, James Szybist, John Thomas, Teresa Barone, Mary Eibl, Eric Nafziger, and Brian Kaul. **2014**. "Novel Characterization of GDI Engine Exhaust for Gasoline and Mid-Level Gasoline-Alcohol Blends." *SAE International Journal of Fuels and Lubricants* 7 (2): 571–79.

4.7. Supplemental:

Table 4-2: Speciated Hydrocarbon Fuel Analysis

Group (Vol %)	F1	F2	F3	F4	F5	F6	F7	F8
Paraffin	14.05	16.60	18.07	21.37	17.68	21.02	21.40	16.35
I-Paraffins	35.98	28.47	26.28	17.82	24.11	20.31	17.82	22.34
Aromatics	23.45	34.70	27.85	32.19	25.67	23.55	32.13	24.02
Mono-Aromatics	21.87	32.50	26.15	30.14	24.12	21.87	30.13	22.55
Naphthalenes	0.46	0.55	0.47	0.55	0.43	0.48	0.51	0.40
Naphth/Olefino-Benz	1.12	1.65	1.22	1.50	1.11	1.19	1.48	1.06
Indenes	0.00	0.00	0.00	0.00	0.00	0.00	0.00	0.00
Naphthenes	16.52	10.13	8.24	5.04	8.06	11.79	5.04	7.21
Mono-Naphthenes	16.52	10.13	8.24	5.04	8.06	11.79	5.04	7.21
Di/Bicyclo-Naphthenes	0.00	0.00	0.00	0.00	0.00	0.00	0.00	0.00
Olefins	9.30	8.55	9.73	8.08	8.90	7.98	8.08	8.14
n-Olefins	7.80	7.46	8.21	7.41	7.86	6.40	7.41	7.29
Iso-Olefins	0.89	0.91	0.93	0.63	0.84	0.95	0.63	0.80
Naphtheno-Olefins	0.60	0.17	0.58	0.03	0.19	0.63	0.03	0.05
Di-Olefins	0.00	0.00	0.00	0.00	0.00	0.00	0.00	0.00
Oxygenates	0.00	0.00	9.24	14.53	14.91	14.23	14.53	20.90
Unidentified	0.68	1.52	0.57	0.94	0.66	1.09	0.97	1.00

Table 4-3: Main physiochemical properties of the test fuels

Property	Fuel 1	Fuel 2	Fuel 3	Fuel 4	Fuel 5	Fuel 6	Fuel 7	Fuel 8
Fuel Classification	LA E0	HA E0	LA E10	HA E10	LA E15	LA E15	HA E15	LA E20
Research Octane Number	91.7	91.0	91.5	90.8	94.4	92.9	91.2	96.8
Motor Octane Number	84.5	83.4	84.0	83.1	85.2	84.2	83.7	86.2
Octane Rating	88.1	87.2	87.8	87.0	89.8	88.6	87.4	91.5
Total Aromatic (vol %)	21.2	29.4	21.4	29.1	20.3	21.8	29.3	19.1
Ethanol Content (vol %)	0.00	0.00	9.98	9.62	14.72	14.77	14.74	19.61
C_6 Aromatics (vol %)	0.5	0.6	0.6	0.6	0.5	0.5	0.6	0.5
C_7-C_9 Aromatics (vol %)	15.8	22.3	15.7	22.3	14.9	16.1	22.3	14.1
C_{10+} Aromatics (vol %)	4.9	6.7	5.1	6.3	4.8	5.1	6.4	4.5
Olefins (vol %)	7.9	6.5	7.0	8.1	6.5	7.3	8.6	6.0
Saturate Content (vol %)	70.9	64.1	61.7	53.1	58.5	56.1	47.4	55.3
Hydrogen Content (wt %)	14.06	13.65	13.79	13.13	13.51	13.38	13.02	13.54
Carbon Content (wt %)	85.94	86.35	82.52	83.29	81.07	81.19	81.52	79.26
Oxygen Content (wt %)	0.00	0.00	3.69	3.57	5.42	5.43	5.48	7.20
C/H Ratio (wt/wt)	6.111	6.326	5.984	6.342	6.002	6.066	6.260	5.852
H/C Ratio (mole/mole)	1.950	1.884	1.991	1.879	1.986	1.965	1.904	2.036
O/C Ratio (mole/mole)	0.000	0.000	0.034	0.032	0.050	0.050	0.050	0.068
Heat of Combustion [MJ/kg]	43.77	43.50	41.82	41.72	40.95	40.97	40.76	40.13
Specific Gravity @ 60.0 F	0.7416	0.7544	0.7455	0.7565	0.7482	0.7505	0.7599	0.7507
Density @ 15.56 C (g/cm^3)	0.7409	0.7537	0.7448	0.7557	0.7474	0.7497	0.7592	0.7499
RVP @ 100 F (psi)	8.86	8.76	8.97	9.20	8.77	9.09	9.09	8.59
Distillation, IBP	32.6	31.1	36.3	33.2	37.4	36.1	35.3	35.9
Distillation, 10% (°C)	53.3	51.5	53.0	51.7	53.4	52.2	53.4	54.1
Distillation, 20% (°C)	65.3	64.7	58.1	58.3	58.8	57.5	60.1	59.8
Distillation, 30% (°C)	76.2	78.6	62.4	63.8	63.4	62.1	65.4	64.5
Distillation, 40% (°C)	87.1	94.5	66.2	68.3	67.4	66.1	69.6	68.4
Distillation, 50% (°C)	100.4	112.6	87.0	97.4	70.9	69.8	72.9	71.8
Distillation, 60% (°C)	114.8	127.4	111.3	121.1	102.8	90.2	112.7	74.7
Distillation, 70% (°C)	126.4	140.7	125.9	136.9	124.0	124.2	133.4	120.2
Distillation, 80% (°C)	139.8)	156.1	139.7	152.0	138.1	142.3	150.9	135.5
Distillation, 90% (°C)	160.2	172.4	158.6	169.4	157.8	162.6	169.7	155.0
Distillation, 95% (°C)	177.5	182.8	175.8	182.5	175.9	179.2	182.2	173.8
Distillation, Dry Point (°C)	202.2	204.4	202.1	204.4	202.3	203.4	204.3	202.2
Recovery (vol %)	97.5	97.7	97.9	97.8	97.5	98.1	97.7	98.1

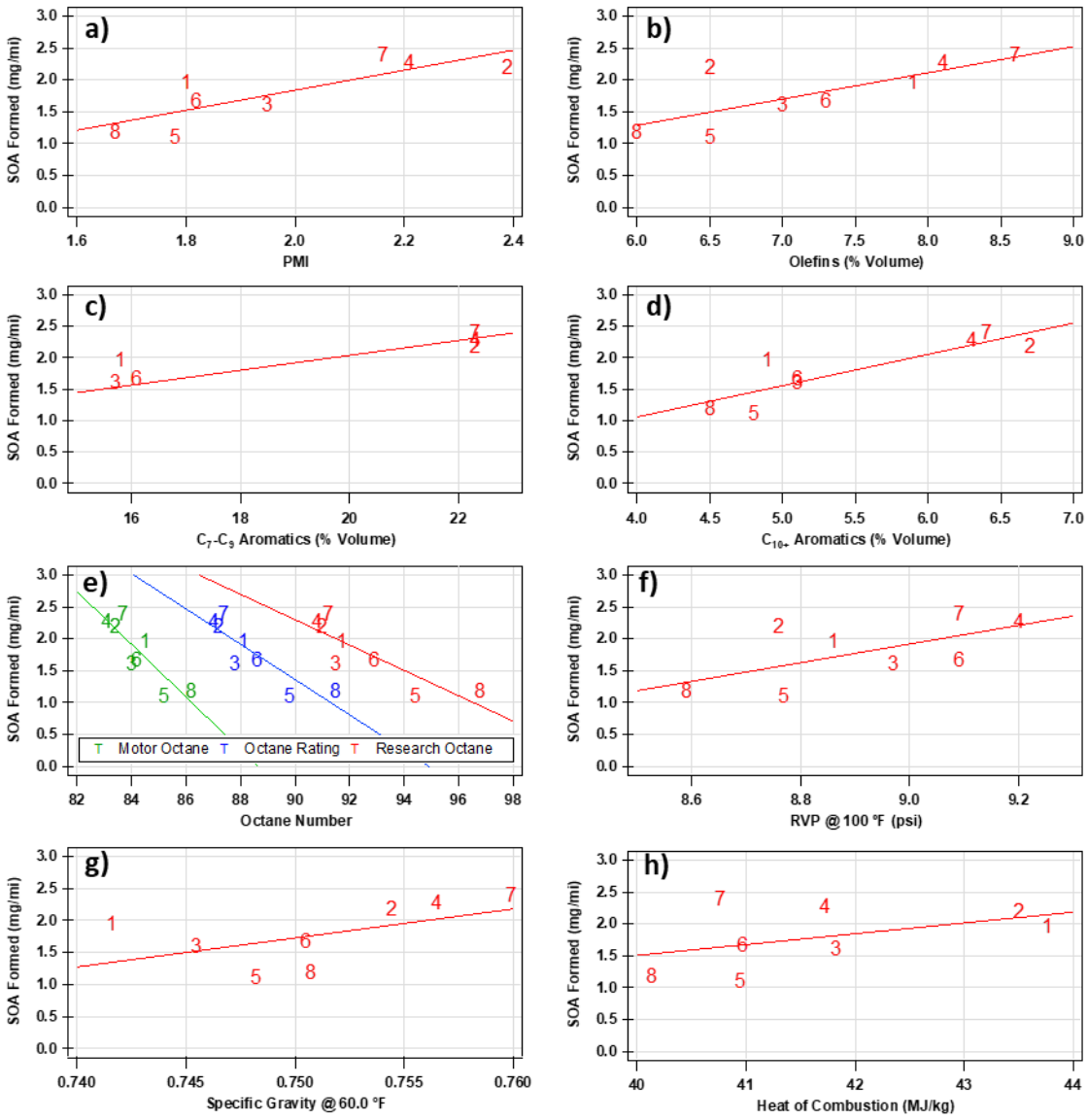

Figure 4-13: Correlation of SOA formation to a)fuel PMI, b) Olefin Content, c) C_7-C_9 aromatic content (% volume), d) C_{10+} aromatic content (%volume), e) Octane numbers, f) RVP @ 100 °F, g) Specific gravity @ 60 °F, h) Heat of combustion (MJ/kg). Fuels are signified by number on the plot.

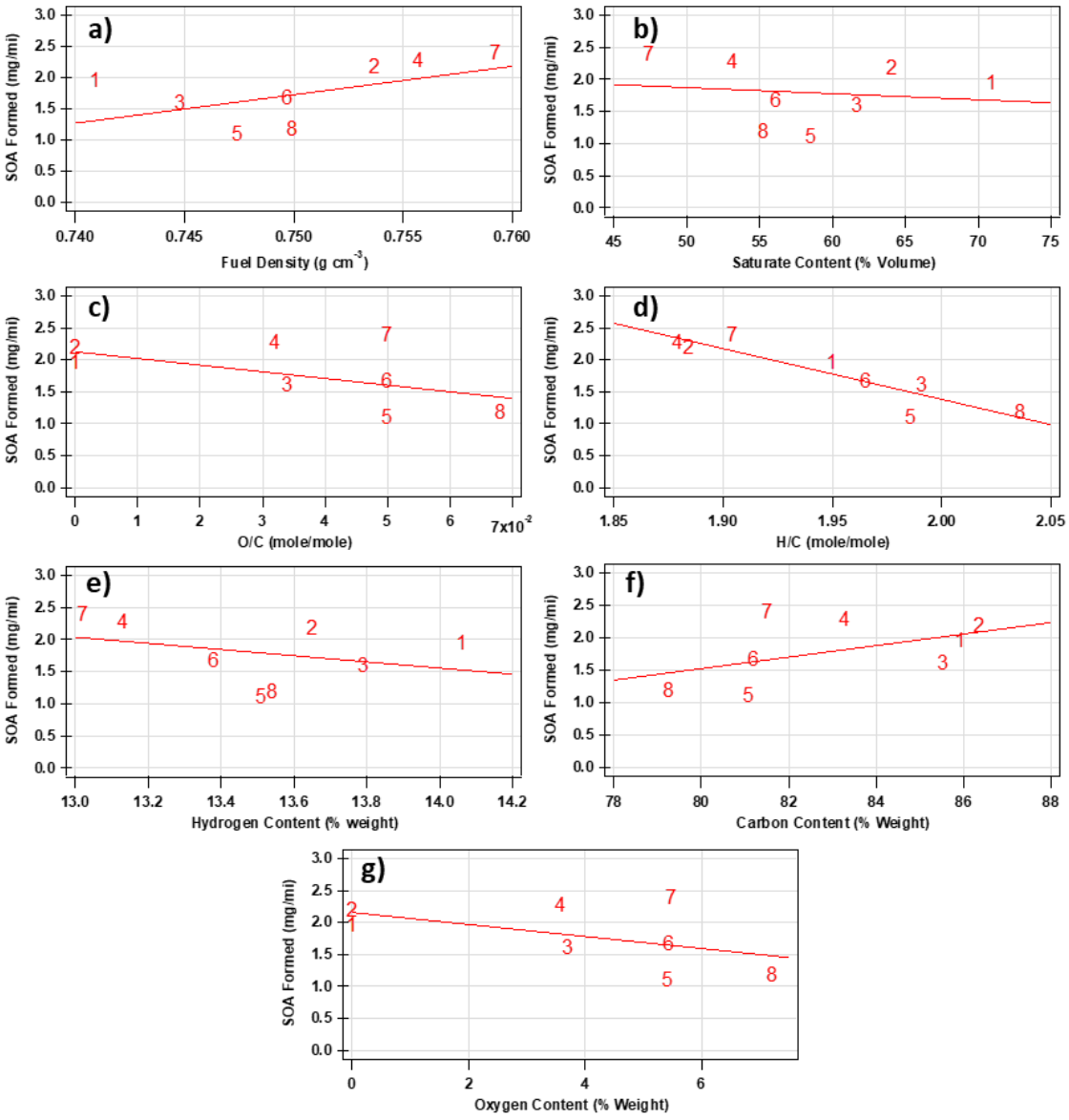

Figure 4-14: Correlation of SOA formation to a) Fuel density (g cm^{-3}), b) Saturate content (% volume), c) O:C (mole/mole), d) H:C (mole/mole), e) Hydrogen content (% weight), f) Carbon Content (% weight), g) Oxygen content (% weight). Fuels are signified by number on the plot.

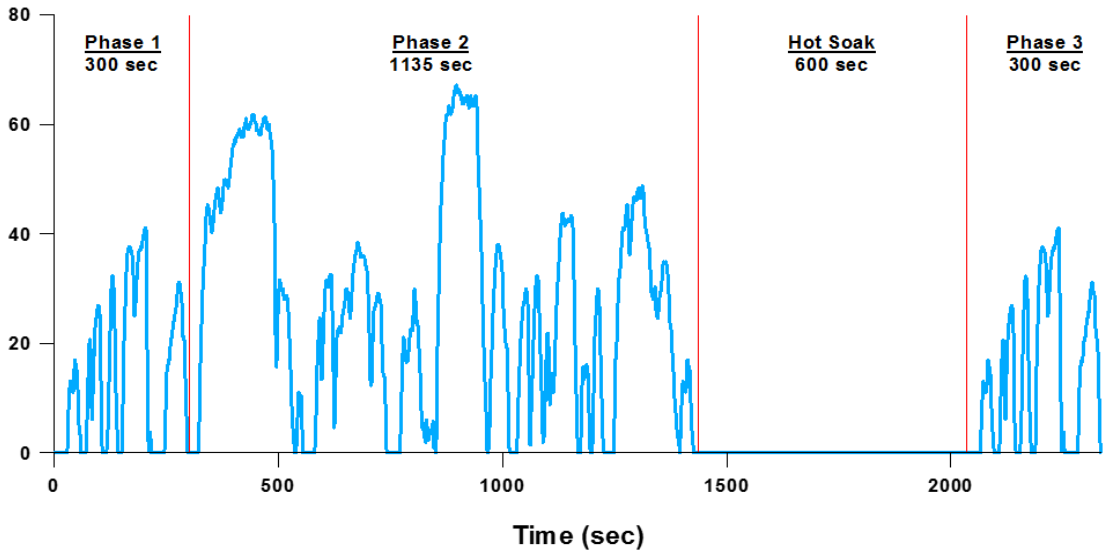

Figure 4-15: LA92 or Unified Driving Cycle (UC) comprised of three phases; Cold-start, urban, and hot-start phases. The vehicle's engine is turned off for the duration of the hot soak.

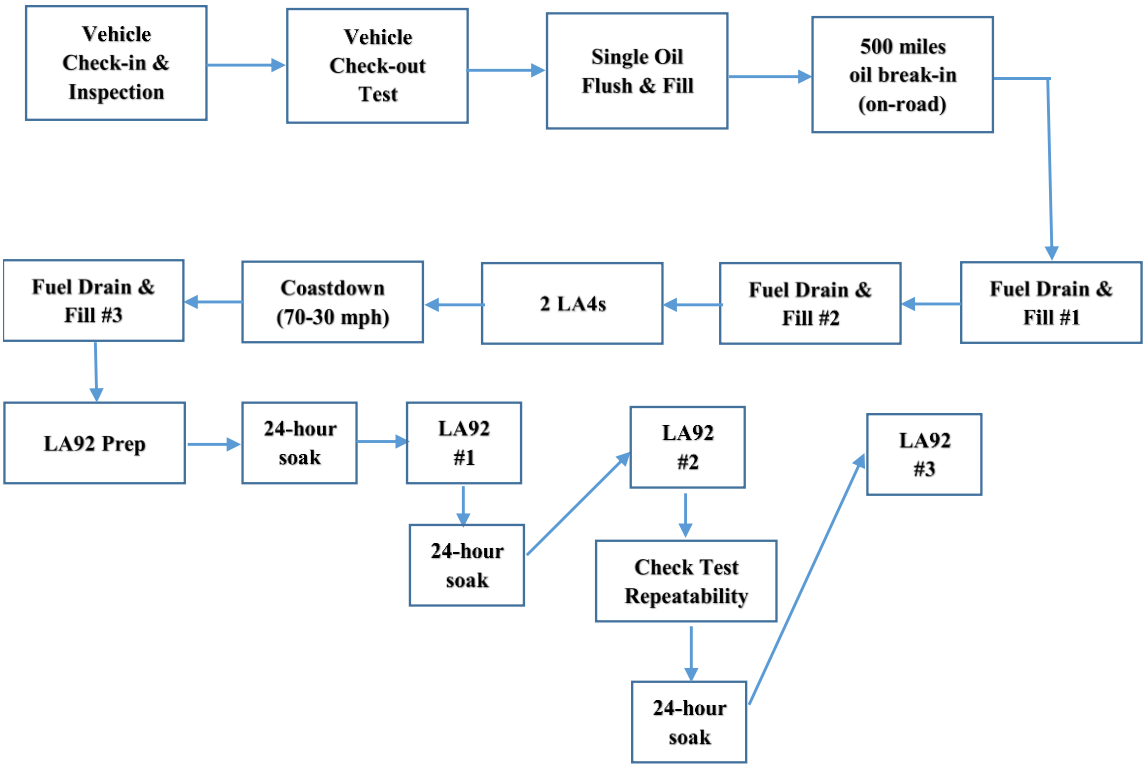

Figure 4-16: Flow chart showing the preconditioning and test procedure for the vehicle after a fuel change.

The fuel content also had little effect on the bulk size distribution of the particles emitted from the vehicle after dilution in the chamber. For all fuels, the emissions from the vehicle was a broad, unimodal, Gaussian distribution of particles, centered at ~75 nm. Even though the distribution was similar, the value for the peak diameter was reliant on the different fuel compositions. Similar to the mass, there was no clear trend for peak diameter solely in relation to ethanol content, however, there was a strong positive correlation to the aromatic content of the fuel. When the vehicle was operated on the high aromatic fuels, the average peak diameter of the aerosol was at 79.3 nm ± 4.1 nm compared to 64.3 nm ± 1.7 nm when operated on the lower aromatic fuels (Figure 4-17). When separated by aromatic groupings, there did appear to be a positive correlation to ethanol content and peak diameter size (Figure 4-17).

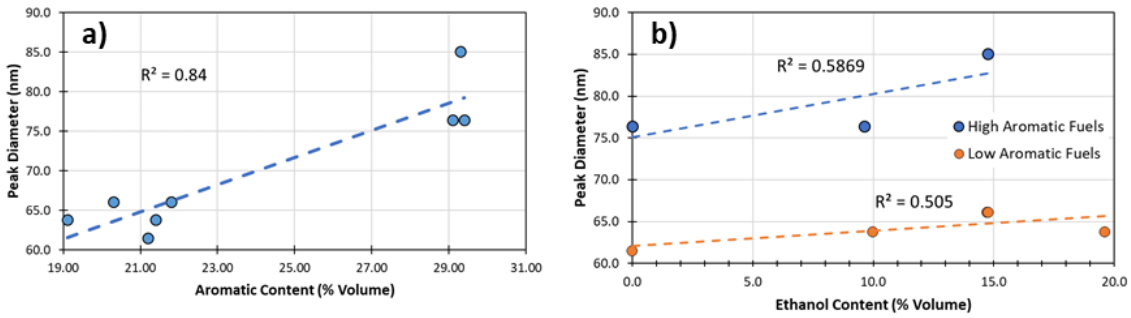

Figure 4-17: Average peak diameter of the initial diluted tailpipe exhaust distribution vs aromatic (a) and ethanol (b) content (% volume) of the fuels

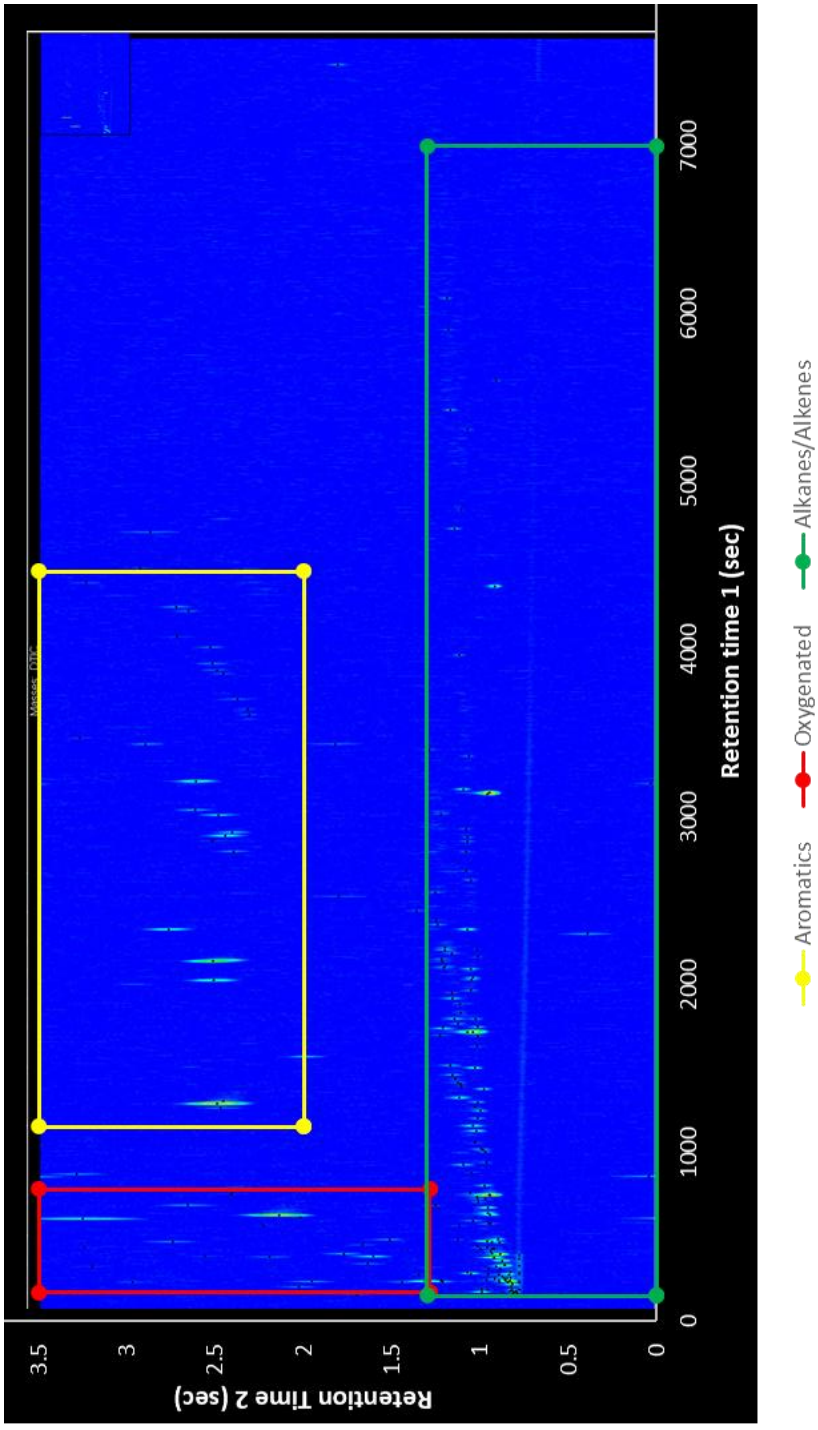

Figure 4-18: Example of a chromatograph utilizing the GCxGC setup described in 4.7.1. Generalizations on composition were made utilizing the boxes displayed.

4.7.1 GCxGC Procedure:

The sorbent tubes used for collection were 8.9 cm long x 0.64 cm (od) stainless steel tubes with an inert, SilcoTek coating; each cartridge contained a dual-sorbent bed composed of 100 mg Tenax TA 35/60 and 200 mg Carbograph 1 TD 60/80 in series (Camsco, Inc., Houston, TX). Prior to use, each sorbent tube was conditioned at 320 ^{o}C for one hour with a continuous flow of ultra-pure nitrogen. All sampled sorbent tubes were below 0^{o}C and analyzed within three months from collection.

For each irradiation experiment, gas samples were collected from both the CVS and MACh. When sampling from the CVS, the apparatus was connected via a Teflon sample line (~30 cm long x 0.64 cm od) directly to the CVS. Samples were collected at 100 mL/min for the duration of each driving cycle (excluding the hot soak). Samples collecting diluted exhaust from MACh collected for 30 min at 100 mL/min prior to irradiation. For all collection, a Teflon filter was placed upstream of the sorbent tube to prevent particles from reaching the sorbent tube.

Three background samples that mimicked a driving cycle were taken from the CVS; three blank sorbent tubes were also retained. One breakthrough test was conducted per fuel to determine which compounds were incompletely trapped on a single sorbent tube. Three background samples were also collected from the mobile chamber.

Prior to desorption, a gaseous internal standard mixture (1,2-Dichlorobenzene-D4, 1-Bromo-4-flurobenzene, Fluorobenzene, Toluene-D8) was automatically added to each sorbent tube. Sorbent tube samples were thermally desorbed using an automated thermal

desorber (ATD, TurboMatrix 650, Perkin Elmer, Waltham, MA). Each sorbent tube was desorbed (300^{o}C, 12 min, 50 mL/min) onto a Tenax focusing trap (-20^{o}C). The trap was then desorbed (300^{o}C, 4 min) via a fused silica transfer line at 235^{o}C to the GC×GC–ToFMS (Pegasus 4-D, Leco Corp., St. Joseph, MI). The analytical column set included a DB-VRX primary column and a Stabilwax secondary column. The GCxGC–ToFMS conditions are summarized in Table 4-4. A hydrocarbon standard mixture (PiONA mix, RESTEK, Bellefonte, PA) containing 133 compounds (alkanes, alkenes, and aromatic hydrocarbons) was analyzed to positively identify those compounds.

Data were processed using a reference method within the ChromaTOF software package (LECO Corp., St. Joseph, MI). The sample with the highest number of peaks (~187) was selected as a reference and compounds were positively identified, where possible, based on the PiONA standards. A peak was not used in the analysis if the mass spectral match similarity with the National Institute of Standard Technology (NIST) mass spectral database was less than 700. If a compound could not be positively identified a group name and carbon number (e.g. C6-Paraffin) was assigned based on neighboring peaks. The remaining samples were processed using the reference sample. Applying the reference method ensured that compounds were consistently named across all samples. The peak area of each analyte was then background corrected. The background samples collected for the CVS and chamber, were checked for consistency. For the peaks that were significantly higher or lower the average values between the three samples were used. Compounds were removed from consideration if their peak areas were ≤ 0 following background correction.

Table 4-4: GCxGC sampling and detection specifications for the collected samples from both the CVS and the chamber

Mass injected	8.3% (CVS), 18.4% (Chamber)
Column flow	1.8 mL min^{-1}
Primary column	DB-VRX, 30m, 0.25mm I.D., 1.4 μm film (Agilent, Santa Clara, CA)
Primary oven program	35 °C for 10 min, 1.25 °C min^{-1} to 170 °C, 10 °C min^{-1} to 185 °C
GC x GC modulation	3.5s period, 0.75s hot pulse
GC x GC modulator	Trapped with cold gas from liquid nitrogen, then hot pulse at 50 °C above
Secondary column	Stabilwax, 1.5 m, 0.25mm I.D., 0.5 μm film (Restek, Bellefonte, PA)
Secondary oven	15 °C above primary oven
MS detector	225 °C, Electron impact, 70 eV
MS data acquisition	227 spectra s^{-1}, 34-550 amu

Chapter 5: Exploring the Secondary Organic Aerosol Formation Potential and Subsequent Secondary Trends from Gasoline Direct Injection Vehicles with Varying Experimental Conditions

Patrick Roth [1,2], David R. Cocker III[1,2], Georgios Karavalakis [1,2], Akua Asa-Awuku [1,2,3]

1. Bourns College of Engineering, Center for Environmental Research and Technology (CE-CERT), University of California, 1084 Columbia Avenue, Riverside, California 92507, United States
2. Department of Chemical and Environmental Engineering, Bourns College of Engineering, University of California, Riverside, California 92521, United States
3. Department of Chemical and Bimolecular Engineering, A. James Clark School of Engineering, University of Maryland, College Park, 4418 Stadium Dr., College Park, MD, 20702

5.1. Abstract:

The goal of this chapter was to aggregate all data collected from all vehicle exhaust irradiation experiments utilizing UCR's Mobile Atmospheric Chamber, and find trends in the secondary aerosol formation. The SOA formation potential measured in this work were right in line with previous experiments with chambers exploring the secondary potential of vehicle exhaust. We observed a decrease in the secondary organic aerosol potential of the vehicle exhaust as the certification standard increased. Similarly as the ethanol content of the fuel increased, so did the secondary organic aerosol potential.

In regards to observed trends in the exhaust, not surprisingly, as the NMHC emissions increased, so did the SOA formation potential. The trend was very strong in emissions over 20 mg/mi however there was much more variability in the lower emission levels (<20 mg/mi). This variation in trend was most likely due to the differences in the composition of the complex NMHC mixture.

Next the yield of the vehicle exhaust were explored, and the trend was quite broad when looking at all tests as a whole. However, when exploring the similar reaction conditions, it was found that in the lower VOC:NOx ratio conditions, there was a strong log normal trend where the yield appeared to plateau around 0.13. In the higher VOC;NOx regime the yield was found to be much higher with a plateau around 0.35. More relationships with the yield and various concentrations were also explored. No trends with the formation of inorganic salt were found.

5.2. Introduction:

In the atmosphere, NOx, and volatile organic compounds (VOCs) can undergo atmospheric photo-oxidation, resulting in the formation of secondary lower volatility organic gases. As the gases continue to react, the volatility of the gases decrease until ultimately condensing onto existing particles, thus increasing the atmospheric organic aerosol mass. The formation of organic mass as a result of VOC oxidation is classified as secondary organic aerosol or SOA (Getner, et al, 2009; Odum, et al, 2009).

A considerable source of VOCs emitted in urban areas, are attributed to mobile sources operating on fossil fuel. Gasoline vehicles (in comparison with diesel vehicles) are more influential emitters of reactive organic gases; and contribute to increased SOA formation in high traffic areas. This is due to the hundreds of light hydrocarbon species in gasoline that are known SOA precursors (Gentner, et al, 2017). Bahreini et al (2012) showed that gasoline exhaust is the main source of SOA in the Los Angeles basin from ambient SOA measurements utilizing an AMS.

Past vehicle tailpipe experiments have concluded that the gaseous emissions from similar certification standard vehicles are comparable, however differences are observed between varying certification standards (Saliba et al 2017). Similarly, when comparing the emissions from vehicles operated on varying composition of fuels, it has been found that the vehicle exhaust has the potential to vary greatly (Suarez-Bertoa, et al 2015). The variation in gaseous emission from varying fuel content can lead to differences in the fractional chemical composition of the VOCs emissions, which directly affects the SOA formation potential.

The total VOC's measured at the tailpipe are typically classified as the total hydrocarbon (THC) emission factor. Methane can constitute a considerable portion of the THC, so another distinction in the gases measured at the tailpipe is looking at the non-methane hydrocarbons (NMHC). Little work has been done to understand the effect of fuel composition on the variations of NMHC composition thus affecting the SOA formation potential from vehicle exhaust. In addition to NMHC composition, several factors (e.g., oxidants, OH, NOx etc) can influence atmospheric SOA formation from tailpipe emissions. Due to all of these complex factors, models attempting to predict SOA formation in the atmosphere are not able to account for the total measured SOA mass (Volkamer, et al 2006).

Modelers attempting to predict the formation of secondary organic aerosol from specific emissions rely on experimental data for quantification. Typically, experiments simulate a wide range of reactant concentrations, and experimental conditions for the single precursor to allow a range of yields for SOA formation. Works investigating these yields typically focus on single precursor reactions due to the complexity of the photochemistry. Little work has been done exploring the yield of formation from complex emission mixtures, such as vehicle exhaust, due to the added complexity of composition of reactive organic gases and NOx emissions.

As stated, yield of reactants are typically the easiest way to predict SOA formation in the atmosphere. The yield (Y) is defined as the mass of the organic aerosol formed (M_o) divided by the amount of hydrocarbon consumed (ΔTHC) (Odum, et al 1996; 1997). The equation for yield is shown below.

$$Y = \frac{\Delta M_o}{\Delta THC}$$

The goal of this chapter is to aggregate all data collected from the vehicles tested thus far utilizing UCR's Mobile Atmospheric Chamber (MACh), and attempt to relate to previously peer reviewed works, and find trends in the SOA formation potential. This chapter will focus on SOA formation and only touch on the inorganic secondary aerosol due to the complexity and uncertainty associated with SOA formation. Specifically, we will find trends in the SOA formation potential for gasoline vehicle exhaust which may ultimately allow modelers to more accurately predict atmospheric SOA concentrations from anthropogenic vehicular exhaust.

5.3. Experimental:

All tests were conducted in CE-CERT's Vehicle Emissions Research Laboratory (VERL), on a Burke E. Porter 48-inch single-roll electric dynamometer. A Pierburg Positive Displacement Pump-Constant Volume Sampling (PDP-CVS) system was used to obtain standard bag measurements for total hydrocarbons (THC), carbon monoxide (CO), nitrogen oxides (NOx), non-methane hydrocarbons (NMHC), and carbon dioxide (CO_2). Bag measurements were made with a Pierburg AMA-4000 bench.

5.3.1 Chamber Experiments:

The photochemical aging experiments were carried out in UCR's (University of California, Riverside) Mobile Atmospheric Chamber (MACh). The MACh consists of a 30 m^3 2 mil fluorinated ethylene propylene Teflon film reactor. Briefly, the reactor is enclosed in a segmented, lightweight aluminum frame fitted with wheels and a static resistant/UV blackout tarp. It is surrounded by 600 15 W, 18", T8 black light fluorescent bulbs that serve as a photochemical light source.

Prior to each irradiation experiment, the chamber was cleaned by injecting O_3, H_2O_2, and purified air (AADCO 737 air purifier) and was irradiated with UV light. The AADCO air consists of no detectable reactive compounds (i.e., H_2O, NOx, CO, O_3, hydrocarbons) to minimize background reactions in experiments. The chamber was then subsequently emptied and filled repeatedly until all gases and particles were measured to be below detection limit (H_2O < -50°C dew point, NOx, CO, HC, and O_3 at ~0 ppb, and PM=0 µg

m^{-3}) then flushed with purified air overnight. Prior to the injection of vehicle exhaust, the chamber was half-filled with the AADCO air.

The dilute exhaust was injected from the PDP-CVS into MACh during an LA92 cycle (excluding the hot soak). The exhaust was injected utilizing two Ejector Dilutors (Air-Vac TD11OH) in parallel, connected to a home built clean air system with filters and desiccants to remove the PM (HEPA filters), water (silica gel columns), NOx (Purafil), CO (Carulite canister), and hydrocarbons (activated charcoal) from the dilution air. The injection lines consisted of 8.5 m of 0.5" stainless steel tubing. The dilution setup was designed to allow a variation of dilution from 50:1 up to 200:1 by varying the dilution air and CVS flow. MACh utilized gravitational forces to ensure a positive pressure inside the reactor, such that potential holes in the Teflon surface of the chamber will force air to flow out of the reactor. This minimized the contamination and dilution of the exhaust throughout the experiment.

For all experiments, after the exhaust was collected, the chamber was filled to maximum volume with purified air. A concentration of 1.0 ppm of H_2O_2 was also injected to act as an OH radical source. Prior to irradiation, the primary exhaust was evaluated for about 30 min to help characterize the diluted tailpipe composition. The emissions were then photo-oxidized continuously for 7-10 hours. The exhaust was monitored during photo-oxidation utilizing a host of gaseous and particulate instruments allowing for real time evaluation of the aged exhaust. All chamber experiments were concluded when the wall-loss corrected aerosol mass formation, and the ozone concentration plateaued.

The SOA formation potential from vehicle exhaust is complex, and can be affected by a host of different conditions. Previous work has altered the concentrations of VOC's (addition of propene), and also the concentration of NOx (addition of HONO) (Gordon, et al, 2014) in an attempt to create similar reaction conditions test to test. All experiments in this work only utilized the emissions from the vehicle exhaust, and did not attempt to alter any VOC or NOx concentrations (excluding V8. More information can be found in Chapter 3 of this dissertation).

5.3.2 MACh Instrumentation:

Particle phase instrumentation included a commercial scanning mobility particle sizer (SMPS) consisting of a TSI 3080 Electrostatic Classifier, TSI 3081 long column Differential Mobility Analyzer (DMA) column, and a TSI ultrafine condensation particle counter (CPC) 3776. The 3776 CPC was operated in 'low flow mode' with a sample flow of 0.3 LPM and the sheath flow was set to 3.0 LPM. The SMPS measured electrical mobility diameters from 14.6 nm to 661.2 nm. Black carbon mass was measured with an AVL Micro Soot Sensor (MSS) with a high power laser diode operating at 802 nm with a photoacoustic sensor.

For the chemical composition of aerosol, an Aerodyne high-resolution time-of-flight aerosol mass spectrometer (HR-ToF-AMS) was used (Aiken, et al, 2008). The HR-ToF-AMS provided real-time information of the non-refractory aerosol, including sulfate, nitrate, ammonium, chloride, and organic. The HR-ToF-AMS was operated in both V and W modes, and the data processing was completed using the ToF-AMS Analysis Toolkit

1.57 and ToF-AMS HR analysis 1.16. The Unit Mass Resolution (UMR) and HR Frag table for CO_2 were altered from the assumed concentration of 370 ppm to the measured CO_2 concentration using a LI-COR ® LI-840A CO_2/H_2O analyzer.

A Kanomax APM analyzer system was used to measure particle effective density. The APM was paired with a home built SMPS. Particles were initially selected by mass and later passed through a scanning DMA column where an effective density based on the electrical mobility diameter was calculated. The APM has the ability to select aerosol with a mass from 0.30 to 50.0 fg, which is equivalent to a particle of unit density with a diameter of 50 to 400 nm. A more detailed summary of the APM-SMPS system is described in Malloy, et al, 2009.

SMPS data was used for the calculation of the volume of aerosol during the irradiation experiments. All SMPS data was corrected for particle wall losses using first order wall loss kinetics, as described in detail by Cocker et al. 2001. Vapor wall losses have been assumed and measured to be insignificant in past chamber experiments (Vu et al, 2018). From the volume, mass was calculated by using effective density measurements. Final mass calculations were determined from the effective density and volume calculated at the end of the irradiation experiments.

5.3.3 Vehicles:

Table 5-1: Information on all vehicles, tested with the MACh, number in left column indicatex the number of experimental configurations (data points) for each vehicle

Designation	Make, Model	M.Y.	Displacement	Certification Standard	Exptl. Config.
V1	**Hyundai, Accent**	2015	1.8 L	LEVII	1
V2	**Honda, Accord**	2015	3.6 L	LEVII	1
V3	**Kia, Soul**	2016	2.0 L	LEVII	1
V4	**Chevy, Impala**	2016	3.5 L	LEVII	1
V5	**Mazda, Mazda 3**	2016	2.0 L	LEVIII	2
V6	**Ford, Fusion**	2016	1.5 L	LEVII	2
V7	**Ford, Focus**	2016	2.0 L	LEV II	8
V8	**Chevy, Equinox**	2017	2.4 L	LEV II	8
VX	**Ford, Fusion**	2017	1.5 L	LEVIII	8

The vehicles that are reported in this chapter are all vehicles tested thus far at UCR utilizing the Mobile Atmospheric Chamber (MACh). The vehicles fall into four different projects with different funding sources. V1-V4 were funded by AQMD and focused on the SOA formation from GDI vehicles of different makes and models. The engines all had different displacements and relatively low mileage. All vehicles were of the same certification standard (LEVII). The main focus of this study was to classify the chamber, and gain an understanding of the secondary aerosol potential from GDI vehicles. All vehicles were tested over a cold-start LA92 in triplicate. A more detailed analysis of this work can be found in Vu et al (2018).

The next project included V5 and V6, which was funded by AQMD and MECA. The focus of the study was to investigate the secondary aerosol production from two low

mileage GDI vehicles with and without a catalyzed GPF. This study is first of its kind, as there is no current information on how a catalyzed GPF can alter the secondary aerosol potential from vehicle exhaust, however one project looked at secondary aerosol from a vehicle operated with a standard GPF (Pieber, et al, 2018). For this work both V5 and V6 were tested over a cold-start LA92 both with and without a catalyzed GPF in triplicate. A more detailed analysis of this work can be found in Chapter 2 of this dissertation.

The third project included V7 and V8, and was funded by ICM Inc. The goal of this project was to observe the effects that high ethanol fuel blends can have on both the tailpipe and the secondary aerosol formation from vehicle exhaust. This study evaluated four fuels, including two low ethanol content fuels (E10 and E10 high aromatic), a moderate ethanol content fuel (E30), and a high ethanol content fuel (E78). Another focus of the study was to evaluate the effect of driving cycle on each fuel. For this study, both vehicles, on each fuel, were tested over both a cold-start and hot-start LA92 in triplicate. Similar work was done by Timonen et al (2017) who found lower SOA production with higher ethanol blending when they tested a GDI FFV over the NEDC using a potential aerosol mass (PAM) reactor. They also reported that the cold-start phase of the cycle dominated the SOA production. More information on this project can be found in Chapter 3 of this dissertation.

The final project completed utilizing MACh was funded by Growth Energy. The focus of this study was to evaluate the effects of ethanol and aromatic content of fuel at lower ethanol fuel blends (E0-E20). In this work, the fuel blends were closer to what is commercially available and spans the range of aromatic content that can be found across

the country. In this work, eight fuels were tested, two E0s, two E10s, 3 E15s, and an E20. This study allowed the evaluation of similar fuels with small variations to determine what factors in fuel can change the secondary aerosol formation potential of the emission. The vehicle was tested on all eight fuels over a cold-start LA92 driving cycle in duplicate. More information on this work can be found in Chapter 4 of this dissertation.

All the data shown in this chapter will be the averaged secondary aerosol formation for each testing condition. This work splits data into multiple groupings. The first grouping is set by the certification standard (LEVII and LEVII). The LEVII grouping includes V1-V4, V5, V5 GPF, V7 E10, V7 HA E10, V8 E10, and V8 HA E10 (all cold-start). The LEVIII grouping includes, V5, V5 GPF, and all VX tests. This was done to keep similar driving cycles (all cold-start LA92 tests), and all similar composition fuels (all E0-E20 fuels).

The second set of groupings only focused on the ethanol content of the fuel. In the E0-E20 grouping included V1-V6 (including V5 GPF and V6 GPF), V7 E10s (only cold-start), and all VX tests. The E30-E78 included V7 and V8 all tests for E30 and E78. For the high ethanol blends the hot-start tests were included due to a lack of data points.

5.4. Summary:

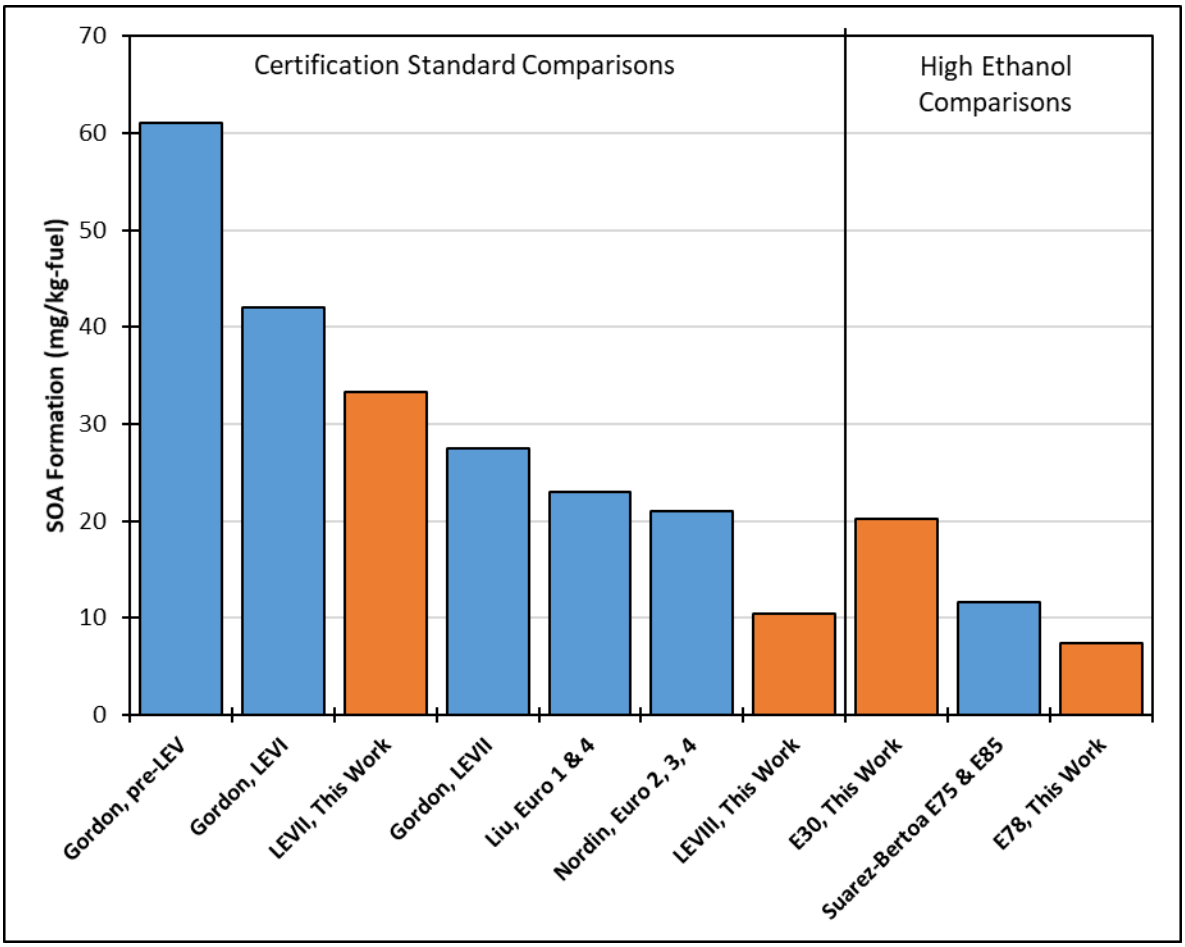

Figure 5-1: SOA formation measured in this work (orange) compared to previously peer reviewed publications (blue). Comparisons were make for the certification standards (left) and for similar ethanol fuel compositions (right)

When compared with previous peer reviewed studies exploring the SOA formation from gasoline powered vehicles, this work falls right in line with what has been previously measured. Gordon et al (2014) measured the SOA formation of 15 light-duty gasoline vehicles with a model year range from 1987 to 2011. These vehicles were categorized by

certification standards of pre-LEV, LEVI, and LEVII. All vehicles were tested over a cold-start LA92 (identical to this work), and measured the SOA formation in an atmospheric chamber. The vehicles were tested on typical commercial, E10 fuel. The SOA formation potential dropped as the certification standard became more stringent. For the LEVII certification standard, Gordon measured 27.5 mg/kg-fuel compared to the 33.2 mg/kg-fuel measured in this work. Liu et al (2015) and Nordin et al (2013) also measured the SOA formation potential from gasoline vehicle exhaust and found that with the Euro1-4 emissions the SOA formation potential was approximately 22 mg/kg-fuel on average. This is slightly higher than what was measured for the LEVIII for this work at 10.5 mg/kg-fuel.

In regards to the higher ethanol content fuel, Suarez-Bertoa et al (2015) looked at the SOA formation potential of a GDI vehicle (Euro 5a certification standard) measured that on average there was an SOA formation potential of 11.6 mg/kg-fuel. This once again is right in line what was measured in this work for the E30 fuels and the E78 fuels tested. Ultimately, this work falls right in line with many previous studies.

5.4.1 Non-Methane Hydrocarbon Relationships:

The secondary organic aerosol formation (SOA) formed from vehicles in Table 1 are compared to their respective non-methane hydrocarbons (NMHC) emission factor. In the following comparisons, all vehicles, and fuels will be initially combined into a single plot. The data will then be separated by varying engine certifications, and fuel compositions to further explore notable trends.

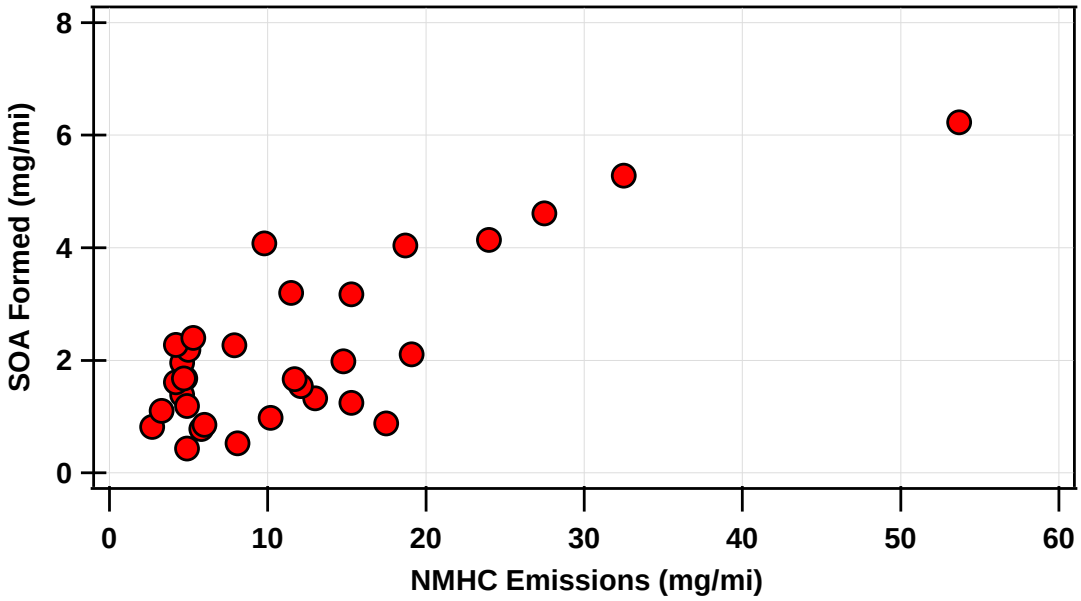

Figure 5-2: Plot comparing the SOA formation to the NMHC emissions of the nine vehicles tested, with all fuels, and all driving cycles included

Figure 5-2 shows the SOA formation for all vehicles, in all testing configurations vs the NMHC emission factor from the vehicles. There is a convincing increasing trend in SOA formation with the increased NMHC emissions. This result is expected due to NMHC emissions being the complex mixture consisting of the reactants that undergo oxidation reactions to ultimately form SOA (Kroll and Seinfeld, 2008). The increasing trend is definitive, however there is variability in the measured data. The higher emitting vehicles (NMHC emissions >20mg/mi) display a linear increasing trend. When the emission factor increases, there is a simultaneous and consistent increase in the SOA formation.

The aerosol formation from the experiments with lower NMHC emission factors (<20 mg/mi), however, display much more variability. This result could be due to a host

of reasons; lower VOC concentrations in the chamber experiments, variability in the composition of the NMHC emissions, or error within the formation and measurement of SOA in chamber experiments. The duration of this section will focus on separating and evaluating the variations in the experimental conditions.

The first distinction in aerosol formation explored focused on observing any variability due to engine certification standards. Previous work by Gordon et al observed different SOA formation from different engine certification standards. Thus here we explore if any clustering was present in the data set. Specifically, we probe two different certification standards of vehicles; LEVII (V1, V2, V3, V4, V6, V7, V8) and LEVIII (V5, VX). In this figure only similar fuel tests, and the similar drive cycle tests were included. Meaning in the below figure, only cold-start LA92 cycles, and only vehicle tests were operated on fuel containing 0%-20% ethanol content by volume.

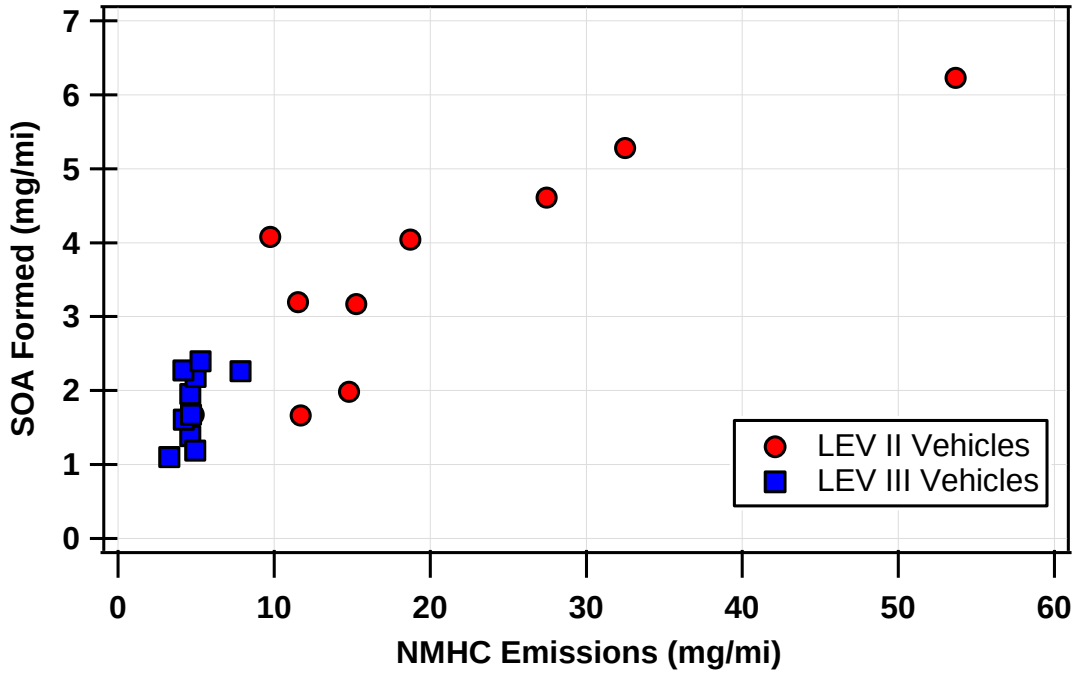

Figure 5-3: Plot of the SOA formation vs NMHC emissions for the cold-start LA92 driving cycles, and E0-E20 fuels separated by certification standard of the engine (LEVII (red) & LEVIII(blue))

Figure 5-3 shows some obvious clustering with the two different certification standards. The older more relaxed certification standard LEV II has more spread in NMHC emissions and SOA formation, while the more stringent certification LEVIII bunched to the lower left corner. On average the NMHC emissions were reduced from 20.03 mg/mi to 4.87 mg/mi (76% reduction). As a result, the SOA formation was decreased from 3.59 mg/mi to 1.80 mg/mi (50% reduction). This, in addition to the 36% average reduction in the tailpipe PM, ultimately results in a 42% reduction in the total carbonaceous aerosol emitted from the vehicles (including black carbon, POA, and SOA). The results indicate

that as the certification standards are increasing, regulators are effectively reducing the tailpipe aerosol and also reducing the SOA potential from vehicle exhaust.

Next, to further explore the variation observed in the lower emissions factors in Figure 5-2, the vehicles were split by the fuels. Variations in fuel's ethanol content are directly related to the varying gas phase composition and thus SOA forming potential of the emissions. For this comparison, the vehicles were split into two categories; low ethanol blends (0-20% ethanol by volume), and mid to high ethanol blends (30%-78% ethanol by volume). All results in this comparison utilized data on similar driving cycles (cold-start LA92), however for the very few experiments with E30-E78 fuels all drive cycles (hot-start and cold-start LA92) were used in the analysis.

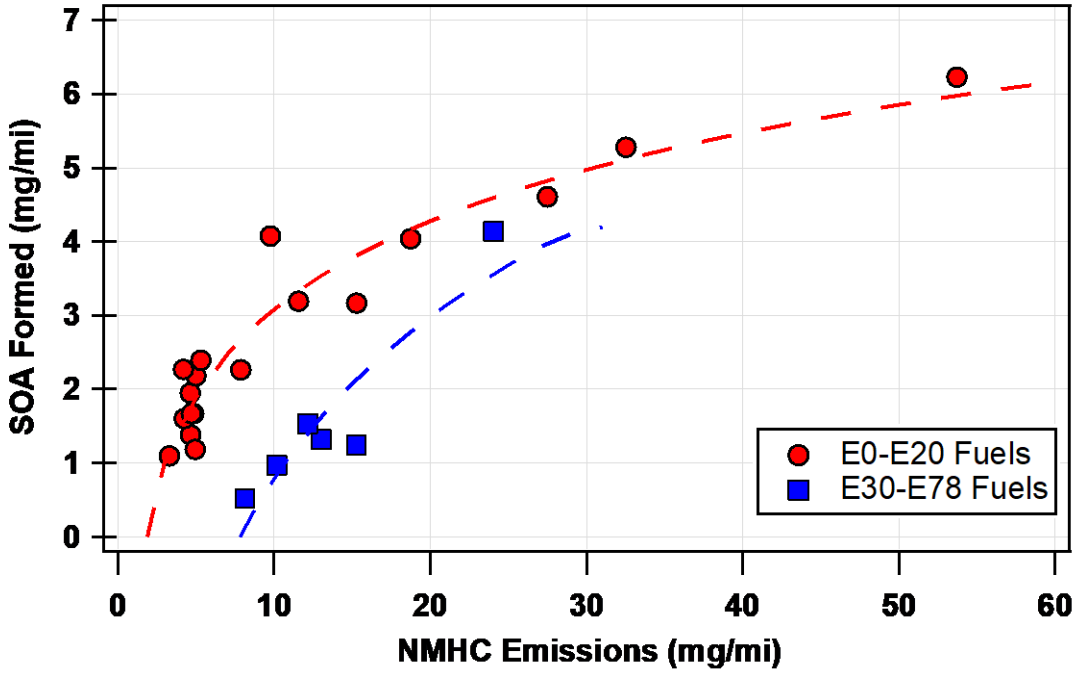

Figure 5-4: Plot of the SOA formation vs NMHC emissions for the cold-start LA92 driving cycle experiments operated on the E0-E20 test fuels, and all driving cycle experiments operated on the E30-E78 fuels

Contrary to Figure 5-3, where the different certification standards clustered together, the groups in Figure 5-4 showed similar increasing trends between the two categories with the main difference being the shift right for the mid to high ethanol blended fuels. The experiments shown for the E0-E20 fuels show a strong natural log relationship between NMHC emissions and SOA formation (R^2=0.92). This relationship agrees with the work done by Saliba et al (2017) where the composition of the emissions are similar enough such that a trend can be observed between the emission factors of the NMHC and SOA. Interestingly, the high ethanol blends also display a trend (R^2=0.83) even with the limited data points. This distribution falls below the lower ethanol fuel blend trend line,

indicating that a similar NMHC emission factor will result in a lower SOA formation potential.

The NMHC emission factors for the two fuel content groups were virtually identical with an average of 13.8 mg/mi for both the E0-E20 and the E30-E78 groups. However, when comparing the average SOA formation from these two groups, there is a 46% reduction in the SOA for the high ethanol blends compared to the low ethanol blends. This is most likely attributable to variations in the composition of the NMHC emitted from the tailpipe. The reduction is reasonable, as the addition of ethanol will displace some of the heavier, less volatile components in fuel. Less volatile compounds require fewer reactions to form SOA. The results shown here indicate that similar mass emissions are yielding smaller, more volatile products which would ultimately have lower yields of SOA formation.

5.4.2 Yield Relationships:

For the yield calculations, it was assumed that 100% of the total hydrocarbon (THC) emissions were consumed. The yield varied based on the concentration of HC present, and the reactivity of the environment (i.e. VOC:NOx ratio). Typically the yield curves are lognormal in distribution and at the plateau, would be considered the maximum yield of formation from a single precursor or mixture.

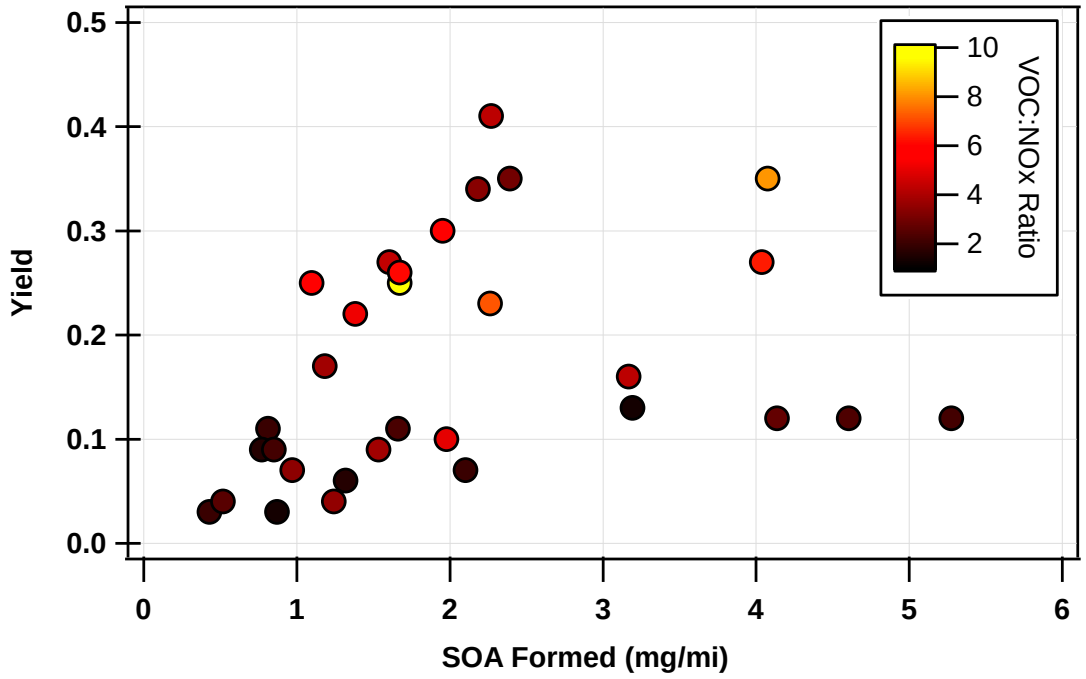

Figure 5-5: Yield vs the SOA formed for the vehicle exhaust irradiation experiments from all vehicles, driving conditions, and fuels

Figure 5-5 shows all vehicles, in all testing configurations and fuels, vs the SOA formed in the irradiation experiments. In Figure 5-5 there is no convincing trend (natural log trend with R^2=0.14). With this wide spread variation in yields and SOA formation, modelers would struggle to have confidence in a predicted SOA yield from the emissions data. However, the deviation in the data does seem to display trends in regards to the VOC:NOx ratios (color scale). To further investigate this, the experiments were separated into two groups; a VOC limited regime (VOC:NOx ratio <3) and a moderate VOC regime (10 > VOC:NOx > 3) as shown in Figure 5-6 and Figure 5-7. The moderate VOC regime would be most similar to atmospheric conditions.

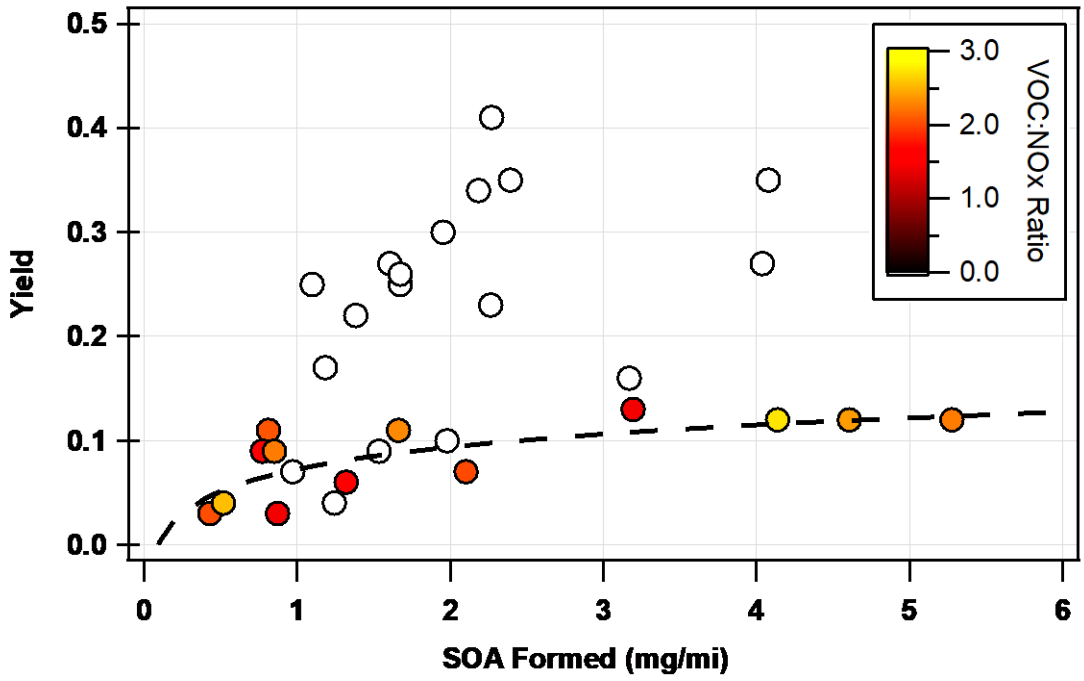

Figure 5-6: Yield vs the SOA formed for the vehicle exhaust irradiation experiments for all experimental conditions with a VOC:NOx ratio less than 3.0 (white circles are experiments with VOC:NOx greater than 3.0)

Figure 5-6 shows only the yields for vehicle tests with an VOC:NOx ratio below 3.0. The experiments in this category would be considered to be VOC limited. Previous work studying yield in different conditions have found that in VOC limited or excess NOx environments, produce a lower SOA yield (Kroll, et al, 2005). This is what is observed for the vehicles measured throughout this work. A log normal fit line was calculated for these subset of experiments, and it was found that the plateau that is typical in yield curves appears to level off around 0.13 indicating that in a regime with excess NOx, it is expected for 13% of the tailpipe NMHC emissions mass to ultimately form SOA mass. The R^2 for

the log normal trend for the VOC limited regime was measured to be *0.56* which still displays a large variability however due to the complexity of the experiments, is much improved.

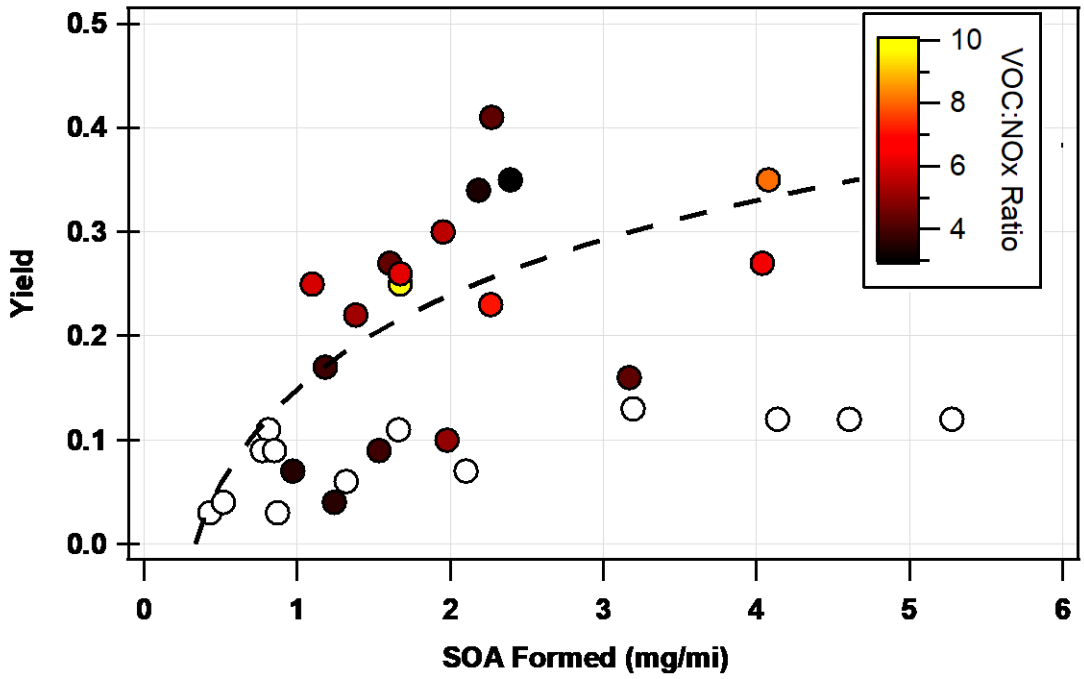

Figure 5-7: Yield vs the SOA formed for the vehicle exhaust irradiation experiments for all experimental conditions with a VOC:NOx ratio between 3.0 and 10.0 (white circles are experiments with VOC:NOx less than 3.0)

Figure 5-7 shows the more atmospherically relevant VOC:NOx ratios; between 3 and 10. In this regime, the yield curve increases much more quickly, resulting in a higher plateau level (~0.35). The log normal R^2 did increase up to *0.27* displaying a stronger trend, however there still is quite a bit of variability with this data. Experiments with similar SOA formation, have much higher yields meaning less NMHC emissions are

needed to form comparable SOA. As a result, in these conditions, reactivity is increased in relation to the organic species resulting in a larger SOA formation. The values measured here are in the same realm of yield as many aromatic species (Benzene 27%, Toluene 30%, xylenes 35% yields etc) (Derwent, et al, 2010). This may indicate that SOA formation from vehicle exhaust most commonly mimics the yields measured for single aromatic species.

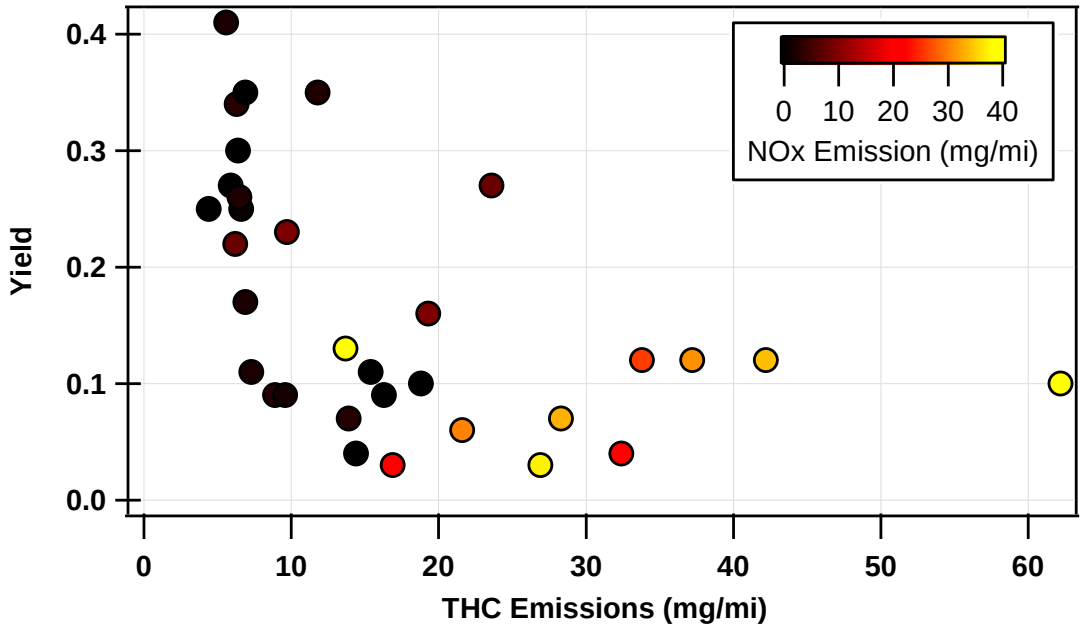

Figure 5-8: SOA yield vs the THC emission factor for all vehicle tests in all driving cycles and fuel compositions. The color scale relates to the NOx emission factor

Another relationship that was explored was the SOA yield vs the THC emissions. This result displayed some interesting results where the highest yields measured correlated with the lowest THC emission factors. This is contrary to what typically occurs, where increased gas phase concentration, results in a higher SOA yield, given other reactive gas

phase species are constant. One reason may be that for all vehicles with a low THC emission factor, the NOx emission factors were also low. This resulted in a "low NOx" regime as discussed in the previous section.

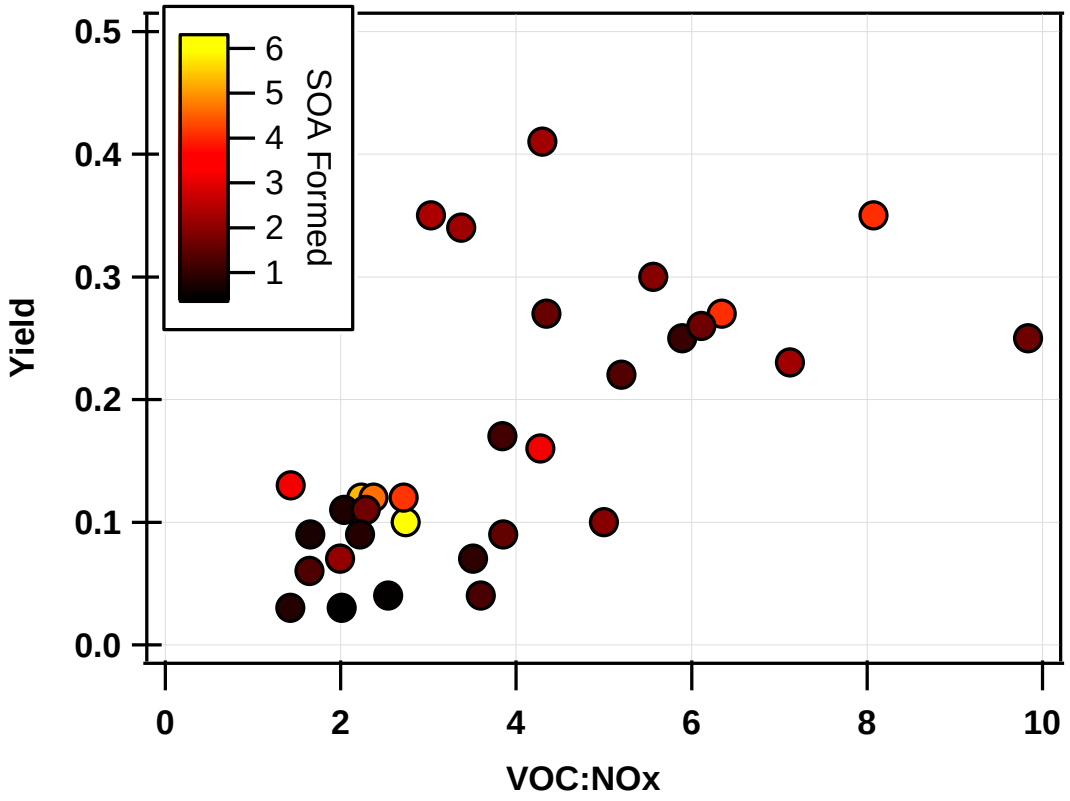

Figure 5-9: SOA yield vs the VOC:NOx ratio for all vehicles in all driving conditions, and fuel compositions. The color scale relates to the SOA emission factor measured in irradiation experiments.

The last trend with yield that was explored focused on the the yield vs the THC:NOx ratio (with color determined by the amount of SOA formed) (Figure 5-9). As the VOC:NOx ratio increased, so did the measured yield. This conclusion was reported in

the relationship with the two different yield curves, however this is a new way to visulize the effect that the reactivity can have on the yields. With this, it is hard to conclude what SOA would form in which condition so it is not as useful for researchers when exploring the SOA potential from the vehicle exhaust.

5.4.3 Secondary Inorganic Trends

The inorganic aerosol formation that was observed in these chamber experiments, consisted of mainly ammonium nitrate. Ammonium nitrate is formed when nitric acid (formed through the oxidation of NO_x) reacts with gaseous NH_3. Ammonia is a secondary pollutant of the three way catalyst (TWC) rather than combustion product and is generated from NO and H_2 during the water gas shift reaction of CO (Suarez-Bertoa, et al, 2014). Ammonia formation in the TWC is enhanced at rich conditions where more CO can produce more H_2 (Calirotte, et al, 2013).

The ammonia concentrations were not measured for a majority of the tests, however it has been found that ammonia emissions correlate with CO emissions, due to the previously mentioned water gas shift reaction.

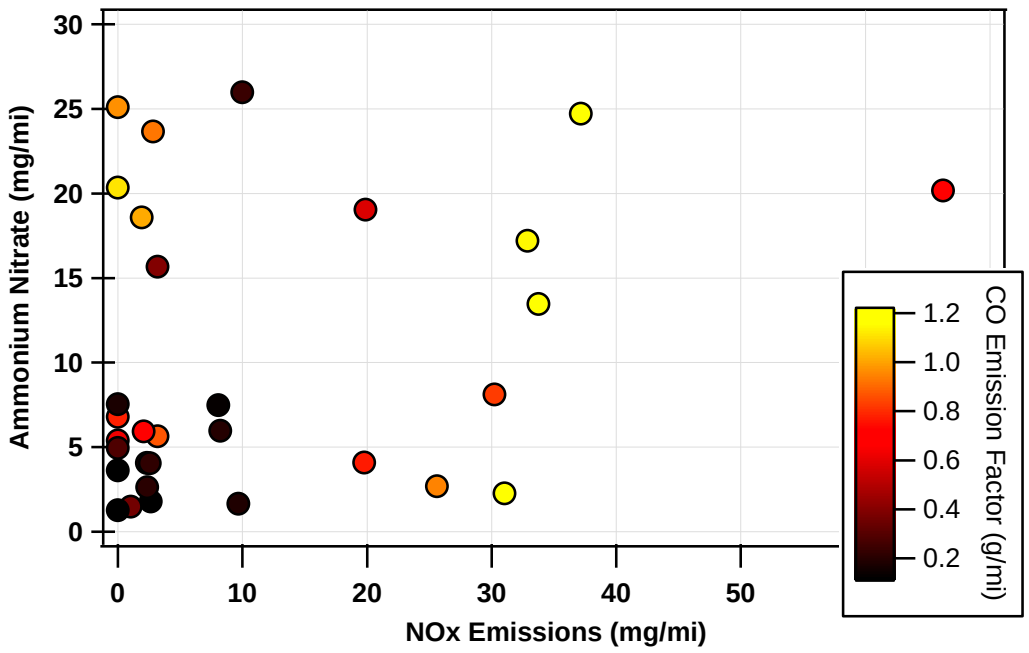

Figure 5-10: Ammonium nitrate formation vs the NOx emission factor for all vehicles over all test cycles, and fuels (color indicates CO emission factor)

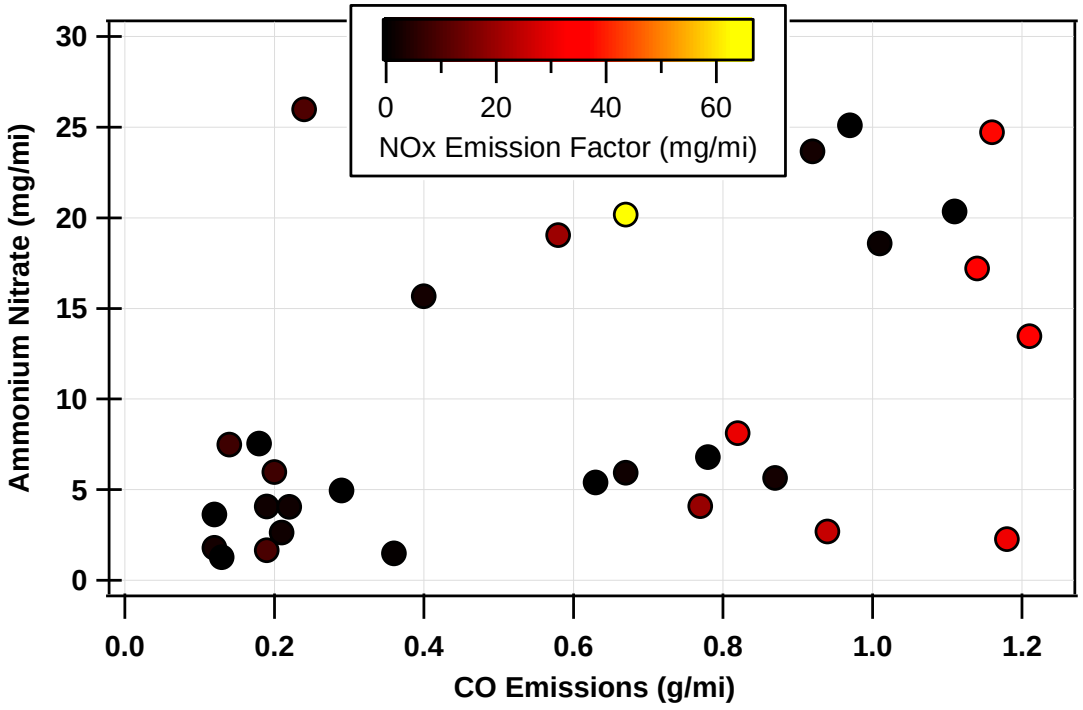

Figure 5-11: Ammonium nitrate formation vs the CO emission factor for all vehicles over all test cycles, and fuels (color indicates NOx emission factor)

Figure 5-10, and Figure 5-11 show the relationship with the ammonium nitrate formation and the emission factors for both NOx and CO. Neither CO nor NOx have a strong increasing trend with the ammonium nitrate concentration. From this it may be gathered that it is a combination of the two, or other factors may change the amount of formation from the system. It is also possible that the ammonia emissions from the GDI engines do not closely mimic the CO emissions as previously reported. More work is needed to fully understand the inorganic aerosol formation from the vehicle exhaust.

5.5. Conclusions & Future Work:

Strong trends were observed in the NMHC emission factor vs the SOA formation factor graphs (Figure 5-2). Within these data points, it was found that the stricter regulations (LEVII to LEVII) resulted in a 50% reduction in the SOA formation potential (42% reduction in total carbonaceous aerosol) (Figure 5-3). Another factor that affected the NMHC emissions' reactivity was the fuel composition (Figure 5-4). The trend for the mid to high ethanol fuel blends shifted to higher NMHC emission factors, indicating that a higher mass of emission was necessary for a similar SOA formation when compared to the lower ethanol fuel blends.

When utilizing the calculated yield for the experiments, no strong trend was observed when looking at the reactions as a whole (Figure 5-5). However, when the experiments were split into the VOC limited regime (VOC:NOx ratio <3) and moderate VOC regime (10 > VOC:NOx > 3), two stronger trends emerged (Figure 5-6, Figure 5-7). In the VOC limited regime, a smaller fraction of the total hydrocarbon mass converted to SOA mass; indicating the reaction of VOCs were constrained.

All vehicle tests completed utilizing UCR's Mobile Atmospheric Chamber has only measured emissions from GDI vehicles. In the future a study looking at the comparisons between older technology PFI engines compared to GDI engines with some varying conditions (driving conditions or fuels) may be useful to see if the mass of SOA formation are similar. Furthermore, it would be interesting compare the reactivity of the exhaust to see if the yield of PFI vehicles fall on a similar trend to what was observed for the GDI vehicles over the different reaction conditions. With this information, a more specific yield

could be determined for the different technologies and could be applied to vehicular emission models. With this information, modelers may be able to close the gap between predicted and measured SOA in the atmosphere.

Another important note from this work, is that the yield trends in this chapter may be specific to the emissions measured from cold-start LA92 driving cycles. As confirmed here, yield can vary due to a host of reasons, so it may be imperative for future researchers to investigate other driving conditions. If the vehicles are found to have varying composition of reactive organic gases in emissions due to variations in driving cycle, more work will be needed to understand how that will affect the SOA yield from the vehicle emissions.

The ammonium nitrate formation that was also measured did not appear to have any strong trends with the NOx or CO emission factors. More work is needed to determine the main contributing factor of the inorganic salt formation. It may also be important to measure the ammonia concentrations at the tailpipe. This may better allow the understanding of the formation of the inorganic salt in these irradiation experiments. It may also allow modelers to understand vehicular emissions impact on ammonium nitrate formation in the atmosphere. The emissions of ammonia from the tailpipe is not currently garnering much attention.

5.6. References:

1) Gentner, Drew R., Robert A. Harley, Angela M. Miller, and Allen H. Goldstein. **2009**. "Diurnal and Seasonal Variability of Gasoline-Related Volatile Organic Compound Emissions in Riverside, California." *Environmental Science & Technology* 43 (12): 4247–52.
2) Odum, J. R., T. P. Jungkamp, R. J. Griffin, R. C. Flagan, and J. H. Seinfeld. **1997**. "The Atmospheric Aerosol-Forming Potential of Whole Gasoline Vapor." *Science* 276 (5309): 96–99.
3) Gentner, D.R.; Jathar, S.H.; Gordon, T.D.; Bahreini, R.; Day, D.A.; Haddad, I.E.; Haynes, P.L.; Pieber, S.M.; Platt, S.M.; De Gouw, J.; Goldstein, A.H.; Harley, R.A.; Jimenez, J.L.; Prevot, A.S.H.; Robinson A.L. Review of urban secondary organic aerosol formation from gasoline and diesel motor vehicle emissions. *Environ. Sci. Technol.* **2017**, *51*, 1074-1093.
4) Bahreini, R.; Middlebrook, A. M.; de Gouw, J. A.; Warneke, C.; Trainer, M.; Brock, C. A.; Stark, H.; Brown, S. S.; Dube, W. P.; Gilman, J. B.; Hall, K.; Holloway, J. S.; Kuster, W. C.; Perring, A. E.; Prevot, A. S. H.; Schwarz, J. P.; Spackman, J. R.; Szidat, S.; Wagner, N. L.; Weber, R. J.; Zotter, P.; Parrish, D. D. Gasoline emissions dominate over diesel in formation of secondary organic aerosol mass. *Geophys. Res. Lett*. **2012**, *39*, L06805, doi: 10.1029/2011GL050718.
5) Saliba, G.; Saleh, R.; Zhao, Y.; Presto, A.A.; Lamber, A.T.; Frodin, B.; Sardar, S.; Maldonado, H.; Maddox, C.; May, A.A.; Drozd, G.T.; Goldstein, A.H.; Russell, L.M.; Hagen,, F.; Robinson, A.L. Comparison of gasoline direct-injection (GDI) and port fuel injection (PFI) vehicle emissions: Emission Certification standards, cold-start, secondary organic aerosol formation potential, and potential climate impacts. *Environ. Sci. Technol.* **2017**, *51*, 6542-6552.
6) Suarez-Bertoa, R.; Zardini, A.A.; Keuken, H.; Astorga, C. Impact of ethanol containing gasoline blends on emissions from a flex-fuel vehicle tested over the Worldwide Harmonized Light duty Test Cycle (WLTC). *Fuel* **2015**, *143*, 173-182.

7) Volkamer, Rainer, Jose L. Jimenez, Federico San Martini, Katja Dzepina, Qi Zhang, Dara Salcedo, Luisa T. Molina, Douglas R. Worsnop, and Mario J. Molina. **2006**. "Secondary Organic Aerosol Formation from Anthropogenic Air Pollution: Rapid and Higher than Expected." *Geophysical Research Letters* 33 (17): 4407.

8) Odum, Jay R., Thorsten Hoffmann, Frank Bowman, Don Collins, Richard C. Flagan, and John H. Seinfeld. **1996**. "Gas/particle Partitioning and Secondary Organic Aerosol Yields." *Environmental Science & Technology* 30 (8): 2580–85.

9) Aiken, A. C.; DeCarlo, P. F.; Kroll, J. H.; Worsnop, D. R.; Huffman, J. A.; Docherty, K. S.; Ulbrich, I. M.; Mohr, C.; Kimmel, J. R.; Sueper, D.; Sun, Y.; Zhang, Q.; Trimborn, A.; Northway, M.; Ziemann, P. J.;, Canagaratna, M. R.; Onasch, T. B.; Alfarra, M. R.; Prevot, A. S. H.,; Dommen, J.,; Duplissy, J.; Metzger, A.; Baltensperger, U.; Jimenez, J. L. O/C and OM/OC ratios of primary, secondary, and ambient organic aerosols with high-resolution time-of-flight aerosol mass spectrometry. *Environ. Sci. Technol.* **2008**, *42*, 4478-4485.

10) Decarlo

11) Malloy, Q.; Nakao, S.; Qi, L.; Austin, R. L.; Stothers, C.; Hagino, H.; Cocker, D. R. Real-Time Aerosol Density Determination Utilizing a Modified Scanning Mobility Particle Sizer-Aerosol Particle Mass Analyzer system. *Aerosol Sci. Technol.* **2009**, *43*, 673–678.

12) Cocker, D. R.; Flagan, R. C.; Seinfeld, J. H. State-of-the-art chamber facility for studying atmospheric aerosol chemistry. *Environ. Sci. Technol.* **2001**, *35*, 2594-2601.

13) Vu, D.; Roth, P.; Berte, T.; Yang, J.; Cocker D.; Durbin T.; Karavalakis, G.; Asa-Awuku, A. Using a new Mobile Atmospheric Chamber (MACh) to investigate the formation of secondary aerosols from mobile sources: The case of gasoline direct injection vehicles. Journal of Aerosol Science, Manuscript Under Review.

14) Pieber, S. M.; Kumar, N. K.; Klein, F.; Comte, P.; Bhattu, D.; Dommen, J.; Bruns, E. A.; Kilic, D.; El Haddad, I.; Keller, A.; Czerwinski, J.; Heeb, N.; Baltensperger, U.; Slowik, J. G.; Prévôt, A. S. H. Gas phase composition and secondary organic

aerosol formation from gasoline direct injection vehicles investigated in batch and flow reactors: effects of prototype gasoline particle filters. *Atmos. Chem. Phys.* **2018**, *18*, 9929-9954.

15) Timonen, Hilkka, Panu Karjalainen, Erkka Saukko, Sanna Saarikoski, Päivi Aakko-Saksa, Pauli Simonen, Timo Murtonen, et al. **2017**. "Influence of Fuel Ethanol Content on Primary Emissions and Secondary Aerosol Formation Potential for a Modern Flex-Fuel Gasoline Vehicle." *Atmospheric Chemistry and Physics* 17 (8): 5311–29.

16) Gordon, T. D., A. A. Presto, A. A. May, N. T. Nguyen, E. M. Lipsky, N. M. Donahue, A. Gutierrez, et al. **2014**. "Secondary Organic Aerosol Formation Exceeds Primary Particulate Matter Emissions for Light-Duty Gasoline Vehicles." *Atmospheric Chemistry and Physics* 14 (9): 4661–78.

17) Nordin, E. Z.; Eriksson, A. C.; Roldin, P.; Nilsson, P. T.; Carlsson, J. E.; Kajos, M. K.; Hellén, H.; Wittbom, C.; Rissler, J.; Löndahl, J.; Swietlicki, E.; Svenningsson, B.; Bohgard, M.; Kulmala, M.; Hallquist, M.; Pagels, J. H. Secondary organic aerosol formation from idling gasoline passenger vehicle emissions investigated in a smog chamber. *Atmos. Chem. Phys.* **2013**, *13*, 6101-6116.

18) Liu, T.; Wang, X.; Deng, W.; Hu, Q.; Ding, X.; Zhang, Y.; He, Q.; Zhang, Z.; Lu, S.; Bi, X.; Chan, J.; Yu, J. Secondary organic aerosol formation from photochemical aging of light-duty gasoline vehicle exhausts in a smog chamber. *Atmos. Chem. Phys.* **2015**, *15*, 9049-9062.

19) Kroll, J.H.; Seinfeld, J.H. Chemistry of secondary organic aerosol: Formation and evolution of low-volatility organics in the atmosphere. *Atmospheric Environment* **2008**, *42*, 3593-3624.

20) Kroll, Jesse H., Nga L. Ng, Shane M. Murphy, Richard C. Flagan, and John H. Seinfeld. **2005**. "Secondary Organic Aerosol Formation from Isoprene Photooxidation under High-NOx Conditions." *Geophysical Research Letters* 32 (18). https://agupubs.onlinelibrary.wiley.com/doi/abs/10.1029/2005GL023637.

21) Derwent, Richard G., Michael E. Jenkin, Steven R. Utembe, Dudley E. Shallcross, Tim P. Murrells, and Neil R. Passant. **2010**. "Secondary Organic Aerosol Formation from a Large Number of Reactive Man-Made Organic Compounds." *The Science of the Total Environment* 408 (16): 3374–81.

22) Suarez-Bertoa, R., A. A. Zardini, and C. Astorga. **2014**. "Ammonia Exhaust Emissions from Spark Ignition Vehicles over the New European Driving Cycle." *Atmospheric Environment* 97 (November): 43–53.

23) Clairotte, M., T. W. Adam, A. A. Zardini, U. Manfredi, G. Martini, A. Krasenbrink, A. Vicet, E. Tournié, and C. Astorga. **2013**. "Effects of Low Temperature on the Cold Start Gaseous Emissions from Light Duty Vehicles Fuelled by Ethanol-Blended Gasoline." *Applied Energy* 102 (February): 44–54.